Disorder-induced spin liquids

Tomás Stephen Northam de la Fuente

A DISSERTATION SUBMITTED TO THE UNIVERSITY OF LONDON FOR THE DEGREE OF DOCTOR OF PHILOSOPHY

December 2022

Declaration of Authorship

I, Tomás Stephen Northam de la Fuente, hereby declare that this thesis and the work presented in it is entirely my own. Where I have consulted the work of others, this is always clearly stated.

Signed: _____

Date: _____

Abstract

Structural and magnetic studies of the disorder-induced classical spin liquid $Ho_2Ti_{2-x}Sc_xO_{7-x/2}$ and the candidate quantum spin liquid Pr_2ScNbO_7 were performed through a combination of neutron scattering techniques and computational modelling.

Disorder was investigated in $Ho_2Ti_{2-x}Sc_xO_{7-x/2}$ with $x = 0$, $x = 0.1$ and $x = 0.5$ by doping with Sc ions. The difference in valency between Ti^{4+} and Sc^{3+} led to the need for charge compensating oxygen vacancies. This allowed the introduction of oxygen vacancies in a controlled manner throughout the structure uniformly. Total scattering and structural diffuse scattering measurements were performed in conjunction with RMC fits, Bragg refinements and *ab initio* density functional theory (DFT) calculations to determine the location of the vacancies. Not only was it found that the vacancies are located at O(2) sites but, in addition, other O(2) ions were displaced towards the centre of the tetrahedra formed by the B-sites.

Crystal electric field (CEF) measurements were performed to determine the effect of the vacancies on the single-ion magnetism. It was found that the ground state doublet of the Ho ions next to a vacancy split into two singlets separated by an energy of 0.12 meV. However, calculations performed at 0.5 K and with a 0.1 T applied magnetic field show that the Ho ions next to a vacancy developed a moment of 6.2 μ_B mostly along the $\langle 111 \rangle$ direction but with a 15.2° tilt towards the vacancy. Magnetic diffuse scattering measurements were performed to study the effects of disorder on the cooperative magnetism. While the resulting scattering is qualitatively similar to that of stoichiometric $Ho_2Ti_2O_7$ [1, 2], the pinch point width broadened as the levels of doping increased. It is possible that this broadening is caused by the tilting of the moments at the defective-Ho sites.

The structural arrangement of Sc and Nb ions in the highly substituted Pr_2ScNbO_7 system was studied by means of neutron scattering, DFT and RMC fits. It was found that the structure with the lowest energy contains a charge ice structure with equal numbers of Sc and Nb ions in each tetrahedron and with chains of alternating Sc and Nb. However, this structure is chemically frustrated, since the alternating chains cannot be accommodated in all directions. Total scattering calculations show that no long-range order of this lowest energy structure exists, and diffuse scattering calculations using a single unit cell of the lowest energy structure are in excellent agreement with the measured data. This suggests that the structure comprises small domains of the lowest energy structure with Sc/Nb disorder at the domain walls.

CEF analyses were performed on Pr_2ScNbO_7 to study the effect of the disorder on the single-ion magnetism. CEF fits were performed on the data, assuming a D_{3d} symmetry at the Pr sites. This resulted in a doublet ground state, with the first excited state at 2.7 meV. The lowest energy DFT structure contains two different Pr sites. Point-charge-model CEF calculations predict singlet ground states for both Pr sites, with the first excited state at 1.2 meV and 4.6 meV. Furthermore, both sites form spiral one-dimensional chains. Magnetic diffuse scattering measurements were performed to study the effects of the disorder on the cooperative magnetism, producing uncorrelated scattering. The one-dimensional arrangement of these ions could explain the measured uncorrelated scattering. These measurements were used to extract a Pr effective magnetic moment of 2.10(8) μ_B. Finally, low energy excitation studies show that, when subtracting the 5 K data from the lower temperature data, a peak near 0.7 meV energy transfer is present, very similar to the ones found in $Pr_2Zr_2O_7$ [3] and $Pr_2Hf_2O_7$ [4], which were claimed to be a signature of cooperative quantum fluctuations.

Acknowledgements

The work performed in this thesis could have not been done without the support of the people that help me in many aspects of my life.

To my RHUL supervisor Jon Goff, thank you for all the guidance and help throughout these past three years, and for giving me an even more profound appreciation for the experimental sciences. Even in the most difficult times, your constant support was a great source of reassurance. And, of course, thank you for putting up with all my questions. Working with you has been a great opportunity.

To my ILL supervisor Lucile Mangin-Thro, for all those long days performing experiments, aligning crystals and, of course, for the constant optimism. Thank you for putting up with me and my constant visits to your office. You were a huge inspiration and made me realise that I want to pursue a career as an instrument scientist. And of course Andrew Wildes, for those quick discussions where we started with a single science question and spent hours talking about a million other things.

To Thomas Hicken for performing all those DFT calculations and for all the discussions on the data interpretation. To Claudio Castelnovo, Li Ern and Attila Szabó, for their theoretical interpretations, predictions and calculations. To Dharmalingam Prabhakaran and Cole Mauws, for growing incredible samples, being the only student at the ILL having a "too large sample" problem.

To all the instrument scientists we worked with: David Voneshen, Matthias Gutmann, Tatiana Guidi, Duc Le, Ketty Beauvois, Helen Playford, Ron Smith, Gabriele Sala, Matthew Stone, Christian Balz, Igor Levin and many more. Thanks for all the support and help you provided, especially through a period when many of the experiments were performed remotely. And of course all the other scientist I met at the ILL and ISIS. Let's hope for a collaboration in the near future.

To my family (and my cats), who were there whenever I needed and supported me emotionally. Thank you for taking me in when the pandemic started.

To the entire PhD community at the ILL, for welcoming me in with open arms. Even through a pandemic, we managed to pull through, all of us together with a smile. A special thanks to Ronja for making every lunch break a unique one. And also to Maria, Pelayo and Esther, for making my last summer in Grenoble writing the thesis more bearable.

To all my friends in Spain: Valentina, Alex, Maria Isabel, Alberto, Maria and Pedro. Even though we could only see each other a few times these past three years, every moment with you was unrepeatable. To my longest lasting friend, Carlos. Reminiscing about our childhood was a great break from reality.

To one of my best friends from undergrads, Chris, for those sparse but long conversations about a million and one topics. I blame you for showing me the wonderful world that is experimental physics.

To Berta Ponce, for helping me keep my sanity intact.

Contents

List of Figures

List of Tables

Chapter 1

Introduction

1.1 What are pyrochlores?

The focus of this thesis will be on oxide pyrochlores (or pyrochlore for short), with general formula $A_2B_2O_7$, where the A and B atoms are cations.

Pyrochlores belong to the crystallographic space group $Fd\bar{3}m$ (227) and contain 8 formula units per conventional unit cell. The lattice of the pyrochlore can be separated into 2 sub-lattices, as figure 1.1 shows, with the first sub-lattice composed of the B cations surrounded by 6 O(2) ions, and a second sub-lattice composed of the A cations forming tetrahedra surrounding O(1) ions. Because of this, the general formula of pyrochlores is sometimes expressed as $A_2B_2O(2)_6O(1)$. These two sub-lattices form a cubic unit cell where the side length usually ranges between 9 and 11 Å [6]. The A and B sites form 3D arrays of corner sharing tetrahedra, which has key implications for the magnetic properties of pyrochlores [7], as will be shown later on in the thesis.

Usually, either an A or B site is chosen as the origin for the pyrochlore unit cell. Table 1.1 shows the ion species, location and coordinate for a unit cell with a B site as the origin. The location is composed of two values: a number that represents the multiplicity or how many of that specific ion exist in the unit cell, and a Wyckoff letter to label that specific site (it has no physical meaning) [8]. To generate the entire unit cell structure, each of the coordinates of the 4 distinct ions is added to the 4 site symmetries in the first row of table 1.1. So to generate all A sites you add all the coordinates to (0,0,0), then (0,1/2,1/2), then (1/2,0,1/2); and finally (1/2,1/2,0), and similarly for the other 3 ions. Pyrochlores have 192 possible symmetry operations (an operation on the system that leaves it unchanged), 48 for each site symmetry [8].

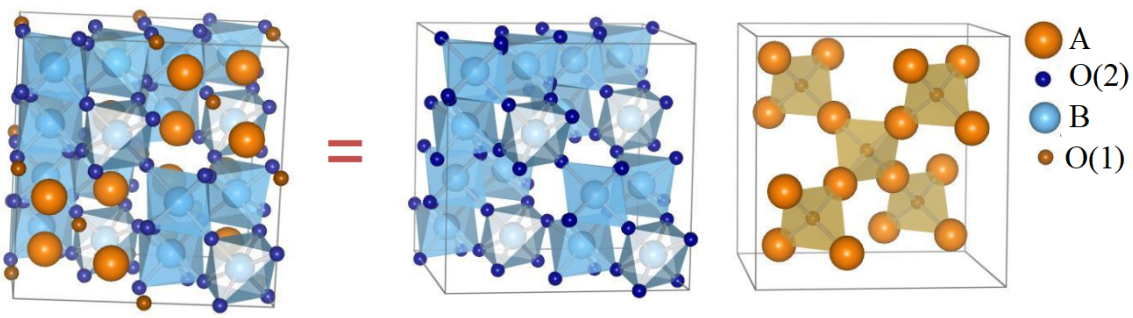

Figure 1.1: Separation of the pyrochlore lattice into 2 sub-lattices. Figure acquired from [5].

Table 1.1: Pyrochlore structure data from [6].

Ion	Location	coordinates
		(0,0,0; 0,1/2,1/2; 1/2,0,1/2; 1/2,1/2,0) +
A	16d	1/2,1/2,1/2; 1/2,1/4,1/4; 1/4,1/2,1/4; 1/4,1/4,1/2
B	16c	0,0,0; 0,1/4,1/4; 1/4,0,1/4; 1/4,1/4,0
O(2)	48f	x,1/8,1/8; -x,7/8,7/8; 1/4-x,1/8,1/8; 3/4+x,7/8,7/8; 1/8,x,1/8; 7/8,-x,7/8; 1/8,1/4-x,1/8; 7/8,3/4+x,7/8; 1/8,1/8,x; 7/8,7/8,-x; 1/8,1/8,1/4-x; 7/8,7/8,3/4+x
O(1)	8b	3/8,3/8,3/8; 5/8,5/8,5/8

The x-coordinate in table 1.1 characterises the "shape" the O ions form around the A and B sites [6]. In the full pyrochlore structure, the A cations have an ionic radius of $\sim$1 Å and have a coordination number of 8, corresponding to 6 O(2) and 2 O(1) nearest neighbour ions, with the A-O(2) bond lengths longer than the A-O(1) bond lengths by 0.2–0.3 Å. On the other hand, B cations have a smaller ionic radius of $\sim$0.6 Å and have a coordination number of 6, corresponding to the octahedra of the surrounding O(2) ions, with all 6 B-O(2) bonds of equal length. These 8 and 6 coordinations are sometimes referred to as cubic and octahedral coordination respectively [6]. However, due to symmetry constraints, either the 8 coordination is a regular cube or the 6 coordination is a regular octahedron, both cannot simultaneously form regular polyhedra. In fact, in most pyrochlores, both coordinations form irregular polyhedra. The shape of the polyhedra is determined by the x-coordinate of the O(2) ions, known as the positional parameter of the pyrochlore. Using a B site as the origin of the cell, when x=0.3125 the 6 coordinate is a perfect octahedron (see figure 1.2a) while when x=0.375 the 8 coordination is a perfect cube (see figure 1.2b). Typical x values range from 0.309 to 0.355 [6].

There are many forms of classifying pyrochlores into subfamilies, but the most common way is by the valency of the A and B cations: (3+,4+) pyrochlores, where the valency of the A and B cations are 3+ and 4+ respectively, and the (2+,5+) pyrochlores with valencies 2+ and 5+. Here the focus will be on (3+,4+), which corresponds to the majority of the pyrochlores. The A^{3+} ions are usually ions such as rare earths, Y and

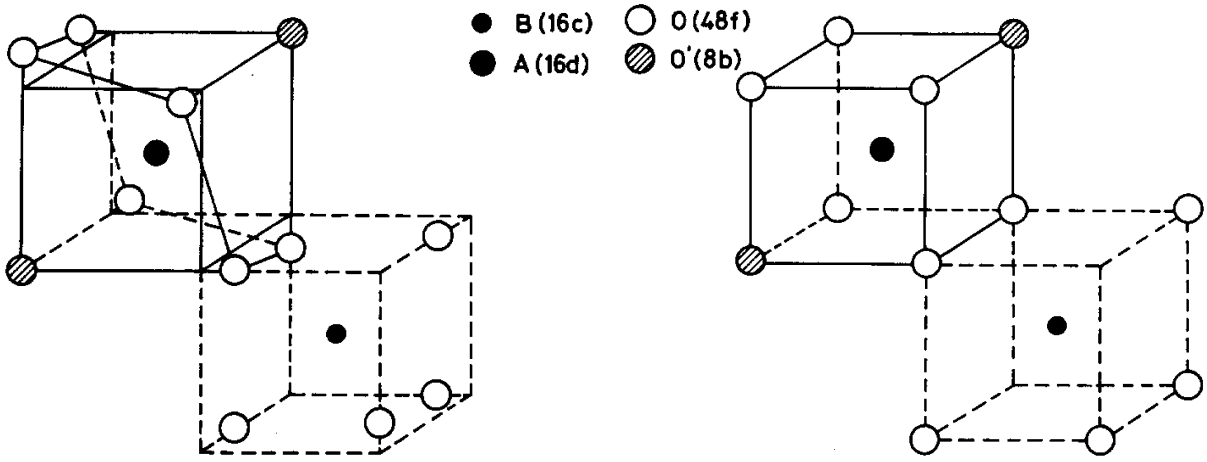

(a) (b)

Figure 1.2: Change in shape of coordination for the A and B ion. (a) When $x = 0.3125$, the oxygen ions form a perfect octahedron around the B ion. (b) When $x = 0.375$, the oxygen ions form a perfect cube around the A ion. Figures acquired from [6].

Bi, while the B^{4+} ions are usually transition metals or any of the group IVa elements [6]. Due to the wide variety of possible A and B combinations, only restricted by the ionic radius and charge neutrality, pyrochlores are of great interest. Pyrochlores exhibit a wide range of properties depending on the precise composition: superconductivity [9, 10], semiconductivity [11, 12], ferromagnetism and antiferromagnetism [13–15], and magnetic frustration which will be one of the foci of this thesis. This diversity of behaviour lends itself the possibility for a wide range of applications, both potential and realised, including: solar energy conversion [16, 17], nuclear waste disposal [18, 19], electrocatalysis [20, 21] and thermal barrier coating [22, 23].

These properties can be altered by introducing disorder into the system in the form of doping (substitution of an A or B ion by a new species), stuffing (changing A ions by B ions or vice-versa), vacancies, etc. In this thesis, the main focus will be on pyrochlores with disorder arising from ion substitution on the B sites and oxygen removal. If a large amount of these types of disorder is introduced in a pyrochlore, a phase transition may occur to a defect fluorite structure ($[AB]_2\,O_7$) [24].

Before describing the defect fluorite, the "ideal" fluorite needs to be considered. In the fluorite structure (BO_2) shown in figure 1.3a, the cations form edge shearing tetrahedra, since all of them are of the same species [25]. In pyrochlores, on the other hand, half of the tetrahedra are formed by the A cations and the other half by the B cations, and thus the cations form corner sharing tetrahedra. If the tetrahedra of a fluorite were labelled like those from a pyrochlore, one can distinguish from figure 1.3 three different oxygen sites: the 48f sites (O(2) ions), surrounded by two A and two B sites, the 8b sites (O(1) ions), surrounded by 4 A sites, and the 8a sites surrounded by 4 B sites [25]. The key difference between the pyrochlore and a fluorite is that the 8a site in a fluorite is always occupied by an oxygen, while in a pyrochlore the 8a site is empty. Furthermore, the x value of the 48f oxygen in a fluorite is 0.375. The defect fluorite is a variant of the fluorite where the A and B cations are randomly distributed and not separated as in the pyrochlore, and all oxygen sites are occupied equally with an average probability of 7/8, i.e. an oxygen vacancy can be found in any of the 3 oxygen sites [25]. An example of a phase transition from a pyrochlore to a defect fluorite was found in $Ho_2Ti_{2-x}Zr_xO_7$ by Drey *et al.* [26] at

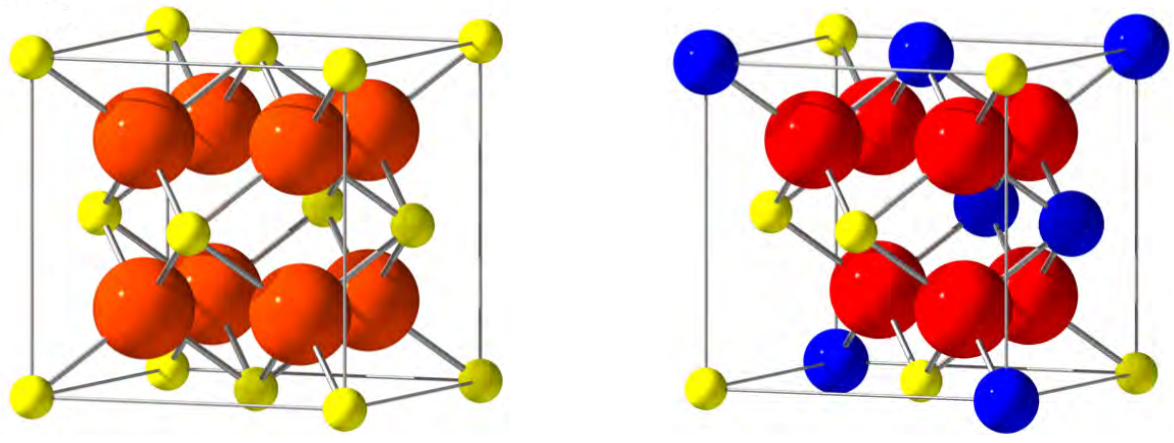

(a) (b)

Figure 1.3: (a) The fluorite structure, with the yellow spheres as the B^{4+} ions and the red spheres as the O^{2-} ions. (b) 1/8 of the pyrochlore structure, with the blue spheres as the A^{3+} ions, the yellow spheres as the B^{4+} ions and the large red spheres as the O^{2-} ions. Figures acquired from [25].

high levels of doping ($x > 1$). Some systems, such as $Ho_2\,(Ti_{1.33}Ho_{0.67})\,O_{6.67}$ [27], may have a mixture of both structures in the form of clusters.

1.2 What are frustrated systems?

Many pyrochlores containing magnetic ions exhibit a property known as frustration. Frustration can arise in many systems, such as liquid crystals [28], colloidal monolayers [29], Core-Collapse Supernova Matter [30] and water ice [31]. However, the focus of this thesis will be on frustration in magnetic systems. The study of magnetically frustrated systems is not new, since these types of systems were being investigated even before the term "frustration" was coined [32, 33]. Due to this frustration, these systems exhibit properties not found in conventional magnets, such as enhanced magnetocaloric effects [34], zero or negative thermal expansion [35], enhanced conductivity [36] and enhanced insulation [37]. Because of this, some of the applications of frustrated magnets are in refrigeration [38] and hardware for implementing neural networks [39].

Depending on the level of disorder, magnetically frustrated systems are generally separated into spin glasses, where frustration arises due to site disorder, and geometrically frustrated systems, where disorder is not needed to produce frustration [40]. Geometrically frustrated systems, as the name indicates, arise due to the site-site interactions being in conflict as a result of their arrangement in a particular phase [41]. Because of this, some geometrically frustrated systems are very sensitive to structural disorder, breaking frustration in the presence of small deviations from stoichiometry [42].

One of the origins of geometrical frustration in magnetism is in the exchange interactions and coupling constant $\mathcal{J}$. Depending on the exchange interaction between electrons, given by the sign of $\mathcal{J}$, spins can arrange parallel or antiparallel to each other to minimise the total energy of the system [43]. Thus, in a conventional ferromagnet all the exchange interactions are satisfied by aligning the moments parallel to each other, and similarly in a conventional antiferromagnet with antiparallel neighbouring moments. However, in a magnetically frustrated system the exchange interactions cannot all be satisfied simultaneously [44] which leads to the system having a highly degenerate ground state since there is no unique arrangement of magnetic moments that minimises the energy. This degeneracy is not unique to just magnetic systems, as a system with a highly degenerate ground state is often called frustrated independent if the system is magnetic or not [41]. This degeneracy results in these systems having a non-zero residual entropy (entropy that persists even if the system is cooled arbitrarily close to 0 K) which can be controlled by an external magnetic field [41]. The evolution of the entropy with temperature allows for the determination of frustrated systems experimentally, with the drop in entropy near the ordering temperature for unfrustrated magnets being much more pronounced than for frustrated magnets [40].

Another very common method of experimentally identifying geometrically frustrated systems is through the magnetic susceptibility χ. At high temperatures, the susceptibility follows the Curie-Weiss law [40]

$$\chi = \frac{C_C}{T - \Theta_{CW}} \tag{1.1}$$

where C_C is the Curie constant, T the temperature and Θ_{CW} the Curie-Weiss temperature defined as the temperature below which the ferromagnetic or antiferromagnetic interactions activate [45]. Θ_{CW} is generally also used to indicate the strength of the dominant

magnetic interaction [46]. Usually it is $1/\chi$ that is studied as a function of temperature, since at high temperatures $1/\chi$ follows a straight line. However, in conventional magnets, as the temperature reaches Θ_{CW}, $1/\chi$ diverges from its linear dependence. This is a way of measuring the ordering temperature T_C of magnetic systems, which for unfrustrated systems $T_C \approx |\Theta_{CW}|$. In frustrated systems the ordering temperature is much lower due to the competition of the different exchange interactions that an individual moment feels, resulting in $1/\chi$ diverging from its linear dependence at a much lower temperature than Θ_{CW}. Due to these competing interactions, T_C is sometimes defined as the temperature at which ordering freezes out [47, 48].

With the definitions of T_C and Θ_{CW}, the degree of frustration in a magnetic system can be defined using the frustration parameter f [49]

$$f = \frac{|\Theta_{CW}|}{T_C} \tag{1.2}$$

This parameter can take any value between 1 for a ferromagnet [40] to ∞ for quantum spin liquid systems, which will be discussed further in the thesis. Non-frustrated antiferromagnetic systems have an f value between 2 and 5 [50]. A system with $f > 10$ is said to be strongly frustrated and where simple theories such as mean-field theory fail [40]. Finally, it is worth mentioning that the frustration parameter is not only highly dependent on the shape or structure of the lattice, but also on the dimensionality of the system [49].

In 2D systems, and to an extent in 3D as it will be shown later on, structures with triangular symmetry very commonly exhibit a form of geometric frustration. In a 2D system, the simplest way to visualise a geometrically frustrated magnetic system is through the triangular antiferromagnetic lattice, shown in figure 1.4a, where the spins are equidistant to each other and feel the same nearest neighbour antiferromagnetic interaction. One can see that if spins 1 and 2 are antiparallel, i.e. are satisfying the nearest neighbour

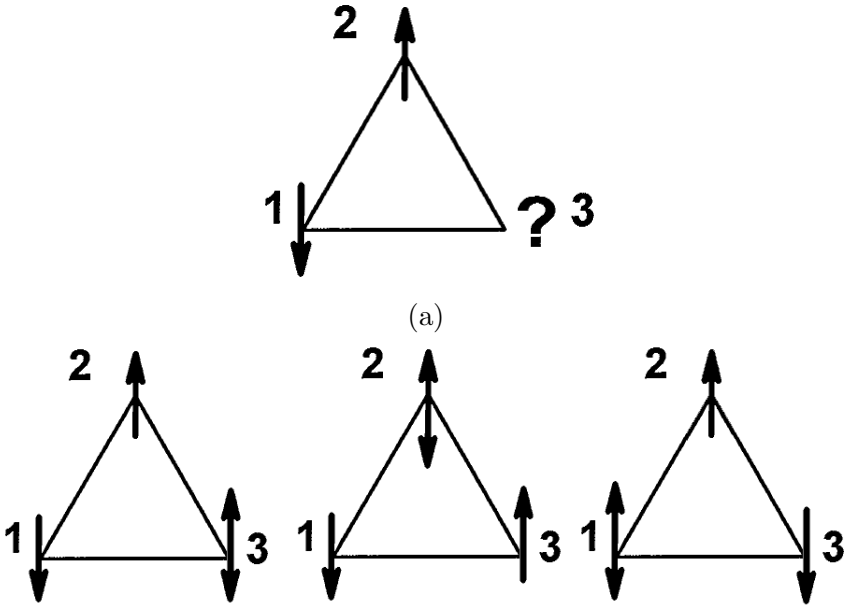

(a)

(b)

Figure 1.4: (a) Representation of the 2D triangular antiferromagnetic frustrated system. (b) The 6 possible ground state configurations of this system. Figures acquired from [51].

antiferromagnetic interaction, spin 3 can only satisfy the exchange interaction with one of the two other spins. For this particular example, the system would have 6 possible configurations for the ground state: spin 3 antiparallel (parallel) to 2 and parallel (antiparallel) to 1, and similarly for spin 1 (spins 2 and 3 are antiparallel) and 2 (spins 1 and 3 are antiparallel) [47]. This arrangement is valid if the system described above has an axis constraint, where the spin can only be parallel or antiparticle to a certain direction. This is commonly known as an Ising system. However, if the spins are allowed to rotate freely in the plane (XY-system), the ground state arrangement would be formed by each spin vector at 120° with each other [52]. This 120° arrangement arises from the minimisation of the Hamiltonian $\hat{\mathcal{H}}$. The simplest expression of $\hat{\mathcal{H}}$ that this system can have if we assume ONLY nearest neighbour interaction is [53]

$$\hat{\mathcal{H}} = -\mathcal{J}\sum_{\langle ij\rangle}\mathbf{S}_i\cdot\mathbf{S}_j = -\frac{\mathcal{J}}{2}\sum_{\triangle}(\mathbf{S}_1+\mathbf{S}_2+\mathbf{S}_3)^2_{\triangle} + \text{constant terms} \tag{1.3}$$

where $\mathcal{J}$ is the coupling constant which for this case is negative because the exchange interactions are antiferromagnetic [43], $\mathbf{S}$ is the vector spin and $\triangle$ refers to the triangle structure from figure 1.4. One can see that to minimise this Hamiltonian, the summation of the triangle needs to be zero, thus resulting in a 120° rotation.

These triangular structures can be arranged in many ways to form 2D lattices. One such structure is the kagome lattice, shown in figure 1.5, where each spin has four nearest neighbours. Figure 1.5 shows two possible ground state configurations for a kagome structure where spins are allowed to rotate freely in the plane: $Q = 0$ state (figure 1.5a) where all spins point either in or out of each triangle, or $Q = \sqrt{3}\times\sqrt{3}$ (figure 1.5b) where spins are coplanar [54].

It is worth pointing out that a perfect kagome structure is not always needed to maintain geometrical frustration [56–58]. The distorted kagome lattice shown in figure 1.6 still exhibits all the properties of a geometrically frustrated magnetic system. An example of a system with the shown distorted kagome lattice is the organically templated iron fluo-

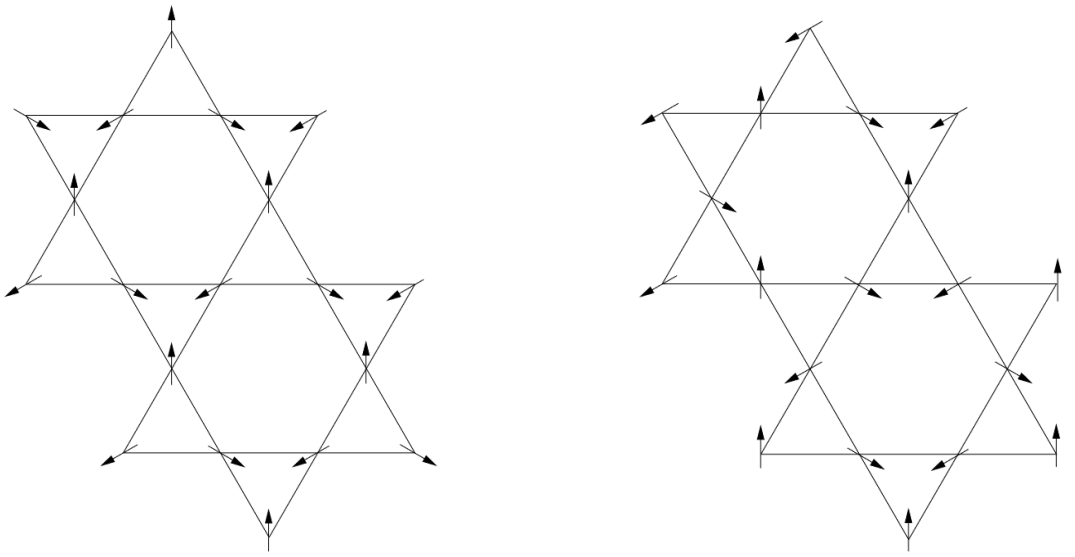

(a) (b)

Figure 1.5: Illustration of (a) the $Q = 0$ and (b) $Q = \sqrt{3}\times\sqrt{3}$ ground state of the kagome lattice. Figures acquired from [55].

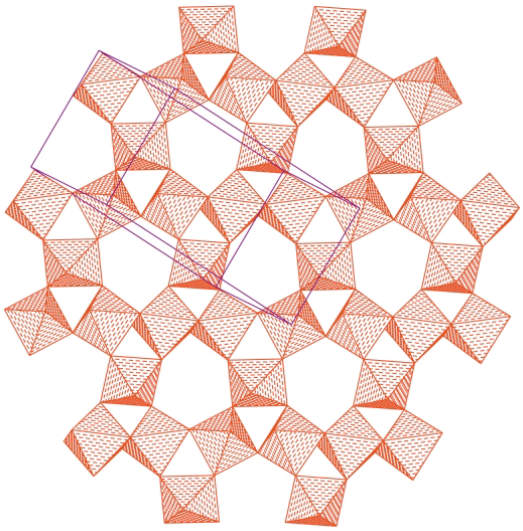

Figure 1.6: Polyhedral view of the 2D network of corner/edge-sharing iron octahedra in **I**. Figure acquired from [56].

rosulfate $[H_3N\,(CH_2)_2\,NH_2\,(CH_2)_2\,NH_2\,(CH_2)_2\,NH_3]\,[Fe^{II}_3F_6\,(SO_4)_2]$, **I** for short [56]. This system is particularly interesting because despite exhibiting the properties of a frustrated system, such as the divergence of the susceptibility, the system also exhibits magnetic hysteresis below 18 K which is not common in kagome systems [49, 50, 56]. This is indicative of ferrimagnetic interactions, where spins want to align antiparallel to each other but the magnitude of the spin or moment pointing in one direction is not the same as the spin pointing in the opposite direction [59].

The base of many geometrically frustrated 3D systems is the triangular structure, just like in 2D, which commonly arranges to form tetrahedra. As figure 1.7a shows, the density of tetrahedra can vary from a closely packed structure, which is the case for the FCC structure, to isolated non-interacting tetrahedra [40]. The pyrochlore, which is the main focus of this thesis, sits in between these two extreme cases.

Just as with the 2D kagome lattice, many of the pyrochlores that exhibit Ising frustration are those in which the spins at the corners of the tetrahedra can only point either towards or away from the centre of the tetrahedra [60], or in other words the system has axial anisotropy along the $\langle 111 \rangle$ direction. However, unlike the 2D kagome lattice, frustration occurs if nearest neighbour ferromagnetic interactions are present such that a spin pointing in/out wants its neighbours to point in the same direction. This results in a two-in-two-out structure like the one shown in figure 1.7b, satisfied in 6 equivalent ways.

1.3 Spin liquid

An example of a family of geometrically frustrated systems, and the focus of this thesis, is the spin liquid. A spin liquid is a dynamic arrangement of strongly correlated spins that does not exhibit long-range order [61]. As a comparison, a spin glass has a static arrangement of spins with no long-range order [40].

Spin liquids are often divided in two groups: the quantum spin liquid (QSL), with some candidates given by [62–65], and the classical spin liquid (CSL), with examples given by [66–68]. The key difference between the QSL and CSL systems is the presence of entanglement. QSLs exhibit long-range quantum entanglement in which electronic spins reside in a macroscopic superposition of infinitely many microstates, whereas CSLs

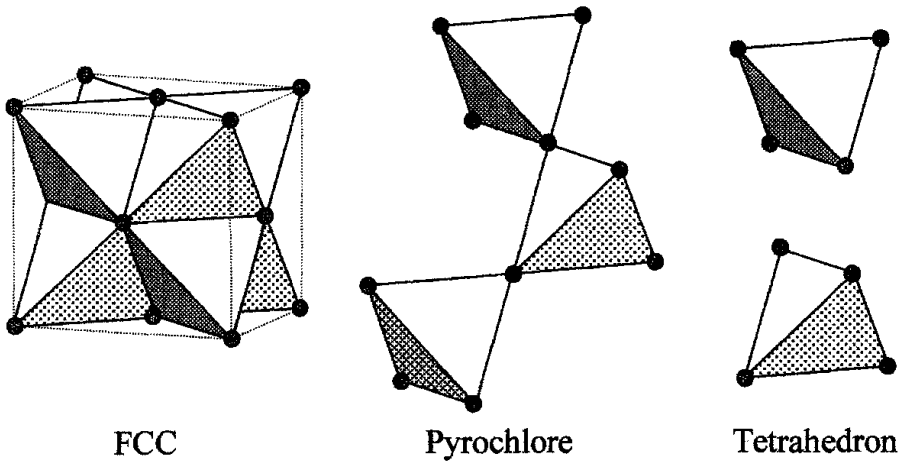

(a)

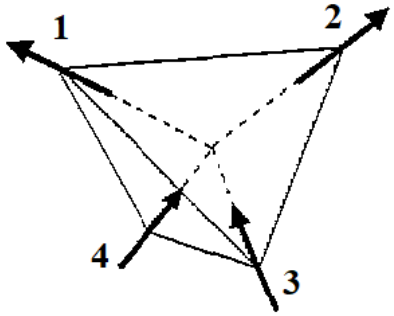

(b)

Figure 1.7: (a) The transition from a dense tetrahedral lattice to a sparse system of non-interacting tetrahedra in 3D. (b) The ground state of a single tetrahedron of spins with ferromagnetic interactions. Figures acquired from [60] and [40] respectively.

contain particles in localised states [61]. Entanglement in QSLs will be discussed later on in more detail.

Other parameters can be used to differentiate between a QSL and a CSL. Systems with small moments are more likely to exhibit QSL behaviour, since a smaller moment tends to mean larger quantum fluctuations, hence a QSL is more likely to be stabilised. In addition, both systems have different temperature dependencies. In QSL systems the spins fluctuate even at 0 K [47], resulting in the frustrated parameter being ∞. On the other hand, some CSL families do have a freezing temperature T_C. T_C is usually much smaller than Θ_{CW}, and thus this CSLs have a large but finite f value. Some CSLs have even been observed to freeze into an order state, such is the case of $Li_9Fe_3(P_2O_7)_3(PO_4)_2$ [66].

Thus, three different temperature regimes can be defined [48]:

1. The $T > \Theta_{CW}$ regime, which corresponds to the paramagnetic phase of the system.

2. The $\Theta_{CW} > T > T_C$ regime, where spins should order but the system inhibits this due to the geometric arrangement of the exchange interactions. This regime is usually termed a cooperative paramagnet [69] and can be of interest due to the highly non-trivial physics that can emerge here, as attested on the spinel $ZnCr_2O_4$ [70].

3. The $T < T_C$ regime. In a QSL, this regime should not exist, and the system should remain disordered down to 0 K. In some CSL, the spin fluctuations slow down dramatically as the temperature is reduced towards T_C.

In the following sections, two families of spin liquids will be discussed in more detail: the classical spin ice and the QSL.

1.3.1 Classical spin ice

Before diving into the topic of classical spin ice, it is worth discussing the water ice system. The molecule of water consists of two H and a single O atom. These two are held together by a covalent bond, that is, they share electrons through the bonds to complete the valence shell. Water ice is the crystalline forms of liquid water. However, the crystal structure of water ice can take many forms depending on the pressure and temperature [71, 72]. At ambient pressure, water ice can be found most commonly in the hexagonal ice form (I_h) [73], shown in figure 1.8.

Two molecules of water (H_2O) can form a hydrogen bond due to the dipolar nature of the molecule. Since the O atom shares two electrons with two H atoms, the side of the H_2O molecule containing the H atoms is less negatively charged than the opposing side. This makes the H_2O molecules electric dipoles, resulting in the negatively charged end of one water molecule orienting itself to be close to the positive end of a nearby molecule, forming a hydrogen bond [74]. While this type of bond is much weaker than the covalent bond, its range is much larger.

Each H_2O molecule can form four hydrogen bonds: each H with an O of a near H_2O, and the O with an H from two near H_2O molecules [74]. From the perspective of an O atom, this corresponds to having 2 nearby H (covalent bonds) and two far away H atoms (hydrogen bonds). This is known as the Bernal-Fowler ice rule [75], and it is this rule that makes the water ice a non-magnetic geometrically frustrated system, since the H atoms can be arranged in 6 possible ways to satisfy this rule, which inhibits the system from reaching an order state at the lowest temperatures.

This was confirmed when measuring the low-temperature properties of water ice, resulting in the system having a finite residual entropy characteristic of frustrated systems. The entropy of water ice was first calculated by Pauling [31] using the number of possible configurations of hydrogen bonds which can be formed. For every O atom, 16 possible configurations of the surrounding H exist, but only 6 of them obey the Bernal-Fowler ice rule. In addition, every O has a total of 2 full H atoms ($4\times1/2$ H since each H atom

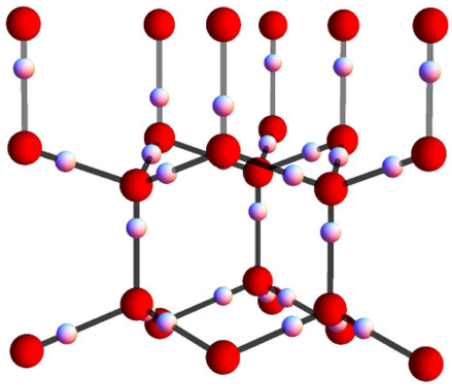

Figure 1.8: Crystal structure of hexagonal water ice (I_h). Figure acquired from [73].

is shared between two O atoms). Thus, for a system with N_{O} O atoms, the number of possible ground states is

$$W = 2^{2N_{\mathrm{O}}} \times \left(\frac{6}{16}\right)^{N_{\mathrm{O}}} = \left(\frac{3}{2}\right)^{N_{\mathrm{O}}} \tag{1.4}$$

since each O–O bond can have two possible positions for the H, giving $2^{2N_{\mathrm{O}}}$ possible H configurations. Using the formula of the configurational entropy S per O atom, the residual entropy of ice is

$$\mathrm{S} = \mathrm{k_B} \ln W = N\mathrm{k_B} \ln \frac{3}{2} \approx 3.36 \text{ J/mol K} \tag{1.5}$$

Experimentally, the entropy cannot be observed directly, but it is the change in entropy between two temperatures that is measured. The entropy in water ice was first measured by Giauque *et al.* [76], where the specific heat $C(T)$ was measured between 10 K and the gas phase. The entropy was then extracted by integrating the $C(T)/T$ between the two mentioned limits. The difference between this entropy and the absolute entropy for the gas phase gave a residual entropy of 3.42 J/mol K [76], similar to the calculated value. Finally, neutron diffraction measurements have helped to confirm the structural configuration of H atoms [77–79]. It is worth noting that these calculations and measurements are in bulk samples, as layered ice has been show to not obey the Bernal-Fowler ice rule [80].

With these ideas, let us discuss the classical spin ice system. A classical spin ice is a type of classical spin liquid formed mainly in pyrochlores of structure $\mathrm{R_2B_2O_7}$, where the R cations are magnetic rare-earth ions and the B cations are usually non-magnetic [81]. It was P. W. Anderson [82] who first observed how an Ising magnetic model on the pyrochlore lattice could exhibit a ground state entropy equivalent to that of water ice. These systems were later called "spin ice" and were first observed experimentally 4 decades later by Harris *et al.* [83].

The distinctive feature of a classical spin ice is the ground state configuration of the spins at the corners of the tetrahedra of rare earths following a very similar rule to the ice rule in water ice: each tetrahedron must have two spins pointing in and two spins pointing out [84]. This two-in-two-out (2I2O) rule is also named the "ice rule". For these systems to be frustrated and part of the classical spin liquid family, the interactions between the 4 spins of the corner sharing tetrahedra must be ferromagnetic and must have a strong single-site Ising anisotropy along the local $\langle 111 \rangle$ axes [85]. The similarities between water ice and classical spin ice can be seen more clearly in figure 1.9.

Because the overall net spin interaction needs to be a ferromagnetic for the ice rules to be satisfied, not all rare-earth pyrochlores are classical spin ice. $\mathrm{Nd_2Zr_2O_7}$ for example, has antiferromagnetically coupled Ising spins, and thus in the ground state the spins are pointing either all in or all out (AIAO) of the tetrahedra [86].

Due to the similarities with water ice, one can see that the ground state entropy of classical spin ice systems can be calculated in a very similar way to that of water ice. A pyrochlore with N_{T} tetrahedra contains $2N_{\mathrm{T}}$ spins since, just as with water ice, each spin is "shared" between two tetrahedra. Just as with water ice, there are only 6 possible configurations of spins out of the full 16 that satisfy the ice-rules, and the spins can point either towards or away from the centre of a tetrahedron. Thus, the number of ground states can be estimated to be [88]

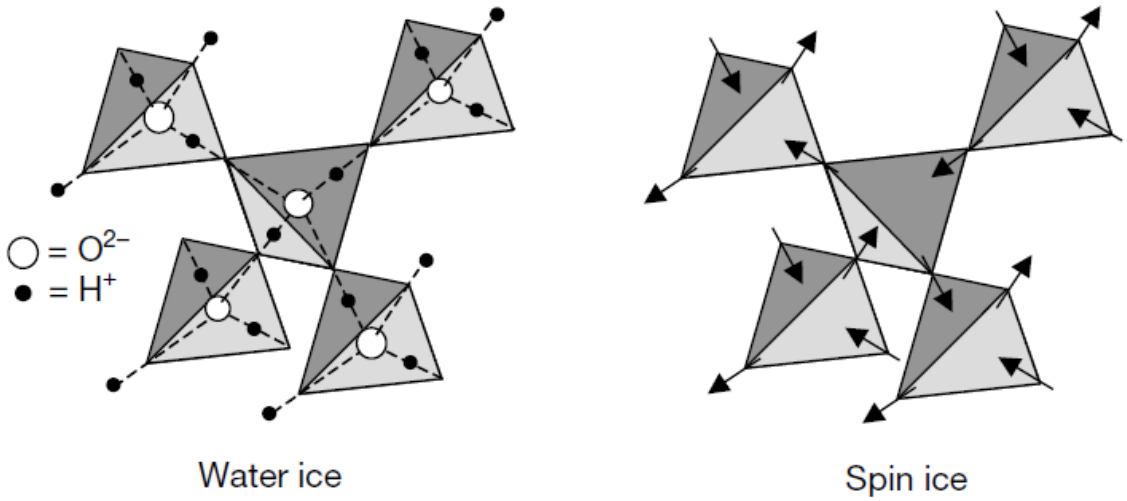

(a) (b)

Figure 1.9: Schematic representation of frustration in (a) water ice and (b) classical spin ice. Figures acquired from [87].

$$W_S = 2^{2N_T} \times \left(\frac{6}{16}\right)^{N_T} = \left(\frac{3}{2}\right)^{N_T} \tag{1.6}$$

and using the same equation for the entropy, but dividing by 2 to get the entropy per spin, one arrives at a value of $(k_B/2)\ln(3/2)$. The entropy of $Dy_2Ti_2O_7$ was determined by Ramirez *et al.*[89] following a method similar to the method used by Giauque *et al.* [76]: measuring the specific heat from 300 mK to 10 K (in the paramagnetic regime), as figure 1.10 shows. This produced a residual entropy close to 3.72 J/mol K, similar to the entropy calculated by Pauling in water ice [31], and even closer to the one measured experimentally [76]. A similar result was found for $Ho_2Ti_2O_7$ [68].

The $Dy_2Ti_2O_7$ and $Ho_2Ti_2O_7$ systems just mentioned are the two archetype examples of classical spin ice. Both belong to the family of classical spin liquids due to them having a large moment μ, and the moment fluctuations slowing down significantly below 0.65 K [67, 68]. Low temperature calculations of these systems show that the slowing down of the moments prevents the formation of an ordered state [85]. Furthermore, Dy^{3+} in $Dy_2Ti_2O_7$ and Ho^{3+} in $Ho_2Ti_2O_7$ have very similar crystal electric field (CEF) levels, with the first excited levels at 20.9 meV [90] and 20.4 meV [91] respectively. The key difference between the energy levels of these two ions is that Dy^{3+} is a Kramers ion and thus all the energy levels are doublets, while Ho^{3+} is a non-Kramers ion and thus some levels are singlets and some are doublets. Nevertheless, the CEF measurements of both samples show that the moments in both systems have a strong Ising behaviour, i.e. the moments only point along the line connecting the O(1) ions, which is an essential ingredient to their low-temperature spin ice state. Finally, it is because of the large moments and such a strong anisotropy that moment-tunnelling is frozen out at very low temperatures [47, 92].

Since Ho^{3+} and Dy^{3+} are rare earths, both exhibit strong spin-orbit coupling and thus the total angular momentum $J = L + S$ is a good quantum number. The theoretical full magnetic moment can be calculated using [48, 94]

$$\mu = g_J J \mu_B \tag{1.7}$$

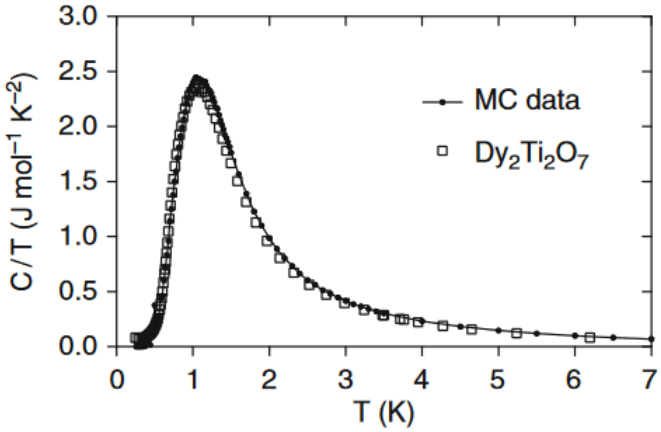

(a)

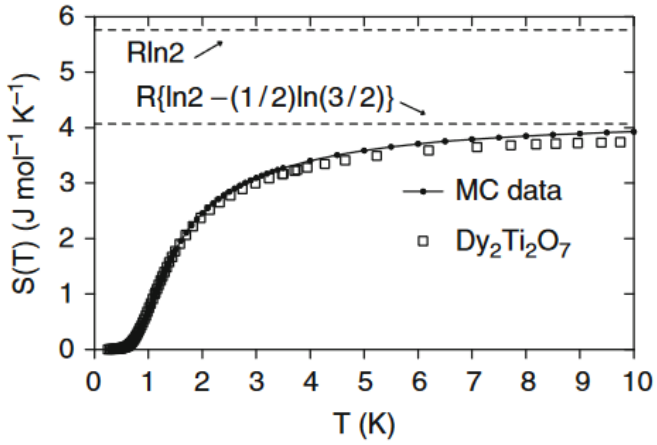

(b)

Figure 1.10: (a) Specific heat and (b) entropy data for $Dy_2Ti_2O_7$. The experimental data is from [89], and the Monte Carlo simulations using the dipolar spin-ice model (and full figures) is from [93] .

where μ_B is the Bohr magneton and g_J is the Landé factor [46]

$$g_J = 1 + \frac{J(J+1) + S(S+1) - L(L+1)}{2J(J+1)} \tag{1.8}$$

where L is the total orbital angular momentum and S is the total spin angular momentum. Both, Ho^{3+} in $Ho_2Ti_2O_7$ and Dy^{3+} in $Dy_2Ti_2O_7$ have a calculated and measured magnetic moment of around $10\mu_B$ [95, 96]. These magnetic moments behave as magnetic dipoles, since they generate a magnetic field that can interact with other nearby magnetic moments [59]. This is similar to water ice, where a side of the molecule is more negatively charge than the other. Thus, because the magnetic moments in these systems are strong, the nearest neighbour exchange interactions are not the only contributor to frustration and the ice rules, but dipolar interactions (magnetic dipole-dipole interaction) also play an important role in classical spin ice systems [85]. Dipolar interactions are specially important at large distances, since their strength decays with distance at a much slower rate than exchange interactions [81].

Because of the presence of the dipolar interactions, the most widely used model for describing these systems is the dipolar spin ice (DSI) model [68] with Hamiltonian

$$\hat{\mathcal{H}} = -\mathcal{J}\sum_{\langle ij\rangle}\mathbf{S}_i^{z_i}\cdot\mathbf{S}_j^{z_j} + \mathcal{D}r_{nn}^3\sum_{i>j}\frac{\mathbf{S}_i^{z_i}\cdot\mathbf{S}_j^{z_j}}{|\mathbf{r}_{ij}|^3} - \frac{3\left(\mathbf{S}_i^{z_i}\cdot\mathbf{r}_{ij}\right)\left(\mathbf{S}_j^{z_j}\cdot\mathbf{r}_{ij}\right)}{|\mathbf{r}_{ij}|^5} \tag{1.9}$$

where $\mathcal{J}$ is the nearest neighbour exchange interaction previously discussed, defined with the convention that $\mathcal{J} < 0$ is antiferromagnetic and $\mathcal{J} > 0$ is ferromagnetic [81], r_{nn} is the distance between two nearest neighbour spins, $\mathbf{r}_{ij}$ is the vector that connects two spins in the system, $\mathbf{S}_i^{z_i}$ is a spin of unit length constrained to only point along its local $z_i = \langle 111\rangle$ (towards or away from the centre of the corner sharing tetrahedra) and $\mathcal{D}$ is the dipolar constant [97]

$$\mathcal{D} = \frac{\mu_0}{4\pi}\frac{\mu^2}{r_{nn}^3} \tag{1.10}$$

where μ_0 is the vacuum permeability. While this equation works well for the basis of $Ho_2Ti_2O_7$ and $Dy_2Ti_2O_7$, it has been speculated in [97] that this form of the Hamiltonian is insufficient to explain the finer details in $Dy_2Ti_2O_7$, and that a better approximation is achieved by including the second and third-nearest neighbour exchange correlations [98]. Nevertheless, the success of this model can be seen in the Monte Carlo calculations for the specific heat and entropy of $Dy_2Ti_2O_7$ in figure 1.10.

Equation (1.9) highlights the importance of the dipolar interactions, as in classical spin ice systems such as $Dy_2Ti_2O_7$ and $Ho_2Ti_2O_7$ the exchange interaction $\mathcal{J}$ can be antiferromagnetic (negative) [81] but the strength of the dipolar interactions makes the overall nearest neighbour interaction effectively ferromagnetic. To better demonstrate the importance of the dipolar interactions, let us consider a simplified case of a single tetrahedron of spins (see figure 1.7b). From the centre of a tetrahedron of magnetic ions, $\mathbf{S}_i^{z_i}$ can take 4 possible values [48]:

$$\mathbf{S}_1^{z_1} = \pm\tfrac{1}{\sqrt{3}}\begin{bmatrix}-1\\-1\\+1\end{bmatrix} \quad \mathbf{S}_2^{z_2} = \pm\tfrac{1}{\sqrt{3}}\begin{bmatrix}+1\\+1\\+1\end{bmatrix} \quad \mathbf{S}_3^{z_3} = \pm\tfrac{1}{\sqrt{3}}\begin{bmatrix}+1\\-1\\-1\end{bmatrix} \quad \mathbf{S}_4^{z_4} = \pm\tfrac{1}{\sqrt{3}}\begin{bmatrix}-1\\+1\\-1\end{bmatrix} \tag{1.11}$$

where a positive (negative) sign corresponds to the spin pointing out (in) of the tetrahedron. One can easily see how the multiplication between two spins can now only be +1/3 if both spins point in or out, or -1/3 if one spin points out and the other in. As such, the first term in equation (1.9) simplifies to [48]

$$-\mathcal{J}\sum_{\langle ij\rangle}\mathbf{S}_i^{z_i}\cdot\mathbf{S}_j^{z_j} = \frac{\mathcal{J}}{3}\sum_{\langle ij\rangle}\sigma_i\sigma_j \quad \text{where} \quad \begin{cases}\sigma_i = +1 & \text{if the spin points out}\\ \sigma_i = -1 & \text{if the spin points in}\end{cases} \tag{1.12}$$

For the second term in equation (1.9), if the tetrahedron is projected onto a plane, the unit vector connecting two nearest neighbour spins will be of the form

$$\mathbf{r}_{ij} = \frac{1}{\sqrt{2}}\begin{bmatrix}\pm1\\\pm1\\0\end{bmatrix} \tag{1.13}$$

with the position of the 0 within the vector and the sign of the other components changing depending on the value of ij. This simplifies the second summation in equation (1.9) to [48]

$$\mathcal{D}r_{nn}^3 \sum_{i>j} \frac{\mathbf{S}_i^{z_i} \cdot \mathbf{S}_j^{z_j}}{|\mathbf{r}_{ij}|^3} - \frac{3\left(\mathbf{S}_i^{z_i} \cdot \mathbf{r}_{ij}\right)\left(\mathbf{S}_j^{z_j} \cdot \mathbf{r}_{ij}\right)}{|\mathbf{r}_{ij}|^5} = \frac{5\mathcal{D}}{3} \sum_{\langle ij \rangle} \sigma_i \sigma_j \tag{1.14}$$

where the sign of σ_i is the same as in equation (1.12). Combining equations (1.12) and (1.14), the Hamiltonian simplifies to [48]

$$\hat{\mathcal{H}} = \mathcal{J}_{\text{eff}} \sum_{\langle ij \rangle} \sigma_i \sigma_j \quad \text{where} \quad \mathcal{J}_{\text{eff}} = \mathcal{J}_{\text{NN}} + \mathcal{D}_{\text{NN}} = \frac{\mathcal{J}}{3} + \frac{5\mathcal{D}}{3} \tag{1.15}$$

a form very similar to the Hamiltonian of the 2D triangular system (see equation (1.3)). This simplified model highlights the importance of the dipolar interactions. The $\mathcal{J}_{\text{NN}}$ and $\mathcal{D}_{\text{NN}}$ constants found for Dy^{3+} in $Dy_2Ti_2O_7$ and Ho^{3+} in $Ho_2Ti_2O_7$ are $\mathcal{J}_{\text{NN}} = -1.24$ K and $\mathcal{D}_{\text{NN}} = 2.35$ K [93], and $\mathcal{J}_{\text{NN}} = -0.52$ K and $\mathcal{D}_{\text{NN}} = 2.35$ K [68] respectively.

The emergent state containing the 2I2O state with spin flip excitations, discussed below, is known as the Coulomb phase [1, 81, 99]. The Coulomb phase is present in many highly frustrated systems, which have local constraints that can be mapped to a divergence-free "flux" [100]. The 2I2O rule is a perfect example of this constraint, since the vector sum of the moments is zero, which is equivalent to a divergence-free "spin field" $\nabla \cdot \mathbf{H}(\mathbf{r}) = 0$ where $\mathbf{H}(\mathbf{r})$ is the field generated by the spin dipoles and $\nabla\cdot$ is commonly referred to as the lattice divergence [81].

The main distinguishing experimental feature in classical spin ice is the pinch point. A pinch point is a bow-tie like structure centred on nuclear Bragg positions that represents saddle points in the magnetic diffuse scattering (diffuse scattering will be defined later on in the thesis) [47]. These pinch points arise due to the long-range order of the divergence-free tetrahedra ($\nabla \cdot \mathbf{H}(\mathbf{r}) = 0$) [101–104]. Below the freezing temperature, all the tetrahedra need to obey the ice rule to minimise the energy and satisfy the spin correlations, resulting in the system having long-range order of the two-in-two-out structure of the tetrahedra, as shown in figure 1.11a for two corner sharing tetrahedra of spins. This does not contradict the findings of Harris *et al.* [60] on the absence of long range order in $Ho_2Ti_2O_7$, since the arrangement of the 4 spins to satisfy the ice rules will vary from tetrahedra to tetrahedra. Thus, just as with Bragg peaks, the long-range order in real space translates onto singularity like features in reciprocal space.

Figure 1.12a shows a $Dy_2Ti_2O_7$ pinch point at (0,2,0), and figure 1.12b shows a $Ho_2Ti_2O_7$ pinch point at (0,0,2). The $Dy_2Ti_2O_7$ pinch point is covered by a Bragg peak because the experiment was performed with unpolarised neutrons, so the scattering shown is the nuclear plus magnetic diffuse scattering. On the other hand, the $Ho_2Ti_2O_7$ pinch point can be seen very clearly as polarised neutrons were used to separate the magnetic and nuclear diffuse scattering. In particular, figure 1.12b shows the spin flip (SF) scattering. Bramwell *et al.* [68] simulated the magnetic diffuse scattering of $Ho_2Ti_2O_7$ using only the nearest neighbour spin ice (NNSI) model ($\mathcal{J}_{\text{NN}} > 0$ and $\mathcal{D}_{\text{NN}} = 0$) and using the full dipolar spin ice model, shown in figure 1.13. While the calculation with just nearest neighbour exchange interactions do produce a bow tie like structure similar to the experimental data, the dipolar interactions are needed to properly reproduce all the features such as the lower intensity at the pinch points.

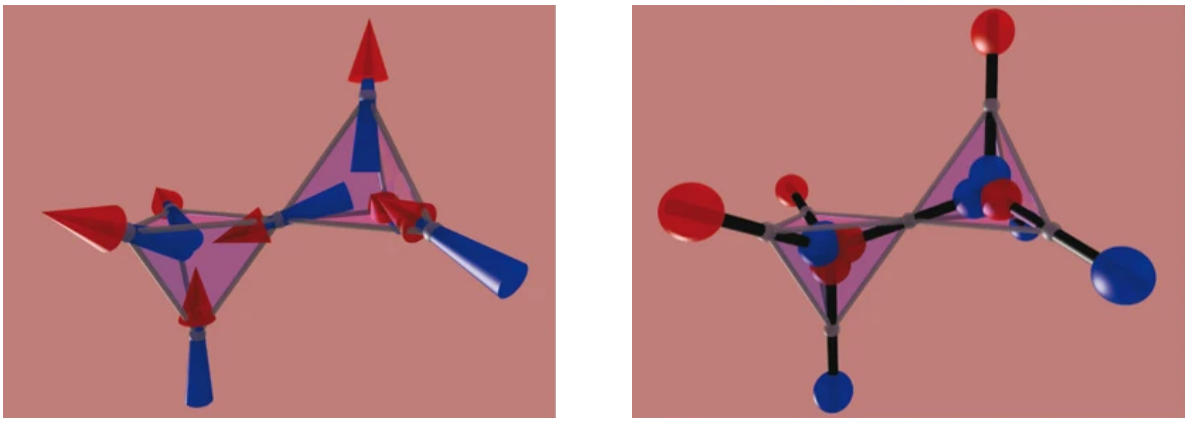

(a) (b)

Figure 1.11: Mapping from spins (dipoles) to dumbbells. (a) Two adjacent tetrahedra obeying the ice rules, with two spins pointing in and two out. (b) The corresponding dumbbell picture obtained by replacing each spin by a pair of opposite magnetic charges. Figures acquired from [105].

In an ideal classical spin ice system below the freezing temperature, all the tetrahedra of magnetic ions obey the ice rule. However, as the temperature is increased, violations of the ice rule can happen in the form of spins flipping, as figure 1.14a shows. These thermal excitations in the form of spin flips result in the violation of the divergence-free flux constraint of the Coulomb phase, i.e. $\nabla \cdot \mathbf{H}(\mathbf{r}) \neq 0$. Because of this, these excitations are commonly known as emergent magnetic monopoles. These excitations are often called "fractionalised" excitations, since the spin dipole fractionalises into two monopoles [105]. Finally, the Coulomb phase is often defined as the quasi-particle vacuum for magnetic monopoles, since it is the only state of mater where these excitations can form [99, 105].

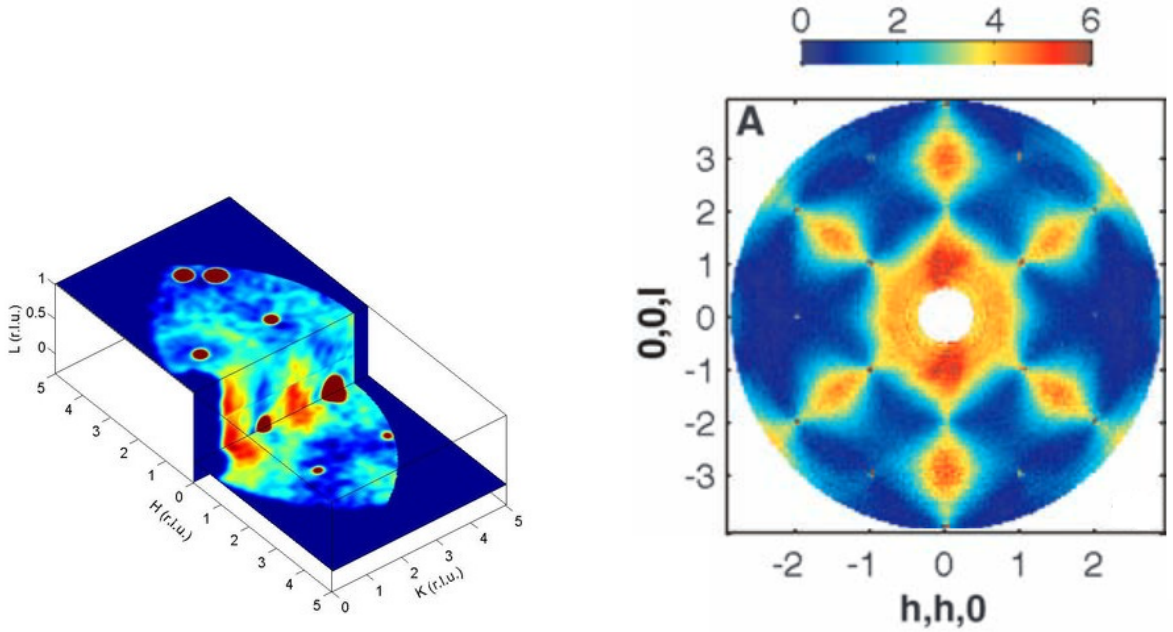

(a) (b)

Figure 1.12: (a) Total diffuse scattering of $Dy_2Ti_2O_7$ measured at 0.7 K. (b) Magnetic diffuse scattering of $Ho_2Ti_2O_7$ measured at 1.7 K. Figures acquired from [106] and [1] respectively.

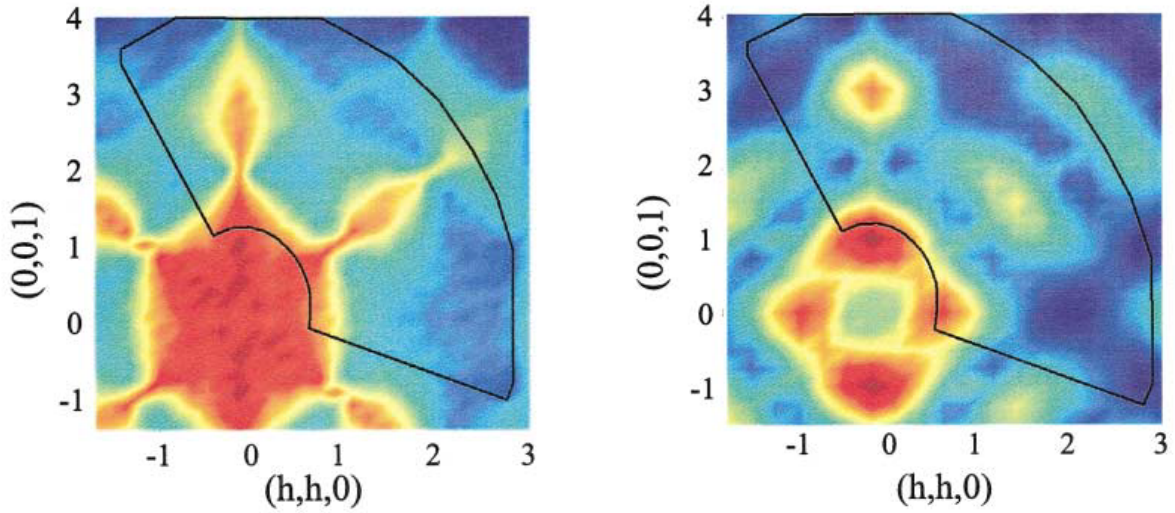

(a) (b)

Figure 1.13: Diffuse scattering calculations of $Ho_2Ti_2O_7$ using (a) the nearest neighbour spin ice model ($\mathcal{J}_{\mathrm{NN}} > 0$ and $\mathcal{D}_{\mathrm{NN}} = 0$) and (b) the dipolar spin ice model. Figures acquired from [68].

Castelnovo *et al.* [105] proposed the "dumbbells" model to describe the emergent magnetic monopoles in the Coulomb phase in terms of magnetic charges. In this model, the spins are replaced by dumbbells consisting of equal and opposite magnetic charges at each end, such that the ice rules are obeyed by the need to have magnetic charge compensation, this is, the summation of the charges needs to be zero. An example of this is shown for two adjacent tetrahedra in figure 1.11b.

The sign of the magnetic charges are assigned so as to recover the dipole moment of each spin, with the magnitude given by $Q = \mu/a_d$ where $a_d = \sqrt{3/2}r_{nn}$ is the diamond lattice (lattice formed by connecting the centre of the corner sharing tetrahedra of spins) bond length. Since each tetrahedron is now composed of a sum of magnetic charges, the energy can be calculated as the pairwise interaction energy of magnetic charges, given by the magnetic Coulomb law [105]

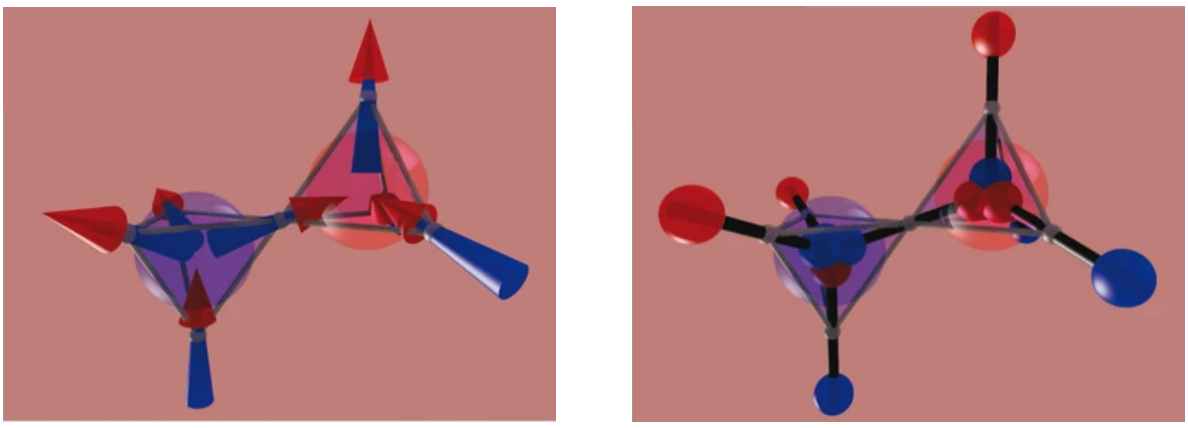

(a) (b)

Figure 1.14: Representation of a thermal excitation in a classical spin ice in (a) the dipole representation by flipping a shared spin, and (b) the "Dumbbell" model by swapping two charges of opposite sign. Figures acquired from [105].

$$\hat{\mathcal{H}} = \frac{\mu_0}{4\pi} \sum_{\alpha<\beta} \frac{Q_\alpha Q_\beta}{r_{\alpha\beta}} + \frac{1}{2}\nu_0 \sum_\alpha Q_\alpha^2 \tag{1.16}$$

where Q_α is the total charge at site α in the diamond lattice (the charge at the centre of a tetrahedron), $r_{\alpha\beta}$ is the distance between the two sites, and the second term is needed to reproduce the net nearest neighbour interaction. Equation 1.16 clearly shows that to minimise the energy, each site needs to be magnetically neutral ($Q_\alpha = 0$) which is only possible if the system obeys the ice rules.

In the dumbbell model, a spin flip is equivalent to swapping two charges of opposite sign. This results in the total magnetic charge of the sites with the shared spin flip no longer being neutral, but with a value of $Q_\alpha = \pm 2\mu/a_d$ [105]. A representation of this excitation in the dumbbell model is shown in figure 1.14b. While the magnetic charge of a monopole is small, since at the same distance the force between two monopoles is 14000 times weaker than the electrostatic force between two electrons, at low temperatures their presence is still measurable [47].

It is worth pointing out that these excitations are termed monopoles because they have magnetic properties similar to Dirac's magnetic monopoles [107], mainly that they both act as magnetic sinks. However, some key differences exist between the two. One of these differences is that, while the charge of Dirac's monopole is quantised, the spin ice monopole can be tuned continuously by applying pressure on the sample and thus changing the value of μ/a_d. The most important difference is that spin ice monopoles are not sources of $\mathbf{B}(\mathbf{r})$ fields, but sources of $\mathbf{H}(\mathbf{r})$ fields appropriate to the condensed matter setting [105], which is still allowed by standard electromagnetic theory [108].

Flipping a single spin is equivalent to simply generating a dipole, since the two emergent monopoles of opposite sign are next to each other, and it requires an energy cost of ~ 0.92 meV [109] and ~ 0.84 meV [110] for $Ho_2Ti_2O_7$ and $Dy_2Ti_2O_7$ respectively, at low temperatures (<1 K). However, subsequent spins can be flipped for zero energy cost until both monopoles are sufficiently apart that they can be considered as isolated monopoles, as 1.15 shows. Thus, these monopoles are deconfined, since it only takes a finite amount of energy to separate them to infinity, i.e. are true elementary excitations of the system. The string of flipped spins is referred to as a "Dirac string", and the Coulombic interaction felt by each pair of monopoles is $-\mu_0 q_m^2/(4\pi r)$ where r is the distance between monopoles and q_m the net monopolar magnetic charge [105]. These excitations can also be found in artificial spin ice, the 2D analogue of 3D spin ice [111].

It is through these excitations that a classical spin ice can fluctuate between different ground states. The simplest example is shown in figure 1.16 where flipping 6 spins, one to create a monopole-antimonopole pair, four to move each monopole around a hexagon of the diamond lattice, and one to annihilate the two monopoles, causes the system to change from one ground state to another.

The presence of monopoles and their effects in an applied magnetic field was studied by Kadowaki *et al.* [113], where a magnetic field was applied to a single crystal of $Dy_2Ti_2O_7$ along a [111] direction. Along this direction, the pyrochlore lattice consists of a stacking of triangular and kagome lattices, as figure 1.17a shows. In a weak applied field, the spins forming the triangular lattice align to the applied field, while the spins in the kagome lattice arrange in a two-in-one-out or two-out-one-in structure so as to satisfy the ice rules (the kagome ice state). As the applied field increases, the concentration of monopoles increases until a critical field is reached where the spins realise a fully

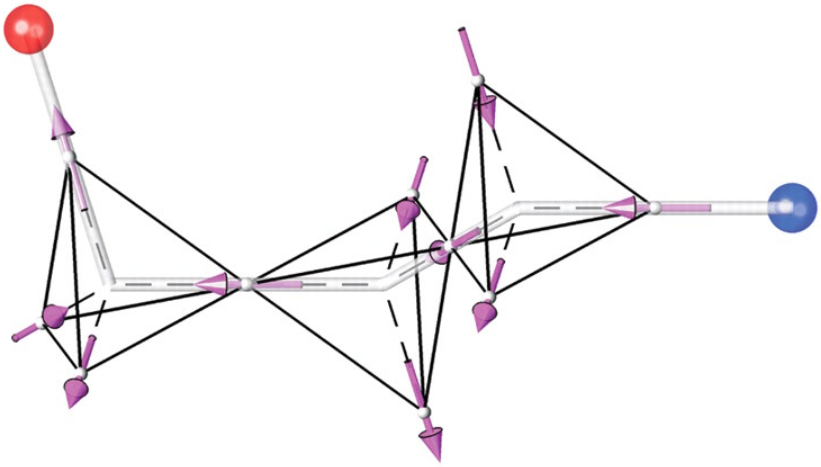

Figure 1.15: Monopoles of opposite charge separated by a string of flipped spins (a Dirac string). The pink arrows indicate spins, and the blue and red spheres indicate monopoles. Figure acquired from [1].

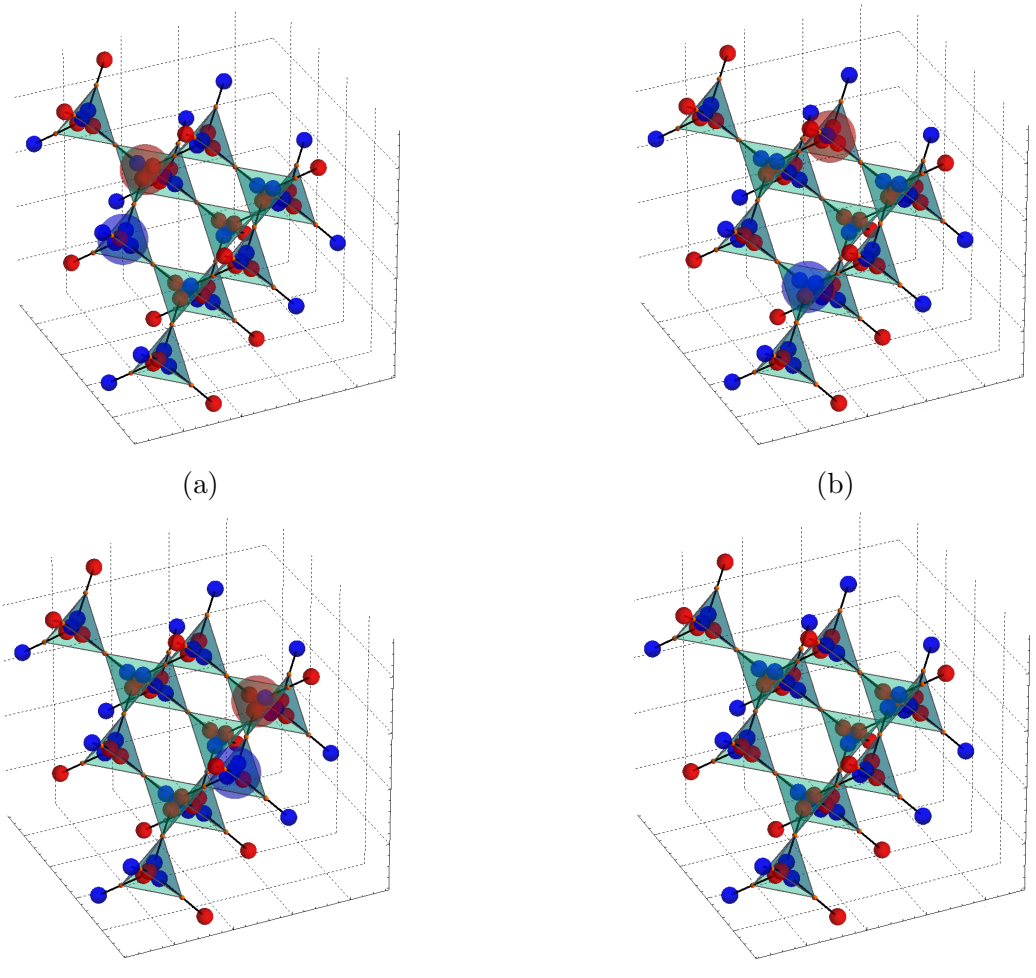

(a) (b)

(c) (d)

Figure 1.16: (a) A monopole-antimonopole pair is created by flipping a spin. (b), (c) Flipping adjacent spins moves the defects to the next tetrahedra. (d) The last spin flip annihilates the two monopoles, restoring the ground state of the system. Figures acquired from [112].

ordered, staggered arrangement of monopoles, as figure 1.17b shows. This was observed with neutron scattering in the form of a weakened kagome ice scattering pattern and an increase of the diffuse scattering around Bragg points.

The Dirac strings were studied by Morris *et al.* [106] in $Dy_2Ti_2O_7$ by applying a magnetic field along the $\langle 100 \rangle$ direction of the sample. If a strong saturating field h_s is applied in this direction, the system reaches a non-degenerate ground state but with the tetrahedra still obeying the ice rules, i.e. free of monopoles. Since the sample was studied just above the temperature at which magnetic monopoles can form, sparse thermally excited monopole-antimonopole pairs start to appear as the magnetic field is lowered, which separate by flipping adjacent spins. The flipped spins simulate a random walk biased in a direction opposite to the applied field, i.e. the Dirac strings are oriented antiparallel to the applied field, as figure 1.18a shows. The experimental signature of these Dirac strings observed via neutron scattering is the presence of a set of cone like structures emanating from Bragg points, as figure 1.18b shows. These were well reproduced by the calculation shown in figure 1.18c assuming a random walk of the monopoles weakly biased to be antiparallel to the direction of the applied field.

Muons have also been used to characterise magnetic monopoles in $Ho_2Ti_2O_7$ and $Dy_2Ti_2O_7$. For example, the first reported experimental studies of magnetic monopoles in spin ice using transverse field muon spin rotation obtained a value for the magnetic charge in agreement with theory [114]. However, interpretation of results using this technique has proved controversial [115].

An alternative experimental method of detecting monopole excitations and measuring the length of the Dirac string is by the broadening of the pinch points. The width of the pinch point is inversely related to the correlation length of the ice rules (distance over which the tetrahedra obey the two-in-two-out rule) ξ_{ice}. Since a monopole is defined as a violation of the ice rules via a spin flip, their presence would cause the correlation length ξ_{ice} to decrease, which is manifested by the broadening of the pinch point. This was observed by Fennell *et al.* [1] who measured the width of the (0,0,2) pinch point of $Ho_2Ti_2O_7$ (see figure 1.12b) between 1.7K and 50K, as figure 1.19a shows. Since the distance over which the ice rules are obeyed is the same as the distance between two

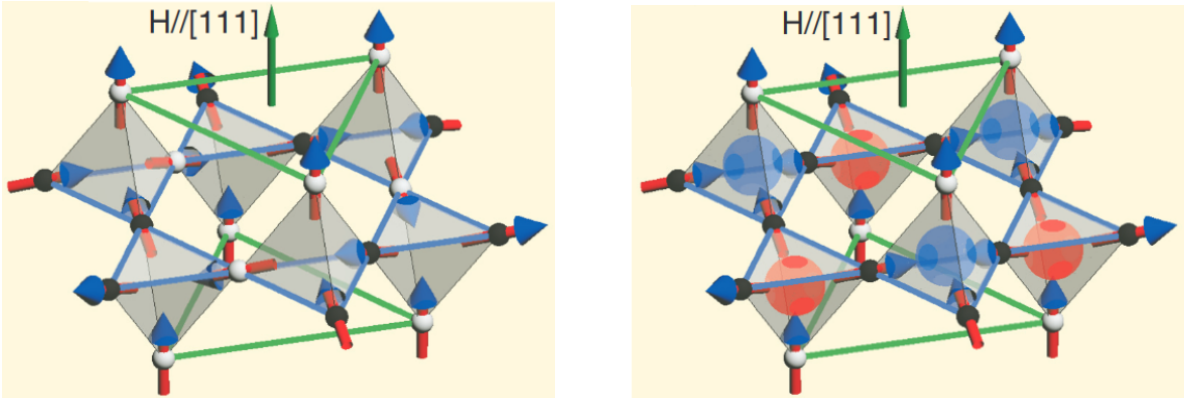

(a) (b)

Figure 1.17: (a) Stacked triangular and kagome lattices in $Dy_2Ti_2O_7$, shown by green and blue lines, respectively, along a [111] direction. Under small [111] magnetic fields, spins on the kagome lattice remain in the disordered kagome ice state. (b) As the magnetic field is increased, spins orient to form a fully ordered, staggered arrangement of monopoles. Figures acquired from [113].

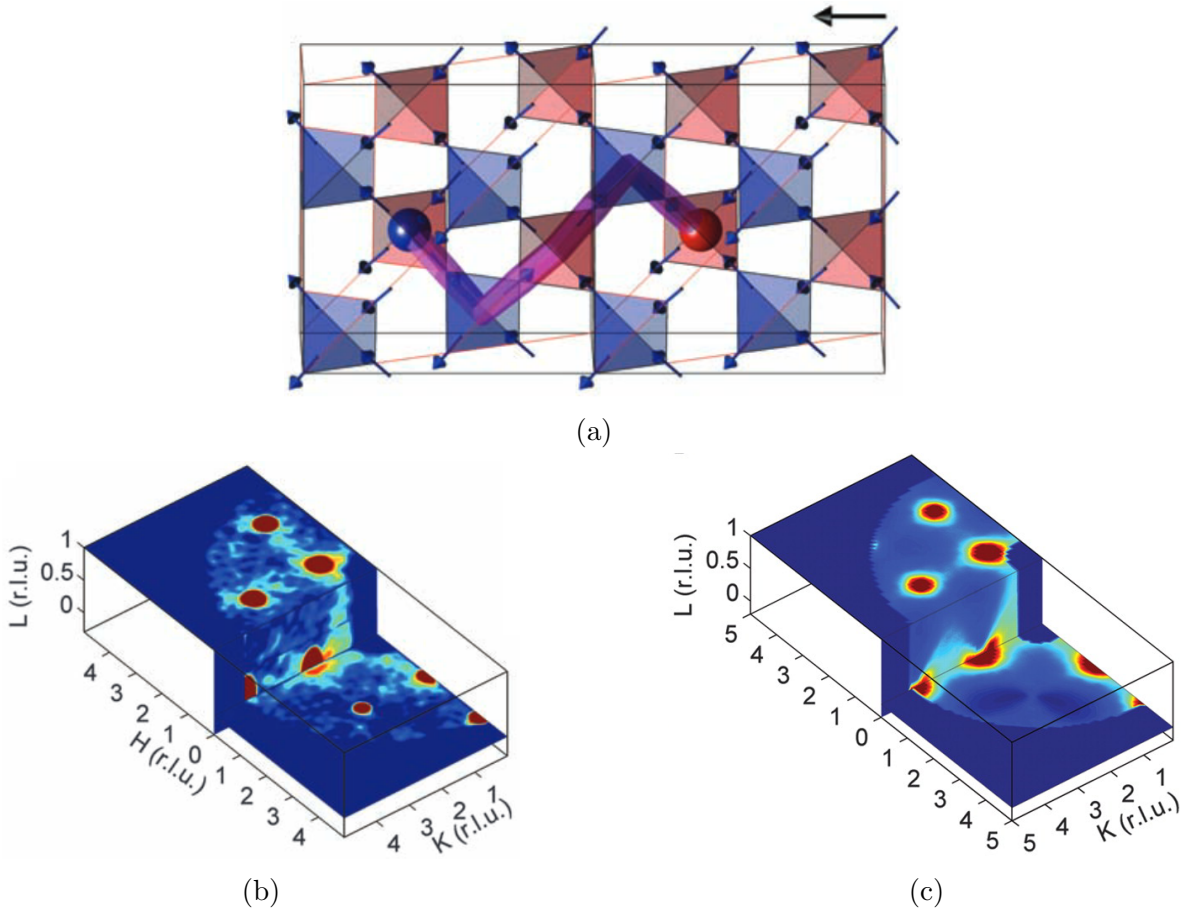

(a)

(b)

(c)

Figure 1.18: (a) Arrangement of spins in a magnetic field just below h_s applied along a [100] direction. The spins in the Dirac string are aligned antiparallel to the applied field. (b) 3D representation of the single-crystal $Dy_2Ti_2O_7$ neutron diffraction data at 0.7 K in a magnetic field 30% below h_s, showing a cone of scattering emanating from the (0,2,0) Bragg peak. (c) Calculation of the diffuse scattering characteristic of weakly biased random-walk correlations. Figures acquired from [106].

monopoles, ξ_{ice} can also be used as a measure of the Dirac string length. Fennell *et al.* concluded that ξ_{ice} has a temperature variation that is consistent with an essential singularity $\approx e^{(B/T)}$, as figure 1.19b shows, where $B = 1.7 \pm 0.1$ K for $Ho_2Ti_2O_7$, a value close to the measured $\mathcal{J}_{\text{eff}} = 1.8$ K for the same system [68].

Monopoles can also be found in the presence of disorder by removing spins through the replacement of magnetic ions by non-magnetic ions, as it was found by [116] in $Ho_{2-x}Y_xTi_2O_7$ where Ho^{3+} ions were replaced by non-magnetic Y^{3+} ions. More detail of this effect will be given later on in the thesis.

1.3.2 Quantum Spin liquid

In 1973, P.W. Anderson proposed that the ground state of some antiferromagnetic frustrated systems could be described by the resonating valence bond (RVB) model [117]. The main idea of the RVB model is that any two antiparallel spins pair up to form a spin singlet with a total spin $S = 0$ and vanishing net magnetic moment [118]. This is to be compared with the Néel state where only after the average the total spins is zero [46]. Such a singlet is sometimes called "single valence bond", and it represents the maximally quantum entangled state between two spins. If the system has strong quantum

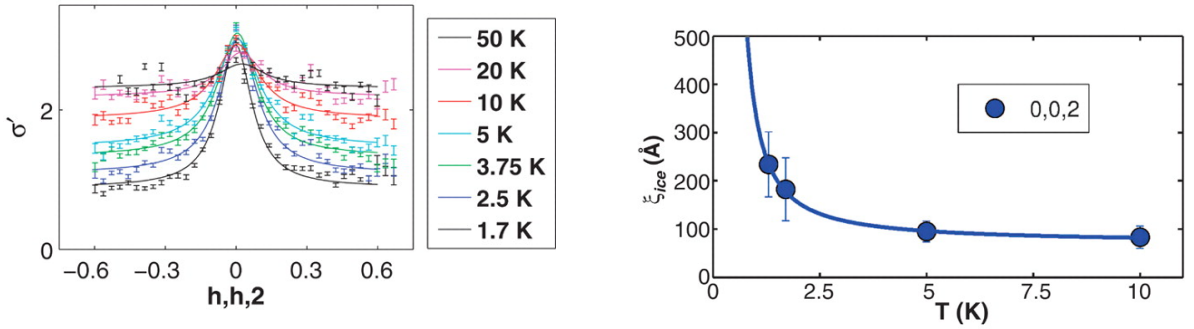

(a) (b)

Figure 1.19: (a) SF scattering at the (0,0,2) pinch point of $Ho_2Ti_2O_7$ at increasing temperatures. A Lorentzian is fitted to each pinch point. (b) Temperature dependence of ξ_{ice} extracted from the Lorentzian fits fitted to an exponential divergence in T^{-1}. Figures acquired from [1].

fluctuations arising from the geometrical frustration, the singlets will not arrange in any particular order [44]. However, if the quantum mechanical fluctuations are too weak such that each spin is entangled only with one other spin (static and localised), the system is known as a valence band solid (VBS) [47]. An example of two spins and a square lattice system is shown in figure 1.20.

The wave function of the RVB state is defined as a linear superposition of all possible configurations of the singlets, this includes short range (figure 1.21a) and long range (figure 1.21b) bonds [44, 47]. In such a state, the strongly entangled spins do not form any ordered magnetic structure and the spins continue to fluctuate even at 0 K. Such a state was termed QSL. Anderson proposed this model to describe the ground state of the spin-1/2 Heisenberg antiferromagnet on the 2D triangular lattice. While in the end this model proved not correct for this particular system, since the spins oriented at 120° to one another, it did emphasise the importance of frustration to stabilise a QSL state [61]. QSLs can be grouped into classes depending on aspects such as the dimension, distribution of valence bond lengths, etc. These classes are described by what is known as a Gauge theory

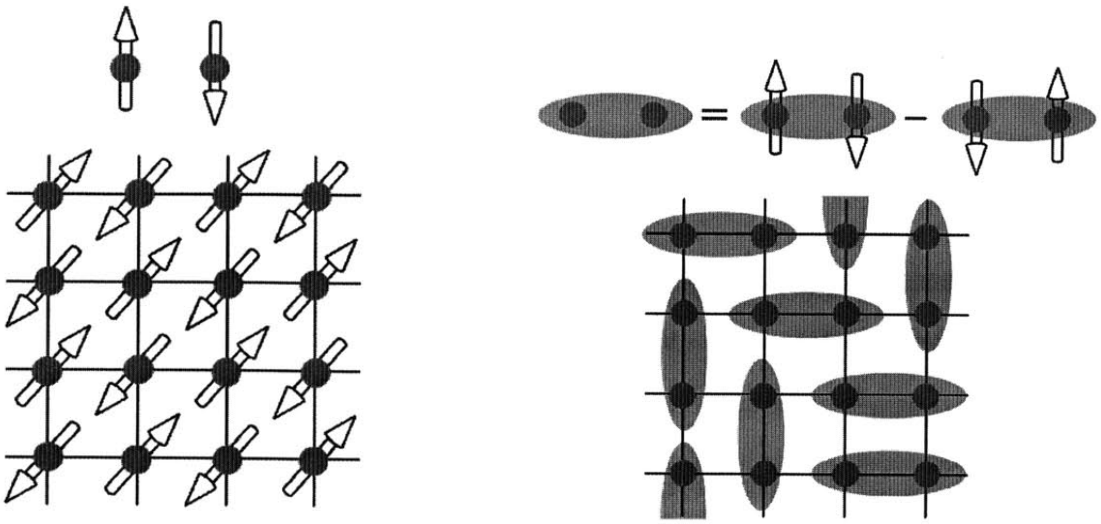

(a) (b)

Figure 1.20: Cartoon picture of the (a) Néel and (b) Anderson RVB state for (top) just two spins and (bottom) a square lattice. Figures acquired from [118].

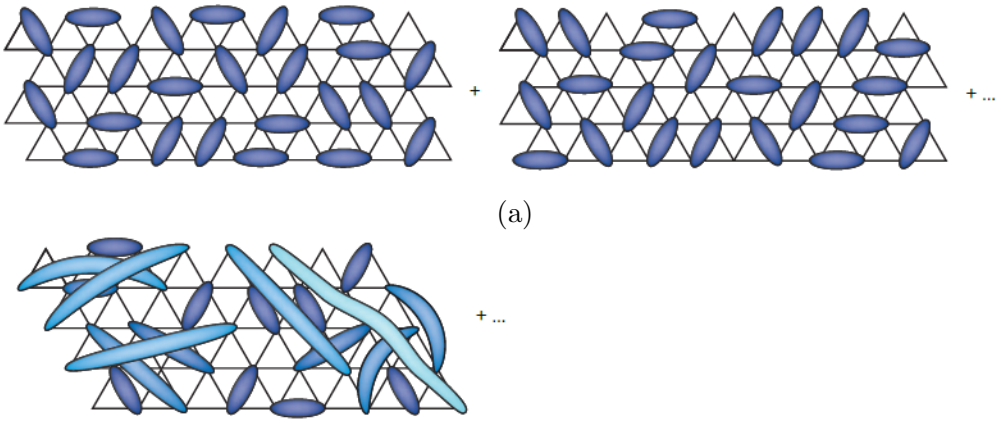

(a)

(b)

Figure 1.21: Representation of the superposition of all the possible pairings of spins for (a) short range and (b) long range single valence bonds. Entangled spin-zero singlets of two $S = 1/2$ spins are indicated by ovals that cover two points on the triangular lattice. Figures acquired from [47].

[119]. In this theory, the variational wave functions are approximate representations of ground states of an associated field theory, with this field theory consisting of fractionalised excitations coupled to fluctuating gauge fields. The gauge fields will change depending on the class of QSL: gapped, gapless, etc.

These fractionalised exotic excitations are possible in QSLs due to the presence of entangled spin states. In general, excitations can be classified on two grounds: electron-like, with half-odd-integer spin (usually $S = 1/2$) and charge $\pm e$, or magnon-like, with integer spin (usually $S = 1$) and neutral charge [47]. QSLs can exhibit fractionalised excitations named "spinons" with half-odd-integer spin (usually $S = 1/2$) and neutral charge [47]. The magnetic monopole in spin ice described in the previous section is an example of a fractionalised excitation. These excitations are formed when a spin is excluded from forming an entangled state or by breaking an entangled state [118]. In fact, these excitations are similar to monopoles in a spin ice, where once created no extra energy is needed for the spinons to propagate in the system (deconfined excitations). This propagation can be understood as the system moving through the different possible degenerate ground states [47]. Valence bonds formed by spins that are far apart are more weakly bound and thus can be "broken" to form free spins with relatively little energy. [47]. QSLs with a substantial contribution of longer range entangled states are known as QSL states with gapless excitations [118]. On the other hand, the spins might be so strongly entangled that excitations are not possible [120]. While these excitations are well understood in the spin-1/2 Heisenberg antiferromagnetic chain, where spinons form the domain walls that are free to propagate away from each other [121], their nature in 2D and 3D systems is less clear. In 2D and 3D, spinons can have varied character depending on the class of QSL. They may obey Fermi-Dirac or Bose-Einstein statistics, and some theories propose that spinons may form a partially filled band with a Fermi surface, known as spinon Fermi-surface state [61].

Another key feature of QSLs is that the moments continue to fluctuate even at 0 K. As mentioned before, some CSLs have a finite temperature T_C below which the system falls out of equilibrium, with the spin fluctuations significantly slowing down. This is due to the large energy barrier between ground states and the weak quantum amplitude

for such large spins to cooperatively tunnel through these barriers [47, 92]. This effect can be seen, for example, on the previously described classical spin ice $Dy_2Ti_2O_7$ and $Ho_2Ti_2O_7$, where ac-susceptibility measurements show slowing of the dynamics with time scales in the order of decades [122, 123]. In QSL the spins continue to fluctuate even at 0 K due to the strong quantum effects and the reduced energy barriers. This is similar to the quantum harmonic oscillator, which retains its zero-point motion even in the ground state [61, 124].

Due to the large degree of geometrical frustration, systems with 2D triangular or kagome structures or 3D pyrochlore systems are said to be the most promising QSL candidates. However, in general the discussion of possible QSL candidates is more centred on 2D systems, since the reduced dimensionality enhances the quantum fluctuations needed for QSLs [44].

To identify a QSL experimentally, the measurements would ideally have to be performed at 0 K. This is not allowed by the third law of thermodynamics [125], and thus the measurements are usually performed at temperatures far below the strength of the magnetic exchange coupling [44]. In this region, the 0 K properties can be well approximated. A good indicator of a QSL is the lack of magnetic order and lack of spin freezing at very low T. This information can be extracted by measuring the magnetic susceptibility, which also provides information on the strength of the magnetic interactions through the Curie-Weiss temperature Θ_{CW}. With this, the frustration parameter can also be calculated to determine the strength of the frustration. An ideal QSL should have $f = \infty$, but the finite T measurements as well as intrinsic disorder in the materials will limit this value [47]. In addition, microscopic probes such as muon spin relaxation (μSR) [126, 127] and nuclear magnetic resonance (NMR) [128] are also commonly used to determine the local magnetic environment.

At present, no technique exists that can be used to directly measured the long-range entanglement in QSLs, only indirectly through the presence of fractionalised excitations [44]. The specific heat is a common technique used to study the presence of magnetic excitations. It is important that the specific heat has no defined peaks, since these peaks indicate a phase transition. The presence of a peak in the specific heat well below Θ_{CW} indicates that significant spin entropy is being loss, establishing the possibility of a long range magnetic order, and a peak like the one shown in figure 1.10 indicates a transition to a frozen-spin phase [89]. Furthermore, the experimental signature of the excitations is a broad continuum spectrum, making inelastic neutron scattering (INS) a very commonly used technique. INS also has the added benefit of providing information on magnetic correlations [47]. Other commonly used techniques include NMR and electron spin resonance.

A 2D triangular QSL candidate that was studied using some of the techniques described above is $1T - TaS_2$. This system undergoes a metal to Mott insulator transition at 180 K where 13 Ta^{4+} form a hexagonal star of David, 12 of them forming the corners of the star and an isolated Ta in the centre, giving rise to a net $S = 1/2$ for each star of David, as figure 1.22a shows. Ribak *et al.* [129] performed susceptibility, heat capacity and μSR measurements. The susceptibility data, shown in figure 1.22b results in $\Theta_{CW} = 2.1$ K and an exchange constant $\mathcal{J} = 0.1$ K, much smaller than the exchange constants of Ho and Dy in $Ho_2Ti_2O_7$ and $Dy_2Ti_2O_7$. The heat capacity, shown in figure 1.22c shows a linear increase with temperature for all magnetic fields which could be from thermally excited spinons as some models of gapless QSL [47, 130] suggest. However,

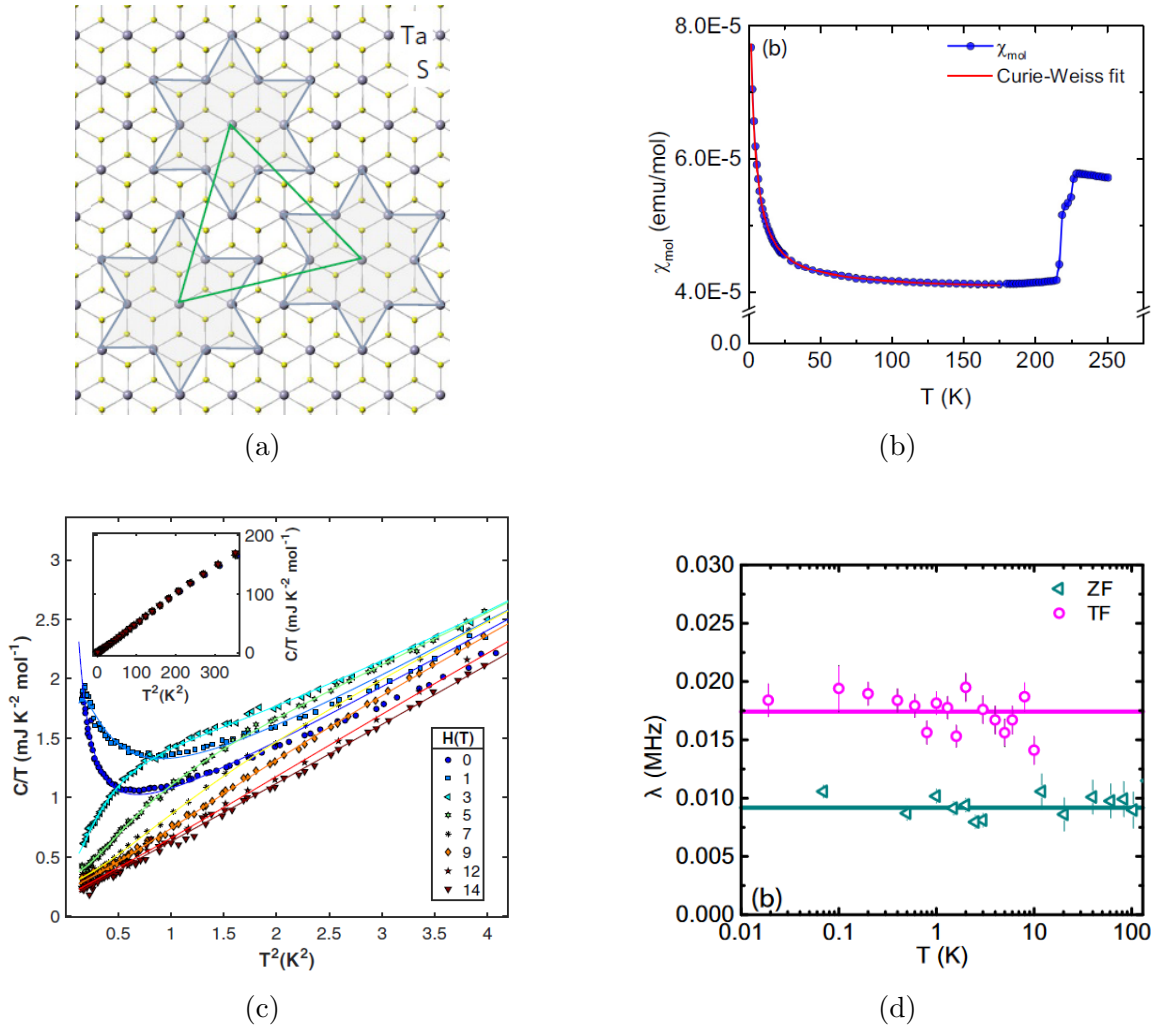

Figure 1.22: (a) Structure formed by $1T - TaS_2$. (b) Magnetic molar susceptibility as a function of T. (c) Heat capacity measurements at eight applied fields. (d) Temperature dependence of the muon damping rate (λ) with and without an applied field. Figure (a) acquired from [127] and figures (b) to (d) acquired from [129].

further studies are needed to confirm this. Finally, the muon data in figure 1.22d shows no change of the muon damping rate (λ) at multiple temperatures, indicating the absence of frozen moments. If frozen moments were found in the sample, an increase in λ would be observed. Whether this material is a QSL is under debate [127, 131, 132].

Another 2D QSL candidate worth mentioning is the 2D spin-1/2 kagome lattice $ZnCu_3(OD)_6Cl_2$, also called herbertsmithite, where the Cu^{2+} ions form 2D spin-1/2 kagome planes separated by the nonmagnetic Zn^{2+} ions. A single crystal of this system was studied by Han *et al.* [133] using INS techniques. The scattering in reciprocal space with an energy integration range between 1 meV and 9 meV, shown in figure 1.23a, has the shape of broadened hexagonal rings. Comparison of these data with calculations suggest that the nearest-neighbour spin singlet model is not enough to explain the data and longer-range correlations are needed. The intensity as a function of both energy and Q, shown in figure 1.23b, shows very broad continuous features, a clear signature of spinons. Furthermore, Han *et al.* did not find any indication of a spin gap down to 0.25 meV meaning that this system could be a gapless $U(1)$ QSL.

Chillal *et al.* [134] recently studied a QSL candidate in a 3D system that does not have

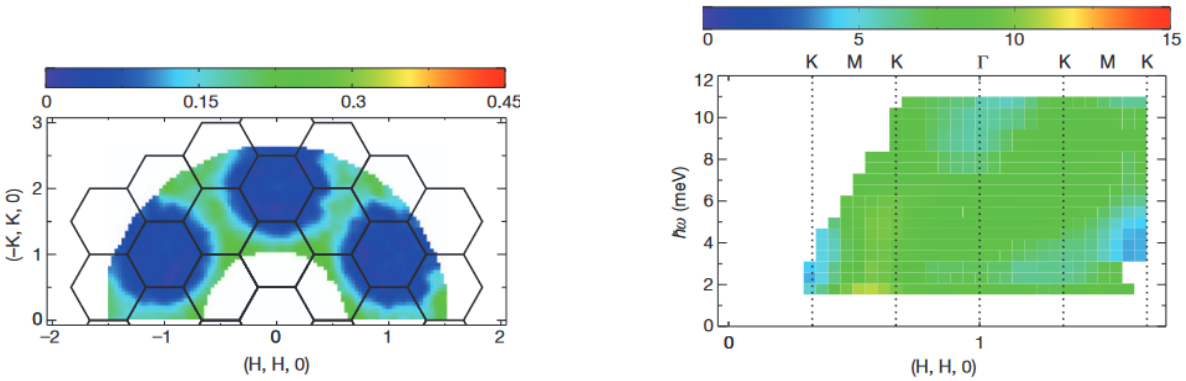

(a) (b)

Figure 1.23: Scattering data of the 2D spin-1/2 kagome lattice $ZnCu_3(OD)_6Cl_2$. (a) Intensity in reciprocal space with a constant integration range of 1 meV to 9 meV. (b) Magnetic dispersion along the high-symmetry [110] direction. Figures acquired from [133].

a pyrochlore structure. The sample studied was $PbCuTe_2O_6$, a 3D system consisting of $S = 1/2$ Cu^{+2} magnetic moments which interact antiferromagnaetically and form a three-dimensional network of corner-sharing triangles, as figure 1.24a shows. Previous studies of the magnetic susceptibility and specific heat by Koteswararao *et al.* [135] indicated no evidence for long-range magnetic order or static magnetism. This is in agreement with Chillal *et al.* μSR measurements shown in figure 1.24b, inferred from the rapid decay of the depolarisation with time. Figure 1.24c shows the excitation spectrum of a powder sample measured at 0.1 K while figure 1.24d shows the excitation spectrum of a single crystal at a constant energy transfer of 0.5 meV and 0.1 K. Both of these measurements show continuous, broad diffuse bands of magnetic signal, indicative of deconfined spinon excitations. Modelling of the data suggest that it is the presence of strong quantum fluctuations that destroy long-range magnetic order or any static magnetism in the ground state. However, Chillal *et al.* suggests the need to further study this system to more conclusively determine if it is gapped or gapless.

It is worth noting that, while all the systems studied shown above do seem like promising QSLs, their conclusions are still highly debated since these systems could also be spin glasses. Both of these systems have similar behaviour and experimental signatures, such as the absence of long-range magnetic order and the presence of continuous broad INS spectra [136]. The key difference between QSLs and spin glasses is the spin glasses having a freezing temperature, but it may be below the temperatures available experimentally.

Due to their many unique properties, QSLs also hold great application potential. One such application is in topological quantum computing. This is due to the presence of long-range quantum entanglement that can potentially be exploited to realise robust quantum computation [137]. Furthermore, spinons are believed to hold the key to creating more robust quantum bits since they are expected to be resistant to noise and external interference, a necessary ingredient for reliable quantum computing. However, many experiments are still needed to demonstrate how these quantum bits can be manipulated and encoded. Another promising application is in superconductivity. QSLs are Mott insulators where, unlike a band insulator where the bands are either full or empty, the bands are half filled [44]. Because of this, P. W. Anderson proposed that high temperature superconductivity in copper oxide superconductors can evolve from a spin liquid state

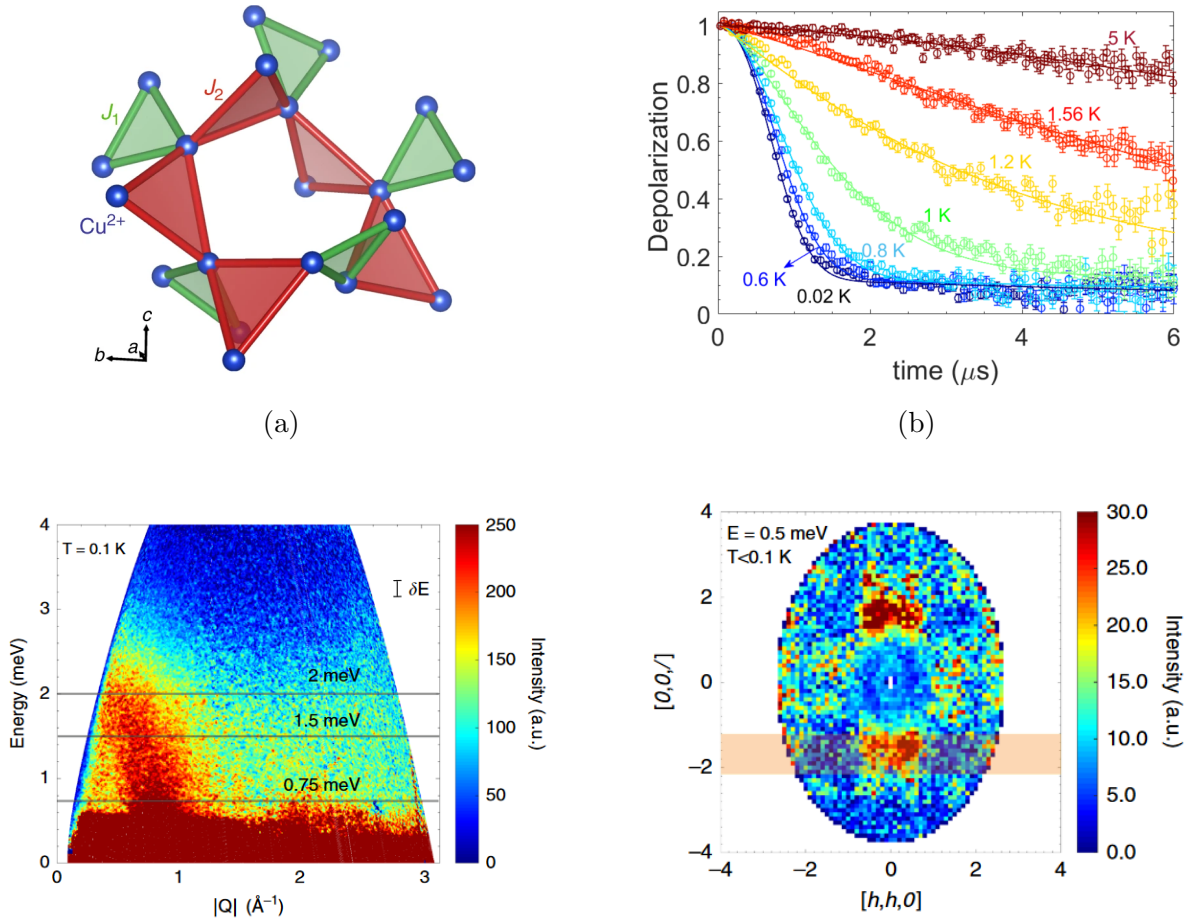

Figure 1.24: (a) Three-dimensional network of corner-sharing triangles of Cu^{2+} in $PbCuTe_2O_6$. (b) μSR spectra as a function of temperature. Excitation spectra obtained (c) on a powder and (d) on a single crystal. The single crystal data is at a constant energy transfer of 0.5 meV. Figures acquired from [134].

[138]. However, to achieve this, additional doping or large pressures are needed to reach the superconducting state. A recent example of this is in the QSL candidate $NaYbSe_2$ studied by Jia *et al.* [139]. $NaYbSe_2$ has a perfect triangular lattice, an ideal structure for QSL behaviour. In addition, measurements performed at 50 mK show no spin freezing or long-range magnetic order [140]. Jia *et al.* performed resistivity measurements at low temperatures and high pressures. They found that this system underwent a transition to a superconducting state when pressures higher than 103.4 GPa were applied, with the resistance dropping sharply below 8 K.

Finally, it is worth discussing the quantum analogue of the classical spin ice, the quantum spin ice. The quantum spin ice (QSI) is a type of $U(1)$ QSL [141] where spin ice configurations tunnel among themselves, i.e. a generalisation of the classical spin ice (CSI) integrating quantum fluctuations [104]. In a spin ice, the dominant tunnelling process involves flipping loops of spins that point nose-to-tail on a hexagonal plaquette, as figure 1.25 shows.

An interesting property of QSI systems is the presence of emergent photons. The two-in-two-out 'ice rule' acting on each tetrahedron leads to a manifold of degenerate ground states. This rule arises due to the spin correlations of each tetrahedron satisfying

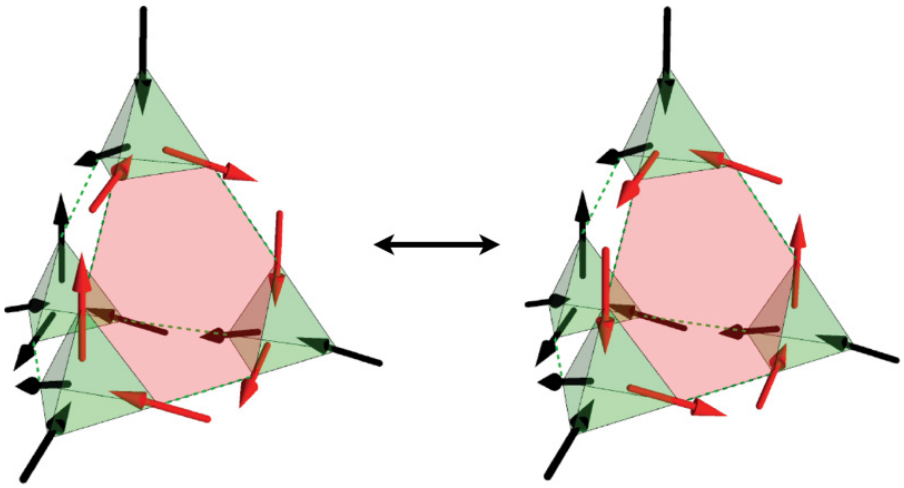

Figure 1.25: Illustration of the simplest tunnelling process between different spin-ice configurations. Figure acquired from [104].

$\nabla \cdot \mathbf{H}(\mathbf{r}) = 0$. An emergent gauge field $\mathbf{A}(\mathbf{r})$ can be defined as $\mathbf{H}(\mathbf{r}) = \nabla \times \mathbf{A}(\mathbf{r})$. In a CSI, due to the spin fluctuations slowing down significantly below the freezing temperature, this gauge field is effectively constant in time. However, the quantum fluctuations in a QSI system result in the two-in-two-out states no longer being static, but dynamic, making the emergent gauge field change in time. This gives rise to an electric field through $\mathbf{E}(\mathbf{r}) = -\frac{\partial \mathbf{A}(\mathbf{r})}{\partial t}$ and a ground state governed by Maxwell equation [104]

$$\mathcal{S}_{Maxwell} = \frac{1}{8\pi} \int \left[\mathbf{E}(\mathbf{r})^2 - c^2 \mathbf{H}(\mathbf{r})^2 \right] \mathrm{d}t \mathrm{d}^3\mathbf{r} \tag{1.17}$$

Any state of the QSI described by this equation supports linearly dispersing transverse excitations of the gauge field in the form of gapless emergent photons with a speed of light c [104].

Furthermore, just as with CSI, magnetic monopoles can also be found in QSI systems. These monopoles are very similar to the ones found in CSI, with the key difference that in a QSI the monopoles hop coherently and form waves [104]. Experimentally, the main difference between CSI and QSI is that, while in CSI the pinch points do not change below the freezing temperature, in a QSI pinch points are suppressed as temperatures are lowered, disappearing at $T = 0$ [104, 142]. This is because as the temperature decreases, quantum effects tune the system into a quantum spin liquid. Finally, unlike in CSI where the residual entropy is the same as the water ice entropy, as it was shown above, in a QSI the residual entropy is predicted to vanish at zero temperature due to the system having a single quantum mechanical ground state formed through the superposition of many classical ice configurations [142].

One of the most compelling families of materials thought to exhibit this QSI behaviour are praseodymium-based pyrochlores, since in these materials the dipolar interactions are reduced by an order of magnitude in comparison to that for Dy^{3+} or Ho^{3+}. The reduced dipolar interaction reduces the energy barrier between ground states, enhancing the importance of quantum fluctuations and tunnelling between ground states. In addition, since Pr ions have fewer electrons than Ho and Dy, the 4f wave function is spatially extended [143], and can then be largely overlapped with the O 2p orbitals of the O(1) ions [144]. This will lead to superexchange interactions between Pr ions through the O(1) ions,

which is believed to be the leading interaction [144]. Recently, Sibille *et al.* [4] performed INS measurements on $Pr_2Hf_2O_7$ at 50mK. The quasi-elastic data shown in figure 1.26a show the general shape observed in pyrochlore materials with spin ice correlations. Figure 1.26b shows radial and transverse cuts of the (0,0,2) pinch point. These cuts show how the measured pinch points seem to be suppressed relative to a CSI model calculation. Sibille *et al.* claims that the agreement with the predictions of a lattice field theory of the photon excitations of a QSI [104] is better. The fit of this theory to the data indicates a speed of light $c \approx 3.6$ m/s for the emergent photons.

1.3.2.1 Disorder in QSL

So far, all the discussion on spin liquids has been focused on materials where no disorder was assumed. This is because frustration, a key ingredient of QSLs, can be broken by a lattice distortion. However, Savary *et al.* [145] proposed the use of disorder itself to generate long range quantum entanglement in pyrochlores based on non-Kramers ions. The idea is that structural imperfections around the magnetic sites act as transverse fields which act on the doubly degenerate ground state. These transverse fields induce tunnelling between spin ice ground states, which stabilises the $U(1)$ QSL. The idea of disorder induced QSL was focused around $Ho_2Ti_2O_7$ and $Pr_2Zr_2O_7$ because they have a large separation between the ground state and the first excited states. As such, there will be no mixing between these two states when the transverse field is applied, an essential ingredient for a $U(1)$ QSL [141]. Figure 1.27 shows the predicted phase diagram as a function of disorder for quantum spin ice, which includes two true quantum spin liquids [145].

Rare-earth ions can be classified as Kramers (Yb^{3+} and Dy^{3+}) or non-Kramers (Ho^{3+} and Pr^{3+}) depending on whether the number of 4f electrons is odd or even, respectively. In Kramers ions all the energy levels are degenerate (doublets), while in non-Kramers ions non-degenerate levels (singlets) are allowed. Furthermore, a permanent magnetic moment

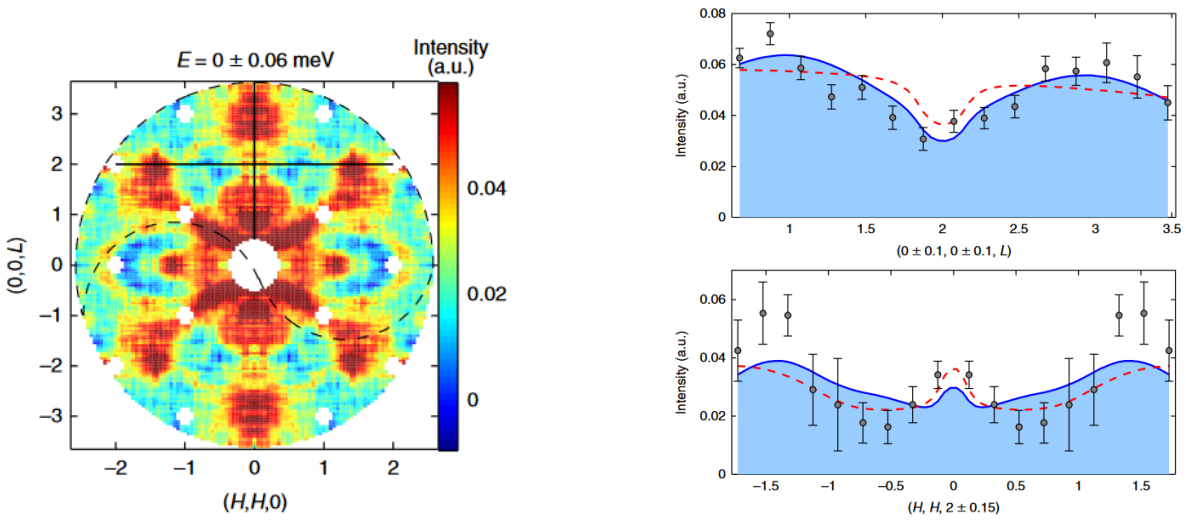

(a) (b)

Figure 1.26: Scattering data of $Pr_2Hf_2O_7$ collected using time-of-flight INS at 50 mK with unpolarised neutrons. (a) 2D elastic data integrated around zero energy transfer. (b) Radial (top) and transverse (bottom) cuts through the (0,0,2) pinch point and comparison with a model calculation of a CSI (red dashed line) and a QSI (solid blue line). Figures acquired from [4].

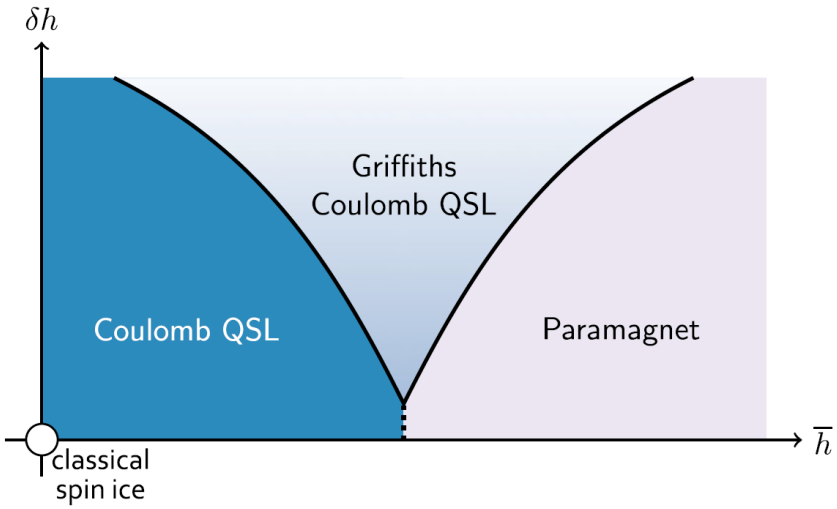

Figure 1.27: Phase diagram in the mean strength of disorder ($\bar{h}$) – disorder (δh) plane. Figure acquired from [145].

can be associated only with a degenerate ground state. Thus, a magnetic non-Kramers ion is one with a doubly degenerate ground state (doublet ground state). The fact that Ho^{3+} and Pr^{3+} have doublet ground states with large moments is a consequence of the symmetry of the crystal electric field (CEF) in pyrochlores. The reason why Savary *et al.* [145] proposed non-magnetic structural distortions in systems with non-Kramers ions is because disorder can lower the symmetry of the rare-earth sites. This will generate a different CEF, which will be explained later on in the thesis, which can split the doublet ground state into two singlets formed by superpositions of the original doublet states.

1.4 Motivation

In this thesis, the effects of two kinds of disorder on Ho^{3+} and Pr^{3+} pyrochlore systems was studied using neutrons. The effects of introducing disorder in the form of substitution and vacancies of non-magnetic ions in $Ho_2Ti_2O_7$ was studied by doping this system with Sc ions on the B-sites. However, due to the difference in charge valency between Ti^{4+} and Sc^{3+}, this doping reduced the "amount of positive charge" in the system, and thus charge compensating O vacancies were introduced. In addition, the effects of strains on the magnetism was studied on Pr_2ScNbO_7. The combination of trivalent Sc^{3+} and pentavalent Nb^{5+} cations in equal quantities is a way to introduce local strains without the complication of introducing charge-compensating oxygen vacancies.

To determine the origin of the disorder of both systems (location of vacancy for the Ho system and ordering of Sc/Nb ions for the Pr system), total scattering measurements and diffuse scattering measurements were performed using multiple instruments. The resulting data were analysed with Bragg refinement, RMC fits and density functional theory (DFT) calculations. Once the origin of the disorder was known, the effects on the magnetism were studied by performing crystal electric field measurements to extract the energy levels of the Ho^{3+} and Pr^{3+} ions in the presence of disorder. In addition, the effects of disorder on the cooperative magnetism was studied by performing magnetic diffuse scattering measurements.

Neutrons are particularly useful for studying disordered systems such as these because of the ability to isolate the structural and the magnetic diffuse scattering with neutron polarisation analysis, as will be discussed later. Furthermore, if x-rays were to be used,

the effect of O ions would be difficult to study since, in the presence of Ho or Pr ions, these ions are invisible. Not only that, but due to the similar number of electrons in Ti and Sc, the effect of doping Sc ions in $Ho_2Ti_2O_7$ could not be distinguished using x-rays.

Chapter 2

Theory of neutron scattering

2.1 The crystal lattice

2.1.1 Real space

For the purposes of this thesis, the focus will be on single crystals and powders. A crystal is a solid material whose constituents (atoms, ions, molecules, ...) are arranged in a highly ordered microscopic structure [146]. To describe a crystal, it is necessary to define a set of coordinate axis. The 2D system shown in figure 2.1 will be used to illustrate this concept. The origin of the system can be anywhere, but the convention is to use one of the atoms. These axes are sometime called lattice vectors and are identified by a length (lattice constant) and the angle between them. The position of all equivalent points (or lattice points) are found with the lattice vectors using [147]

$$\mathbf{r} = h\mathbf{a} + k\mathbf{b} \quad \text{or} \quad \mathbf{r} = h\mathbf{a} + k\mathbf{b} + l\mathbf{c} \tag{2.1}$$

for a 2D and a 3D system respectively, where **a**, **b** and **c** are the lattice vectors and h, k and l can take any possible integer value and are called Miller indices. This will generate the crystal lattice, shown as the set of dark dots in figure 2.1. In 2D every possible crystal lattice can be classified into one of 5 possible types, and in 3D there are 14 possible types. These are called the Bravais lattices [147].

The set of lattice vectors forms a unit cell, the region of space which can be repeatedly stacked to assemble the crystal lattice without gaps. As it is shown in figure 2.1, the unit cell can change depending on the chosen set of lattice vectors. With this, two types of unit cells can be chosen: a primitive unit cell (vectors **a** and **b** in figure 2.1), containing a single lattice point (the smallest possible primitive unit cell is called the Wigner–Seitz cell), and a conventional unit cell (vectors **a'** and **b'** in figure 2.1), which is chosen because it is more symmetric [146]. Figure 1.1 shows the conventional unit cell of the pyrochlore.

To fully describe the crystal structure, the content inside of the unit cell needs to be defined. This is called the basis and is given by the group of atoms associated with each lattice point, which completely generate the structure [147]. For the 2D example in figure 2.1, the basis is given by the green dots to the right of the lattice. In a pyrochlore, the basis for the conventional unit cell is given in table 1.1. When combining the crystal lattice with the basis, in 3D 230 possible space groups exist [146], with the pyrochlore belonging to space group 227 labelled $Fd\bar{3}m$.

Finally, it is sometimes useful to define lattice planes or directions. A plane is defined

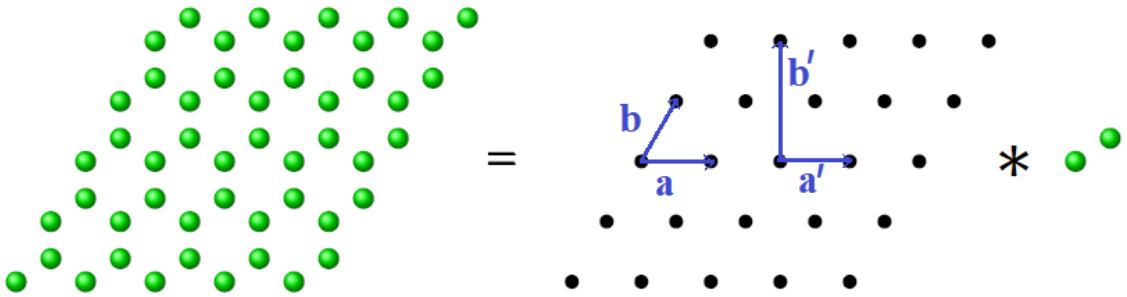

Figure 2.1: 2D system with ions forming a regular structure. The structure is separated into the lattice and the basis. Figure acquired from [146].

by where it intercepts in the crystal lattice such that, in 3D, the plane nearest the origin will have intercepts at a/h, b/k and c/l, where a, b and c are the lengths of the chosen lattice vectors [147]. The notation used with lattice planes is (hkl) (the Miller indices in ()-brackets), with the set of symmetrically equivalent planes denoted as $\{hkl\}$. So a plane that intercepts at the halfway point of each axis of the unit cell is called the (222) plane. Similarly, a direction is defined in terms of the lattice vectors using equation (2.1) and the notation used is $[hkl]$ (the Miller indices in []-brackets), with the set of symmetrically equivalent directions denoted as $\langle hkl \rangle$ [147]. For both, directions and planes, a bar $^-$ on top of a value indicates a negative integer ($\bar{1} = -1$).

2.1.2 Reciprocal space

A useful concept in crystallography is the use of reciprocal space, also known as momentum space or k-space. It allows for the description of a parameter space in terms of the momentum change. Similarly to real space, in reciprocal space a reciprocal lattice for a system exists and is defined as the Fourier transform of the crystal lattice. As it will be made clearer later, this is the space that is measured with diffraction experiments.

The reciprocal lattice vectors are related to the real space lattice vectors as [147]

$$\mathbf{a}^* = \frac{2\pi(\mathbf{b} \times \mathbf{c})}{\mathbf{a}(\mathbf{b} \times \mathbf{c})} \qquad \mathbf{b}^* = \frac{2\pi(\mathbf{c} \times \mathbf{a})}{\mathbf{a}(\mathbf{b} \times \mathbf{c})} \qquad \mathbf{c}^* = \frac{2\pi(\mathbf{a} \times \mathbf{b})}{\mathbf{a}(\mathbf{b} \times \mathbf{c})} \tag{2.2}$$

where, just as with the crystal structure, the location of a point is defined by the reciprocal lattice vector [147]

$$\boldsymbol{\tau} = h\mathbf{a}^* + k\mathbf{b}^* + l\mathbf{c}^* \tag{2.3}$$

where h, k and l are also Miller indices. Finally, just as with the crystal lattice, in the reciprocal lattice a unit cell can also be defined with $\mathbf{a}^*$, $\mathbf{b}^*$ and $\mathbf{c}^*$. The first Brillouin zone in reciprocal space is the equivalent of the primitive unit cell in real space, and plays a key role in structure determination.

2.2 Diffraction

Multiple probes, such as x-rays, electrons and muons, can be used to study and determine crystal structures as well as their properties. However, for the purposes of this thesis, the focus will be on the use of neutrons to study crystals.

Neutron scattering is a signal-limited technique and, therefore large-scale sources, reactor or accelerator facilities are required. However, neutrons have significant advantages

over x-rays for certain types of experiments. Neutrons interact with the nucleus via the nuclear strong force, which varies randomly across the periodic table but always with the same order of magnitude. This makes neutrons more sensitive to the positions of lighter elements, including oxygen, than x-rays. In addition, neutrons, which are a spin 1/2 particle, have a magnetic moment with which they can interact with the spin of the unpaired electrons and the spin of the nucleus through dipole-dipole effects. This means that for neutrons the magnetic cross-section is comparable to the nuclear cross-section, in contrast to x-rays where the charge scattering dominates the magnetic scattering. Hence, neutrons are the first choice for studies of magnetic ordering and excitations. Other interactions can be neglected for the purposes of this thesis, such as interactions with the electric field via a spin-orbit and Foldy interactions [46].

Finally, as it will be discussed later on, the energies with which neutrons are generated is of the same order as many excitations in condensed matter, making them an ideal probe to study many dynamic events. This is in contrast to x-rays where energies tend to be many orders of magnitude greater than excitations and where, although inelastic experiments are now possible at synchrotrons, they are more challenging. However, while the focus of this thesis is on neutrons, it is worth noting that both neutrons and x-rays are used to probe the dynamics of systems since they are generated with different energy ranges and thus probe different types of excitations.

2.2.1 Neutron scattering

Consider a beam of neutrons all with energy E heading towards a target called the scattering system. The geometry of the problem is shown in figure 2.2. Neutron scattering aims to measure the probability that, after interacting with the scattering system, a neutron scatters into a certain solid angle $\mathrm{d}\Omega$ within a final energy range $\mathrm{d}E_f$ and final spin S. In an experiment, the basic quantity that is measured (ignoring polarisation which will be discussed later one) is the partial differential cross-section $\frac{\mathrm{d}^2\sigma}{\mathrm{d}\Omega \mathrm{d}E_f}$ where the cross-section σ is the probability of scattering [148].

2.2.1.1 Scattering from a single fixed atom

For simplicity, let us consider first scattering from a single fixed nucleus with no magnetism (the spin state of the neutron does not change). Since the wave-particle duality also affects neutrons, an estimate of the de Broglie wavelength for the neutron can be calculated using the mass of the neutron $\mathrm{m_n} = 1.675 \times 10^{-27}$ Kg and an energy in the meV order (typical energy used in neutron scattering). This gives a wavelength of the order of 10^{-10} m = 1 Å, much larger than the range of the strong nuclear force of around 10^{-15} m [149]. As such, we can use the result from diffraction theory that states that if waves of any kind (in this case the incident neutron) are scattered by an object much smaller (the fixed nucleus) than the incoming wave, the scattered wave is spherically symmetric.

A neutron moving along the (arbitrary) z axis can be expressed by the wave function [149]

$$\psi_{\mathrm{in}} = e^{ikz} \tag{2.4}$$

where $k = 2\pi/\lambda$ is the wavevector. After scattering, the wave function of the neutron at a distance r from the target can be written as [149]

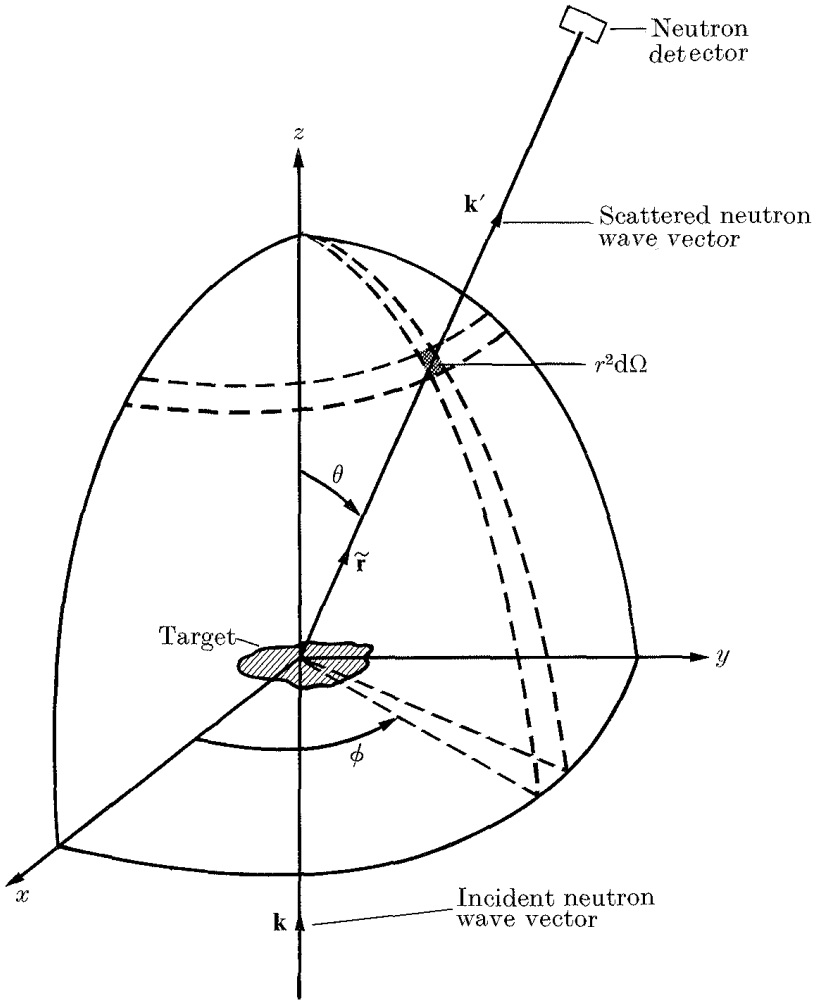

Figure 2.2: Neutron scattering geometry. Figure acquired from [148].

$$\psi_{\text{sc}} = -\frac{b}{r} e^{ikr} \tag{2.5}$$

In this particular example, both wave functions have a normalisation factor of 1, and the scattering process is elastic, i.e. there is no transfer of momentum from the neutron to the nucleus and thus $k = k_i = k_f$. It is worth noting that, in reality, both k and r are vectors and the exponential in equations (2.4) and (2.5) should be $\exp\{i\mathbf{k} \cdot \mathbf{r}\}$, where $|\mathbf{k}| = k$ and $|\mathbf{r}| = r$.

The quantity b in equation (2.5) is known as the scattering length, which has a real and imaginary part and depends on the target nucleus. Two types of nuclei exist: The first type is nuclei where b depends on the energy of the neutron. For this type, the scattering is a resonance phenomenon associated with the formation of compound nuclei [149]. The imaginary part of b is important since it corresponds to the absorption. For the purposes of this thesis, the focus will be on nuclei where the imaginary part of b is small, which corresponds to the majority of atoms, and we can treat this quantity as purely real [149].

With ψ_{in} and ψ_{sc} we can extract the scattering cross-section σ. Since the scattering process is elastic, the neutron energy is unchanged, and thus the partial differential cross-section simplifies to the differential cross-section $\frac{\mathrm{d}\sigma}{\mathrm{d}\Omega}$ which is defined as the number of neutrons scattered per second into $\mathrm{d}\Omega$ in the direction $(2\theta, \phi)$ per unit area of the beam

[150]. If v is the velocity of the neutron, then the number of scattered neutrons going through the area $\mathrm{d}S$ per second is given by $v\mathrm{d}S|\psi_{\mathrm{sc}}|^2 = vb^2\mathrm{d}\Omega$ and the flux of incident neutrons is given by $\Phi = v|\psi_{\mathrm{in}}|^2 = v$. Thus, from the definition of the differential cross-section [149]

$$\frac{\mathrm{d}\sigma}{\mathrm{d}\Omega} = \frac{vb^2\mathrm{d}\Omega}{\Phi\mathrm{d}\Omega} \tag{2.6}$$

which, when integrating over all possible angles ($\theta : 0 \to \pi$ and $\phi : 0 \to 2\pi$) and using the definition $\mathrm{d}\Omega = \sin(\theta)\mathrm{d}\theta\mathrm{d}\phi$ results in an expression of the cross-section of the form [149]

$$\sigma = 4\pi b^2 \tag{2.7}$$

with units of m^2.

2.2.2 Crystal structure determination

2.2.2.1 Bragg's law

As described above, the neutron de Broglie wavelength is of the order of 1Å, of the order of interatomic distances in solids and liquids. Because of this, the crystal structure acts as a diffraction grating for the incoming neutrons [147]. Interference between the scattered neutrons will produce different scattering intensity patterns, with which we can extract information such as the structure and lattice parameters.

The most basic analysis of the resulting intensity pattern follows from Bragg's Law: scattering can be detected when the incident neutrons are scattered coherently, this is, for a scattering angle of 2θ the path difference must be an integer multiple of the wavelength [147]. To see this, consider scattering from a single plane of atoms, as shown in figure 2.3a, with an incident angle θ. The waves that scatter at the two points A and D will only interfere constructively if AB = CD, in other words, if $\theta = \varphi$. Thus, the neutron is deflected through an angle 2θ.

However, it is also necessary for multiple planes to scatter in phase [147], as shown in figure 2.3b. In this case, not only the angles need to be the same, but the path difference must be an integer numbers of wavelengths (ABC = $n\lambda$). This is written mathematically in Bragg's law as [147]

$$n\lambda = 2d\sin(\theta) \tag{2.8}$$

where d is the spacing between lattice planes, n is the diffraction order, θ is the scattering

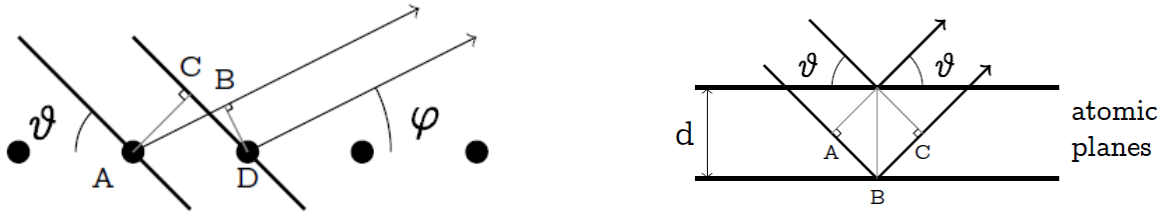

(a) (b)

Figure 2.3: (a) A single plane of lattice points and (b) a stack of planes separated by a distance d where the neutron incident angle is θ. Figures acquired from [146].

angle and λ is the wavelength of the incident neutron. In addition, it is useful to relate this expression to reciprocal space. A useful quantity in diffraction is the wavevector transfer $\mathbf{Q}$, which is defined as the difference between the incident and final wavevector, $\mathbf{k}_i - \mathbf{k}_f$. As figure 2.4 shows, if the scattering is elastic, so $|\mathbf{k}_i| = |\mathbf{k}_f| = |\mathbf{k}|$, $\mathbf{Q}$ must be perpendicular to the scattering plane and the geometry must satisfy [146]

$$\frac{|\mathbf{Q}|}{2} = |\mathbf{k}| \sin(\theta) = \frac{2\pi}{\lambda} \sin(\theta) \tag{2.9}$$

which, using equation (2.8), can be reduced to [146]

$$|\mathbf{Q}| = \frac{4\pi \sin(\theta)}{\lambda} = \frac{2\pi}{d} \tag{2.10}$$

which relates the inter-plane distance to the wavevector transfer.

2.2.2.2 Scattering from a crystal

Since a crystal can be separated into the lattice and the basis, the distance $\mathbf{r}_j$ of an ion j from an arbitrary origin can be defined as

$$\mathbf{r}_j = \mathbf{r}_\upsilon + \mathbf{R}_\Upsilon \tag{2.11}$$

where $\mathbf{R}_\Upsilon$ is the distance from the origin to lattice point Υ and $\mathbf{r}_\upsilon$ is the distance from the lattice point to ion υ. If the origin of each unit cell is at the lattice point, then $\mathbf{r}_\upsilon$ is also the distance from the origin of that unit cell.

If the scattering is elastic, the expression for the differential cross-section found for a single bound nucleus can be extended for a system with N nuclei by summing over all possible ion locations. For this, we can use the expression from equation (2.5) but considering a more general case where $|\mathbf{k}_i| \neq |\mathbf{k}_f|$ and the scattering ion is a distance $\mathbf{r}_j$ from the arbitrary origin. Thus, scattering from the j^{th} ion with scattering length b_j will contribute a small amount to the scattered wave [150]:

$$[\delta\psi_{\text{sc}}]_j = -b_j e^{i\mathbf{k}_i \cdot \mathbf{r}_j} \frac{e^{i\mathbf{k}_f \cdot |\mathbf{D} - \mathbf{r}_j|}}{|\mathbf{D} - \mathbf{r}_j|} = -b_j e^{i\mathbf{k}_f \cdot \mathbf{D}} \frac{e^{i\mathbf{Q} \cdot \mathbf{r}_j}}{|\mathbf{D} - \mathbf{r}_j|} \tag{2.12}$$

where $\mathbf{D}$ is an arbitrary position, usually the distance from the arbitrary origin to the detector. The full expression for the scattered wave is simply found by considering the contribution from all N atoms

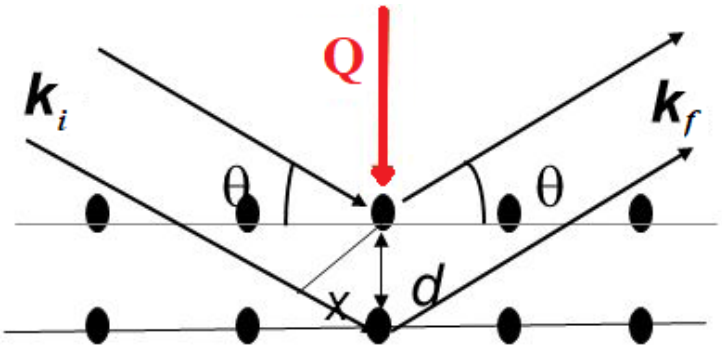

Figure 2.4: Schematic of the change of wavevector $\mathbf{k}$. Figure acquired from [151].

$$\psi_{\text{sc}} = -e^{i\mathbf{k}_f \cdot \mathbf{D}} \sum_{j=1}^{N} b_j \frac{e^{i\mathbf{Q}\cdot\mathbf{r}_j}}{|\mathbf{D} - \mathbf{r}_j|} \tag{2.13}$$

It is worth pointing out that this scattered wave is a simplification from the Born approximation, where it is assumed that the incident wave does not interfere with the scattered wave (weak scattering) [150]. In addition, events in which neutrons are deflected multiple times are ignored. This equation can be further simplified in the Fraunhofer or *far-field* limit, where it is assumed that the distance from the origin to the detector $\mathbf{D}$ is much larger than the typical size of a crystal [150]

$$|\mathbf{D} - \mathbf{r}_j| \approx |\mathbf{D}| = D \tag{2.14}$$

The scattered wave then has a modulus squared

$$|\psi_{\text{sc}}|^2 = \frac{1}{D^2} \left| \sum_{j=1}^{N} b_j e^{i\mathbf{Q}\cdot\mathbf{r}_j} \right|^2 \tag{2.15}$$

Finally, using the definition of the differential cross-section from before, the neutron count rate measured in the detector is given by [46]

$$I\left(\mathbf{Q}\right) = \frac{\mathrm{d}\sigma}{\mathrm{d}\Omega} \propto \left| \sum_{j=1}^{N} b_j e^{i\mathbf{Q}\cdot\mathbf{r}_j} \right|^2 \tag{2.16}$$

If the crystal being scattered from is composed by N unit cells, each cell with n atoms (the basis), the expression above can be further decomposed using equation (2.11) into two parts

$$I\left(\mathbf{Q}\right) \propto \left| \sum_{\Upsilon}^{N} e^{i\mathbf{Q}\cdot\mathbf{R}_\Upsilon} \sum_{\upsilon}^{n} b_\upsilon e^{i\mathbf{Q}\cdot\mathbf{r}_\upsilon} \right|^2 \tag{2.17}$$

where the first summation is the *symmetry* term and the second the *structure factor*. One can see that the symmetry term will be non-zero when $\mathbf{Q} \cdot \mathbf{R}_\Upsilon$ gives an integer number of 2π. Using equations (2.1) and (2.3), one can see that this is only possible if

$$\mathbf{Q} \cdot \mathbf{a} = 2\pi h \quad \text{and} \quad \mathbf{Q} \cdot \mathbf{b} = 2\pi k \quad \text{and} \quad \mathbf{Q} \cdot \mathbf{c} = 2\pi l \tag{2.18}$$

where h, k and l are integers (the Miller indices). This is known as the Laue condition, which states that the momentum transfer to the crystal must coincide with a reciprocal lattice vector ($\mathbf{Q} = \boldsymbol{\tau}$) for scattering to be possible [147]. This is also the condition for constructive interference. If this condition is satisfied, the symmetry term will be a constant and the exponent in the structure factor can be modified [147]

$$I\left(\mathbf{Q}\right) \propto \left| \sum_{\upsilon}^{n} b_\upsilon e^{i2\pi(hu_\upsilon + kv_\upsilon + lw_\upsilon)} \right|^2 \tag{2.19}$$

where we have used the fact that the position of the ions can be expressed as $\mathbf{r}_\upsilon = u_\upsilon \mathbf{a} + v_\upsilon \mathbf{b} + w_\upsilon \mathbf{c}$, this is as fractions of the lattice vectors. One can see that, depending

on the location of the ion in the unit cell, the relative intensity of the scattered beam will change even when the Laue condition is satisfied. It is with this that not only the structure of a crystal can be determined, but also the relative position of the different species of ions within the crystal.

Each crystallographic space group has a different combination of h, k and l values that produce a non-zero structure factor. For example, a face centre cubic (FCC) crystal will give a non-zero structure factor when h, k and l are either all odd or all even [146]. Thus, if for a given crystal the set of h, k and l values that produce non-zero structure factors are determined, then the crystal can be classified into one of the possible crystallographic space groups.

Since the focus of the thesis is on neutron scattering, it is worth describing one of the benefits of neutrons over x-rays. Because x-rays interact with the cloud of electrons surrounding the nucleus, the probability of an x-ray interacting with an ion increases with atomic number. As such, when studying systems such as $Ho_2Ti_2O_7$, the O is practically invisible to the x-ray, and we would get information mainly from the Ho. The scattering lengths of Ho, Ti and O are 8.01 fm, -3.44 fm and 5.80 fm respectively [152], different enough for the neutrons to easily differentiate between them. Furthermore, x-rays cannot differentiate between a Ti and a Sc, since they are next to each other in the periodic table. However, because Ti has a negative b and Sc a positive b, the neutron can distinguish between them easily. In general, as figure 2.5 shows, the values of all the bs are around the same order of magnitude, but different enough for the neutron to distinguish them. This property of the scattering length is very useful when studying materials with defects such as vacancies, or when the sample is doped with a new type of ion.

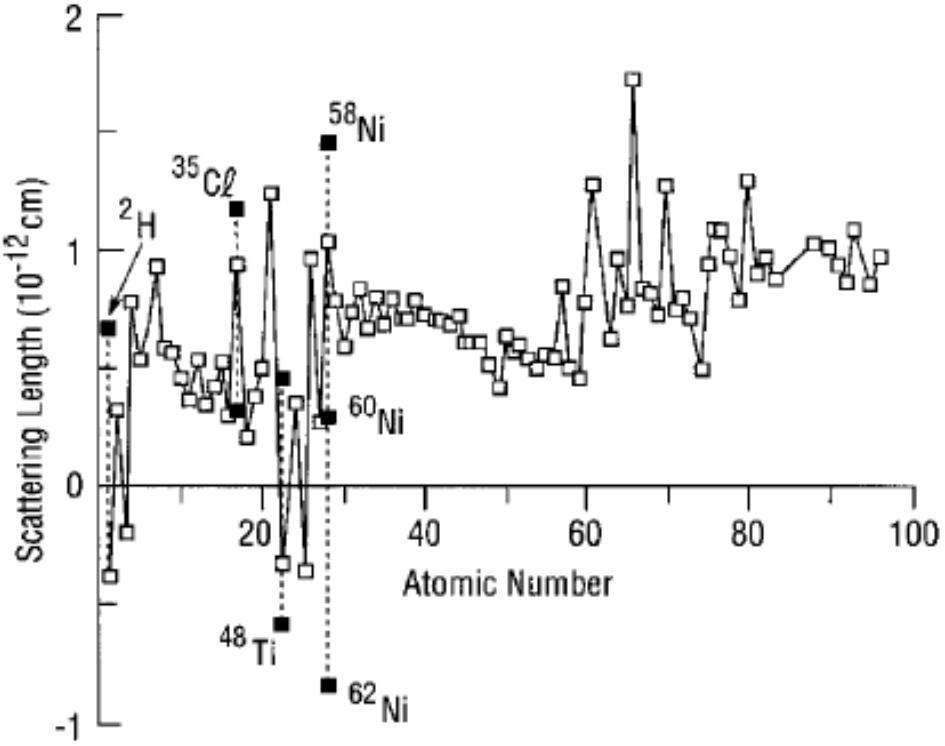

Figure 2.5: Variation of coherent scattering length with atomic number (open squares). Variation of coherent scattering length among isotopes is indicated for several cases by the filled squares. Figure acquired from [153].

2.2.3 General expression for neutron scattering

The general expression for the partial differential cross-section used in a scattering experiment with magnetic contributions and inelastic effects is [154]

$$\frac{\mathrm{d}^2\sigma}{\mathrm{d}\Omega \mathrm{d}E_f}(\mathbf{Q},\hbar\omega) = \frac{k_f}{k_i}\left(\frac{m}{2\pi\hbar^2}\right)^2 \sum_{\sigma_i,\sigma_f}\sum_{n_0,n_1} p\left(\sigma_i\right) p\left(n_0\right) \left|\left\langle \mathbf{k}_f\sigma_f n_1|V|\mathbf{k}_i\sigma_i n_0\right\rangle\right|^2 \delta\left(\epsilon_1-\epsilon_0+\hbar\omega\right) \tag{2.20}$$

where $\mathbf{k}_i$ and $\mathbf{k}_f$ are the neutron initial and final wavevector, m is the neutron mass, σ_i and σ_f are the initial and final neutron spin state, n_0 and n_1 are the quantum numbers for the initial and final state of the target system, ϵ_0 and ϵ_1 are the initial and final energy of the target system, $V(r)$ is the interaction potential, $\hbar\omega$ is the energy transfer given by

$$\hbar\omega = E_i - E_f \tag{2.21}$$

where E_i and E_f are the initial and final energy of the neutron, $p\left(\sigma_i\right)$ is the probability of finding the neutron in the initial spin state σ_i and $p\left(n_0\right)$ is the probability of finding the target system in state n_0.

The δ function at the end represents the energy conservation law that must be satisfied in an experiment: $E_i+\epsilon_0 = E_f+\epsilon_1$ [149]. For the purposes of this thesis, two types of interaction potentials will be considered: nuclear interaction potential V_N and magnetic interaction potential V_M. The total interaction potential is simply given by the sum of the two. Because of the $||^2$ in equation (2.20), the resulting interaction potential will be composed of a purely magnetic component, a purely nuclear component and a component formed by a mix of the nuclear and magnetic potential. For the systems studied in this thesis, the mixed terms which are commonly known as "Nuclear Magnetic Interference" terms can be neglected.

2.2.3.1 Nuclear interaction potential

From the simple case described above on scattering from a single bound nucleus and scattering from a crystal with N ions, the nuclear interaction potential can be expressed as [154]

$$V_N\left(\mathbf{r}\right) = \frac{2\pi\hbar^2}{m}\sum_j^N b_j\delta\left(\mathbf{R}-\mathbf{r}_j\right) \tag{2.22}$$

which is known as the Fermi pseudopontial [148] and where b is the scattering length. Consider a system with no magnetism. Inserting equation (2.22) into (2.20) gives [149]

$$\frac{\mathrm{d}^2\sigma}{\mathrm{d}\Omega \mathrm{d}E_f}(\mathbf{Q},\hbar\omega) = \frac{k_f}{k_i}\left(\frac{1}{2\pi\hbar}\right)\sum_{j,j'} b_j b_{j'}\int_{-\infty}^{\infty}\langle e^{-i\mathbf{Q}\cdot\mathbf{r}_{j'}(0)}e^{i\mathbf{Q}\cdot\mathbf{r}_j(t)}\rangle e^{-i\omega t}\mathrm{d}t \tag{2.23}$$

where the notation $\langle AB\rangle = \sum_{n_0,n_1} p\left(n_0\right)\left\langle n_0|A|n_1\right\rangle\left\langle n_1|B|n_0\right\rangle$ [149] was used as well as the following equalities:

$$\delta\left(\epsilon_1-\epsilon_0+\hbar\omega\right) = \frac{1}{2\pi\hbar}\int_{-\infty}^{\infty} e^{-i(\epsilon_0-\epsilon_1)t/\hbar}e^{-i\omega t}\mathrm{d}t \tag{2.24}$$

$$e^{i\mathcal{H}t/\hbar}|n\rangle = e^{iEt/\hbar}|n\rangle \tag{2.25}$$

$$e^{i\mathbf{Q}\cdot\mathbf{r}_j(t)} = e^{i\mathcal{H}t/\hbar}e^{i\mathbf{Q}\cdot\mathbf{r}_j}e^{-i\mathcal{H}t/\hbar} \tag{2.26}$$

where $\mathcal{H}$ is the Hamiltonian of the system.

In a system formed by different isotopes, it is usual to assume that there is no correlation between the values of b for any two nuclei [46]. Consider a large number of scattering systems, all the same regarding the positions, but each having a different isotope distribution on the sites. Provided the system contains a large number of nuclei (a condition usually well satisfied) the cross-section measured is very close to the cross-section averaged over all the systems. Thus [149]

$$b_j b_{j'} \to \overline{b_j b_{j'}} \tag{2.27}$$

where the bar gives the average over the isotropic distribution [46]. On the assumption of no correlation between b values [149]

$$\overline{b_j b_{j'}} = \begin{cases} \left|\overline{b}\right|^2 & \text{if } j \neq j' \\ \overline{|b|^2} & \text{if } j = j' \end{cases} \tag{2.28}$$

where

$$\overline{b} = \sum_i p_i b_i \qquad \text{and} \qquad \overline{b^2} = \sum_i p_i b_i^2 \tag{2.29}$$

where p_i is the relative frequency. With this, two new cross-sections can be defined: the coherent cross-section $\sigma_{coh} = 4\pi\left|\overline{b}\right|^2$ and the incoherent cross-section $\sigma_{inc} = 4\pi\left(\overline{|b|^2} - \left|\overline{b}\right|^2\right)$. As such, the partial differential cross-section can be separated into two parts [149]

$$\frac{\mathrm{d}^2\sigma}{\mathrm{d}\Omega\mathrm{d}E_f} = \left(\frac{\mathrm{d}^2\sigma}{\mathrm{d}\Omega\mathrm{d}E_f}\right)_{\text{coh}} + \left(\frac{\mathrm{d}^2\sigma}{\mathrm{d}\Omega\mathrm{d}E_f}\right)_{\text{inc}} \tag{2.30}$$

where, the first term is the coherent scattering term and the second the incoherent scattering term. Physically, in the coherent scattering, there is interference between scattered neutron waves from different ions, which gives information on the relative positions of the ions [155]. In the incoherent scattering, on the other hand, there is no interference and it depends only on which atoms are present, irrespective of their arrangement [46, 155].

In a real system at a finite temperature, the ions will vibrate around a central equilibrium point. Because of this, the position of an ion is described by $\mathbf{r}_j(t) = \mathbf{r}_j + \mathbf{u}_j(t)$, where $\mathbf{r}_j$ is described by equation (2.11) and $\mathbf{u}_j(t)$ is the isotropic displacement parameter and represents the displacement from equilibrium. Inserting this into equation (2.23) and using $\langle e^A e^B\rangle = e^{\frac{1}{2}\left(\langle A^2\rangle + \langle B^2\rangle\right)}e^{\langle AB\rangle}$ [46] gives [149]

$$\frac{\mathrm{d}^2\sigma}{\mathrm{d}\Omega\mathrm{d}E_f}(\mathbf{Q},\hbar\omega) = \frac{k_f}{k_i}\left(\frac{1}{2\pi\hbar}\right)\sum_{j,j'}\overline{b_j b_{j'}}\int_{-\infty}^{\infty} e^{-i\mathbf{Q}\cdot\left(\mathbf{r}_{j'}-\mathbf{r}_j\right)}e^{-\left(W_{j'}(\mathbf{Q})+W_j(\mathbf{Q})\right)} e^{\left\langle\left(\mathbf{Q}\cdot\mathbf{u}_{j'}(0)\right)\left(\mathbf{Q}\cdot\mathbf{u}_j(t)\right)\right\rangle}e^{-i\omega t}\mathrm{d}t \tag{2.31}$$

where $W(\mathbf{Q}) = \frac{1}{2}\langle(\mathbf{Q}\cdot\mathbf{u})^2\rangle$ is the Debye-Waller factor. In general, $\mathbf{u}$ is a 3×3 matrix with each term of the matrix representing the strength of the vibration in a given direction. The last $\mathbf{Q}$ dependant exponential term in equation (2.31) can be expanded in a series of the form $e^{\langle AB\rangle} = 1 + \langle AB\rangle + \frac{1}{2!}\langle AB\rangle^2$. If only the first term of the expansion is retained, then we arrive at the form of equation (2.31) appropriate for elastic scattering [149]

$$\frac{\mathrm{d}\sigma}{\mathrm{d}\Omega}(\mathbf{Q}) = N\frac{(2\pi)^3}{v_0}\sum_{\tau}|\sum_{\upsilon}\overline{b_\upsilon}e^{i\mathbf{Q}\cdot\mathbf{r}_\upsilon}e^{-W_\upsilon(\mathbf{Q})}|^2\delta\left(\mathbf{Q}-\boldsymbol{\tau}\right) + N\sum_{\upsilon}\left(\overline{b_\upsilon^2} - \left(\overline{b_\upsilon}\right)^2\right)e^{-2W_\upsilon(\mathbf{Q})} \tag{2.32}$$

where N is the number of unit cells, v_0 is the volume of the unit cell, and the first term is equivalent to equation (2.19) but with the Debye-Waller factor included. Here, the first term is the coherent elastic scattering term and the second the incoherent elastic scattering term.

2.2.3.2 Magnetic interaction potential

Due to having a non-zero spin, neutrons, just like electrons, have magnetic dipole moment given by [149]

$$\boldsymbol{\mu}_\mathrm{n} = -\gamma\mu_\mathrm{N}\hat{\boldsymbol{\sigma}} \tag{2.33}$$

where $\gamma = 1.913$, μ_N is the nuclear magneton and $\hat{\boldsymbol{\sigma}}$ is the neutron Pauli spin operator. Since neutrons interact with unpaired electrons which generate a magnetic field $\mathbf{B}_e$, the magnetic interaction potential can be written as [154]

$$V_M = -\boldsymbol{\mu}_\mathrm{n}\cdot\mathbf{B}_e \tag{2.34}$$

The magnetic field of the electron can be further separated into a term arising from the spin and a term arising from the orbital motion.

An important effect to consider is that neutrons are sensitive only to the part of the electron magnetism which is perpendicular to $\mathbf{Q}$. This is because of the divergence free rule of Maxwells equations $\nabla\cdot\mathbf{B}_e(\mathbf{r}) = 0$ which Fourier transforms to $\mathbf{Q}\cdot\mathbf{B}_e(\mathbf{Q}) = 0$. Consider first the case of a single electron. Using the relation between the magnetic field and vector potential $\mathbf{B}_e = \nabla\times\mathbf{A}$, the definition $\mathbf{A} = \nabla\times\frac{\mu_\mathrm{e}}{r}$ [154], and the Fourier transform $\mathcal{F}(\nabla\times) = -i\mathbf{Q}\times$ [154]

$$\begin{aligned}
\langle\boldsymbol{k}_f s_f\rho_f|V_m|\boldsymbol{i}_f s_i\rho_i\rangle &= \langle\mathbf{k}_f\sigma_f n_1|-\boldsymbol{\mu}_\mathrm{n}\cdot\nabla\times\left(\nabla\times\frac{\boldsymbol{\mu}_\mathrm{e}}{r}\right)|\mathbf{k}_i\sigma_i n_0\rangle \\
&= \langle\sigma_f n_1|\boldsymbol{\mu}_\mathrm{n}\cdot\left(\hat{\mathbf{Q}}\times\left(\hat{\mathbf{Q}}\times\boldsymbol{\mu}_\mathrm{e}(\mathbf{Q})\right)\right)|\sigma_i n_0\rangle \\
&= \langle\sigma_f n_1|-\boldsymbol{\mu}_\mathrm{n}\cdot\left(\hat{\mathbf{Q}}\times\left(\boldsymbol{\mu}_\mathrm{e}(\mathbf{Q})\times\hat{\mathbf{Q}}\right)\right)|\sigma_i n_0\rangle \\
&\propto \langle\sigma_f n_1|-\hat{\boldsymbol{\sigma}}\cdot\boldsymbol{\mu}_{\mathrm{e}\perp}(\mathbf{Q})|\sigma_i n_0\rangle
\end{aligned} \tag{2.35}$$

Generalizing to the entire scattering system with $\sum\boldsymbol{\mu}_{\mathrm{e}\perp}(\mathbf{Q}) = \mathbf{M}_\perp(\boldsymbol{Q})$ and using $\mu_\mathrm{N} = \frac{e\hbar}{2m_p}$, equation (2.20) for a purely magnetic system becomes [154]

$$\frac{\mathrm{d}^2\sigma}{\mathrm{d}\Omega \mathrm{d}E_f}(\mathbf{Q},\hbar\omega) = \frac{k_f}{k_i}\left(\gamma r_0\right)^2 \sum_{\sigma_i,\sigma_f}\sum_{n_0,n_1} p\left(\sigma_i\right) p\left(n_0\right) \left|\left\langle \sigma_f n_1 | \hat{\boldsymbol{\sigma}}\cdot\mathbf{M}_\perp\left(\mathbf{Q}\right)|\sigma_i n_0\right\rangle\right|^2 \delta\left(\epsilon_1-\epsilon_0+\hbar\omega\right) \tag{2.36}$$

where r_0 is the classical radius of the electron [149]. Since $\hat{\boldsymbol{\sigma}}$ only depends on the spin coordinate of the neutron and $\mathbf{M}_\perp$ only depends on the electron coordinate,

$$\left\langle \sigma_f n_1 | \hat{\boldsymbol{\sigma}}\cdot\mathbf{M}_\perp\left(\mathbf{Q}\right)|\sigma_i n_0\right\rangle = \left\langle \sigma_f|\hat{\boldsymbol{\sigma}}|\sigma_i\right\rangle \left\langle n_1|\mathbf{M}_\perp\left(\mathbf{Q}\right)|n_0\right\rangle \tag{2.37}$$

Thus, for an incident beam of unpolarised neutrons, equation (2.36) becomes [149]

$$\begin{aligned}\frac{\mathrm{d}^2\sigma}{\mathrm{d}\Omega \mathrm{d}E_f}(\mathbf{Q},\hbar\omega) = \frac{k_f}{k_i}\left(\gamma r_0\right)^2 &\sum_{\alpha\beta}\left(\delta_{\alpha\beta}-\hat{\mathrm{Q}}_\alpha\hat{\mathrm{Q}}_\beta\right) \\ &\times \sum_{n_0,n_1} p\left(n_0\right)\left\langle n_0|\mathrm{M}^*_\alpha\left(\mathbf{Q}\right)|n_1\right\rangle \left\langle n_1|\mathrm{M}_\beta\left(\mathbf{Q}\right)|n_0\right\rangle \delta\left(\epsilon_1-\epsilon_0+\hbar\omega\right)\end{aligned} \tag{2.38}$$

where the equality

$$\mathbf{M}_\perp\left(\mathbf{Q}\right)^*\mathbf{M}_\perp\left(\mathbf{Q}\right) = \sum_{\alpha\beta}\left(\delta_{\alpha\beta}-\hat{\mathrm{Q}}_\alpha\hat{\mathrm{Q}}_\beta\right)\mathrm{M}^*_\alpha\left(\mathbf{Q}\right)\mathrm{M}_\beta\left(\mathbf{Q}\right) \tag{2.39}$$

was used with $\alpha,\beta = x$, y and z. Equation (2.38) relates to a general system. It is useful to consider the case of neutron scattering due to spin only, i.e. ignoring the orbital angular moment of the electron. In this case, and just as with the purely nuclear case, the position of the j^{th} unpaired electron can be written as $\mathbf{r}_j\left(t\right) = \mathbf{r}_j + \mathbf{r}_\zeta\left(t\right)$, where $\mathbf{r}_j$ is described by equation (2.11) and $\mathbf{r}_\zeta\left(t\right)$ is the distance from the nucleus to the ζ^{th} unpaired electron. Then [149]

$$\mathbf{M}\left(\mathbf{Q}\right) = \sum_j e^{i\mathbf{Q}\cdot\mathbf{r}_j}\sum_\zeta e^{i\mathbf{Q}\cdot\mathbf{r}_\zeta(t)}\mathbf{s}_\zeta \tag{2.40}$$

where $\mathbf{s}_\upsilon$ is the spin angular momentum operator. With this, equation (2.38) can be written as [149]

$$\begin{aligned}\frac{\mathrm{d}^2\sigma}{\mathrm{d}\Omega \mathrm{d}E_f}(\mathbf{Q},\hbar\omega) = \frac{k_f}{k_i}\left(\gamma r_0\right)^2 &\sum_{\alpha\beta}\left(\delta_{\alpha\beta}-\hat{\mathrm{Q}}_\alpha\hat{\mathrm{Q}}_\beta\right)\sum_{j,j'} f^*_{j'}\left(\mathbf{Q}\right) f_j\left(\mathbf{Q}\right)\sum_{n_0,n_1} p\left(n_0\right) \\ &\times \left\langle n_0|e^{-i\mathbf{Q}\cdot\mathbf{r}_{j'}}S^\alpha_{j'}\left(\mathbf{Q}\right)|n_1\right\rangle \left\langle n_1|e^{i\mathbf{Q}\cdot\mathbf{r}_j}S^\beta_j\left(\mathbf{Q}\right)|n_0\right\rangle \delta\left(\epsilon_1-\epsilon_0+\hbar\omega\right)\end{aligned} \tag{2.41}$$

where $\alpha,\beta = x$, y and z, S^β_j is the β component of the spin angular momentum of atom j, and $f_j\left(\mathbf{Q}\right)$ is the magnetic form factor, the equivalent to the scattering length b for the nuclear interaction. Unlike b, $f\left(\mathbf{Q}\right)$ has a $\mathbf{Q}$ dependence. This is because the magnetic interaction takes place within the electron cloud surrounding the nucleus and as such, we can no longer treat the interacting atom as a point like object. In addition, not only $f\left(\mathbf{Q}\right)$ changes from species to species, but it also changes depending on the charge of the

ion. This is because the unpaired electron can be in an s, p, d or f orbital, which will have an effect on the shape of $f(\mathbf{Q})$ [46].

An example of the magnetic form factor for Mn^{2+} in MnO is shown in figure 2.6. In a system where both, nuclear and magnetic interactions exist, the measured scattering will contain a combination of nuclear effects and magnetic effects. However, the magnetic effects will be mainly visible at low $\mathbf{Q}$ values. This is because of the decay of $f(\mathbf{Q})$ with $\mathbf{Q}$. This is specially useful in inelastic scattering processes, which will be discussed later, where magnetic excitations are more visible at low $\mathbf{Q}$ due to the magnetic form factor, but hidden at high $\mathbf{Q}$ by the phononic contribution that increases with $|\mathbf{Q}|^2$.

Just as with the nuclear interaction case, elastic magnetic scattering is possible, and the differential cross-section has the form (following steps similar as with the nuclear scattering) [46]

$$\frac{\mathrm{d}\sigma}{\mathrm{d}\Omega}(\mathbf{Q}) = N\frac{(2\pi)^3}{v_\mathrm{m}}\sum_\tau \left|\left(\hat{\mathbf{Q}}\times\left(\mathbf{F}_\mathrm{M}(\mathbf{Q})\times\hat{\mathbf{Q}}\right)\right)\right|^2 \delta(\mathbf{Q}-\boldsymbol{\tau}_\mathrm{m}) \tag{2.42}$$

where N_m is the number of magnetic unit cells, v_m is the volume of the magnetic unit cell, $\boldsymbol{\tau}_\mathrm{m}$ are reciprocal lattice vectors for the magnetic lattice, and

$$\mathbf{F}_\mathrm{M}(\mathbf{Q}) = \frac{\gamma r_0}{2\mu_\mathrm{B}}\sum_j \boldsymbol{\mu}_j f_j(\mathbf{Q})\, e^{i\mathbf{Q}\cdot\mathbf{r}_j} e^{-W_j(\mathbf{Q})} \tag{2.43}$$

is the magnetic structure factor, which has a very similar form to the coherent term in equation (2.32). Here, $\boldsymbol{\mu}_j$ is the magnetic moment of the j^{th} magnetic ion. In the same way that different crystals will produce different nuclear Bragg peak patterns depending on the nuclear structure, a system that exhibits long range magnetic order will produce magnetic Bragg peaks. Furthermore, the location of the magnetic Bragg peaks gives information on the magnetic lattice of the crystal and the intensities give information on the location of the magnetic ions within the unit cell and the magnetic moments on each

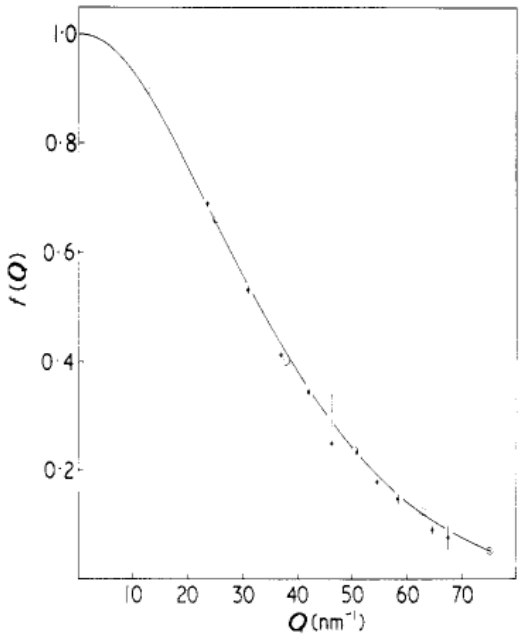

Figure 2.6: Magnetic form factor for Mn^{2+} in MnO. Figure acquired from [156].

ion. It is worth pointing out that the magnetic Bragg peaks do not necessarily need to appear at the same locations as the nuclear Bragg peaks.

2.3 Inelastic scattering

Most of the discussion so far has been assuming elastic scattering, where $k_i = k_f$ and there is no energy exchange between the scattering system and the incoming neutron. However, in neutron scattering, time-dependent effects, i.e. the dynamics of the system, are also of interest. To study these effects, inelastic scattering is needed.

In inelastic neutron scattering, there is an exchange of both energy ($E_i \neq E_f$) and momentum ($k_i \neq k_f$) [157]. To visualise the change of momentum, it is useful to represent the wavevectors with a scattering triangle, as shown in figure 2.7, where $\mathbf{Q} = \mathbf{k}_i - \mathbf{k}_f$. As figure 2.7b shows, two forms of inelastic scattering exist, depending on whether the energy is transferred to (energy loss) or from (energy gain) the scattering system. The energy transfer is computed using [158]

$$\Delta E = \frac{\hbar^2 \left|\boldsymbol{k}_i\right|^2}{2m} - \frac{\hbar^2 \left|\boldsymbol{k}_f\right|^2}{2m} \tag{2.44}$$

For positive ΔE (energy transfer from the neutron to the system), the limit is given by the incident energy of the neutron E_i, since the neutron cannot transfer more energy to the system than "what it has". Depending on the amount of energy transfer, different dynamic effects can be measured, as figure 2.8 shows, where in general the larger the energy transfer the faster the dynamic effect [159]. A limiting case of inelastic scattering

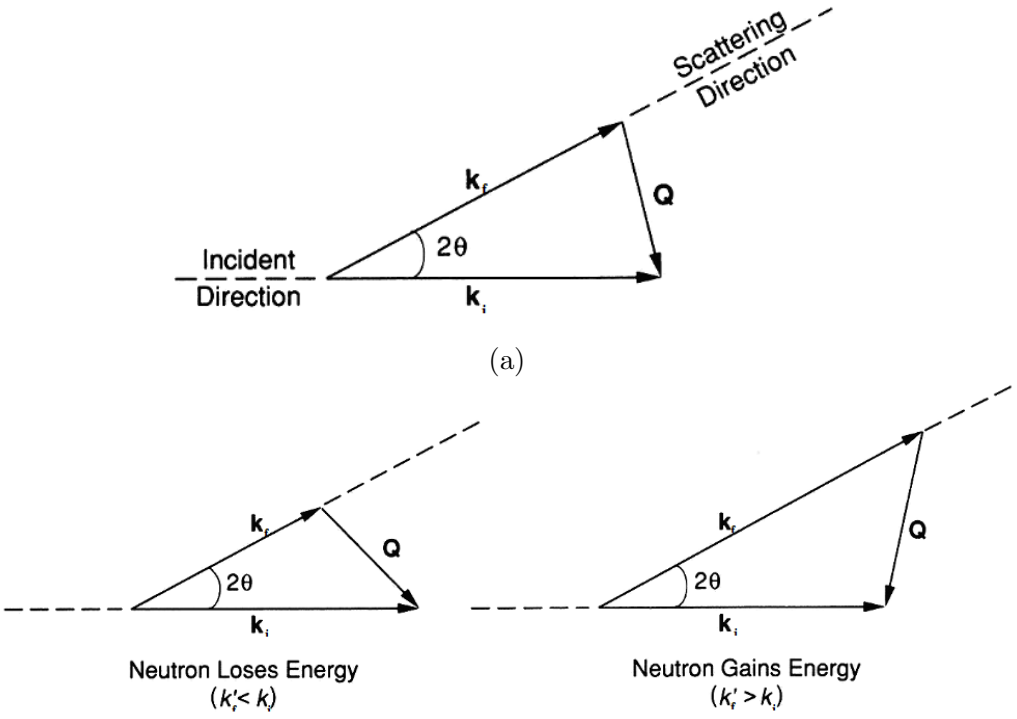

Figure 2.7: Scattering triangles for (a) an elastic scattering event in which the neutron is deflected but does not gain or lose energy (so that $k_i = k_f$) and (b) inelastic scattering in which the neutron either loses energy ($k_i > k_f$) or gains energy ($k_i < k_f$) during the interaction with the sample. Figures acquired from [157].

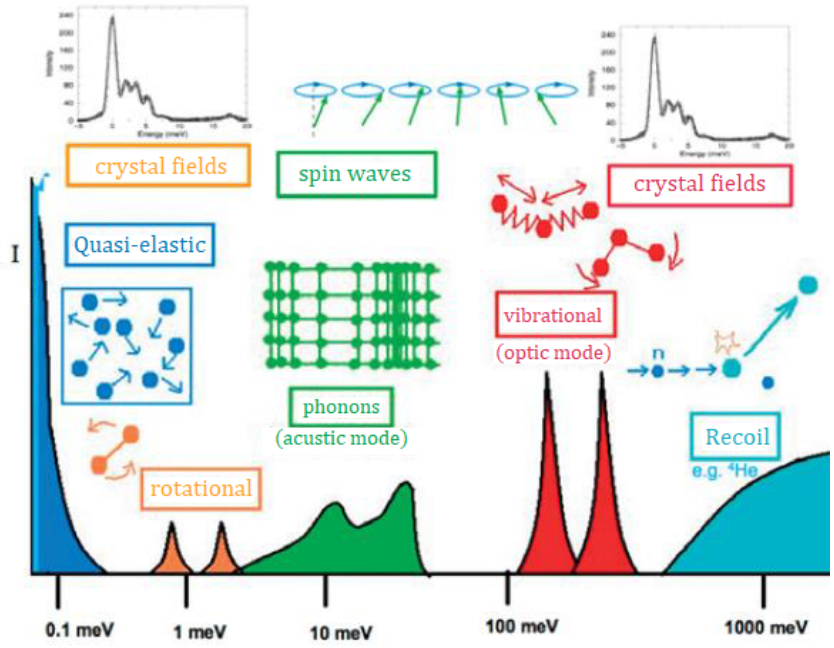

Figure 2.8: Energy ranges spanned by inelastic neutron scattering. Figure acquired from [159].

exist called quasi-elastic scattering, in which the energy transferred is much smaller than the incident energy.

The intensity measured by an energy loss (neutron loses energy) interaction and an energy gain (neutron gains energy) interaction will not have the same strength, represented as I in figure 2.8. This is because of the detailed balance condition [158]

$$\frac{\mathrm{d}^2\sigma}{\mathrm{d}\Omega \mathrm{d}E_f}(-\mathbf{Q}, -\hbar\omega) = e^{-\frac{\hbar\omega}{\mathrm{k_B}T}} \frac{\mathrm{d}^2\sigma}{\mathrm{d}\Omega \mathrm{d}E_f}(\mathbf{Q}, \hbar\omega) \tag{2.45}$$

for systems in thermal equilibrium. Physically, this condition states that the population of energy levels with energy $\hbar\omega$ is proportional to $e^{-\frac{\hbar\omega}{\mathrm{k_B}T}}$ [46]. To view this effect, consider the transition between energy levels. At $T = 0$ K no energy levels above the ground state are populated, energy gain interactions are not possible, and hence there is no intensity for neutron energy gain. At high temperatures, an almost equal population would be expected in both levels, and thus one would expect similar scattering intensity for energy gain and loss. However, due to the exponential factor, the intensity from energy gain events will be smaller [158].

In general, inelastic scattering can arise from either magnetic or nuclear interactions. Furthermore, the information acquired can be due to localised events, occurring at a single site in the crystal, or collective events, such as phonons or spin waves which involve multiple ions. In this thesis, only localised magnetic excitations called crystal electric field excitations will be considered.

2.3.1 Crystal electric field excitations

The energy levels of a free ion are different from the energy levels of that same ion inside a crystal. The electrons of a magnetic ion inside a crystal experience an extra electrostatic field from the electrons of the surrounding ions and, to a lesser extent, the field from covalent bonding [46]. All fields from all the ions and bonds combine to form a

crystal electric field (CEF) or ligand field. The CEF interacts with the orbital part of the electronic wave function, producing a splitting of the energy levels. An example of this is shown in figure 2.9 for Pr^{4+} in PrO_2 for a CEF of cubic symmetry. The form of the CEF will depend on the surrounding ions, and as such the splitting of the energy levels will change between ions depending on the symmetry of the system [160]. The new energy levels produced after splitting are commonly known as CEF levels.

The strength of the CEF will depend on the type of ion and the location of the unpaired electron. In most rare-earth ions with 4f orbitals, the CEF levels are weak and more sensitive to the presence of disorder [46]. It is for this reason that the effect on the CEF levels is very important to determine the single ion properties of rare earths, especially in crystals with some kind of disorder that can affect the surroundings of the magnetic ion. Furthermore, because the spin-orbit coupling is not affected, the total angular momentum quantum number J can still be used [46].

CEFs play an important role on the single ion properties of magnetic ions for multiple reasons [96]. CEFs affect the magnetic ground state of the ion, that is, it can make the ion magnetic (doublet ground state) or non-magnetic (singlet ground state). If the ion is magnetic, the CEF will affect the preferred direction of the spin, what is commonly known as easy plane (XY behaviour) or easy axis (Ising behaviour). This is important in pyrochlores, as CEFs determine if the spin is Ising (pointing along the line connecting the O(1) ions), XY (in the plane perpendicular to the line connecting the O(1) ions) or Heisenberg (isotropic) [96]. Finally, in most rare-earth ions, when k_BT is smaller than the CEF splitting the magnetic moment is partially quenched relative to the free ion moment [46].

The transitions of electrons between CEF levels, are known as CEF excitations. Non-localised excitations such as phonons and spin waves are expressed as waves of ions or spins, and as such they have a dispersion relation relating the wave vector $\mathbf{Q}$ with the energy of the excitation E [162]. However, CEF excitations are localised (cannot be

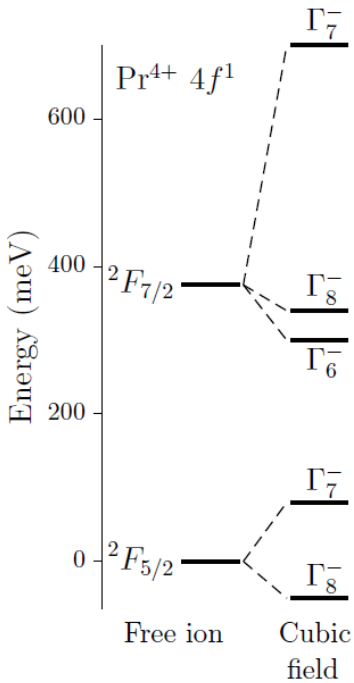

Figure 2.9: Single-ion energy level scheme for Pr^{4+} in PrO_2. Figure acquired from [161].

defined as a wave of particles or spins), since only one ion is involved, and as such no $\mathbf{Q} - E$ relation exists (dispersionless). Experimentally, only lines at a constant energy can be observed, with the intensity of the line decreasing with increasing $\mathbf{Q}$ due to the $\mathbf{Q}$ dependence of the magnetic form factor. Rosenkranz *et al.* [91] studied the CEF levels of Ho^{3+} in $Ho_2Ti_2O_7$ shown in figure 2.10a. Figure 2.10b shows the energy spectrum at 10 K and 150 K with multiple neutron incident energies. The $E_i = 6$ meV data at 150 K shows the effect of the detailed balance condition, with the intensity of the energy gain data lower than the intensity of the energy loss data. Furthermore, at higher temperatures, transitions between different CEF levels are observed, due to them being thermally populated.

2.4 Diffuse scattering

So far, the focus on elastic scattering has been on Bragg scattering, this is, scattering at integer values of the Miller indices. However, Bragg scattering only gives information on the average crystal structure. This is useful to determine general information such as the space group. In addition, so far the assumption has been that the target system had a near-infinite perfect periodicity, with all unit cells being exactly the same. However, materials with deviations from ideal crystallinity are also of interest, since the deviations from long-range order may help explain physical phenomena such as colossal magnetoresistance [163], relaxor ferroelectricity [164], fast ion conduction [165], and geometric frustration [145, 166]. In this thesis, the discussion will be focus on systems that do not completely deviate from order and that still exhibit a distinguishable average structure, i.e. system with partial disorder.

While deviation from ideal crystallinity can be found in many forms, in this thesis the focus will be on deviations due to substitution of an ion by another and deviation due to missing ions (vacancies). These changes to the ideal lattice will produce a distortion field that will affect all the surrounding ions, not only displacing them from the "ideal" lattice position but in some cases changing their magnetic properties.

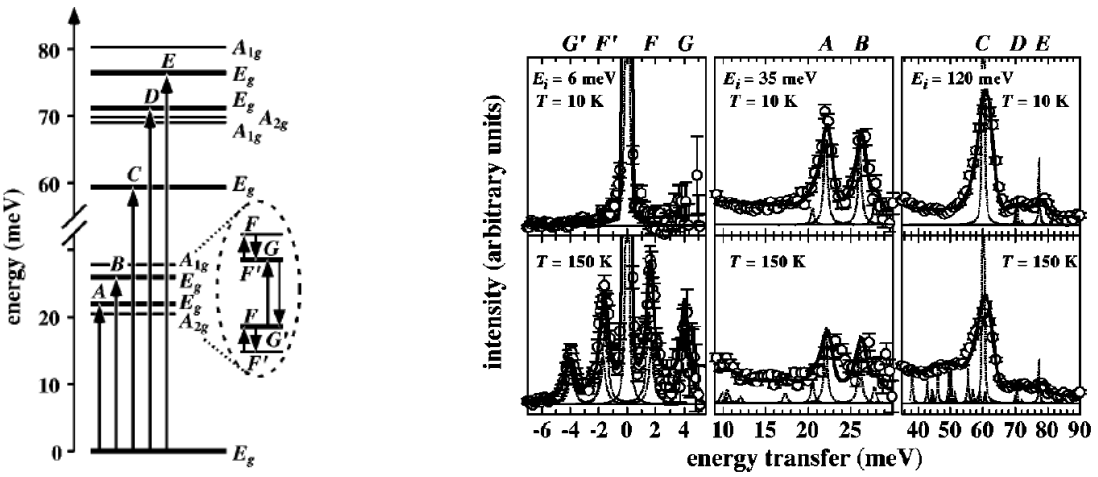

(a) (b)

Figure 2.10: (a) CEF energy level scheme for the Ho^{3+} ion in $Ho_2Ti_2O_7$. The arrows denote observed transitions. (b) Comparison between the CEF spectra measured at 10 K and 150 K at 3 different neutron incident energies and the calculated spectrum, including instrumental resolution and intrinsic broadening of the transitions. Figures acquired from [91].

In the presence of disorder, scattering can still arise even when the Laue condition is not satisfied (at a considerably reduced intensity) and as such it is important to not restrict studies to integer values of h, k and l and allow the indices to vary continuously. This scattering, termed diffuse scattering, can appear anywhere in reciprocal space and provides information on the local structure. Diffuse scattering is broad in reciprocal space because it is a short range effect, while repeating structures (unit cells) produce Bragg peaks, which are very intense and sharp in reciprocal space, due to them being of long range order. Furthermore, the diffuse scattering is generally much weaker than Bragg scattering, usually by several orders of magnitude [167].

Experimentally, there are several things to consider when studying diffuse scattering:

1. Since diffuse scattering is broad in reciprocal space, it is important to measure a wide range of angles [167]. Because of this, multi-detector instruments such as D7 from the Institut Laue-Langevin (ILL) and SXD from ISIS, which will be discussed in the following chapter, are ideal for acquired maps such as those from figure 1.12.

2. Because diffuse scattering is much weaker than Bragg scattering, it is preferable to use large crystals or large amounts of powders to increase the amount of scattered neutrons and maximise signal-to-background ratio. In addition, measuring the background and subtracting it from the data is ideal to minimise the contribution of the background in the analysis.

   Some systems might contain both nuclear and magnetic disorder. If unpolarised neutrons are used to study these systems, the measured scattering data will contain a mixture of the nuclear and magnet scattering. However, if polarised neutrons are used then polarisation analysis, which will be discussed further on in the thesis, can be used to properly isolate each contribution.

   Finally, measurements are usually performed at low temperatures, to avoid any thermal contribution such as phonons.

3. Diffuse scattering is usually defined as a quasi-static scattering process in which no energy analysis of the scattered neutron beam is performed. In other words, it is equivalent to taking a "snapshot" of the system [168]. Because of this, it is important to satisfy the quasi-static approximation, i.e. the energy of the incident neutron must be larger than some characteristic energy of the system being studied [169]. When the diffuse scattering is studied, the intensity measured requires a correct integration over all the energy states in the sample for a given $\mathbf{Q}$. The rigorous way to do this would be to perform a careful inelastic scattering experiment over an infinitely large range of neutron energy transfers, express the data as a function of $\boldsymbol{Q}$ and E and then sum the data over E for a given $\mathbf{Q}$. In other words

   $$I(\boldsymbol{Q}) = \int_{-\infty}^{\infty} I(\boldsymbol{Q}, E) dE \tag{2.46}$$

   This is not possible due to time constraints, the ability to produce neutrons in all energy ranges, and so on. As such, in most experiments where a monochromatic beam of neutrons with energy E_i is used, the quasi-static approximation applies

   $$I(\boldsymbol{Q}) = \int_{-\infty}^{E_i} I(\boldsymbol{Q}, E) dE \tag{2.47}$$

However, this approximation is valid if the energy scales in the sample are much smaller than E_i. In other words, in order for the diffuse scattering to contain all the information of an inelastic event with a characteristic energy, the incident energy of the neutron must be larger than that characteristic energy. In magnetism, the limiting value for E_i is usually given by Θ_{CW}, since Θ_{CW} is a measure of the net magnetic interactions. The effects of not satisfying the quasi-static approximation are shown in figure 2.11.

Extracting information from diffuse scattering is essential to understand the local distortions of a system. However, unlike other scattering data, there is no general rule to analyse the diffuse scattering and the interpretation has typically been carried out on a case by case basis [171]. Nevertheless, many methods of modelling diffuse scattering data (which will be described later on in the thesis) usually emerge from variations of Monte-Carlo (MC) and Reverse MC (RMC) approaches, density functional theory (DFT) calculations and Rietveld refinement, with the last one almost exclusively used in powder data. In the following section, the difference method, extensively used in this thesis, is described.

2.4.1 Diffuse scattering difference method

The formalism developed in this section is from [172]. This method is used to model the diffuse scattering of disorder systems using individual defects, such as vacancies, and a small surrounding region of relaxed ions. This allows the modelling of large systems with a small number of parameters. The main idea of the difference method is that the summation over ions may be converted to one over sites by defining the probability of occupation of each site in the crystal. For diffuse scattering, this means that the coherent scattering may be calculated from the occupation of sites relative to the ideal lattice. The most general expression for the neutrons scattering from a crystal is

$$S(\mathbf{Q}) = \frac{1}{N}\left|\sum_j b_j e^{i\mathbf{Q}\cdot\mathbf{r}_j}\right|^2 \tag{2.48}$$

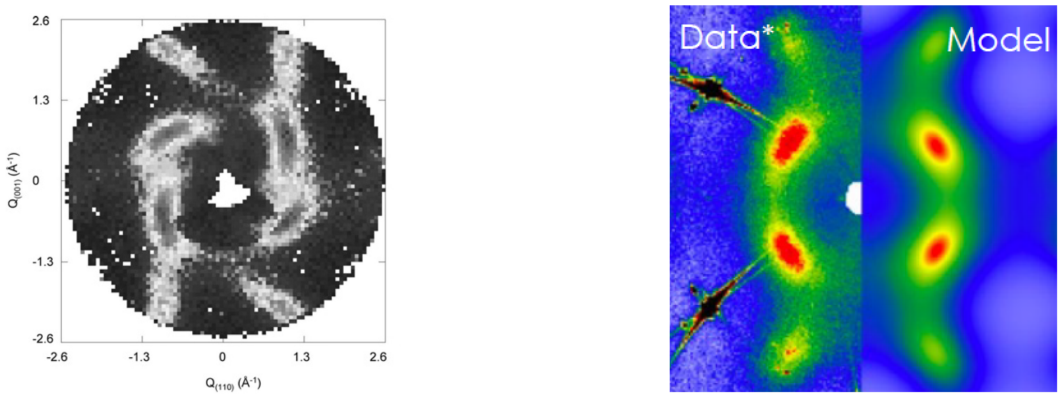

(a) (b)

Figure 2.11: MnO has a $\Theta_{\mathrm{CW}} \approx 500$ K. (a) Data collected using $E_i = 3.6$ meV ≈ 40 K, much lower than Θ_{CW}, resulting in the data having swirly features which are artefacts coming from not satisfying the quasi-static approximation. (b) Data collected using $E_i = 56$ meV ≈ 650 K, above Θ_{CW} and resulting in the spiral features disappearing. Figures acquired from [169] and [170] respectively.

where the summation runs over all N ions in the crystal, b_j is the scattering length of the j^{th} ion and $\mathbf{r}_j$ is the position vector. This can be expressed as a summation over all sites (ideal lattice sites, displaced sites, etc), such that

$$S(\mathbf{Q}) = \frac{1}{N}\left|\sum_j p_j b_j e^{i\mathbf{Q}\cdot\mathbf{r}_j}\right|^2 \tag{2.49}$$

where p_j is the probability of occupation of the j^{th} site. Since in the ideal lattice the probability of occupation is $c_j = 0$ or 1, it is possible to write the expression for the scattering intensity relative to the ideal lattice as

$$S(\mathbf{Q}) = \frac{1}{N}\left|\sum_j c_j b_j e^{i\mathbf{Q}\cdot\mathbf{r}_j} + \sum_j (p_j - c_j) b_j e^{i\mathbf{Q}\cdot\mathbf{r}_j}\right|^2 \tag{2.50}$$

which, defining the first and second term as A and B respectively

$$S_{A+B} = \frac{1}{N}\left|A + B\right|^2 = \frac{1}{N}\left(AA^* + AB^* + BA^* + BB^*\right) \tag{2.51}$$

where the first term gives the scattering from the ideal lattice (Bragg peaks), and the last term gives the diffuse scattering. While diffuse scattering may rise anywhere in reciprocal space, the diffuse scattering near Bragg peaks is usually obscured by the much larger Bragg intensity. However, we are only really interested in the diffuse scattering away from Bragg peaks. Away from Bragg peaks, $A = 0$, so that the cross terms are zero, and just the diffuse scattering term BB^* remains. With this, a diffuse form factor $F_k^D(\mathbf{Q})$ can be defined as

$$F_k^D(\mathbf{Q}) = \sum_j (p_j - c_j) b_j e^{i\mathbf{Q}\cdot\mathbf{r}_j} \tag{2.52}$$

where $(p_j - c_j)$ represents the difference between the real and the ideal lattice. For an interstitial site, or an ion relaxed from its regular site, $p_j - c_j = 1$. For a vacancy, or the site from which an ion is relaxed, $p_j - c_j = -1$. When an ion remains on its regular site $p_j - c_j = 0$. This means that the summation only needs to be performed over a few sites. A Debye-Waller factor $\mathrm{e}^{W_j(\mathbf{Q})}$ for the j^{th} ion can be included in equation 2.52 to take into account the attenuation of the neutron scattering due to temperature and vibration effects. For a system with doping or vacancies, the summation above does not have to be over all the ions in the system, and just over all the ions near the "defect cluster". To see this, consider first a system with a single vacancy. This vacancy will produce a distortion field that will result in a displacement of the surrounding ions. However, to a first approximation, only the closest ions will feel a strong distortion field and thus their displacement will be the largest. For the rest of the ions, the displacement will be minimal and the $F_k^D(\mathbf{Q})$ will be negligible. Thus, the summation only needs to be over the ions surrounding the vacancy, simplifying significantly the calculations.

However, this summation is over a cluster in a single orientation and configuration. If there is no correlation between the positions and orientations of the defect clusters, an incoherent summation needs to be performed over all possible orientations allowed by the crystal symmetry to obtain the coherent scattering per defective ion

$$S^D(\mathbf{Q}) = \frac{1}{N_i N_\mathrm{o}} \left| \sum_k F_k^D(\mathbf{Q}) \right|^2 \tag{2.53}$$

where N_i is the number of defective ions in the cluster and N_o is the number of orientations of the cluster. Pyrochlores belong to the $m\bar{3}m$ point group, where a total of 48 symmetry operations can be performed. These symmetry operations are of the form $(x\ y\ z)$, $(y\ -x\ -z)$ and so on, where x, y and z are the axis of the system. Thus, 48 different $F_k^D(\mathbf{Q})$ need to be calculated.

2.4.2 Pair Distribution Function

Depending on the state of the crystal, the measured diffuse scattering will have different forms. When a single crystal is studied, the mapping of reciprocal space intensities in an area or, with some instruments, volume of interest can be measured. This results in maps like the one shown in figure 2.11. However, when a powdered crystalline material is measured such maps are no longer possible and instead the measurement averages the scattering into a 1D diffraction pattern commonly called total scattering measurements. These 1D diffraction patterns contain all the Bragg and diffuse scattering information which, when Fourier transformed, produce the pair distribution function (PDF) [171].

A PDF is a weighted histogram showing the distribution of all inter-atomic distances in a material, describing the structure of a disordered material [46]. In other words, it is a radial probability density function describing the probability of finding an atom of one type between distance r and $r + \mathrm{d}r$ away from an atom of another type [173].

To find a relation between the PDF and what is measured in an experiment, consider first a monatomic system, this is a system where all the atoms are the same. For such a system, the differential cross-section may be written as [174]

$$\begin{aligned} \frac{1}{N}\frac{\mathrm{d}\sigma}{\mathrm{d}\Omega}(\mathbf{Q}) &= \frac{1}{N}\left[\frac{\mathrm{d}\sigma}{\mathrm{d}\Omega}(\mathbf{Q})\right]^{\mathrm{coh}} + \frac{1}{N}\left[\frac{\mathrm{d}\sigma}{\mathrm{d}\Omega}(\mathbf{Q})\right]^{\mathrm{inc}} \\ &= |\bar{b}|^2 S(\mathbf{Q}) + \left(\overline{|b|^2} - |\bar{b}|^2\right) \\ &= |\bar{b}|^2 \left(S(\mathbf{Q}) - 1\right) + \overline{|b|^2} \end{aligned} \tag{2.54}$$

where $S(\mathbf{Q})$ is the static structure factor (the Debye-Waller factor is ignored). In this equation, the first term is the "distinct" term (interference between different atoms), and the second term is the "self" term (self-interference from individual atoms). Fourier transforming the distinct term gives a definition for the PDF [174]

$$g(\mathbf{r}) - 1 = \frac{1}{\rho_0 \left(2\pi\right)^3} \int \left(S(\mathbf{Q}) - 1\right) e^{-i\mathbf{Q}\cdot\mathbf{r}} \mathrm{d}^3\mathbf{Q} \tag{2.55}$$

where ρ_0 is the total atomic number density, the "-1" on the left-hand side represents the subtraction from forward scattering ($\mathbf{Q} = 0$) and the "-1" on the right-hand side represents the subtraction of the self scattering, which is the self correlation of an atom with itself. In the case of diffraction from isotropic samples, such as powders, liquids or crystals, equation (2.55) can be integrated over angular coordinates to obtain the expression [174]

$$g(r) - 1 = \frac{1}{2\pi^2 r \rho_0} \int_0^\infty Q\,(S(Q) - 1) \sin(Qr) \mathrm{d}Q \tag{2.56}$$

In PDF analysis, alternative expressions are used to extract similar information, such as the reduced PDF [174]

$$D(r) = \frac{2}{\pi} \int_0^\infty Q\,(S(Q) - 1) \sin(Qr) \mathrm{d}Q \tag{2.57}$$

which allows the extraction of the total atomic number density from the initial slope. Furthermore, as figure 2.12 shows, with g(r) the amplitude is damped as the distance from the origin increases, while in D(r) the amplitude does not decrease with distance. Another common alternative is the radial distribution function [174]

$$RDF(r) = 4\pi r^2 \rho_0 g(r) \tag{2.58}$$

which is mainly used to extract the atomic coordination numbers. Examples of PDFs of a monatomic system in a liquid phase are shown in figure 2.12. The reason behind the ripples near the origin is due to the finite size of the data, since it is impossible to have an infinite reciprocal space range. The truncation at Q_{max} produces small features at r-values below inter-atomic distances [175].

Equation (2.56) can be generalised to a multicomponent system by writing the differential cross-section as [46]

$$\frac{1}{N}\frac{\mathrm{d}\sigma}{\mathrm{d}\Omega}(\mathbf{Q}) = \sum_{\alpha,\beta} c_\alpha c_\beta \overline{b_\alpha^* b_\beta}\,(S_{\alpha\beta}(\mathbf{Q}) - 1) + \sum_\alpha c_\alpha \overline{|b_\alpha|^2} \tag{2.59}$$

where $S_{\alpha\beta}(\mathbf{Q})$ are the partial structure factors and c the concentrations of the different species. With this, the partial PDF can be computed in a similar form as before [174]

$$g(r)_{\alpha\beta} - 1 = \frac{1}{2\pi^2 r \rho_0} \int_0^\infty Q\,(S_{\alpha\beta}(Q) - 1) \sin(Qr) \mathrm{d}Q \tag{2.60}$$

Thus, the total PDF $G(r)$ is defined [174]

$$G(r) = \sum_{\alpha,\beta} c_\alpha c_\beta \overline{b_\alpha^* b_\beta}\,[g(r)_{\alpha\beta} - 1] \tag{2.61}$$

(a) (b)

Figure 2.12: Example of the (a) PDF and (b) reduced PDF of a monatomic system in a liquid phase. Figures acquired from [174].

a weighted summation of partial pair distribution functions, each of which describes the probability of finding an atom of one type between distance r and $r + \mathrm{d}r$ away from an atom of another type [173]. There are several experimental considerations that need to be taken to get good PDF data [175]:

1. It is convenient to use high energy neutrons, since this will increase Q_{max}, which will increase the real space resolution. Similarly, good reciprocal space resolution is needed to reduce the broadening of the Bragg peaks and increase the intensity of high-r features [175].

2. Just as with diffuse scattering, background subtraction is essential. The data must be corrected for non-sample scattering, otherwise when it is Fourier transformed, false information can be translated to the PDF which will give us incorrect interpretation of the crystal structure.

Different features of a PDF curve will correspond to different kinds of information. Some examples are the position of a peak which indicates the distance of atomic pairs, the area of peaks which is related to the abundance of relevant pairs weighted by their scattering power (coordination number), and the width of peaks which is related to disorder inside the material, both structural or vibrational [176].

2.5 Polarisation analysis

So far, all of the discussion on neutron theory has been on the assumption that the incoming beam of neutrons is unpolarised, where the spins of all the incoming neutrons are pointing in all possible directions. However, the use of unpolarised neutrons means that the scattering measured is a combination of the nuclear and magnetic diffuse contribution, since the nuclear and magnetic potential appear as summation in equation (2.20). This can be an issue when the magnetic properties of a material are studied, since magnetic diffuse scattering in many systems is weak, and usually obscured by the nuclear diffuse scattering, as well as thermal diffuse scattering caused by phonons and incoherent scattering in the sample [167]. One way to overcome this issue is by modelling the different scattering cross-sections measured and subtracting them from the data to isolate the magnetic scattering. However, this can be tedious and difficult when studying complex materials.

In a neutron experiment, the best way to separate the magnetic and nuclear scattering cross-sections is by analysis of the spin state of the scattered neutrons. To do this, a beam of polarised neutrons is needed, this is a beam where all the neutrons have their spin state along the polarisation direction [167]. Since neutrons are spin-1/2 particles, two possible neutron spin states can be defined relative to the polarisation direction: u for a 'spin up" state and v for a "spin-down" state [149]. The polarisation of a neutron beam is the average over the individual polarisations of the neutrons [177]

$$\mathbf{P} = \frac{1}{N} \sum_j \mathbf{p}_j \tag{2.62}$$

where N is the number of neutrons in the beam, $\mathbf{p}_j$ is the polarisation state of the j^{th} neutron, usually +1 for spin-up state and -1 for spin-down state and $0 \leqslant |\mathbf{P}| \leqslant 1$. In an experiment with polarised neutrons, the spin state of the neutron after scattering is analysed, giving rise to four different cross-sections

$$u \to u \qquad v \to v \qquad v \to u \qquad u \to v \tag{2.63}$$

The first two processes, where the spin state does not change, are called the non-spin-flip (NSF) scattering, and the latter two are called the spin-flip (SF) scattering. Since the spin of the neutron interacts with the spin of the unpaired electrons and the spin of the nuclei, the presence of these four new forms of scattering need to be treated for each one of them.

For the purposes of this thesis, the focus will be on uniaxial polarisation analysis and XYZ polarisation analysis (XYZ–PA) on the D7 instrument at the ILL, a neutron spectrometer with a planar multi-detector in the xy plane and a weak applied field to guide the neutrons [167].

2.5.1 Uniaxial polarisation

When performing uniaxial polarisation measurements, the polarisation direction is usually fixed normal to the scattering plane, commonly defined as the z-axis of the scattering system. As such, the expression of the polarisation of the incoming beam can be described as [167]

$$|\mathbf{P}| = P = \frac{n_u - n_v}{n_u + n_v} \tag{2.64}$$

where n_u and n_v are the number of neutrons in the spin-up and spin-down state, respectively. This expression can alternatively be written as

$$P = \frac{F - 1}{F + 1} \tag{2.65}$$

where $F = n_u/n_v$ is the flipping ratio, which is a measurable quantity [178].

The scattering length b has a spin dependant component, due to the interaction through the strong nuclear force of the neutron spin with the nuclei spin. As such, b can have two possible values: b_+ when $I + 1/2$, i.e. the neutron is aligned parallel to the nuclear spin $\mathbf{I}$, and b_- when $I - 1/2$, i.e. the neutron is aligned antiparallel to the nuclear spin. With this, the scattering length can be expressed as [167]

$$\mathbf{b} = A + B\boldsymbol{\sigma} \cdot \mathbf{I} \tag{2.66}$$

where $\boldsymbol{\sigma}$ is the Pauli spin operator,

$$A = \frac{(I+1)b_+ + Ib_-}{2I+1} \qquad \text{and} \qquad B = \frac{b_+ - b_-}{2I+1} \tag{2.67}$$

Since the scattering length has a spin dependant component, the $\langle \sigma_f | V_N | \sigma_i \rangle$ term for the nuclear potential in equation (2.20) can no longer be ignored. It is worth pointing out that while the neutron and nucleus spin also interact via dipolar interactions, these interactions are much weaker than the electron-neutron dipolar interaction due to the small nuclear moment [179], and will thus be ignored in this discussion. As such, the neutron interacts with the nuclear spin mainly though the strong force and, unlike with electron magnetism, it is sensitive to the component of the nuclear moment parallel to the scattering vector.

From (2.63), four possible cross-sections exist which, combining the nuclear and magnetic potential, results in the Moon–Riste–Koehler (MRK) equations [180]

$$\begin{aligned}
\langle u|V_N + V_M|u\rangle \rightarrow & A - \frac{\gamma r_0}{2} M_{\perp z} + BI_z \\
\langle v|V_N + V_M|v\rangle \rightarrow & A + \frac{\gamma r_0}{2} M_{\perp z} - BI_z \\
\langle u|V_N + V_M|v\rangle \rightarrow & -\frac{\gamma r_0}{2} \left(M_{\perp x} + iM_{\perp y}\right) + B\left(I_x + iI_y\right) \\
\langle v|V_N + V_M|u\rangle \rightarrow & -\frac{\gamma r_0}{2} \left(M_{\perp x} - iM_{\perp y}\right) + B\left(I_x - iI_y\right)
\end{aligned} \tag{2.68}$$

where $M_\perp$ is magnetisation of the sample perpendicular to the scattering vector and I the nuclear spin [167]. The electronic magnetic terms in these equations illustrate one of the main rules of all magnetic uniaxial neutron polarisation analysis measurements: If the polarisation direction is along the z axis [167]

1. NSF scattering is sensitive only to the components of the magnetisation parallel to the z axis.

2. SF scattering is sensitive only to the components of the magnetisation perpendicular to the z axis.

Another general feature that these equations show is that the purely nuclear structural scattering terms are only found in NSF scattering. Finally, since neutrons are not sensitive to the component of the electron magnetism parallel to the scattering vector, a very useful experimental set up is one in which the polarisation direction is fixed to be along the scattering vector $\mathbf{Q}$. This will cause the NSF scattering to contain all the nuclear structural information, and the SF scattering all the electronic magnetic information [177].

2.5.2 XYZ polarisation

In XYZ–PA, NSF and SF scattering is studied with the longitudinal component of the polarisation of the scattered beam along an x, y and z direction, each direction being measured individually. It is common to define the x direction as parallel to Q, the y direction perpendicular to Q in the plane, and the z direction perpendicular to Q out of the plane [46].

Unlike uniaxial polarisation analysis, where complete separation of the nuclear structural, electron magnetic and nuclear magnetic is not possible, XYZ–PA allows for a full separation of all components. To do this, the RMK equations can be generalised to [181]

$$\begin{aligned}
\left(\frac{\mathrm{d}\sigma}{\mathrm{d}\Omega}\right)^{\beta}_{u\rightarrow u} &\propto \mathbf{N} + NM^*_{\perp\beta} + N^*M_{\perp\beta} + M^*_{\perp\beta}M_{\perp\beta} + I^*_\beta I_\beta \\
\left(\frac{\mathrm{d}\sigma}{\mathrm{d}\Omega}\right)^{\beta}_{v\rightarrow v} &\propto \mathbf{N} - NM^*_{\perp\beta} - N^*M_{\perp\beta} + M^*_{\perp\beta}M_{\perp\beta} + I^*_\beta I_\beta
\end{aligned} \tag{2.69}$$

for $u \rightarrow u$ and $v \rightarrow v$ NSF scattering and

$$\left(\frac{\mathrm{d}\sigma}{\mathrm{d}\Omega}\right)^{\beta}_{u\to v} \propto \mathbf{M}^{*}_{\perp}\mathbf{M}_{\perp} - M^{*}_{\perp\beta}M_{\perp\beta} + i\left(\mathbf{M}^{*}_{\perp}\times\mathbf{M}_{\perp}\right)_{\beta} + \mathbf{I}^{*}\mathbf{I} - I^{*}_{\beta}I_{\beta}$$
$$\left(\frac{\mathrm{d}\sigma}{\mathrm{d}\Omega}\right)^{\beta}_{v\to u} \propto \mathbf{M}^{*}_{\perp}\mathbf{M}_{\perp} - M^{*}_{\perp\beta}M_{\perp\beta} - i\left(\mathbf{M}^{*}_{\perp}\times\mathbf{M}_{\perp}\right)_{\beta} + \mathbf{I}^{*}\mathbf{I} - I^{*}_{\beta}I_{\beta} \tag{2.70}$$

for SF scattering, where $\beta = x$, y and z, $\mathbf{N} = N^{*}N$ is the purely nuclear structural scattering term, $\mathbf{M}^{*}_{\perp}\mathbf{M}_{\perp}$ is the dipolar electron magnetic scattering term, $NM_{\perp\beta}$ is the nuclear-magnetic interference (NMI) scattering term, $\mathbf{M}^{*}_{\perp}\times\mathbf{M}_{\perp}$ is the magnetic chiral scattering term and $\mathbf{I}^{*}\mathbf{I}$ is the purely nuclear magnetic scattering term.

In this thesis the instrument used to perform polarisation analysis measurements is D7, which has a planar multi-detector covering a large Q-range. Thus, the angle between the polarisation direction x' and the $\mathbf{Q}$ vectors, commonly known as the Schärpf angle α [182], will be different for all the detectors. This is equivalent to defining a Cartesian coordinate system (x', y', z) for the polarisation and a different coordinate system (x, y, z) for $\mathbf{Q}$, as figure 2.13 shows, which are related by a rotation of α degrees around the vertical z-axis. Since in this instrument all the detectors are on the same plane, the normalised $\mathbf{Q}$ vector can be written as [167]

$$\hat{\mathrm{Q}} = \begin{bmatrix}\cos(\alpha)\\ \sin(\alpha)\\ 0\end{bmatrix} \tag{2.71}$$

which constrains $\mathbf{k}_i$, $\mathbf{k}_f$ and $\mathbf{Q}$ to be on the scattering plane of the multi-detector. In the following sections, multiple ways of combining equations (2.69-2.70) will be shown to separate the nuclear structural, electron magnetic and nuclear spin scattering depending on the system being studied. In addition, it will be assumed that none of the systems exhibit ordering of the nuclear spins. The spin of the nuclei in most samples only order at temperatures in the μK or even nK regime, much lower than typical neutron experiments (at the ILL in France, experiments are performed at temperatures not lower than 40-50 mK). At higher temperatures, the nuclear spin behaves as a paramagnet and the cross-section studied is known as nuclear spin-incoherent (SI) scattering [167].

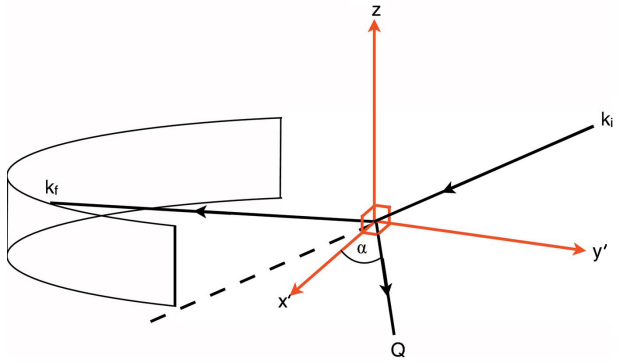

Figure 2.13: The geometry of an XYZ-polarisation analysis experiment. The incident polarisation is oriented alternately along the orthogonal x', y' and z, directions. The Schärpf angle α is the angle between $\mathbf{Q}$ and the arbitrarily positioned x' axis. Figure acquired from [167].

2.5.2.1 Powder samples

Since a powder sample has orientational averaging, it is not possible to distinguish the different components of $\mathbf{M}_\perp$. The information about the in-plane magnetic intensities is recovered from $M^2_{\perp x'} + M^2_{\perp y'} = \left(\sin^2(\alpha) + \cos^2(\alpha)\right) M^2_{\perp y}$. As such, in a powder sample with no nuclear spin ordering, the electron magnetic, nuclear spin-incoherent and structural nuclear can be separated using [181]

$$\begin{aligned}
\left(\frac{\mathrm{d}\sigma}{\mathrm{d}\Omega}\right)_{|\mathbf{M}_\perp|^2} &= 2\left(\left(\frac{\mathrm{d}\sigma}{\mathrm{d}\Omega}\right)^{x'}_{u\to v} + \left(\frac{\mathrm{d}\sigma}{\mathrm{d}\Omega}\right)^{y'}_{u\to v} - 2\left(\frac{\mathrm{d}\sigma}{\mathrm{d}\Omega}\right)^{z}_{u\to v}\right) \\
&= -2\left(\left(\frac{\mathrm{d}\sigma}{\mathrm{d}\Omega}\right)^{x'}_{u\to u} + \left(\frac{\mathrm{d}\sigma}{\mathrm{d}\Omega}\right)^{y'}_{u\to u} - 2\left(\frac{\mathrm{d}\sigma}{\mathrm{d}\Omega}\right)^{z}_{u\to u}\right) \\
\left(\frac{\mathrm{d}\sigma}{\mathrm{d}\Omega}\right)_{\mathrm{SI}} &= \frac{3}{2}\left(-\left(\frac{\mathrm{d}\sigma}{\mathrm{d}\Omega}\right)^{x'}_{u\to v} - \left(\frac{\mathrm{d}\sigma}{\mathrm{d}\Omega}\right)^{y'}_{u\to v} + 3\left(\frac{\mathrm{d}\sigma}{\mathrm{d}\Omega}\right)^{z}_{u\to v}\right) \\
\left(\frac{\mathrm{d}\sigma}{\mathrm{d}\Omega}\right)_{\mathrm{Nuc}} &= \left(\frac{\mathrm{d}\sigma}{\mathrm{d}\Omega}\right)^{z}_{u\to u} - \frac{1}{2}\left(\frac{\mathrm{d}\sigma}{\mathrm{d}\Omega}\right)_{|\mathbf{M}_\perp|^2} - \frac{1}{3}\left(\frac{\mathrm{d}\sigma}{\mathrm{d}\Omega}\right)_{\mathrm{SI}}
\end{aligned} \tag{2.72}$$

for a guide filed that is too weak to induce any significant sample magnetisation, resulting in the intensities not being affected by a polarisation reversal and thus $u \to u = v \to v$ and $u \to v = v \to u$. While strong fields invalidate this, their use allows for the study of correlation and interferences between the nuclear and magnetic scattering through the comparison of the intensities in polarisation reversal. Finally, since the equations above have no α dependence, this method applies for an arbitrarily rotated system in the scattering plane [181].

2.5.2.2 Single crystals

The intrinsic anisotropy and possible polarity of a single crystal may give rise to antisymmetric contributions even in a weak applied field. As such $u \to u \neq v \to v$ and $u \to v \neq v \to u$ for most samples (unless the crystal has no chirality or NMI). In such cases, the quantities [181]

$$\begin{aligned}
\Sigma^\beta_{NSF} &= \frac{1}{2}\left(\left(\frac{\mathrm{d}\sigma}{\mathrm{d}\Omega}\right)^{\beta}_{u\to u} + \left(\frac{\mathrm{d}\sigma}{\mathrm{d}\Omega}\right)^{\beta}_{v\to v}\right) \\
\Sigma^\beta_{SF} &= \frac{1}{2}\left(\left(\frac{\mathrm{d}\sigma}{\mathrm{d}\Omega}\right)^{\beta}_{u\to v} + \left(\frac{\mathrm{d}\sigma}{\mathrm{d}\Omega}\right)^{\beta}_{v\to u}\right)
\end{aligned} \tag{2.73}$$

where $\beta = x$, y and z, need to be used. For a Cartesian coordinate system (x', y', z) rotated by the Schärpf angle α around the vertical z-axis with respect to x parallel to $\mathbf{Q}$, all the scattering contributions can be separated using [181]

$$
\begin{aligned}
\left(\frac{\mathrm{d}\sigma}{\mathrm{d}\Omega}\right)_{\mathrm{Nuc}} &= \frac{1}{2}\left(\Sigma^{x'}_{NSF} + \Sigma^{y'}_{NSF} - \Sigma^{z}_{SF}\right) \\
\left(\frac{\mathrm{d}\sigma}{\mathrm{d}\Omega}\right)_{\mathrm{SI}} &= \frac{3}{2}\left(\frac{\Sigma^{x'}_{NSF} - \Sigma^{y'}_{NSF}}{\cos^2(\alpha) - \sin^2(\alpha)}\right) + \frac{3}{2}\Sigma^{z}_{SF} \\
\left(\frac{\mathrm{d}\sigma}{\mathrm{d}\Omega}\right)_{M_{\perp y}} &= \Sigma^{z}_{SF} - \frac{2}{3}\left(\frac{\mathrm{d}\sigma}{\mathrm{d}\Omega}\right)_{\mathrm{SI}} \\
\left(\frac{\mathrm{d}\sigma}{\mathrm{d}\Omega}\right)_{M_{\perp z}} &= \Sigma^{z}_{NSF} - \frac{1}{3}\left(\frac{\mathrm{d}\sigma}{\mathrm{d}\Omega}\right)_{\mathrm{SI}} - \left(\frac{\mathrm{d}\sigma}{\mathrm{d}\Omega}\right)_{\mathrm{Nuc}}
\end{aligned}
\tag{2.74}
$$

for a single crystal with no nuclear spin ordering, and where $M_{\perp x'} = \sin(\alpha)M_{\perp y}$ and $M_{\perp y'} = \cos(\alpha)M_{\perp y}$. If there are no magnetic-nuclear interference or chirality effects, which is the case for the systems discussed in this thesis, then $\Sigma^{\beta}_{NSF} = \left(\frac{\mathrm{d}\sigma}{\mathrm{d}\Omega}\right)^{\beta}_{u\to u} = \left(\frac{\mathrm{d}\sigma}{\mathrm{d}\Omega}\right)^{\beta}_{v\to v}$ and $\Sigma^{\beta}_{SF} = \frac{1}{2}\left(\frac{\mathrm{d}\sigma}{\mathrm{d}\Omega}\right)^{\beta}_{u\to v} = \left(\frac{\mathrm{d}\sigma}{\mathrm{d}\Omega}\right)^{\beta}_{v\to u}$.

Chapter 3

Instrumentation and computational modelling

3.1 Instrumentation

The experiments that will be discussed in this thesis were performed at the Insititut Laue-Langevin (ILL) in France, ISIS in the United Kingdom and the Spallation Neutron Source (SNS) in the USA.

At the ILL, neutrons are produced in a reactor through fission. Fission sources produce a continuous flux of neutrons with time, meaning that while the reactor runs, the beam of neutrons will not stop [46]. The ILL reactor uses the decay of ^{235}U with a slow neutron to produce, on average, 2.5 fast neutrons plus the daughter nuclei, which can further decay to produce more neutrons. These neutrons will interact with more ^{235}U causing a chain reaction of decays. Since the neutrons produced in the reactions have an energy in the MeV range, moderators are used to "cool" down the neutrons to the meV range. Some of these neutrons are used to continue the chain of decays, while the rest are "extracted" and guided to the instruments. The ILL has three different moderators: liquid hydrogen at 25 K, liquid D_2O at 300 K and a 2400 K graphite source. The neutrons emerging from these moderators are termed cold, thermal, and hot respectively. The reactor at the ILL can operate at a maximum output power of 58 MW, producing a steady flux of neutrons of $1.5 \cdot 10^{15}\text{cm}^{-2}\text{s}^{-1}$ [183].

On the other hand, SNS and ISIS are pulsed spallation sources. Both of these facilities use a technique called spallation [46] where an accelerator is used to produce pulses of protons that travel at velocities close to the speed of light. These protons collide on to a target made of heavy metals. The protons enter the nucleus of the heavy metal, putting the target into a highly excited state which rapidly decays into lighter nuclei and neutrons [46]. Each proton collision produces around 30 neutrons with energies in the MeV range which are slowed down in moderators similar to those used in reactor sources. In contrast to the ILL reactor, ISIS and SNS do not produce a continuous source of neutrons. Instead, a train of pulses of neutrons are produce with a frequency of 50 Hz and 60 Hz for ISIS and SNS respectively [184, 185].

At pulsed spallation sources, Time-of-Flight (ToF) instruments are used. In this case, the flight time of the neutron over a known distance, usually the distance between the moderator and the detector, is used to determine the neutron wavelength using [147]

$$\lambda = \frac{th}{m_n L} \tag{3.1}$$

where t is the time of flight of the neutron, m_n is the mass of the neutron, L is the total length the neutron has to travel, h is Planck's constant and λ is the wavelength of the incident neutron. For elastic scattering, Bragg's law can then be applied to convert the time at which neutrons arrive at a detector into Q space [147]. If inelastic scattering experiments are performed, a monochromator is needed to select the energy of either the incident or the scattered neutron [147]. The case for an instrument with a monochromator, such as a Fermi chopper, before the sample is shown in figure 3.1. In this case, the final energy is determined using [150]

$$t = \frac{m_n}{h}\left(L_1\lambda_i + L_2\lambda_f\right) \tag{3.2}$$

where L_1 is the distance between the monochromator and the sample, L_2 is the distance between the sample and the detector, λ_i is the incident neutron wavelength and λ_f is the scattered neutron wavelength.

In the following sections, brief descriptions of the instruments used to collect the data shown in this thesis are given.

3.1.1 ISIS: SXD

The Single-Crystal Diffractometer SXD instrument is designed to analyse large volumes of reciprocal space of a single-crystal sample [186]. This makes it ideal for studying materials with a defect structure, since it gives the option of comparing the results from computational modelling with many reciprocal planes. Figure 3.2a shows the detectors and, in the centre, the space where the different sample environments are inserted. SXD can use different types of sample environments, such as several types of cryostats and refrigerators, allowing control of the pressure and temperature. Because the detectors are not able to cover all of reciprocal volume from a single measurement, the sample is rotated within the sample environment to fill in the gaps left between the detectors.

With SXD, a polychromatic beam (0.2–10 Å [187]) of neutrons incident on a single-crystal sample and the scattered neutrons are collected in large-area position-sensitive

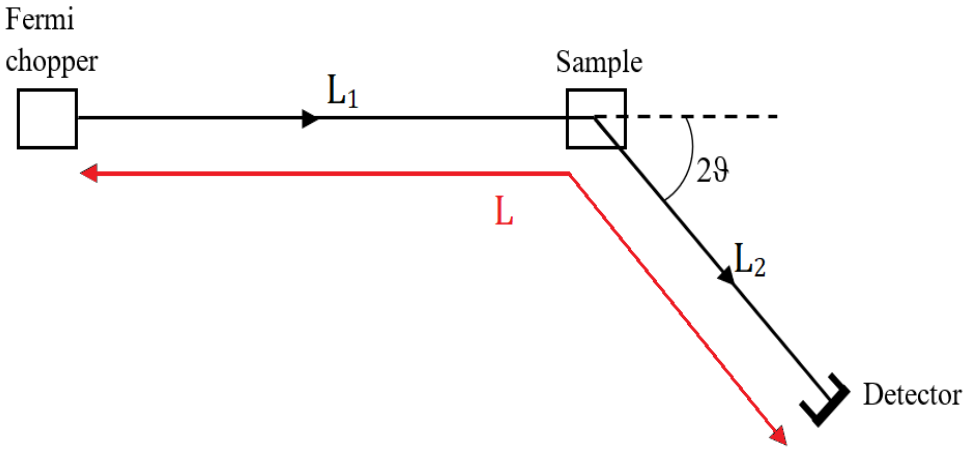

(a)

Figure 3.1: Schematic of the time-of-flight spectrometers. Image acquired from [147].

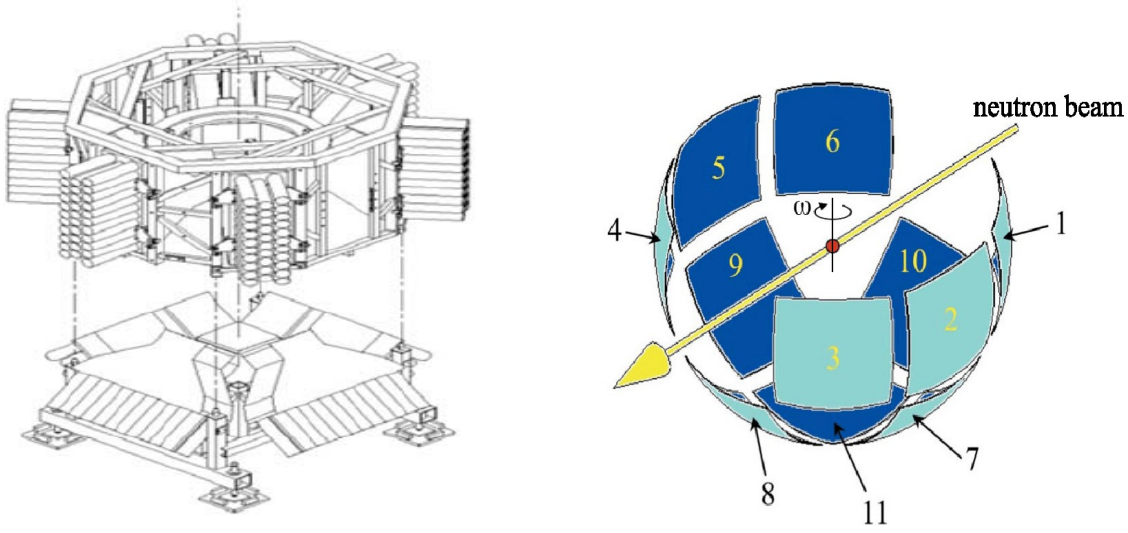

(a) (b)

Figure 3.2: (a) Schematic of the SXD instrument and (b) location of the detectors. Figures acquired from [186].

detectors (PSDs) as a function of neutron time-of-flight (the time the neutron takes to reach the detectors from the spallation target, via the sample), which means that the data from each detector pixel consists of a time-of-flight spectrum [186]. Figure 3.2b shows the detector arrangement. These detectors are arranged to maximise the amount of scattering area detected (around 49.4% according to [186]). Due to the large detector coverage, more Bragg reflections are collected in each crystal orientation, increasing the speed of data collection.

3.1.2 ILL: D7

The D7 instrument is a wide angle multi-detector diffractometer capable of performing polarisation analysis optimised for studying diffuse scattering of single crystals and powder samples. D7 can use neutrons at 3 individual wavelengths that are selected with a monochromator and beryllium filter. The beam is then polarised by going through a focusing bender supermirror, selecting only the neutrons in a spin u state. A guide field is then used to maintain beam polarisation. Finally, just before reaching the sample, the neutrons go through a Mezei-flipper used to flip the spin state of the incoming neutrons [188]. This flipper is used to control the type of scattering: when the flipper is on, SF scattering ($v \rightarrow u$) is measured, and when the flipper is off, NSF scattering ($u \rightarrow u$) is measured. To perform low temperature measurements, D7 can use different sample environments, such as an orange cryostat, that allows measurements down to 1.5 K, and a dilution fridge that allows measurements down to 40–50 mK [189]. A detailed diagram with the different components that form D7 is shown in figure 3.3a. D7 contains a set of XYZ-coils surrounding the sample that produce guide fields used to rotate the incoming polarised beam so that NSF and SF scattering can be measured in 3 orthogonal directions. With this, D7 is capable of performing both uniaxial and XYZ-PA, ideal for separating structural, electron magnetic and nuclear magnetic scattering.

After interacting with the sample, the neutrons can scatter into 132 detectors separated into 3 banks, covering a 2θ detection range of around 6° to 141°. Since D7 is a multi-detector instrument, the polarisation vector cannot be parallel to all $\mathbf{Q}$ vectors. As such, an offset angle α needs to be defined for each detector. As figure 3.3b shows, the D7 α

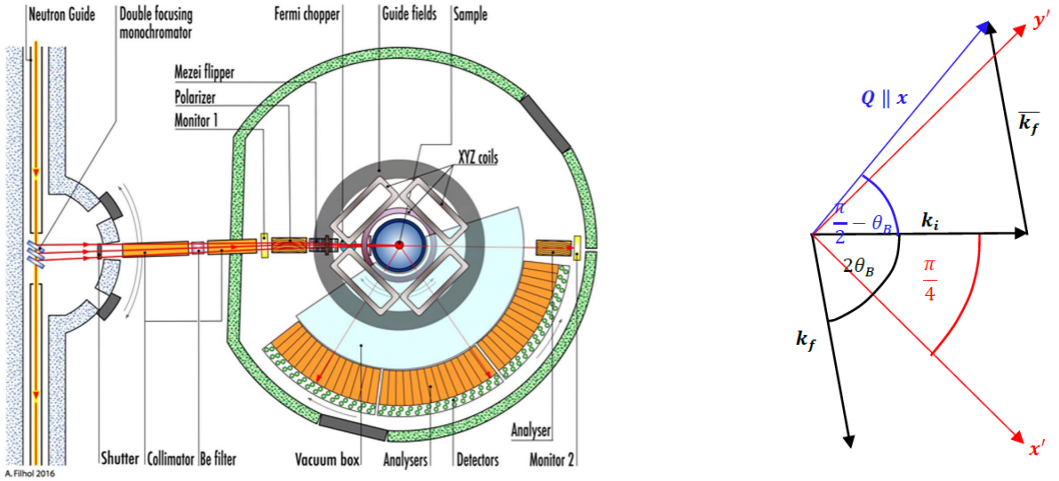

(a) (b)

Figure 3.3: (a) Top view diagram of the D7 diffractometer. (b) Relation between the scattering vectors $\mathbf{k}_i$, $\mathbf{k}_f$ and $\mathbf{Q}$, and the polarisation directions x' and y' in the scattering plane. Figures acquired from [190] and [191] respectively.

angle is defined as the sum of the angle between the x' polarisation direction and $\mathbf{k}_i$ and the angle between $\mathbf{Q}$ and $\mathbf{k}_i$. Since the angle between x' and $\mathbf{k}_i$ is fixed at 45°

$$\alpha = \frac{2\theta}{2} - 90° - 45° = \frac{2\theta}{2} - \frac{3\pi}{4} \tag{3.3}$$

where 2θ is the scattering angle. Finally, just before the detectors, D7 has 66 Schärpf-type bender analysers. These analysers are very similarly to the supermirror polariser before the sample, since they are used to only reflect the spin u neutrons into the detectors.

Unlike SXD, on D7 only a single plane of reciprocal space can be measured at a time. This plane is selected by aligning the sample with respect to the incoming beam before inserting it into the sample environment. Finally, D7 has a Fermi chopper which can be used to operate the instrument as a time-of-flight spectrometer with permanent polarisation analysis. However, the Fermi chopper reduces the incident beam flux substantially, and thus spectroscopy measurements need substantially more measurement time [189].

3.1.3 ISIS: POLARIS and SNS: NOMAD

POLARIS (figure 3.4a) is a high intensity powder diffractometer at ISIS optimised for the rapid characterisation of structures. The high incident neutron flux combined with a large angle detector coverage enables the rapid collection of high quality diffraction data suitable for structure refinement. POLARIS contains 5 large banks covering a 2θ detection range of around 6° to 168° [192]. Just like SXD, POLARIS uses an incident polychromatic neutron beam (0.1–6 Å) [194].

Similarly, the Nanoscale Ordered MAterial Diffractometer (NOMAD) (figure 3.4b) at SNS uses a large bandwidth (0.1–3 Å) of neutron wavelengths and extensive detector coverage to enable structural determinations of local order in crystalline and amorphous materials. NOMAD contains 6 large banks covering a 2θ detection range of around 3° to 175° [195].

Unlike SXD, which can analyse large volumes of reciprocal space (3D data), or D7 which has access to a single planes (2D data), POLARIS and NOMAD are used for powder diffraction, and thus 1D data is collected as a function of magnitude of $\mathbf{Q}$. These data

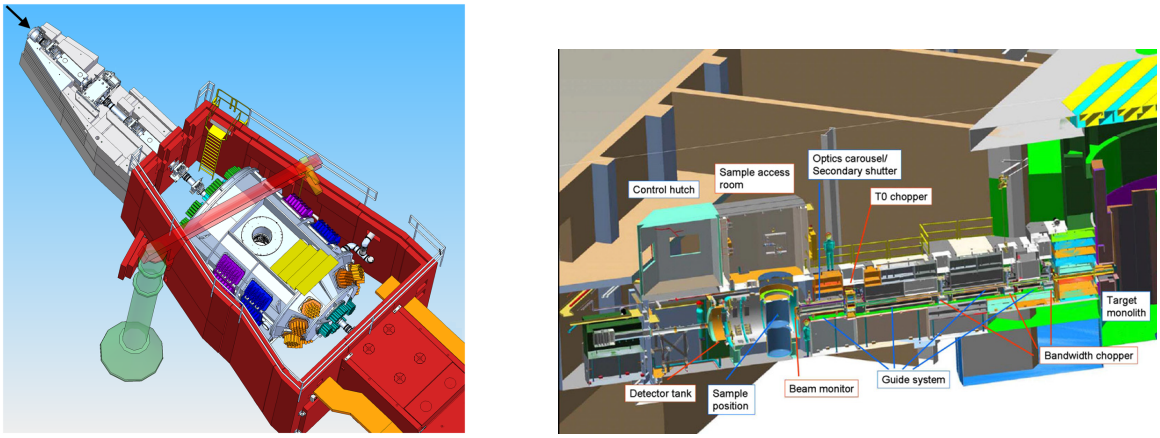

(a) (b)

Figure 3.4: (a) Schematic diagrams showing the layout of the (a) POLARIS and (b) NOMAD instruments. Figures acquired from [192] and [193] respectively.

then give access to high-resolution PDFs.

3.1.4 ISIS: MARI and SNS: SEQUOIA

The Multi-Angle Rotor Instrument (MARI) at ISIS is a time-of-flight direct geometry chopper spectrometer used for studies of magnetic excitations in powder and polycrystalline materials [198]. MARI uses a Fermi chopper to monochromate the incident neutron beam with incident energies (E_i) in the range 7 meV to 1000 meV, and contains a detector array covering a 2θ detection range of around 3° to 135° with an energy resolution of 1.5–8% [199]. These detectors are arranged in a vertical scattering plane, as figure 3.5a shows.

Similarly, SEQUOIA (figure 3.5b) is a direct geometry time-of-flight chopper spectrometer at SNS optimised for high-resolution inelastic neutron scattering studies of magnetic excitations and lattice vibrations [200]. SEQUOIA also has the option of selecting, with the help of a Fermi chopper, a wide range of possible E_i of the incoming neutron beam, between 8 meV and 2000 meV. This allows for the study of many possible inelastic events. SEQUOIA contains a detector array covering a 2θ detection range of around -30° to 60° with an energy resolution of 1–5% [200].

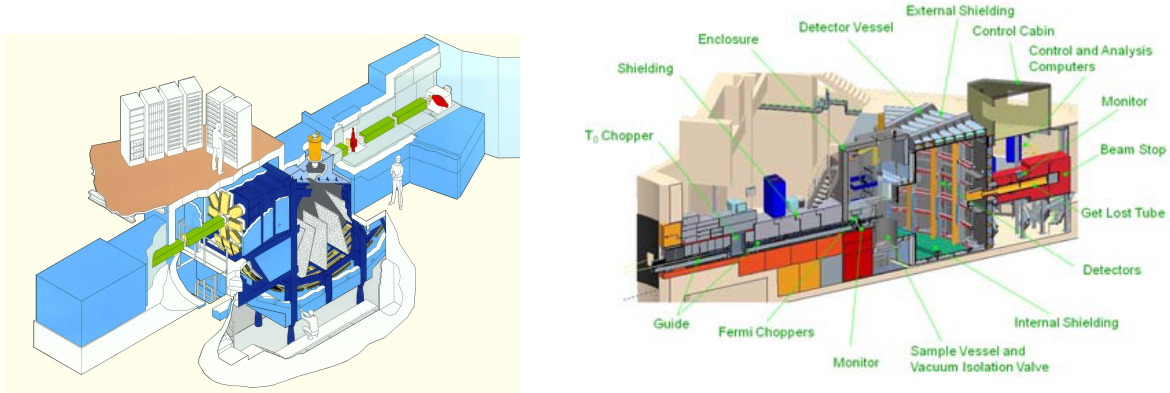

(a) (b)

Figure 3.5: (a) Schematic diagrams showing the layout of the (a) MARI and (b) SEQUOIA instruments. Figures acquired from [196] and [197] respectively.

Unlike the instruments described so far, SEQUOIA and MARI are designed for inelastic scattering measurements, meaning that the data collection is as a function of both wave vector and energy.

3.1.5 ISIS: LET

LET is a time-of-flight direct geometry cold neutron multi-chopper spectrometer at ISIS that, just like MARI and SEQUOIA, is used for the study of dynamics in condensed matter systems [201]. However, LET differs from SEQUOIA and MARI in a few key aspects. LET is optimised to study low energy transfer events with a very high energy resolution. As such, the range of possible incident energies is much smaller, between 0.6 meV and 80 meV, and thus the use of cold neutrons from the second target station. LET contains a detector array covering a 2θ detection range of around -40° to 140° with an energy resolution no higher than 0.8% [202]. The LET detector tank is shown in figure 3.6. In addition, LET does not use a Fermi chopper. Instead, LET uses two sets of fast counter-rotating disk choppers to monochromate the incident beam. This allows control over the pulse width and shape, and maximises the flux for any given resolution [203]. Finally, LET has the option of performing full neutron uniaxial PA using a supermirror polariser and ^{3}He spin filter analyser for the incoming and scattered beam respectively. However, unlike D7 which can perform polarisation analysis down to 40–50 mK, the LET sample environment only permits temperatures no lower than 1.6 K when the polarisation analysis option is used [201].

3.2 Computational modelling

Multiple computational methods were used to model the systems studied and interpret the collected data. For this, programs written by myself and software developed outside the project were used. In the following sections, a brief description of the models used to simulate and analyse the collected data is given.

Figure 3.6: Inside the LET detector tank. Figure acquired from [201].

3.2.1 Monte Carlo and Reverse Monte Carlo

Monte Carlo (MC) and Reverse Monte Carlo (RMC) methods are a broad class of computational algorithms that rely on repeated random sampling to obtain numerical results [204, 205]. Because of this, MC and RMC algorithms are extremely useful for simulating systems with many coupled degrees of freedom, such as disordered systems. In this thesis, the discussion on MC and RMC to study disordered systems will be restricted to their use in nuclear structures. However, it is worth noting that it is very commonly used in modelling the magnetism of spin ice systems.

The starting point of the MC and RMC approach is the same: a supercell formed by $N_i \times N_j \times N_k$ unit cells of the system being studied is constructed. If the system contains vacancies, ions are removed at random within the supercell until the desired concentration of vacancies is acquired. The same procedure is followed for substituting a type of ion by another. The ions in the supercell are then moved at random, but the acceptance of the movement changes depending on the method.

MC works on an energy minimisation procedure. In this thesis a "balls and springs" model was used to calculate the energy of each configuration, where the ions are treated as spherical balls and are connected to their neighbours by a spring with a certain spring constant. The spring constant defines the strength of the bond between two ions. The energy of a single ion i is then calculated using

$$E = \sum_j \frac{1}{2} k_{ij} \Delta x_{ij}^2 \tag{3.4}$$

where the summation runs over all the neighbouring ions, k_{ij} is the spring constant and Δx_{ij} is the change in bond length. With the bond lengths and spring constants defined, the MC process works as follows. First, an ion is chosen at random and its energy E_1 is calculated using equation (3.4). The same ion is then moved in an arbitrary direction and the new energy E_2 is calculated. If $E_2 - E_1 < 0$, i.e. the energy of the system is lowered, the move is accepted. If $E_2 - E_1 > 0$, i.e. the energy of the system is increased, the move is accepted with a probability given by $e^{(-\Delta E/\mathrm{k_B}T)}$ where ΔE is the difference in energy before and after the movement, $\mathrm{k_B}$ is the Boltzmann constant and T is the temperature. This method, commonly known as the Metropolis MC algorithm [204], ensures that the model does not get trapped in a local minimum, and enables the model to converge towards the global minimum. Once the MC procedure is finished, the scattering is computed from the supercell with the ions in the new locations.

In this thesis, a MC program developed in C++ by Sala [112] and Bowman [206] was used for some preliminary calculations. In this program, when an ion was selected to become a vacancy, instead of "removing" the springs connected to such an ion, the springs (bonds) were retained in order to avoid lattice instabilities. However, its occupancy was set to zero in order to remove it from the diffuse scattering calculations at the end of the MC process.

On the other hand, instead of the energy minimisation of MC, the goodness of fit to the data is optimised in RMC. During the RMC simulation, ions selected at random are displaced in arbitrary directions. After each movement, a quantity such as the PDF or the diffuse scattering is calculated and compared with the experimental data. In this thesis, the RMCprofile program [207] was used to perform RMC simulations, which calculates the agreement between the calculated and experimental variable using

$$\chi^2 = \sum_{i=1}^{n} \frac{\left(Y_{\mathrm{exp},i} - Y_{\mathrm{calc},i}\right)^2}{\sigma_i} \tag{3.5}$$

where the summation runs over all the data points, $Y^2_{\mathrm{exp},i}$ and $Y^2_{\mathrm{calc},i}$ are the i^{th} experimental and calculated data points respectively and σ_i is some weighting factor, usually defined by the experimental uncertainty. Similarly to MC, if the movement of the ions decreases χ^2, the change is accepted. If this is not the case, the change is accepted with a probability given by $e^{\left(-\Delta\chi^2/2\right)}$ where $\Delta\chi^2$ is the change in the goodness-of-fit factor.

The halting procedure of both the MC and RMC approach changes depending on the program used. For the MC program used in this thesis, the stopping condition is defined by the number of movements, i.e. the program stops when x number of movements (accepted and rejected) have been performed. On the other hand, the RMCprofile program is time based, meaning that it will run only for the amount of time given in the input. In RMCprofile, the evolution of χ^2 with time can be monitored. In this thesis, the criterion for whether the running time for the RMCprofile is long enough is given by χ^2 converging to a constant value.

3.2.2 Density Functional Theory

The wave function of a system with N electrons and I nuclei is expressed, neglecting time dependence, as a function of the position of all the electrons $\mathbf{r}_N$ and nuclei $\mathbf{R}_I$. However, in the Born-Oppenheimer approximation it is assumed that the nuclei are stationary in time due to them being much more massive than the electrons. Thus, the nuclear degrees of freedom can be separated from the electronic ones and a many-electron and many-nuclei wave function can be written as ψ and ϕ, respectively. In this approximation, the properties of any material can be studied by solving the time dependent and time independent Schrödinger equation [208]. In the Born-Oppenheimer approximation, the Hamiltonian of a system contains three components: the kinetic energy T, the external potential V_{ext} (which may be internal to the sample from the nuclei or external to the sample such as applied fields), and the electron-electron interaction potential V_{e-e}. This is written as [209]

$$\mathcal{H}\psi\left(\mathbf{r}_1, \mathbf{r}_2, ..., \mathbf{r}_N\right) = \left[T + V_{ext} + V_{e-e}\right]\psi\left(\mathbf{r}_1, \mathbf{r}_2, ..., \mathbf{r}_N\right) = E\psi\left(\mathbf{r}_1, \mathbf{r}_2, ..., \mathbf{r}_N\right) \tag{3.6}$$

In reality, the nuclear-nuclear interaction potential and the nuclear kinetic energy are also present, but in this approximation the nuclear-nuclear interactions can be taken as a constant and the nuclear kinetic energy can be taken to be zero. Despite the simplifications, exact solutions of this equation have only been found for simple systems with simple potentials, such as an electron in a potential well. More complicated systems cannot be solved analytically and require numerical solutions, which can be computationally expensive. Over the last 50 years, the method of choice for solving such systems has been density functional theory (DFT) [210].

DFT is a method for first principle (*ab initio*) calculations of structures of, amongst others, crystals, and their interactions. The basis of DFT is the Hohenberg-Kohn (HK) theorem [211], which states that the total energy of a system with a static potential (such as the one from the nuclei) is a unique functional of the charge density, and the minimum value of the total energy functional is the ground state energy of the system. In other words, DFT attempts to solve equation (3.6) in terms of an electron density.

Many methods exist of applying DFT, but one of the most commonly used is via the Kohn-Sham (KS) equations [212], in which N Schrödinger-like equations of the form

$$\mathcal{H}_{\mathrm{KS}}\psi\left(\mathbf{r}\right)_i = \epsilon_i\psi\left(\mathbf{r}\right)_i \tag{3.7}$$

are solved for N non-interacting electrons. The electron density is then written as [208]

$$\rho\left(\mathbf{r}\right) = \sum_{i=1}^{N} f_i\psi\left(\mathbf{r}\right)_i^* \psi\left(\mathbf{r}\right)_i \tag{3.8}$$

where f_i are the fractional occupations which are used for systems with degeneracy, i.e., if $\psi\left(\mathbf{r}\right)_i$ and $\psi\left(\mathbf{r}\right)_{i+1}$ have the same energy. Otherwise, $f_i = 1$ for all wave functions [210]. $\mathcal{H}_{\mathrm{KS}}$ is written as [210]

$$\mathcal{H}_{\mathrm{KS}} = -\frac{\hbar^2}{2m}\nabla^2 + V_{ext} + V_H + V_{XC} \tag{3.9}$$

where the first term on the right-hand side is the kinetic energy, with m the mass of the electron, the second term is the external potential, the third term is the Hartree potential, arising from the Coulomb interaction between one electron and the electron density, and the last term is the exchange-correlation potential, which is a term required to make the non-interacting electrons behave as if they are interacting [209]. While this method is very much an approximation, since it needs a fictitious potential V_{XC} to account for electronic interactions, it has still provided surprisingly accurate predictions when compared with experiments [210]. The correct choice of these potentials will, in theory, give exact results that would be solutions to the Schrödinger equation, and developing the best potentials is an active area of research.

Many DFT implementations exist for solving these kinds of equations. Throughout this thesis, the CASTEP program [213] has been used for geometrical optimisation. The methodology implemented in CASTEP is the KS-DFT approach just described, where a set of one-electron Schrödinger KS equations are solved using the plane-wave pseudopotential approach in which each wave function is written in a plane wave basis set defined by use of periodic boundary conditions. Furthermore, a pseudopotential is used to replace the atomic nucleus and core electrons by a fixed effective potential to increase the calculation efficiency [208].

It is worth noting that, unlike RMC or MC approaches which can model systems with many ions ($\gg 10^4$), DFT can only model systems with (usually) no more than 1000 ions. This is due to the large number of Schrödinger equations that need to be solved and, thus, the large amount of time and computational power needed.

3.2.3 Crystal electric field analysis

To determine the crystal electric field (CEF) levels and the CEF spectrum, the first step is to determine the CEF-Hamiltonian ($\mathcal{H}_{CEF}$). The $\mathcal{H}_{CEF}$ of a magnetic ion is obtained by integration of the CEF potential over the distribution of electrons [46]. If the surrounded ions are treated as isolated charges, neglecting the overlap of orbitals and relativistic effects, the $\mathcal{H}_{CEF}$ of a magnetic ion with a weak CEF (weak coupling scheme [46, 214]) can be written as [215]

$$\mathcal{H}_{CEF} = \sum_{n,m} B_n^m \widehat{O}_n^m \tag{3.10}$$

where $n = 2, 4$ and 6, $m = -n$ to n in steps of 1, B_n^m are the crystal field parameters or B-parameters and $\widehat{O}_n^m$ are the Steven Operators that depend on the total angular momentum quantum number J and have already been tabulated [160, 215, 216]. This form of $\mathcal{H}_{CEF}$ arises as an expansion of the Coulomb potential of the crystal based on the symmetry surrounding the magnetic ion [112]. The number of B-parameters needed to extract the Hamiltonian of an ion in a particular system depends not only on the symmetry of a system, but also on its orientation and origin. In a pyrochlore system with magnetic ions at the A sites, if only the nearest neighbour O(1) and O(2) ions are considered, the expression for the CEF-Hamiltonian only contains six different B parameters [217]

$$\mathcal{H}_{CEF-SI} = B_2^0\widehat{O}_2^0 + B_4^0\widehat{O}_4^0 + B_4^3\widehat{O}_4^3 + B_6^0\widehat{O}_6^0 + B_6^3\widehat{O}_6^3 + B_6^6\widehat{O}_6^6 \tag{3.11}$$

This is because the surrounding O ions form a scalenohedron which belongs to the D_{3d} symmetry point group, and therefore only the 6 B-parameters in equation (3.11) are needed [160]. However, this simple expression is only achieved if the origin of the system is translated to an A site and the system is rotated such that the z-axis is along the O(1)-A-O(1). This is called Prather's convention [112]. In general, the number of B-parameters needed to fully describe a system decreases with increasing symmetry [160].

$\mathcal{H}_{CEF}$ can be diagonalised to extract the eigenvalues (energy levels) and eigenvectors. The eigenvalues (E_i) and eigenvectors (Γ_i) are used to calculate the resulting energy spectrum for a constant temperature and Q using [217]

$$S(\boldsymbol{Q}, \hbar\omega) = \sum_{i,i'} \frac{\left(\sum_\alpha \left| \langle \Gamma_i | \widehat{J}_\alpha | \Gamma_{i'} \rangle \right|^2\right) e^{-\beta E_i}}{\sum_j e^{-\beta E_j}} F\left(E_i - E_{i'} + \hbar\omega\right) \tag{3.12}$$

where i, i' and j index the different energy values and their respective eigenvectors, $\beta = 1/k_B T$, $\alpha = x$, y and z, and $F\left(E_i - E_{i'} + \hbar\omega\right)$ is a convolution of a Lorentzian and Gaussian function to account for energy transition lifetime and instrumental resolution. B-parameters can thus be fitted to the CEF spectrum from an experiment to extract the CEF-Hamiltonian, and with it, the energy levels and eigenvalues of the magnetic ions in the system can be studied.

A method of calculating the B-parameters from first principles is through the point-charge-model (PCM) where the ions surrounding the magnetic ion of interest are treated as point charges. In the PCM, the B-parameters in units of meV are calculated using [214]

$$B_n^m = 1.44 \times 10^4 (0.5292)^n \left(\gamma_{m,n} C_{m,n} \langle r^n \rangle \theta_n\right) \tag{3.13}$$

where $\langle r^n \rangle$ is the expectation value of the radial part of the wave function, θ_n is a numerical factor that depends on the magnetic ion and $C_{m,n}$ is a normalisation factor. $C_{m,n}$, θ_n and $\langle r^n \rangle$ are tabulated values that can be found in [215, 218]. Finally

$$\gamma_{m,n} = -\sum_i^k \frac{q_i}{R_i^{n+1}} \frac{4\pi}{2n+1} Z_{n,m}\left(x_i, y_i, z_i\right) \tag{3.14}$$

where the summation is over all the neighbouring atoms (ligands), R_i is the distance from the magnetic ion to the ligand, q_i is the charge of the ligand and $Z_{n,m}(x_i, y_i, z_i)$ is the tesseral harmonic.

3.2.4 Rietveld refinement

A common method for the study of crystal structures is the powder diffraction method, in which a crystal ground into a powder is used. Total scattering is then used to acquire a 1D diffraction pattern with all reflections of the crystallographic planes visible. In this thesis, total scattering measurements were performed with the Time-of-Flight (ToF) technique previously described.

Multiple methods exist for modelling the diffraction pattern and extracting the structural information. In this thesis, the main technique used was the Rietveld refinement method [219, 220], sometimes also called Bragg refinement. In this method, a diffraction pattern is calculated from an initial guess of possible structures. This calculation contains, not only the Bragg reflections, but also the background of the measurements, the broadening of the peaks due to instrumental resolutions and so on. Just as with RMC, the least square approach is then used to refine the guessed structure until the calculated pattern matches the experimental pattern. One of the parameters used to assess how close the model is to the data is χ^2 [221]

$$\chi^2 = \frac{\sum_{i=1}^{n} w_i \left(Y_{\mathrm{exp},i} - Y_{\mathrm{calc},i}\right)^2}{m - n} \tag{3.15}$$

where m is the total number of points used in the refinement, n is the number of refined parameters, $Y^2_{\mathrm{exp},i}$ and $Y^2_{\mathrm{calc},i}$ are the i^{th} experimental and calculated data points respectively, and $w_i = 1/\sigma^2_{\mathrm{exp},i}$ where $\sigma_{\mathrm{exp},i}$ is the experimental uncertainty in the i^{th} experimental data point. The single-crystal literature often uses the term "goodness of fit" G which is defined by $G^2 = \chi^2$. Another parameter commonly used to determine how good a fit is to the experimental data is the weighed profile R-factor (in %) [221]

$$\mathrm{R}_{wp} = 100 \cdot \left[\frac{\sum_{i=1}^{n} w_i \left(Y_{\mathrm{exp},i} - Y_{\mathrm{calc},i}\right)^2}{\sum_{i=1}^{h} w_i Y^2_{\mathrm{exp},i}} \right]^{1/2} \tag{3.16}$$

The goal with both of these parameters is for $\chi^2 \to 1$ and $\mathrm{R}_{wp} \to 0$. If $\chi^2 < 1$, then either too many variables are being used and the model is fitting to the noise or the standard deviation of the data is overestimated [221]. However, it is worth mentioning that these parameters are only used for guidance in the refinement. It is possible for the calculated pattern to be close to the experimental pattern and still have a large value of χ^2 or R_{wp}, either because the standard deviations are underestimated or the model is incomplete.

In this thesis, the program used to perform Rietveld refinements is FullProf [222]. FullProf is capable of performing Rietveld analysis of single crystal or powder diffraction data collected either with neutrons (constant wavelength or time of flight) or X-ray powder diffraction data collected at constant or variable step in scattering angle 2θ. FullProf allows for the refinement of both nuclear and magnetic structure. Furthermore, some

systems may contain multiple phases (structures), and FullProf allows for the simultaneous refinement of all phases as well as their relative contribution. Finally, FullProf has a wide range of tools for computing and fitting a background to the data, as well as a wide range of functions to account for external inputs such as instrumental resolution and peak shape.

Chapter 4

Structural disorder in $Ho_2Ti_{2-x}Sc_xO_{7-x/2}$

The effect of structural disorder in $Ho_2Ti_2O_7$ was studied by the controlled introduction of Sc ions on the B-sites. Due to the charge difference between the Ti and Sc ions, charge compensating oxygen vacancies were needed to maintain sample charge neutrality. Through total scattering measurements performed on $Ho_2Ti_{2-x}Sc_xO_{7-x/2}$ (HTSO) with $x = 0.0$, $x = 0.1$ and $x = 0.5$ using POLARIS at ISIS, not only was it found that the oxygen vacancies are located at the O(2) sites, but a small percentage of extra O(2) ions are displaced to the centre of the tetrahedra formed by the B-sites, known as 8a site. Density functional theory (DFT) calculations performed in parallel also predicted that, to minimise the energy of the system, an O(2) vacancy is needed with an extra O(2) displaced to an 8a site. Calculations of the structural diffuse scattering were performed with the final DFT structure, which were in excellent agreement with structural diffuse scattering measurements of the $x = 0.5$ HTSO sample performed using SXD and D7 at ISIS and the ILL respectively. Finally, RMC fits were performed to the total scattering data and diffuse scattering simultaneously. These fits predicted that the Sc ions do not form clusters, and are distributed on the B-sites randomly.

4.1 Introduction

Disorder is often regarded as a nuisance in the study of classical and quantum spin liquids, and much effort has been devoted in the past to reduce it as much as possible. However, it has become apparent that it can also be used as a resource to highlight the underlying spin liquid and emergent topological behaviour and to induce altogether new interesting physics phenomena. Recent theoretical calculations show that for spin ice materials with non-Kramers ions, such as $Ho_2Ti_2O_7$, it is possible to tune to a quantum spin liquid state with no long range order by the controlled introduction of structural disorder [145]. One type of disorder that may induce this type of behaviour is the introduction of substitutions or vacancies on the non-magnetic Ti or O sites [145].

The presence of this type of disorder has been studied on other pyrochlores, such as the $Y_2Ti_2O_{7-\delta}$ system studied by Sala *et al.* [223] and $Yb_2Ti_2O_{7-\delta}$ studied by Bowman *et al.* [224]. These disordered oxygen-depleted samples were grown and annealed in a reducing, flowing mixed gas of hydrogen and argon [223]. In each case, it was found that the location of the vacancy changed. As figure 4.1 shows, the $Y_2Ti_2O_{7-\delta}$ system contained vacancies at the O(1) sites, at the centre of the Y tetrahedra, while the $Yb_2Ti_2O_{7-\delta}$

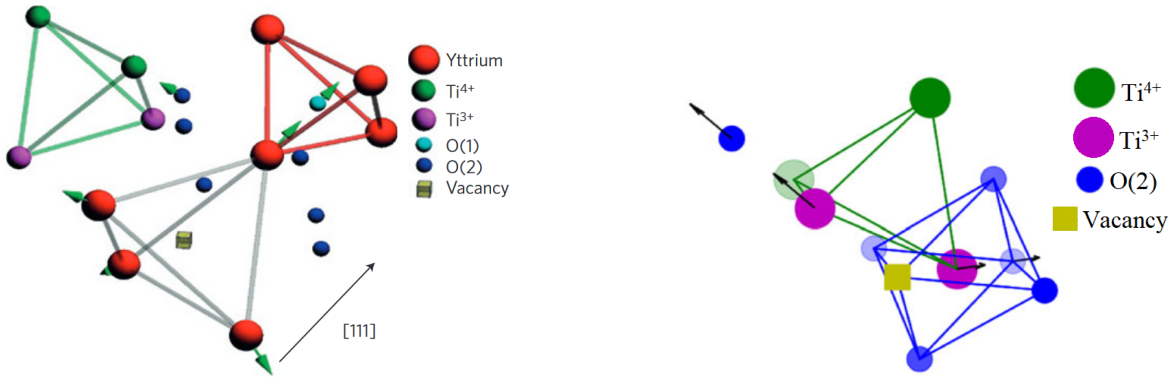

(a) (b)

Figure 4.1: (a) Schematic diagram of O(1) vacancies in $Y_2Ti_2O_{7-\delta}$ and the associated distortion of the surrounding ions, with displacements indicated by green arrows. (b) Schematic diagram of O(2) vacancies in $Yb_2Ti_2O_{7-\delta}$ and the associated distortion of the surrounding ions, with displacements indicated by black arrows. Figures acquired from [223] and [224] respectively.

system contained vacancies at the O(2) sites. Neutron diffuse scattering is an excellent tool to study disorder due to oxygen vacancies, since neutrons are particularly sensitive to vacancies and displacement of oxygen ions. This can be seen in the (h,k,7) structural diffuse scattering planes, shown in figure 4.2, performed on $Y_2Ti_2O_{7-\delta}$ and $Yb_2Ti_2O_{7-\delta}$. These systems produce very different diffuse scattering, with the $Y_2Ti_2O_{7-\delta}$ containing a figure-of-eight pattern with a gap near (0,7,7) and symmetrically equivalent points, while the $Yb_2Ti_2O_{7-\delta}$ system not only has intensity around (0,7,7) and symmetrically equivalent points, but the scattering at high Q is much more pronounced.

A similar type of disorder was studied in $Ho_2Ti_2O_7$ where charge compensating oxygen vacancies were introduced in a controlled and uniform manner by changing a percentage of Ti^{4+} ions by the Sc^{3+} ions. To do this, different amounts of the precursors materials

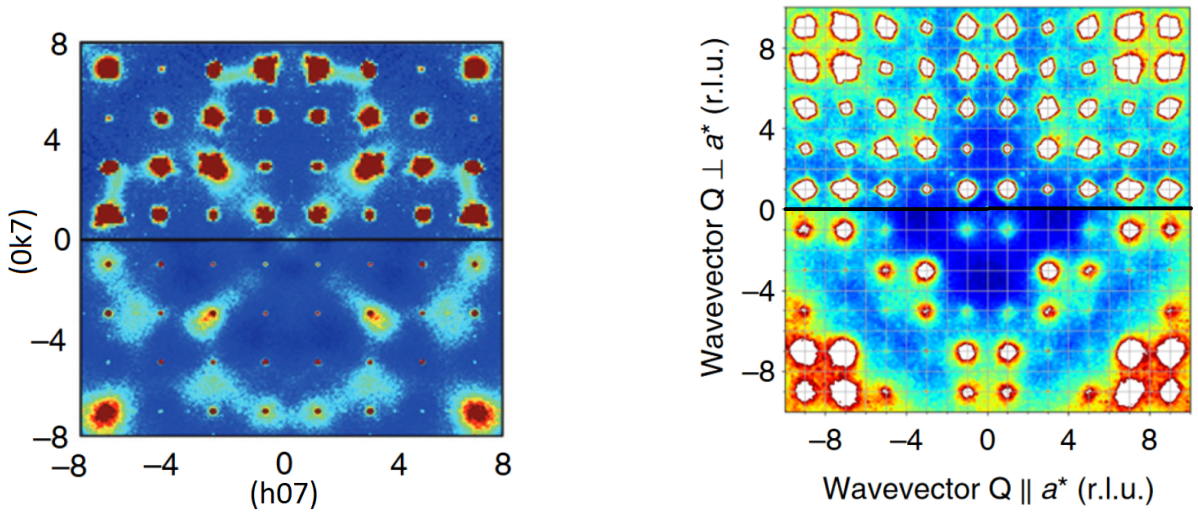

(a) (b)

Figure 4.2: The structural diffuse scattering measured on SXD at ISIS of (a) $Y_2Ti_2O_{7-\delta}$ and (b) $Yb_2Ti_2O_{7-\delta}$. The lower half panels show Monte-Carlo (MC) calculations used to determine the location of the oxygen vacancy. Figures acquired from [223] and [224] respectively.

were mixed until the wanted concentration of Sc ions was achieved. Using this method, disorder will not only arise due to the presence of vacancies, but also due to the difference in ionic radii and charge between the Sc and Ti ions.

This chapter presents neutron scattering data on disordered spin ice $Ho_2Ti_{2-x}Sc_xO_{7-x/2}$ (HTSO) with $x = 0.0$, $x = 0.1$, $x = 0.5$. I will present total scattering measurements on powders of all three samples, alongside Bragg refinements performed to such data to analyse the origin of disorder and to extract the pair distribution functions (PDFs) of all three samples. Structural diffuse scattering measurements were performed on a single crystal of the $x = 0.5$ HTSO sample. The results were analysed with support of geometrical optimisation density functional theory (DFT) calculations, and reverse Monte-Carlo (RMC) fits performed to the SXD and PDF data simultaneously.

4.2 Total scattering measurements

Disorder was induced in $Ho_2Ti_2O_7$ by doping with Sc ions on the B-sites. Due to the charge difference between the Ti^{4+} and Sc^{3+}, this doping left the system negatively charge and charge-compensating oxygen vacancies were needed. However, a pyrochlore contains two distinct oxygen sites, O(1) sites at the centre of the tetrahedra formed by Ho ions, and O(2) sites forming octahedra surrounding the Ti/Sc ions. To determine the location of the oxygen vacancy, total scattering measurements on powder crystals of $Ho_2Ti_{2-x}Sc_xO_{7-x/2}$ (HTSO) with $x = 0.0$, $x = 0.1$ and $x = 0.5$ were performed at room temperature using the POLARIS instrument at ISIS. For this experiment, 3.9 g, 3.1 g and 4.3 g of the $x = 0.0$, $x = 0.1$ and $x = 0.5$ HTSO samples were used respectively, grown by Dharmalingam Prabhakaran using the floating zone method at the Clarendon Laboratory, Oxford University.

The intensity as a function of time of flight (ToF) normalised to the mass of the $x = 0.0$ HTSO sample from detector banks 1 (smallest ToF) and 5 (largest ToF) are shown in figure 4.3. Figure 4.4 shows the combined data from all 5 banks converted to Q-space units. The ToF to Q-space unit conversion was performed using the GudrunN program, where measurements of the empty canister and a vanadium standard sample are used to correct and put the data on an absolute scale. The large difference in scattering between the $x = 0.5$ and $x = 0.0$ HTSO Bragg-scattering data is indicative of the large amount of disorder that has been introduced in this system by the presence of vacancies and Sc

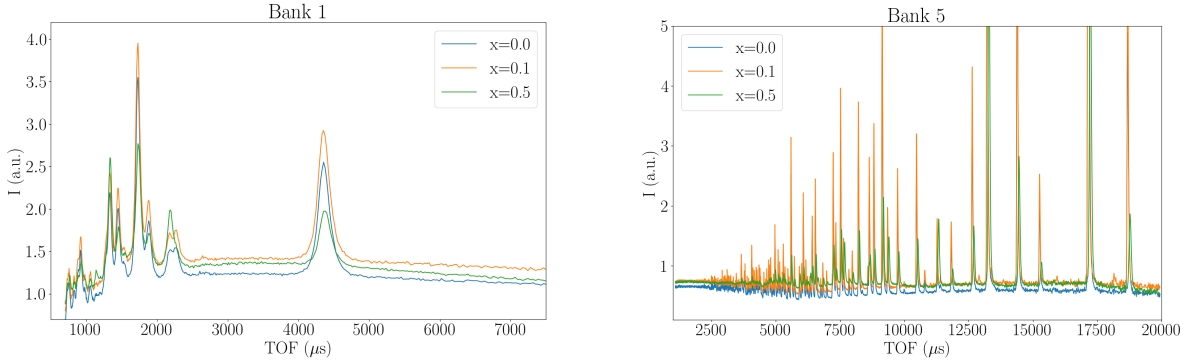

(a) (b)

Figure 4.3: Total scattering data of the $x = 0.0$, $x = 0.1$ and $x = 0.5$ HTSO samples normalised to the mass of the $x = 0.0$ HTSO sample acquired with POLARIS from detector banks (a) 1 and (b) 5.

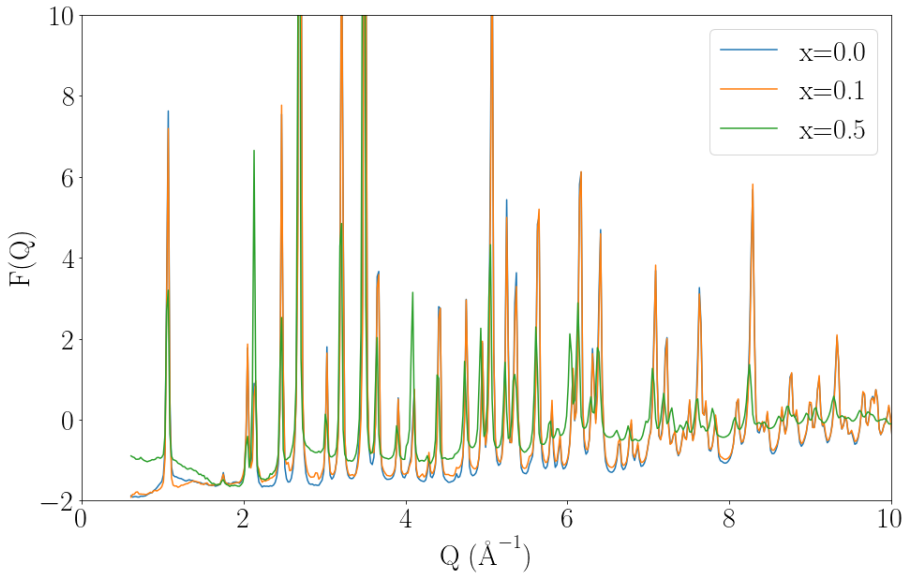

Figure 4.4: Merged corrected data from all 5 banks of the POLARIS instrument and converted to Q-space units.

doping. Not only is there a significant change in the Bragg peak intensities and shapes, but the intensity in between Bragg peaks is also higher due to the large amount of diffuse scattering arising from the disorder. The $x = 0.1$ HTSO Bragg-scattering data on the other hand is still very similar to the $x = 0.0$ HTSO data, indicating that the doping in this system was not enough to cause large changes to the average structure. Since the level of doping of the $x = 0.1$ HTSO system is an intermediate point between the other two, the scattering in between Bragg peaks of the $x = 0.1$ HTSO data is in between the $x = 0.0$ and $x = 0.5$ HTSO data, as figure 4.4 shows. Finally, there seems to be a small shift in the location of the Bragg peaks, especially noticeable for Bragg peaks at large ToF in bank 5. This is an indication of the lattice parameter of the unit cell changing due to the doping and vacancies.

To further analyse the data and extract information such as the true concentration of Sc, as well as the location of the vacancies (O(2) or O(1) sites), Bragg refinements were performed using the FullProf suite [222]. For simplicity, when performing the Bragg refinements, the concentration of Sc and O vacancies was constrained to maintain charge neutrality. In other words, the concentration of Sc (Ti) ions increased (decreased) at the same rate as the concentration of O vacancies increased. Other parameters of interest were also refined, such as the lattice constant and the x coordinate of the O(2) ions, as well as background and instrumental aspects. Since 5 different spectra were measured (one for each POLARIS detector bank), each with a different ToF range, all 5 patterns were refined simultaneously to further constrain the refined parameters.

The first data refined were the $x = 0.5$ HTSO sample data. Two separate refinements were performed, as figure 4.5 and 4.6 show: having vacancies at the O(1) sites (O(1) vacancies) and vacancies at the O(2) sites (O(2) vacancies). As figure 4.5 shows, in bank 5 both models produced similar fits, with the higher ToF Bragg peaks fitting marginally better with the O(2) vacancy model. This is in agreement with the Bragg R-factors (where the measured and calculated integrated Bragg peak intensities are compared) extracted from FullProf, being smaller for the O(2) vacancy model ($R_{Bragg} = 8.24\%$) than for the O(1) vacancy model ($R_{Bragg} = 11.75\%$). Both models also produced similar refinements for the bank 1 data, as figure 4.6 shows. The biggest difference can be found at around

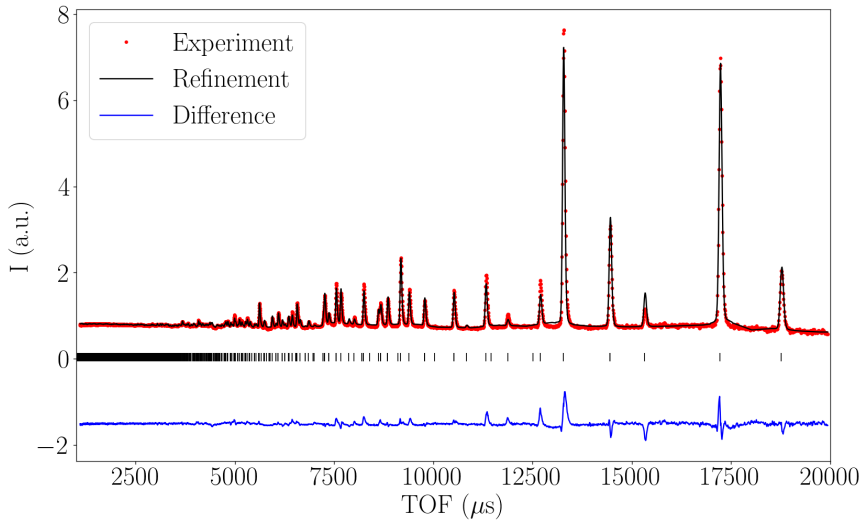

(a)

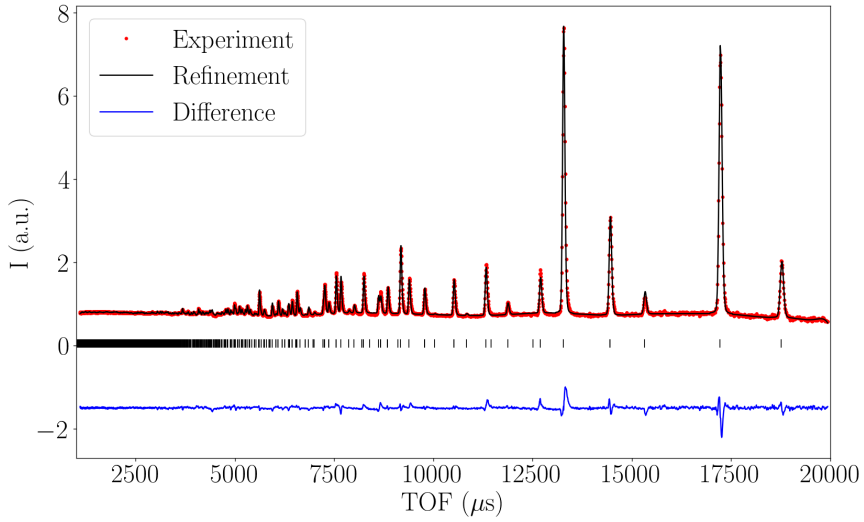

(b)

Figure 4.5: Bragg refinement of the $x = 0.5$ HTSO data from bank 5 using (a) O(1) vacancies and (b) O(2) vacancies. The black vertical markers are the Bragg positions.

2700 μs, where the O(1) vacancy model indicates the presence of an extra Bragg peak while the O(2) vacancy model is almost flat. Because of this, the O(1) vacancy model was discarded, and further analyses were performed only considering O(2) vacancies. Further preference for an O(2) vacancy model was found when comparing the Bragg R-factors, smaller for the O(2) vacancy model ($R_{Bragg} = 2.15\%$) than for the O(1) vacancy model ($R_{Bragg} = 3.36\%$). In addition to this, a refinement was performed assuming a perfect crystal with no vacancies and Sc ions, resulting in a Bragg R-factors of 45.26% and 31.36% for banks 1 and 5 respectively.

With the O(2) model confirmed, one extra parameter of the $x = 0.5$ HTSO system was refined: the presence of O ions at the centre of the tetrahedra of B-sites (8a sites). Due to the proximity of O(2) and 8a sites, it is possible for an O(2) ion to migrate to an 8a site in the presence of disorder. In the Bragg refinement, this displacement was refined by decreasing the concentration of O(2) ions and increasing the concentration of 8a ions. This resulted in a small improvement of the refinement, mostly visible in bank 1, as figure 4.7 shows. Furthermore, the inclusion of this displacement decreased the Bragg R-factor of

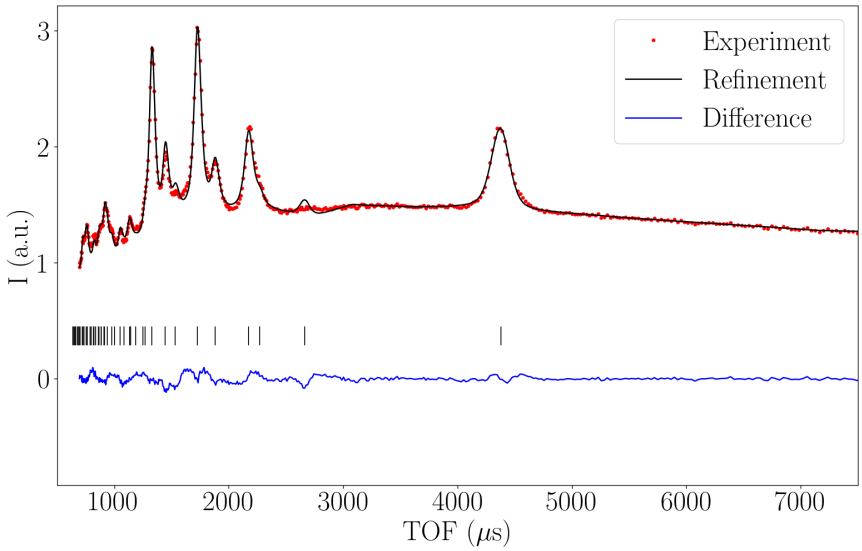

(a)

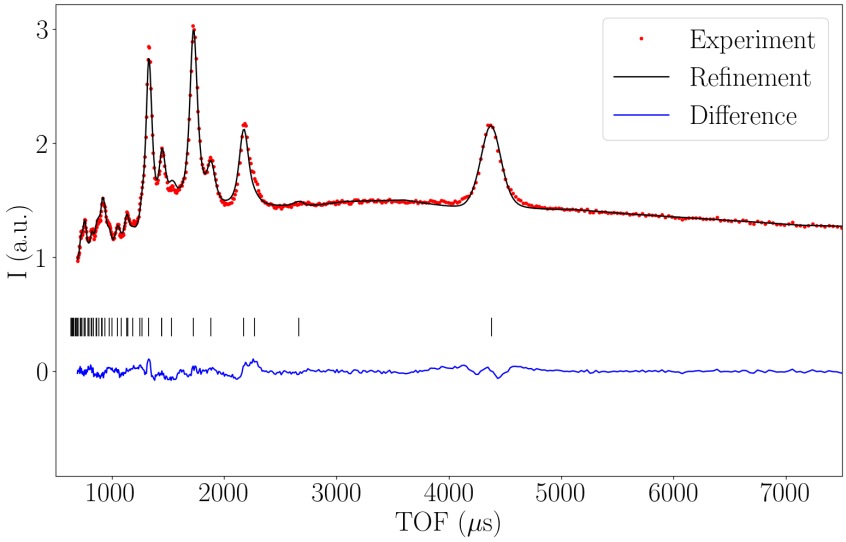

(b)

Figure 4.6: Bragg refinement of the $x = 0.5$ HTSO data from bank 1 using (a) O(1) vacancies and (b) O(2) vacancies. The black vertical markers are the Bragg positions.

the bank 1 fit to 1.71%. This confirms that the origin of the disorder in this system arises from both, the removal of O(2) ions and the displacement of extra O(2) ions to the 8a site. A representation of this is shown in figure 4.8. The inclusion of O(2) ions displacing to the 8a sites was also tested in the O(1) vacancy model, but this only decreased the intensity of the 2700 μs peak by a small amount. Table 4.1 shows the concentration of the vacancies as well as other refined parameters. The final Sc concentration of 23.4%, equivalent to $x = 0.468$ in the sample formula, is close to the nominal 25% that was initially expected.

The possibilities of an extra phase appearing in this system due to the migration of O(2) ions to 8a sites was disregarded, since no new Bragg peaks appear. Finally, all the peaks follow the same width relation, unlike the case of $Ho_2\,(Ti_{1.33}Ho_{0.67})\,O_{6.67}$ studied by Lau *et al.* [27], where there is a mixture of sharp fluorite peaks and broad peaks from small domains of pyrochlore. This is a good indication that the system is formed fully by a pyrochlore phase, and there is no phase mixing of pyrochlore and fluorite. Finally, the

Table 4.1: Refined parameters of all 3 HTSO samples studied.

	$x = 0.5$ HTSO sample	$x = 0.1$ HTSO sample	$x = 0.0$ HTSO sample
Lattice parameter (Å)	10.15(2)	10.10(4)	10.10(6)
x coordinate	0.334(1)	0.329(4)	0.330(1)
Sc concentration (%)	23.4(2)	3.28(1)	–
O(2) vacancy concentration (%)	3.9(2)	0.64(5)	0.52(8)
O(2) ions displaced (%)	0.65(9)	0.13(5)	0.11(6)
R_{Bragg} (bank 1)	1.71%	1.14%	1.87%

possibility of intersite mixing between the Ho and Ti/Sc ions was also considered in the O(1) and O(2) vacancy model, but the Bragg refinement was not able to detect any.

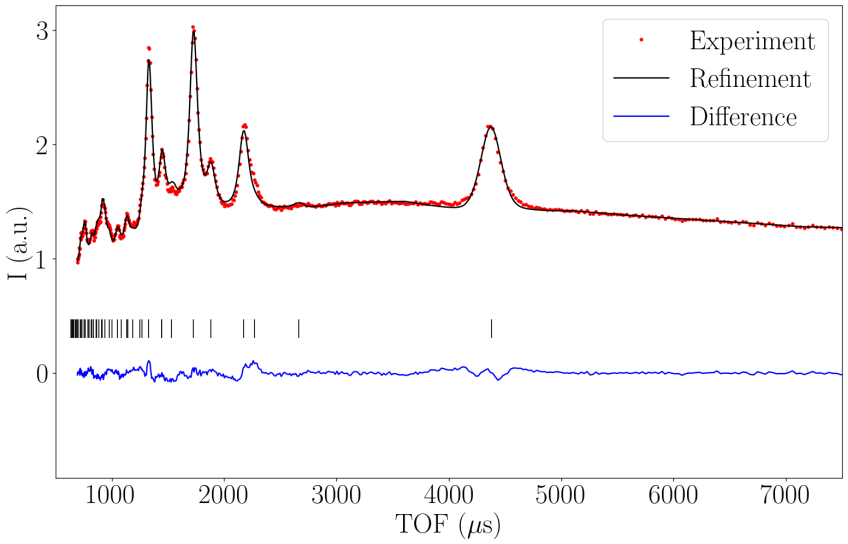

(a)

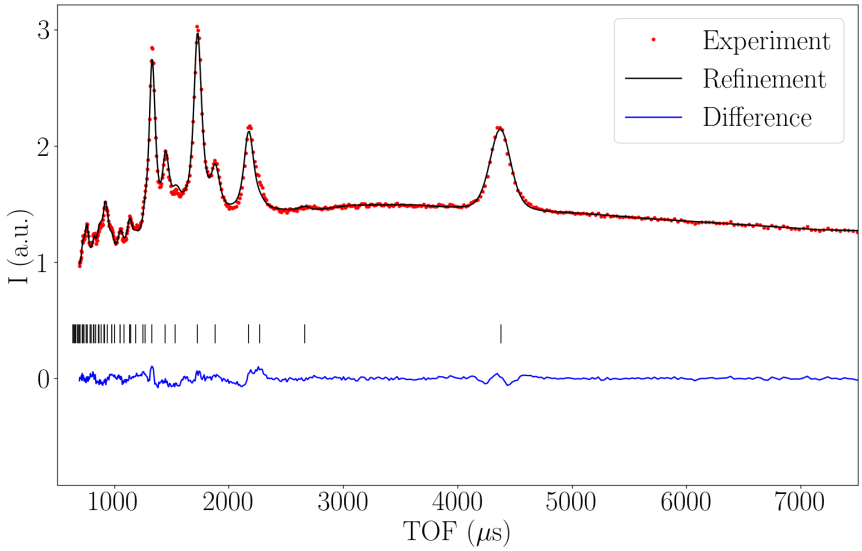

(b)

Figure 4.7: Bragg refinement of the $x = 0.5$ HTSO data from bank 1 using O(2) vacancies (a) with out and (b) with extra O(2) ions displaced to the 8a sites. The black vertical markers are the Bragg positions.

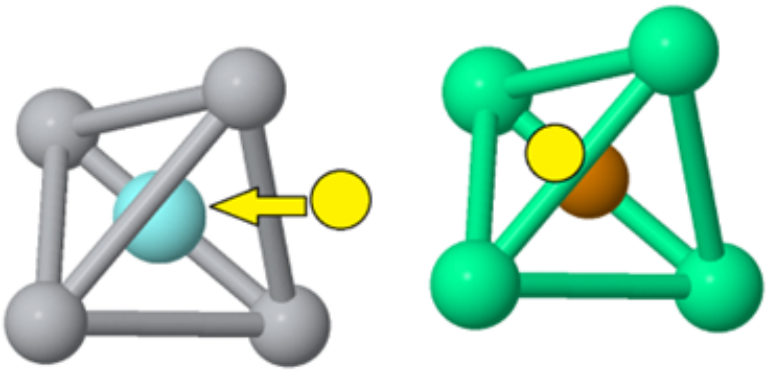

Figure 4.8: Disorder model. Green is the A sites, grey the B sites, brown the O(1) site, blue the 8a site, yellow the vacancies and the arrow indicates the displacement direction.

A similar process was followed with the $x = 0.1$ HTSO data, refining the same parameters as with the $x = 0.5$ HTSO sample with O(1) and O(2) vacancies and with O(2) displacements to 8a sites. As figure 4.9 shows for detector banks 1 and 5, both models produce very similar fits to the data. Furthermore, the resulting Bragg R-factors were also very similar, with the O(1) model R_{Bragg} (0.9%) being marginally smaller than the O(2) model R_{Bragg} (1.1%) for bank 1, but vice versa for bank 5 (4% for the O(1) vacancy model and 3.8% for the O(2) vacancy model). The main difference between both models was found in the vacancy concentration, 0.64(5)% for the O(2) vacancy model and 3.0(1)% for

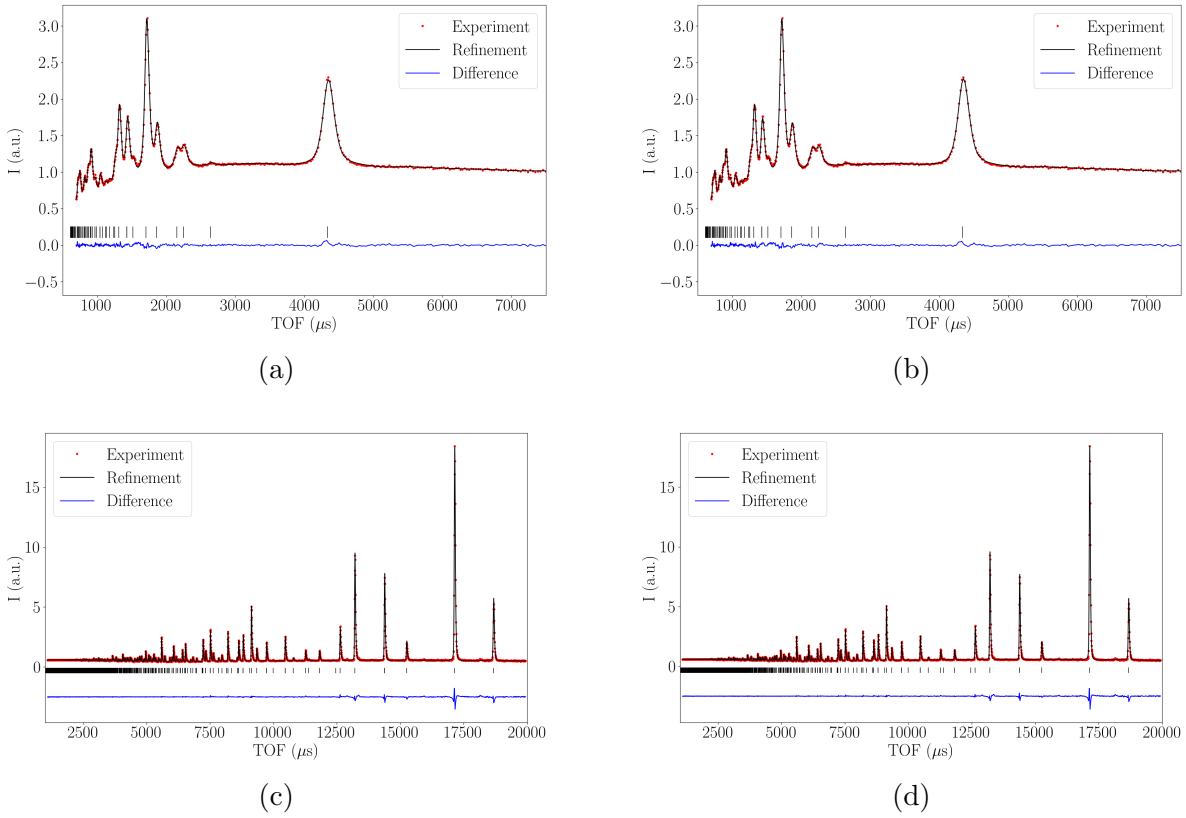

Figure 4.9: Bragg refinement of the $x = 0.1$ HTSO data from bank 1 using (a) O(1) vacancies and (b) O(2) vacancies, and from bank 5 using (c) O(1) vacancies and (d) O(2) vacancies. In all cases, the displacements of O(2) ions to 8a sites was also refined. The black vertical markers are the Bragg positions.

the O(1) vacancy model. For the $x = 0.1$ HTSO system, the expected nominal vacancy concentrations would be 0.83% for O(2) vacancies or 5% for O(1) vacancies. Since the O(2) vacancy model produced a value that is closer to the expected concentration, and due to the Bragg refinement of the $x = 0.5$ HTSO system suggesting O(2) vacancies, it was assumed that the $x = 0.1$ HTSO system also contains O(2) vacancies, with an extra 0.13(5)% of O(2) ions moving towards the 8a sites. Finally, and just as with the $x = 0.5$ HTSO system, no intersite mixing between the A and B sites was found. Table 4.1 shows the concentration of the vacancies as well as other refined parameters. In addition, a refinement was performed assuming a perfect crystal with no vacancies and Sc ions, resulting in a Bragg R-factors of 5.06% and 5.51% for banks 1 and 5 respectively.

The $x = 0.0$ HTSO sample was also refined following a similar process, but with no Sc doping and thus no constraint on the O(1) and O(2) concentration. This refinement was performed to determine if the sample studied had any significant intrinsic disorder that could affect the crystal electric field measurements that will be discussed in the following chapter. The presence of vacancies was considered in this system, since previous studies on the related system $Dy_2Ti_2O_7$ by Sala *et al.* [223] inferred a small concentration of O(1) vacancies. The final fits are shown in figure 4.10. Just as with the $x = 0.1$ HTSO system, both models produce very similar fits to the data, with the Bragg R-factor being smaller for the O(2) vacancy model (1.86% with O(2) vacancies over 1.93% with O(1) vacancies for bank 1 and 3.27% with O(2) vacancies over 3.52% with O(1) vacancies for bank 5). Furthermore, the O(2) vacancy model predicted a 0.52(8)% vacancy concentration,

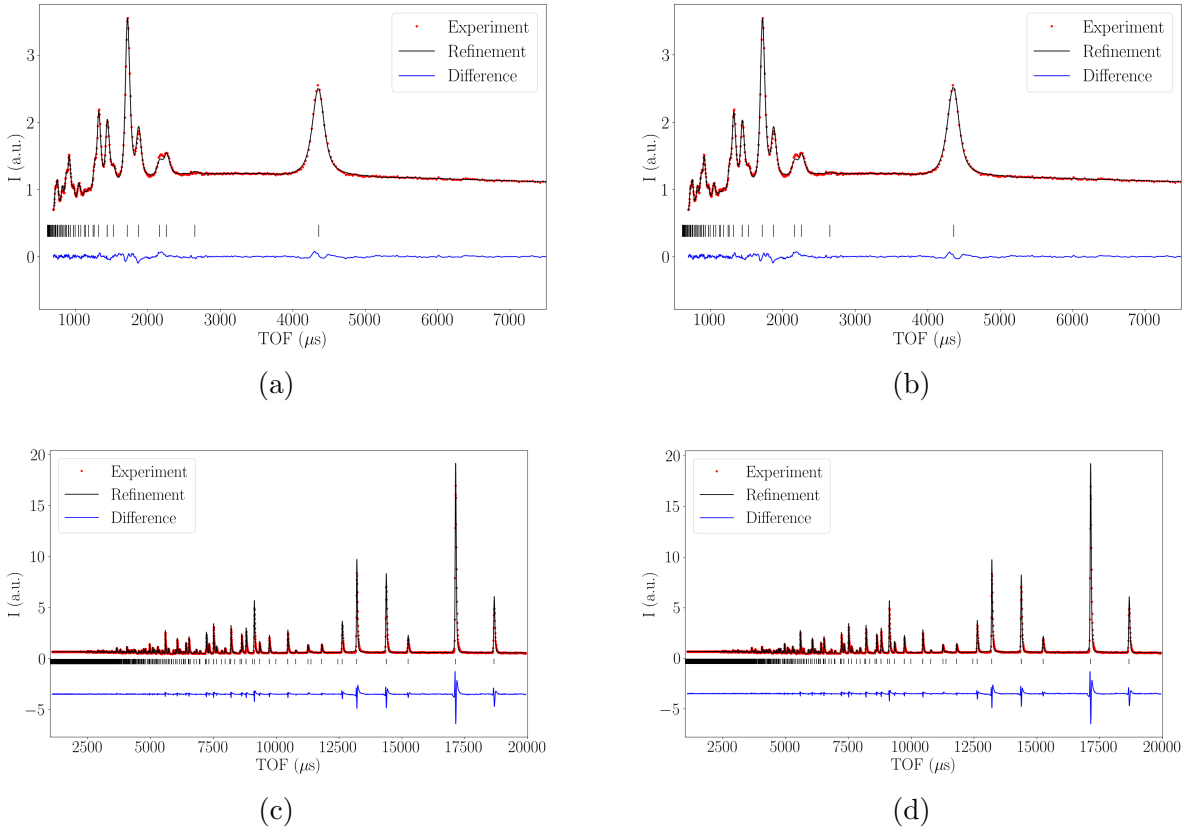

Figure 4.10: Bragg refinement of the $x = 0.0$ HTSO data from bank 1 using (a) O(1) vacancies and (b) O(2) vacancies, and from bank 5 using (c) O(1) vacancies and (d) O(2) vacancies. In all cases, the displacements of O(2) ions to 8a sites was also refined. The black vertical markers are the Bragg positions.

while the O(1) vacancy model predicted a 2.80(5)% vacancy concentration, similar to the concentrations found for the $x = 0.1$ HTSO system. Such similarities explain why the measured data of both systems are so similar. Due to the likeness to the $x = 0.1$ HTSO system, and the results from the $x = 0.5$ HTSO system Bragg refinement, it was concluded that the $x = 0.0$ HTSO system also contains O(2) vacancies, with an extra 0.11(6)% of O(2) ions moving towards the 8a sites. Lastly, and just as with the $x = 0.5$ HTSO system, no intersite mixing between the A and B sites was found. Table 4.1 shows the concentration of the vacancies as well as other refined parameters. In addition, a refinement was performed assuming a perfect crystal with no vacancies and Sc ions, resulting in a Bragg R-factors of 2.48% and 3.25% for banks 1 and 5 respectively. The fact that these Bragg R-factors are close to the ones achieved when a small concentration of vacancies is included is expected, since this is the stoichiometric sample.

With the Bragg refinement finished and knowing the concentration of Sc and vacancies in all three samples, the POLARIS ToF experimental data were converted to a Pair Distribution Function (PDF) data as a function of real space r(Å). This conversion was performed by Helen Playford, one of POLARIS local contacts. To convert the data, the program GudrunN was used. To do this, not only the experimental data and the Bragg refinement information was used, but extra experimental parameters such as the sample mass, container shape and dimensions, and instrumental calibration parameters were also needed. The PDF (G(r)) and reduced PDF (D(r)) of all three samples are shown in figure 4.11. One of the parameters that the GudrunN program needs is the Fourier filter or Minimum radius. This parameter is used to filter out low-r noise/unphysical features from the PDF, and it has to be below the first correlation length in the sample. From published PDFs of other pyrochlores, it was decided that a minimum radius of 1.6 Å was sufficient.

As it was described in 2.4.2, a PDF shows the correlations in a system or the probability of finding an ion at a distance r from the centre of a random atom. Thus, for an ideal system with no intrinsic or extrinsic disorder with all the unit cells repeating perfectly, the G(r) should be zero with sharp peaks at certain distances. However, in real systems ions are displaced from their ideal position due to vibrations and the presence of disorder, which results in a broadening of the peaks. This is what is observed with the PDF and reduced PDF of the $x = 0.0$ HTSO sample. Similarly, the $x = 0.1$ HTSO sample produced a PDF very similar to the $x = 0.0$ HTSO sample PDF, since the level of disorder is similar to the intrinsic disorder in this system. The main difference between the two is in the reduced size of the peaks in G(r) of the $x = 0.1$ HTSO sample compared to the $x = 0.0$ HTSO sample, due to the presence of Sc ions in the system. On the other hand, the $x = 0.5$ HTSO sample has so much disorder that not only the peaks are much broader than the $x = 0.0$ and $x = 0.1$ HTSO samples, but the locations of the peaks are also shifted due to the presence of large amounts of Sc doping and vacancies, which causes major distortions to the position of the nearest neighbour ions.

4.3 Structural diffuse scattering measurements

To study the structural diffuse scattering of the $x = 0.5$ HTSO sample in more detail, measurements on a single crystal of this system were performed using the Single-Crystal Diffractometer SXD at ISIS. This allowed us to measure volumes of reciprocal space, giving access to the structural diffuse scattering in any plane in the volume. As such, there is no need to insert the crystal in any particular orientation. Measurements were performed at

30 K and room temperature. At 30 K, the measurements were performed by rotating the crystal in steps of 20°, with each orientation measuring for 1.5 hours. This was enough to cover all the gaps in between the detectors. On the basis of these data, it was decided that a 40° step size, also each orientation being measured for 1.5 hours, would be sufficient at room temperature. The single crystal was grown by Dharmalingam Prabhakaran using the floating zone method at the Clarendon Laboratory, Oxford University. The data was treated using the SXD2001 software developed by Matthias Gutmann, local contact for SXD, where measurements of the background and a vanadium standard sample are used to process the data. In this program, all the orientations measured were combined and the volume was symmetrised using the $Fd\bar{3}m$ symmetry, the appropriate crystal symmetry for this system [6].

The 30 K and room temperature data were compared to see if there was any significant phononic contribution, since phononic effects increase in intensity with temperature, and thus features present at room temperature and not at 30 K could be ignored in the diffuse scattering modelling. However, as figure 4.12 and 4.13 show, the change in diffuse scattering with temperature is negligible, and thus the phononic effects can be ignored. It is worth pointing out that the structural diffuse scattering found in the (h,k,7) plane is very similar to the structural diffuse scattering measured by Sala *et al.* [223] in the

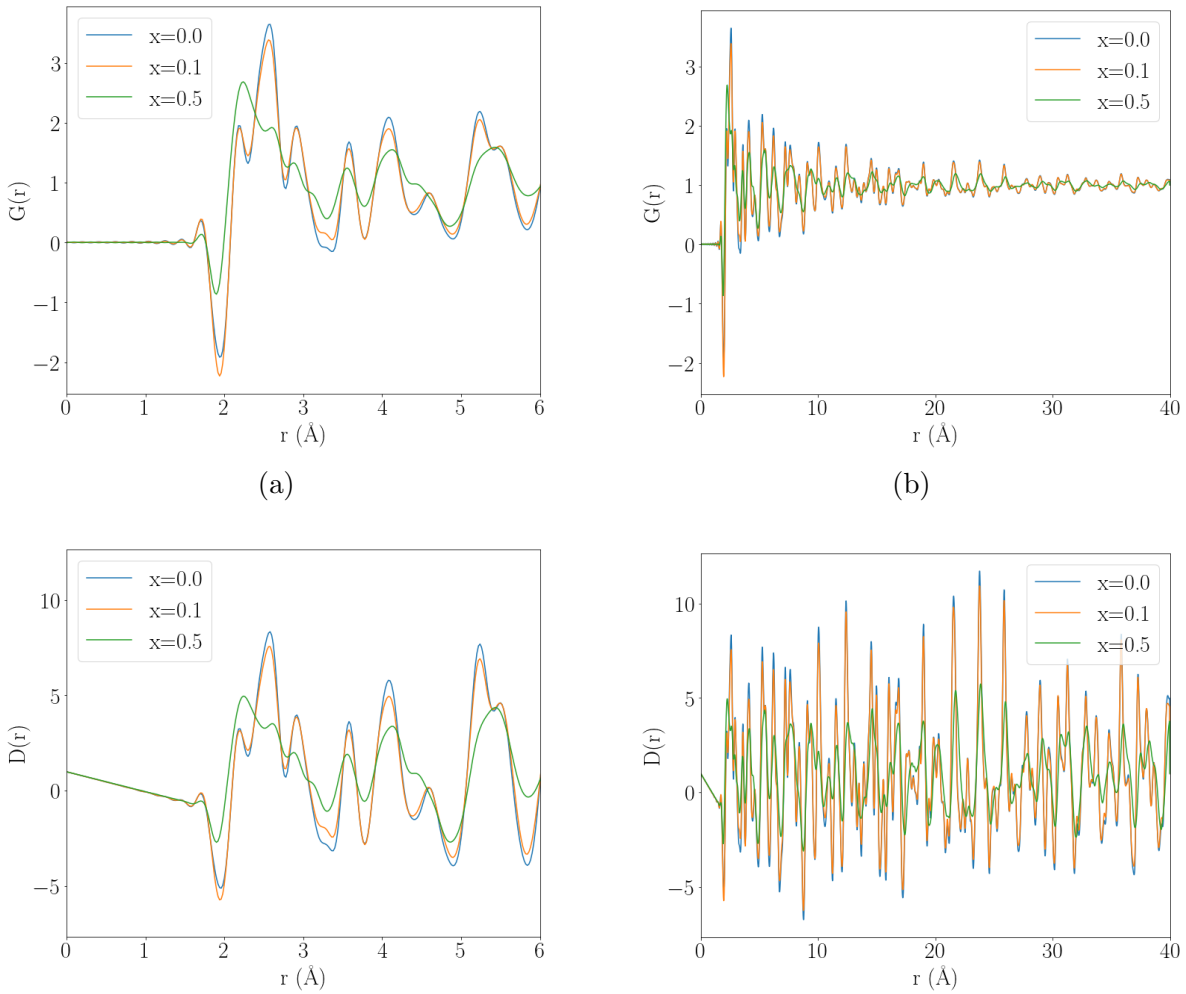

Figure 4.11: (a) and (b) show the PDF (G(r)) and (c) and (d) the reduced PDF (D(r)) of the $x = 0.0$, $x = 0.1$ and $x = 0.5$ HTSO data.

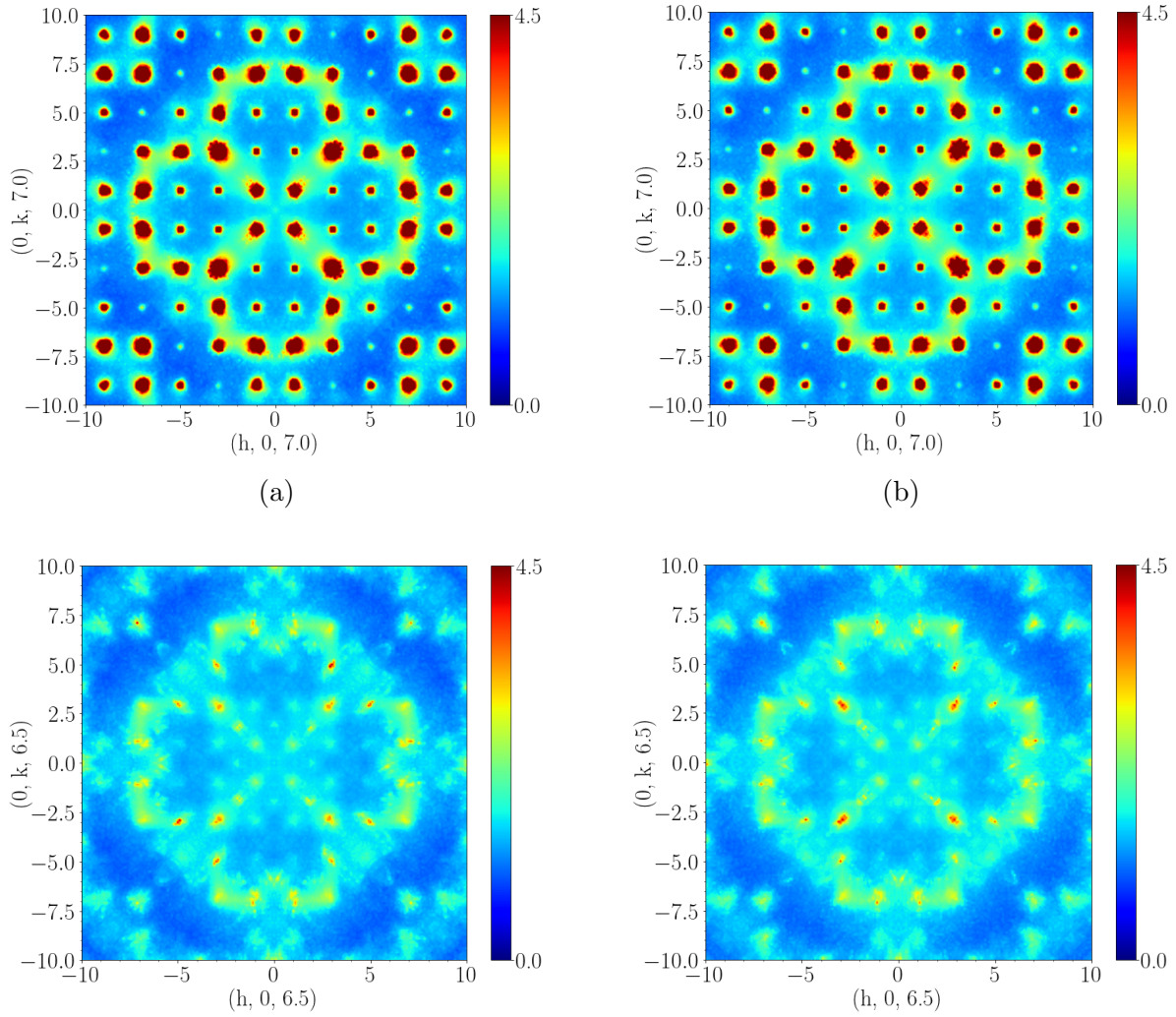

Figure 4.12: Structural diffuse scattering of the $x = 0.5$ HTSO sample acquired with SXD. (a) and (c) show the structural diffuse scattering of the (h,k,7) and (h,k,6.5) planes at 30 K and (b) and (d) the same planes but at room temperature. In this particular comparison, only the orientations measured at 30 K and room temperature are used.

same plane with $Y_2Ti_2O_{7-\delta}$, both producing a very similar figure-of-eight pattern. This was surprising since in this system, Bragg refinements and DFT calculations, described in the following section, predict vacancies at O(2) sites, while Sala *et al.* [223] predicted vacancies at O(1) sites for $Y_2Ti_2O_{7-\delta}$. Nevertheless, some differences do exist between the two, such as more pronounced diffuse scattering around (4,4,7), (6,3,7) and symmetrically equivalent points for the HTSO diffuse scattering, and a less defined figure-of-eigth gap at (0,7,7) and symmetrically equivalent points.

We were also interested in the low Q structural diffuse scattering for later comparison with structural diffuse modelling. To do this, the same crystal was measured with the D7 instrument at the ILL. While with D7 only one plane in reciprocal space can be measured at a time, as opposed to SXD which measures volumes of reciprocal space, the low Q resolution is better, as figure 4.14 shows. Furthermore, the ability to isolate the structural scattering from the paramagnetic background using polarisation analysis greatly improves signal-to-noise and this is particularly helpful at low Q, where the magnetic scattering is strongest. The structural diffuse scattering in the (h,h,l) plane at 220 K acquired with

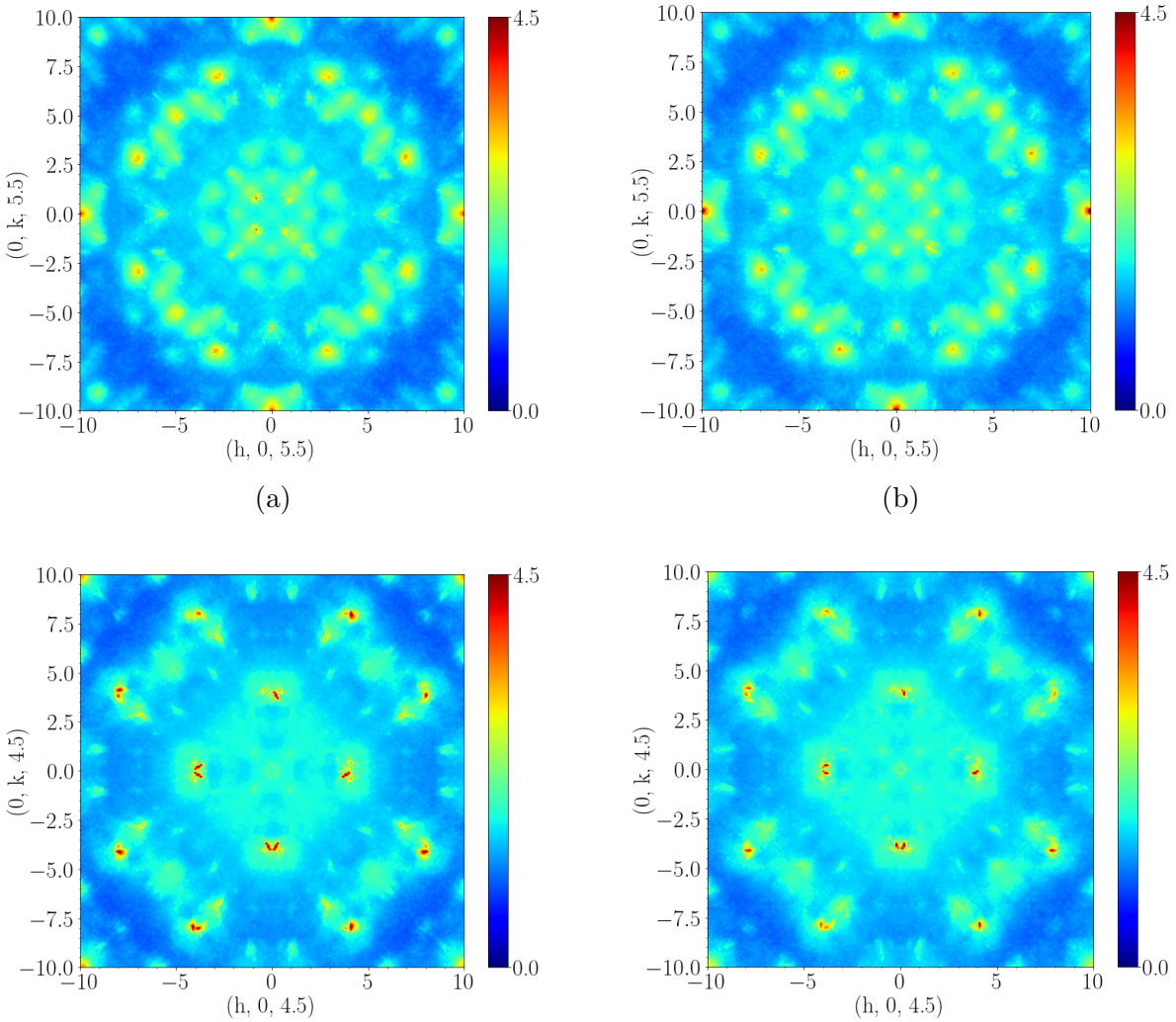

Figure 4.13: Structural diffuse scattering of the $x = 0.5$ HTSO sample acquired with SXD. (a) and (c) show the structural diffuse scattering of the (h,k,5.5) and (h,k,4.5) planes at 30 K and (b) and (d) the same planes but at room temperature. In this particular comparison, only the orientations measured at 30 K and room temperature are used.

D7 is shown in figure 4.14b. More details of the D7 experiment and the data processing will be given when discussing the magnetic diffuse scattering in the following chapter.

4.4 RMC and DFT analysis

To model the diffuse scattering and test if the disorder model from figure 4.8 produces a diffuse scattering like the one measured with SXD and D7, reverse Monte-Carlo (RMC) fits to the diffuse scattering and PDF were performed. To perform these calculations, the program RMCprofile was used [207]. This program, which results from a collaboration between, amongst others, scientists at ISIS and SNS, was chosen because one of the developers is Helen Playford, who was able to provide guidance on which initial settings to use for modelling this system. The way this program works is as follows: an $N_i \times N_j \times N_k$ supercell is created either by the user independently or using an inbuilt subroutine of the program that reads a .cif file (a file that contains the structural information of the system

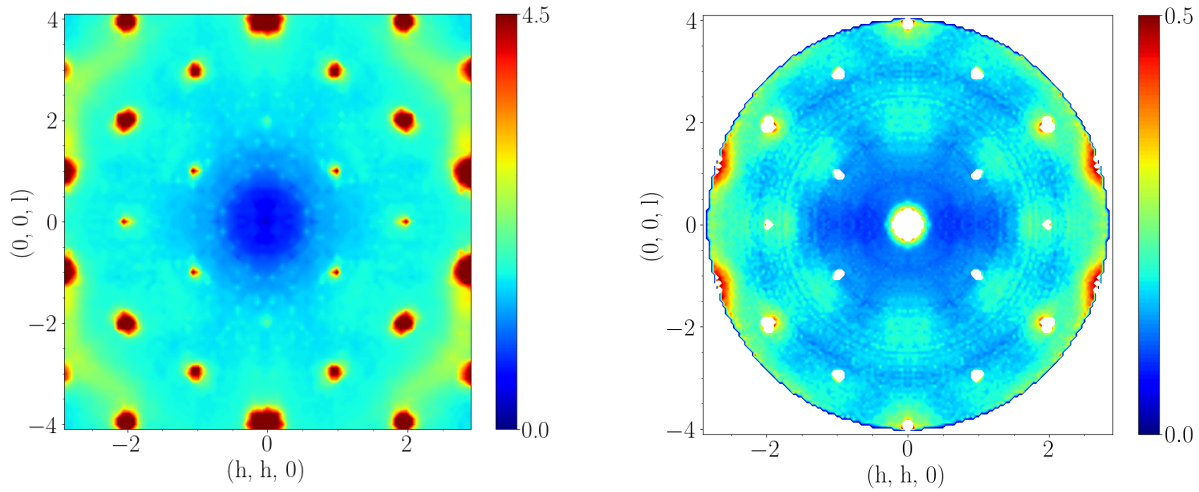

(a) (b)

Figure 4.14: Structural diffuse scattering in the (h,h,l) plane of the $x = 0.5$ HTSO sample. (a) Data acquired with SXD at 30 K and (b) data acquired with D7 at 220 K.

being modelled) and with the information it creates the supercell. This subroutine is useful because the user can specify information such as substituting an ion by another with a certain concentration, or substituting an ion by a vacancy with a certain concentration. Once the supercell is created, the RMC process starts, in which a certain number of ions are displaced in random directions.

Once the ions are displaced, the program calculates aspects specified by the user, such as PDFs and diffuse scattering. The program compares the calculated parameters with the experimental data and if the χ^2 is minimised the displacements are accepted, if not the displacements are accepted with a probability given by $e^{(-\Delta\chi^2/2)}$. RMCprofile is time based, so this process is repeated for an amount of time specified by the user. With RMCprofile, how χ^2 changes with time can be monitored, and its convergence to a constant value can be used to determine how long the program needs to run. In addition to displacing ions, the program also allows swapping ions, meaning that it will also swap the location of two specified ions with a given probability. Finally, the displacement of the ions can be constrained by specifying the max distance an ion can move in each iteration and by specifying the minimum distance between two ions.

For the $x = 0.5$ HTSO system, a $10 \times 10 \times 10$ supercell was created with the concentration of Sc and O(2) vacancies found in the Bragg refinement. Both, the PDF and structural diffuse scattering were fitted simultaneously. An issue with RMC fitting is that, if no constraints are given, the ions will be displaced as much as needed to get a good fit to the experimental data. This can result in unphysical displacements, such as having multiple ions in the same position or ions being displaced long distances. However, in this case, I gave the program enough data to self-constrain the displacement of the ions. The only constraint added was to the vacancies, where it was specified that vacancy sites cannot be displaced, only swapped. With all this information, allowing Ti ions to swap locations with Sc ions and allowing O(2) ions to swap location with vacancies, I found that fitting to the data for 80 hours was enough for the χ^2 to converge to a constant value.

Three different sets of fittings were performed: fitting simultaneously the PDF, the SXD (h,k,7) plane and the SXD (h,k,6.5) plane, fitting simultaneously the PDF, the SXD (h,k,5.5) plane and the SXD (h,k,4.5) plane, and fitting simultaneously the PDF and the

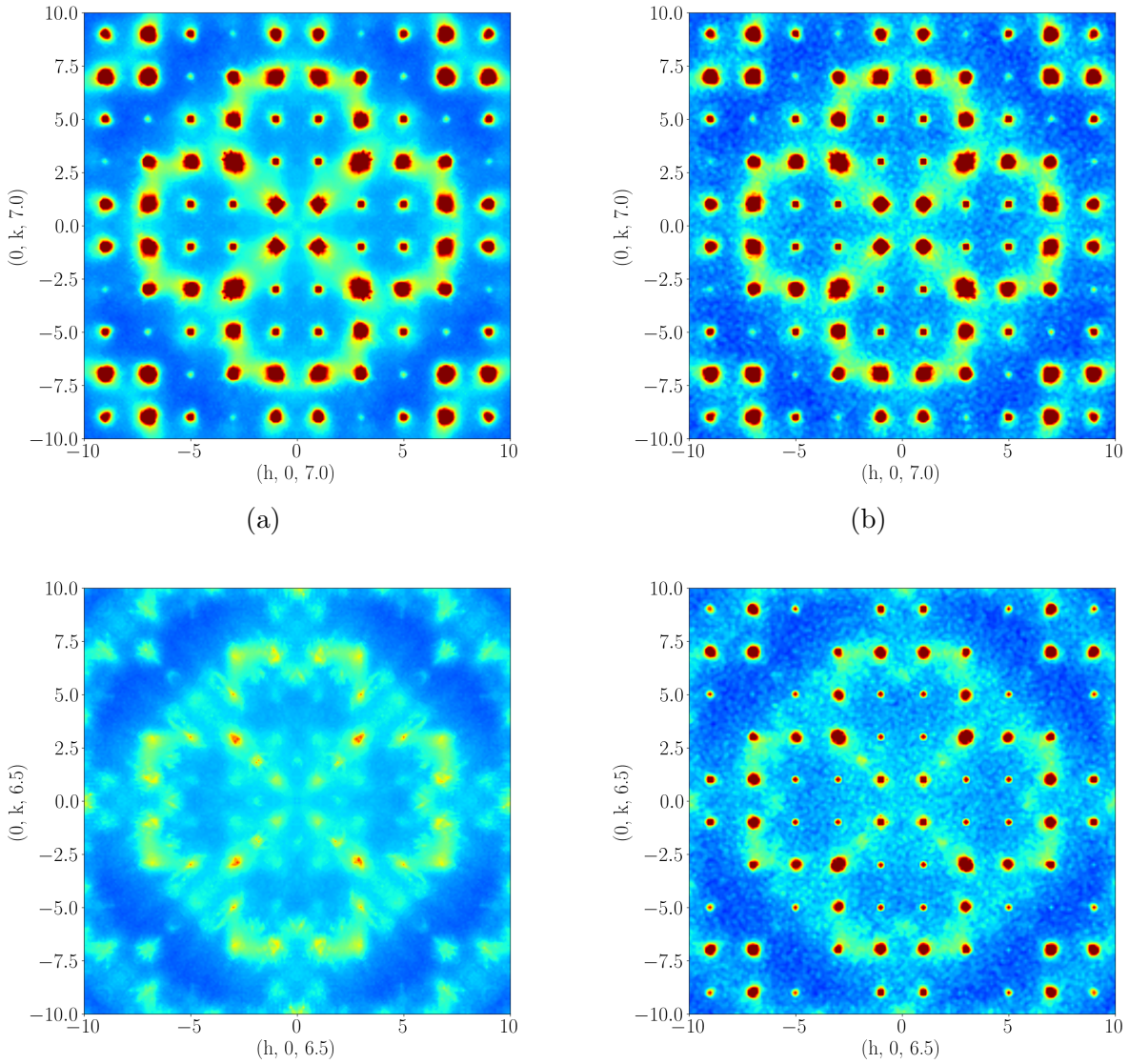

Figure 4.15: RMC fit to the structural diffuse scattering in the (top) (h,k,7) and (botom) (h,k,6.5) planes of the $x = 0.5$ HTSO sample. (left) Experimental data and (right) RMCprofile fit.

D7 (h,h,l) plane. The resulting fits to the diffuse scattering are shown in figures 4.15 to 4.17. The fits to the SXD data are good, reproducing all the main features seen in the experimental data. The biggest difference between the RMC fit and the SXD data is in the (h,k,6.5) data, where the RMC fit produces a set of sharp Bragg peaks that are not present in the experimental data. The (h,k,4.5) and (h,k,5.5) data were fitted simultaneously, and since none of them have Bragg peaks in the experimental data, the RMC program did not reproduce them. However, the (h,k,6.5) data were fitted simultaneously with the (h,k,7) data, which has very pronounced Bragg peaks, and it is possible that the Bragg peak intensity from the (h,k,7) plane leaked into the (h,k,6.5) plane. This was confirmed by doing an RMC fitting just with the (h,k,6.5) data. Finally, the fit to the D7 data is not as good as the fits to the SXD data. It produces vertical and horizontal streaks emanating from the Bragg peaks. This could be artefacts produced by the program when performing fittings to low Q data, since the other planes which are at higher Q values do not have this issue.

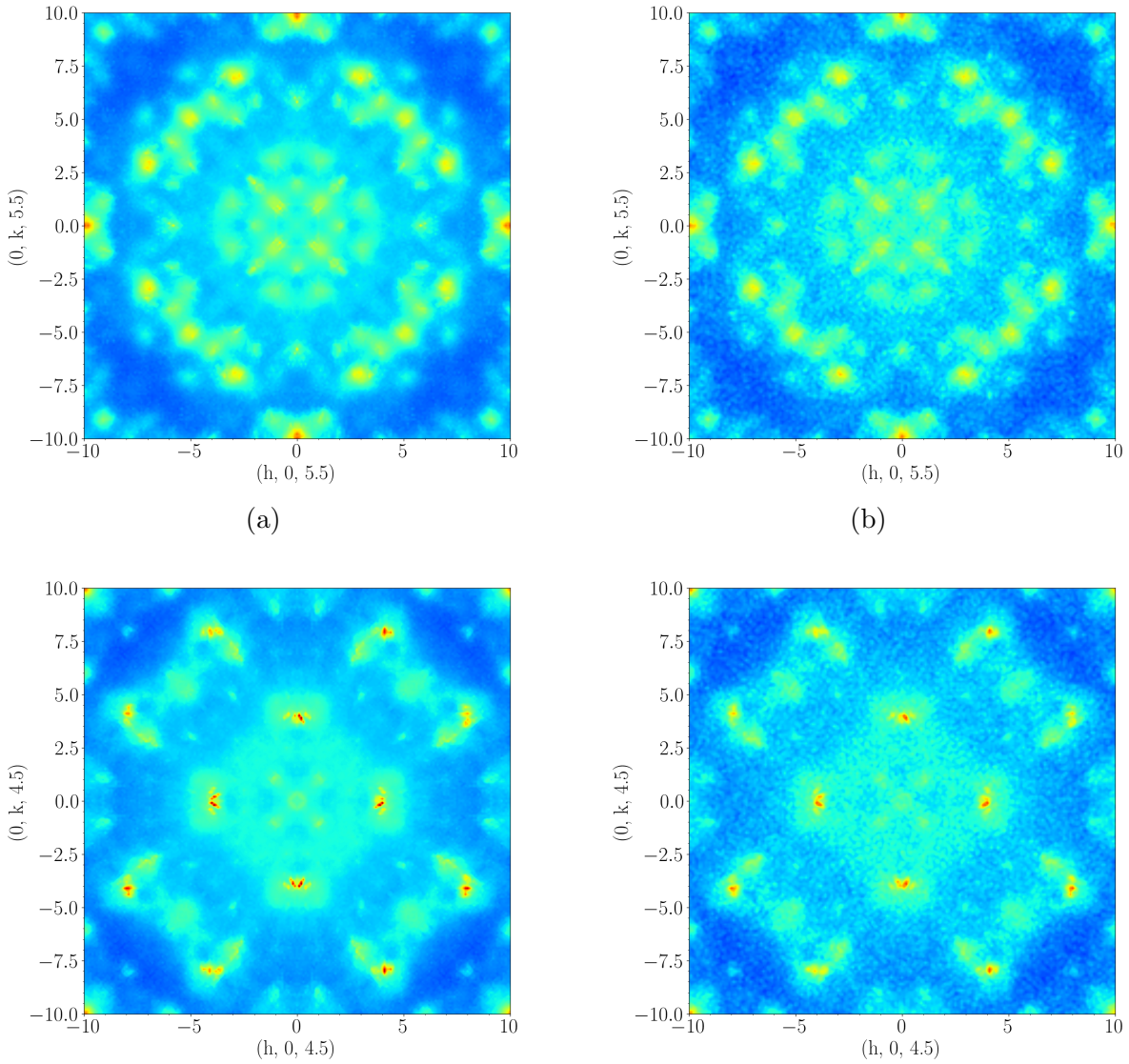

Figure 4.16: RMC fit to the structural diffuse scattering in the (top) (h,k,5.5) and (bottom) (h,k,4.5) planes of the $x = 0.5$ HTSO sample. (left) Experimental data and (right) RMCprofile fit.

Conversely, the resulting fits to the PDFs, shown in figure 4.18, are all very similar independent of the plane, with the PDF fitted with the (h,h,l) plane marginally better than the other two. The PDF fit performed with the (h,h,l) plane being the best one was a surprise, since the diffuse scattering is the worst when compared with the other two calculations. A reason behind this could be due to the weighting given by the program in the calculation. The RMCprofile program was set up so that the χ^2 contribution from the PDF and diffuse scattering was weighted differently, and in each iteration the program changed the weighting automatically. Thus, it is possible that the RMCprofile program gave more weighting to the PDF since it was unable to get a good fit to the (h,h,l) diffuse scattering. Finally, bond length distributions, examples of which will be shown later when discussing the DFT calculations, were examined. All three calculations produced the same bond length distributions. This comparison was performed to confirm that all three calculations had the same minima, and that the RMC did not have different solutions for each scattering plane.

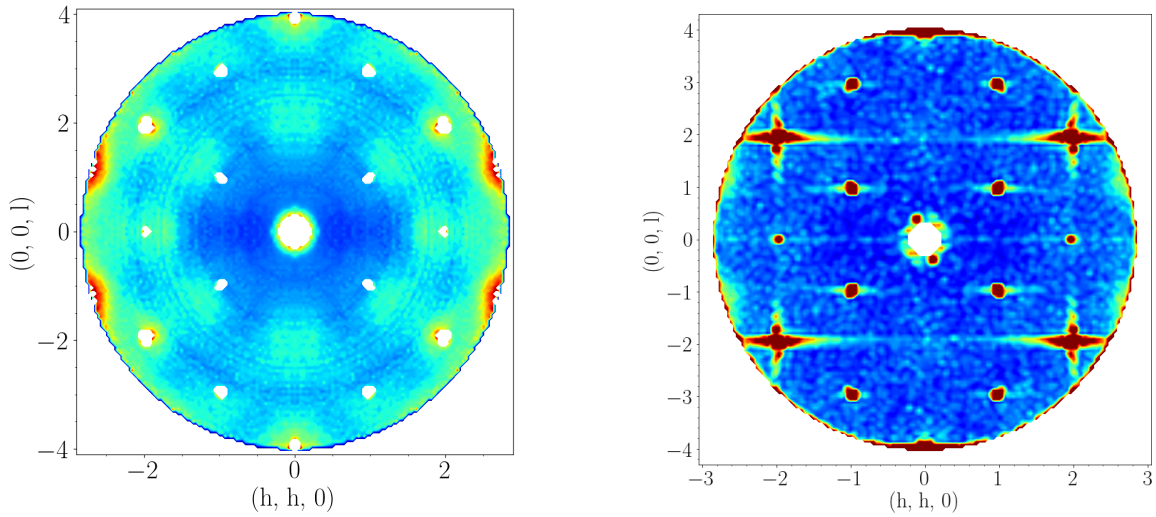

(a) (b)

Figure 4.17: RMC fit to the structural diffuse scattering in the (h,h,l) plane of the $x = 0.5$ HTSO data. (a) Experimental data and (b) RMCprofile fit.

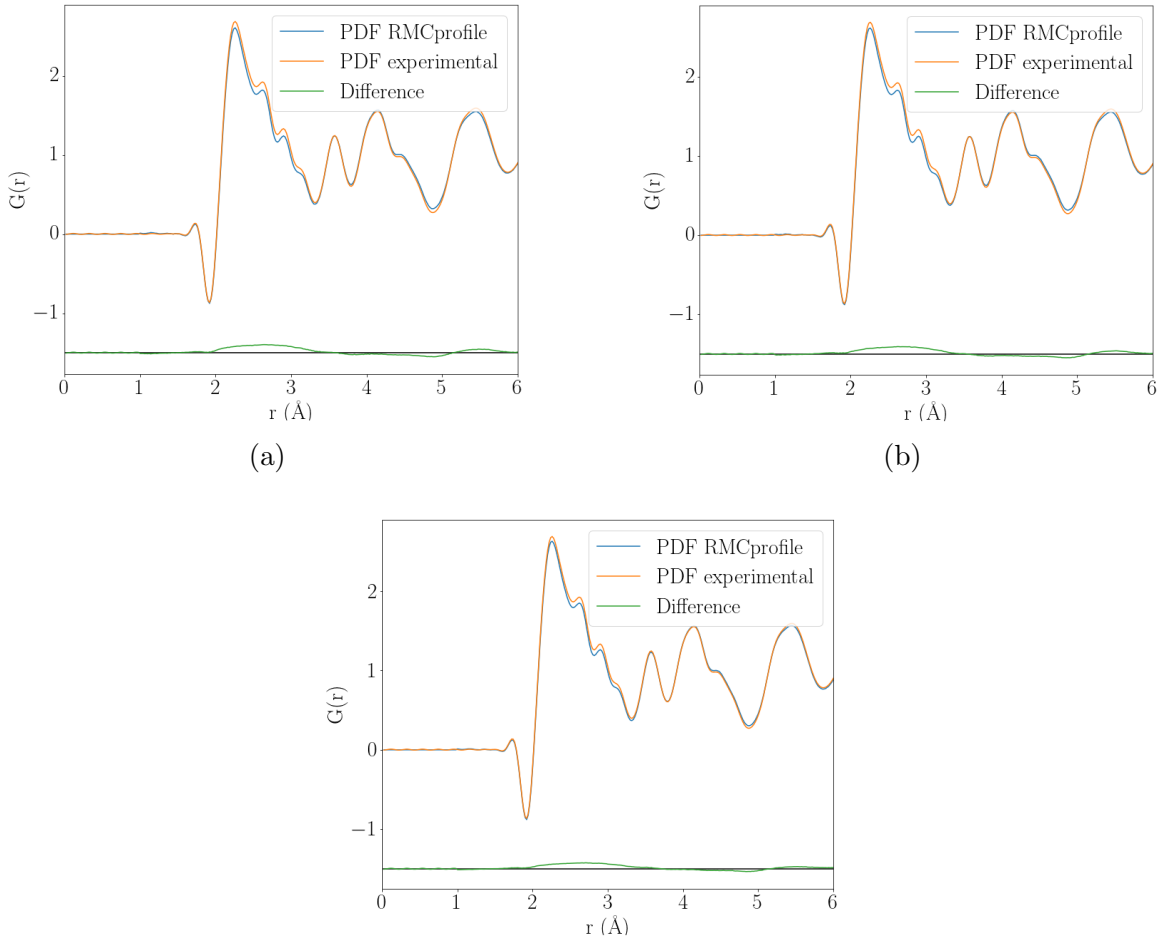

(a) (b)

(c)

Figure 4.18: RMCprofile fit to the PDF of the $x = 0.5$ HTSO system. (a) PDF fitted with the SXD (h,k,7) and (h,k,6.5) planes, (b) PDF fitted with the SXD (h,k,5.5) and (h,k,4.5) planes and (c) PDF fitted with the D7 (h,h,l) plane.

In addition to the RMC fits, density functional theory (DFT) calculations were also performed to model the diffuse scattering of the $x = 0.5$ HTSO system. The calculations were performed using Y instead of Ho, since Y is much lighter than Ho and non-magnetic, and thus the calculations converge faster. These calculations were performed by Thomas Hicken from Royal Holloway University of London. DFT calculations are *ab initio* calculations, meaning that, other than the starting structure, there are no assumptions from the user. In the calculations, a single unit cell of $Y_2Ti_2O_7$ was used with two Ti ions changed by Sc ions and with one O vacancy. 47 inequivalent ways exist of substituting two Ti ions by two Sc ions and removing an O ion. All the DFT calculations with an O(2) vacancy produced a lower energy than the calculations with an O(1) vacancy. Furthermore, the configuration that produced the lowest DFT energy also contained an O(2) ion displaced towards an 8a site. This is in perfect agreement with the Bragg refinements.

With this disordered structure, the structural diffuse scattering was computed by using the difference method described in section 2.4.1, but instead of using the scattering length of Y, using the scattering length of Ho. In this case, the structure that was being subtracted was one with a perfect $Ho_2Ti_2O_7$. This is equivalent to assuming that the size of the disordered region is comparable to the conventional unit cell, with the rest of the lattice taken to be a perfect $Ho_2Ti_2O_7$ structure. Since this disordered structure will be present in the real system in any possible allowed orientation, multiple calculations were performed with the unit cell of the disordered structure in all 48 allowed symmetrically equivalent orientations, with all the calculated patterns added incoherently. The resulting diffuse scattering is shown in figure 4.19. For an *ab initio* calculation and using Y instead of Ho, DFT is in remarkably good agreement with the experimental diffuse scattering, capturing all the features in the (h,h,l) plane, and it is in some qualitative agreement with the scattering for (h,k,7). There are some subtle differences between both, such as the calculations around (1,1,1) in the (h,h,l) plane predicting diffuse scattering closer to the origin than the experimental data, and as Q increases, this differences becomes more pronounced.

Figure 4.20 shows a comparison between the Sc-O(2) and Ti-O(2) bond length distributions predicted by DFT and the RMC fit. Only the occupied O(2) sites were used to extract the distributions, the vacant sites were ignored. Both calculations predict very similar displacements, showing consistency between the different types of procedures used to model the data. Furthermore, figure 4.20 shows the change in the B-O(2) bond length when disorder is introduced. While most of the Ti ions have not changed, still maintaining the stoichiometric Ti-O(2) bond length, there is a clear increase in the Sc-O(2) bond length. This increase is most likely due to the increase in ionic radius of the Sc ion compared to Ti [225] and the decrease in charge.

Finally, both the RMC fits and DFT calculations suggest that there is no particular Sc–Sc correlation. The resulting RMC calculations suggest that the Sc ions are distributed on the B-site tetrahedra randomly, with most of the tetrahedra having either one or no Sc ions, and very few having two or three. This was confirmed by performing a separate calculation where Sc ions were inserted on the B sites of a pyrochlore randomly. The resulting Sc distribution in each tetrahedron matched the RMC fits prediction. Similarly, the DFT is able to reproduce the experimental data using isolated cluster models (isolated clusters of two Sc ions and one vacancy), which is consistent with random occupation of Sc sites. Furthermore, there is nothing in the experimental data to suggest that there are any Sc correlations such as sharper superlattice reflections, so a random distribution of Sc ions on the B sites seems to be a good assumption.

4.5 Summary

The effect of disorder on $Ho_2Ti_2O_7$ was studied by doping with Sc ions, which resulted in the introduction of charge compensating oxygen vacancies. Total scattering measurements on $Ho_2Ti_{2-x}Sc_xO_{7-x/2}$ (HTSO) with $x = 0.0$, $x = 0.1$ and $x = 0.5$ were performed using the POLARIS instrument from ISIS. The resulting data showed that while the $x = 0.0$ and $x = 0.5$ HTSO samples produced very different scattering, the $x = 0.1$ HTSO sample produced scattering very similar to the $x = 0.0$ HTSO sample. Bragg refinements were performed to determine the location of the vacancies. With the $x = 0.5$ HTSO system, not only was it found that the vacancies are located at O(2) sites, with a concentration of 3.9%, close to the nominal 4.17% that was initially expected, but an extra 0.65% of different O(2) were displaced towards the centre of the tetrahedra formed by the B-sites, known as an 8a site. On the other hand, the Bragg refinements performed to

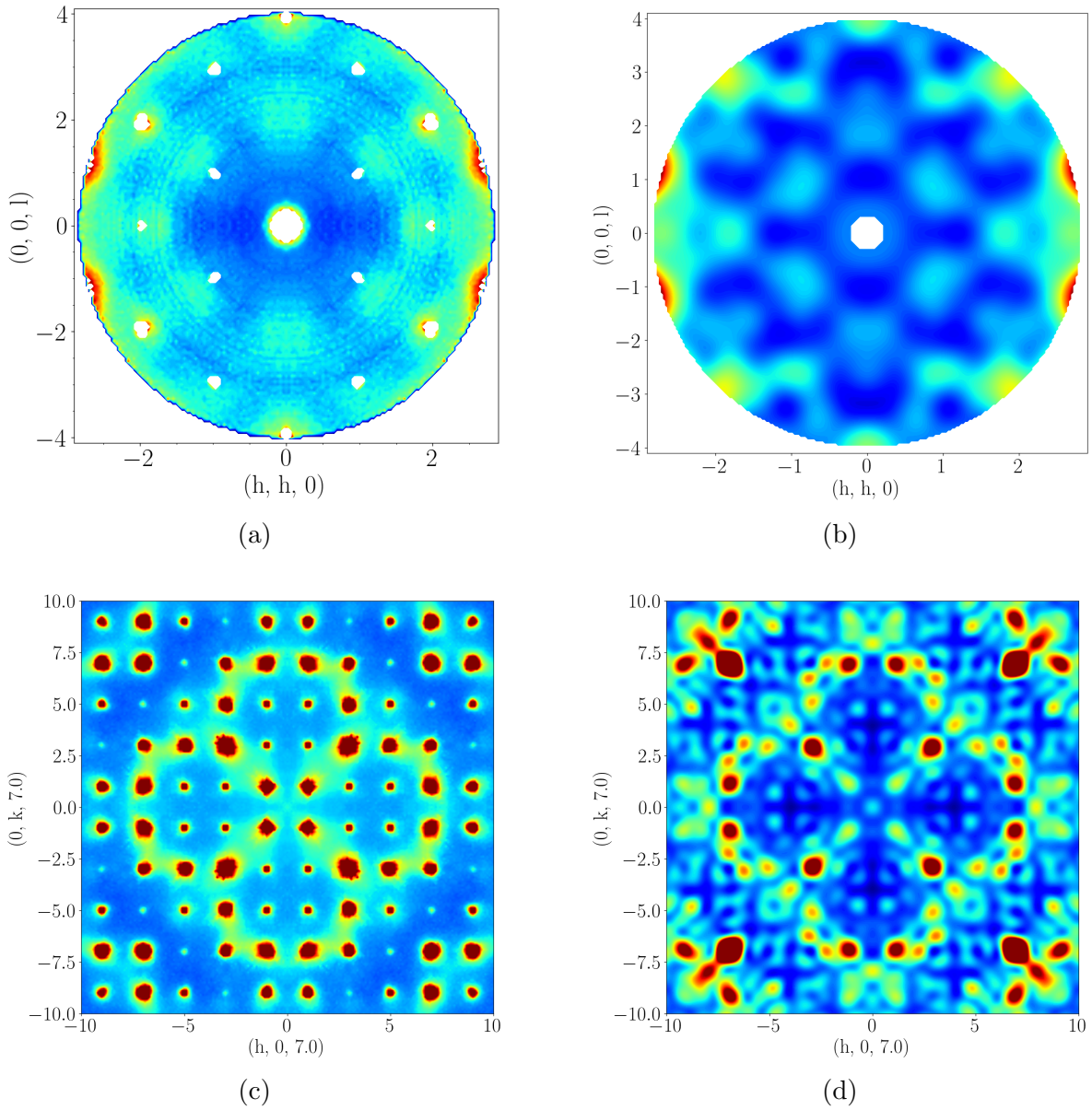

Figure 4.19: Comparison between the (left) experimental structural diffuse scattering and (right) the DFT calculations. (Top) shows the (h,h,l) plane at 220 K and (bottom) the (h,k,7) plane at 30 K.

the $x = 0.0$ and $x = 0.1$ HTSO data produced very similar results if either O(1) or O(2) vacancies were chosen, with the percentage of O(2) vacancies being marginally closer to the nominal expected values. Because of this and from the results from the refinement to the $x = 0.5$ HTSO data, it was concluded that the $x = 0.0$ and $x = 0.1$ HTSO samples also contained O(2) vacancies.

The Bragg refinements and total scattering data were used to extract the pair distribution functions (PDFs) of all three samples. The PDF data of the $x = 0.5$ HTSO sample was used in conjunction with structural diffuse scattering acquired with SXD from ISIS and D7 from the ILL to perform RMC fits. While the resulting calculations produced excellent fits to planes at large (h,k,l) values, the fit to the (h,h,l) plane did not reproduce all the features, producing streaks emanating from Bragg peaks. The reason behind this is unknown, but it is suspected to be an artefact of the fitting program.

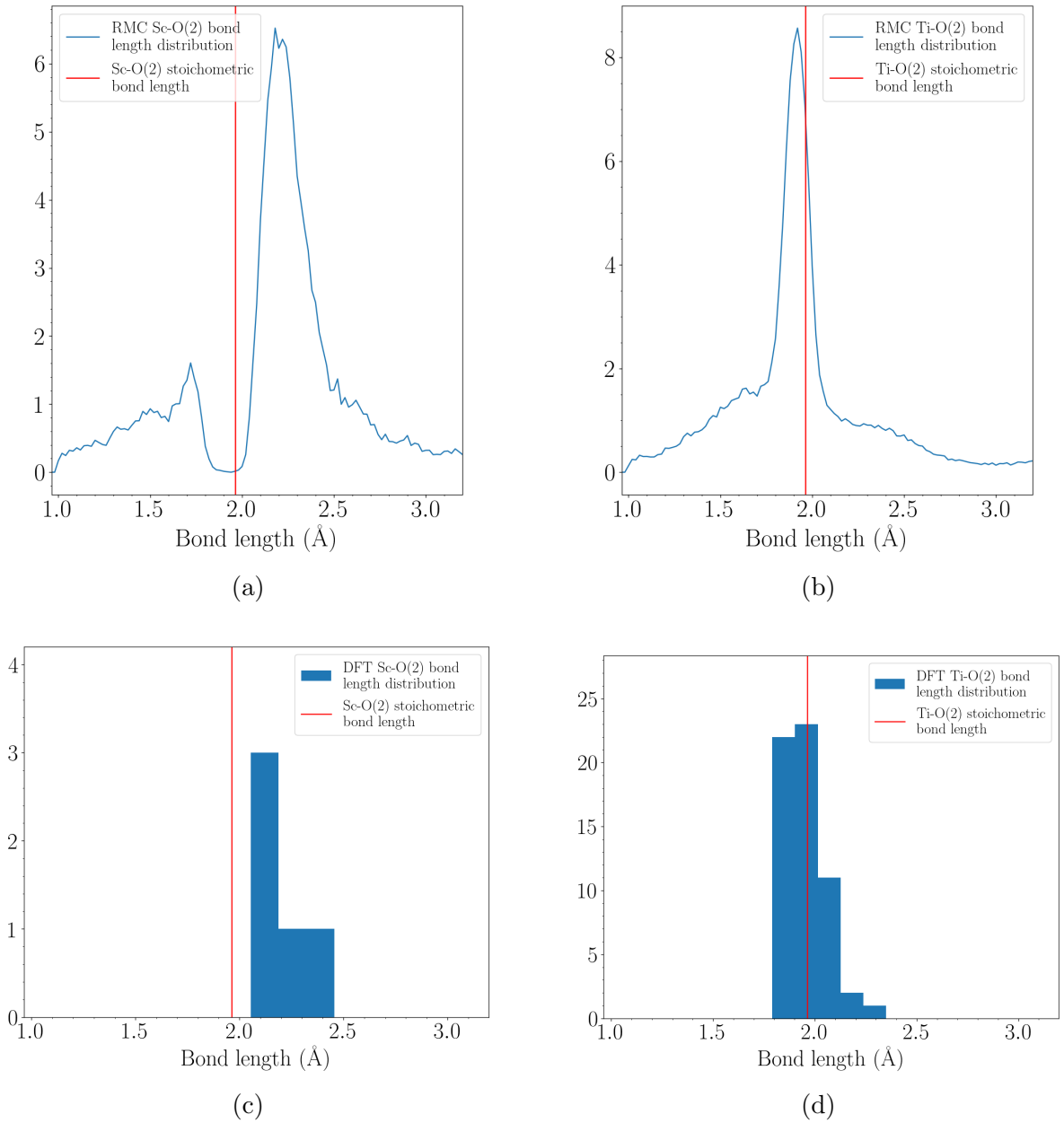

Figure 4.20: Comparison between the RMC fit (up) and DFT (down) bond length distributions for the (left) Sc-O(2) bond lengths and (right) Ti-O(2) bond lengths.

In conjunction to this, density functional theory (DFT) calculations of a unit cell of $Y_2Ti_2O_7$ were performed, but with two Ti ions changed by Sc ions and oxygen vacancies in different locations. It was found that to minimise the energy of the system, an O(2) vacancy and an O(2) displacement to an 8a site is needed, in perfect agreement with the Bragg refinements. Structural diffuse scattering calculations were performed using the disordered structure predicted by the DFT calculation, which were in remarkably good agreement with the experimental data. Finally, both the RMC and DFT do not predict any kind of Sc–Sc correlation, suggesting that the Sc ions are distributed randomly in the B-site tetrahedra.

Chapter 5

Magnetic disorder in $Ho_2Ti_{2-x}Sc_xO_{7-x/2}$

The effect of structural disorder on the magnetic properties of $Ho_2Ti_2O_7$ was studied by the introduction of Sc ions and oxygen vacancies. Crystal electric field (CEF) measurements of $Ho_2Ti_{2-x}Sc_xO_{7-x/2}$ (HTSO) with $x = 0.0$, $x = 0.1$ and $x = 0.5$ were performed using the MARI spectrometer from ISIS to study the effect of the vacancies on the CEF levels of Ho. It was found that the presence of vacancies produced a weak splitting of the ground state doublet of the Ho ions into two singlets separated by an energy of 0.12 meV. Due to the small energy difference between the new ground state and first excited state, it was found through magnetisation calculations that an applied field of 0.1 T is strong enough to mix the ground and first excited sates generating a moment that points along the line connecting the centres of tetrahedra, but with a tilt towards the location of the vacancy. Thus, it is possible that the internal exchange and dipolar fields are strong enough to produce these same effects on the Ho ions next to a vacancy. Magnetic diffuse scattering measurements performed at 50 mK using D7 at the ILL show that while the scattering from the $x = 0.1$ and $x = 0.5$ HTSO systems is qualitatively very similar to the scattering from the stoichiometric $Ho_2Ti_2O_7$ system measured by Fennell *et al.* [1] and Chang *et al.* [2], the width of the HTSO pinch point increases as the level of Sc doping increases. This is different to the $Ho_{2-x}Y_xTi_2O_7$ system studied by Chang *et al.* [116], where the width of the pinch point did not change with increasing levels of Y. It was proposed that the broadening of the pinch point is caused by the presence of the tilted moments.

5.1 Introduction

Recently, it has been proposed that in $Ho_2Ti_2O_7$ the introduction of disorder leads to new degrees of freedom and the formation of topological spin glasses [226]. Sen *et al.* [226] studied theoretically the $Ho_2Ti_2O_7$ system where some of the Ho ions were replaced by non-magnetic ions. They proposed that instead of modelling this system in terms of the remaining spins, the system could be modelled in terms of the missing spins, as figure 5.1b and 5.1c show. In the case of classical spin ice, the chemical substitution of a magnetic ion by a non-magnetic ion leads to the formation of "ghost" spins. Just like in a semiconductor where removing an electron leaves behind a hole that behaves like an electron, in classical spin ice systems, the removal of a spin leaves behind a ghost spin that behaves similarly to a real spin.

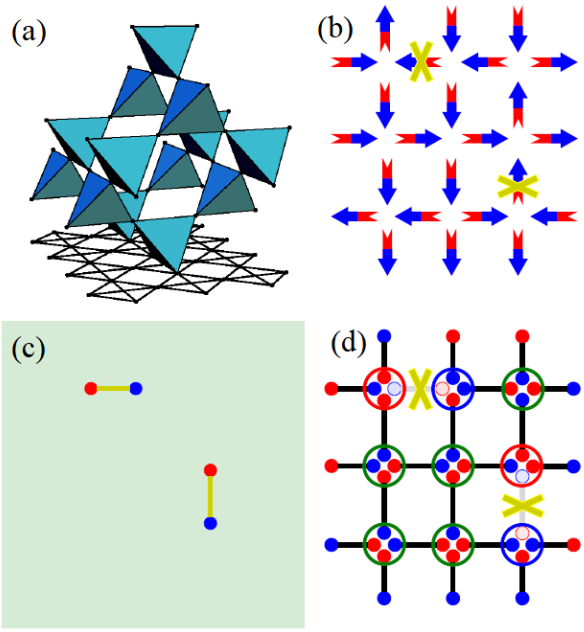

Figure 5.1: (a) Projection of spin ice onto the two-dimensional plane. (b) A spin ice with missing spins (crossed out). (c) A spin ice with missing spins but represented by a small density of ghost spins. (d) Spin ice where the spin have been replaced by dumbbells of equal and opposite magnetic charges (dumbbell model [105]). Figures acquired from [226].

The ghost spins do not disrupt the correlations in spin ice, since they have zero net magnetic charge, so that the pinch points observed in neutron scattering remain intact. This can be understood by the dumbbell model, shown in figure 5.1d. Removing a spin is the same as removing two magnetic charges of opposite sign, which leaves the overall magnetic charge of the system unchanged. This is found to be the case experimentally for the diluted spin ice $Ho_{2-x}Y_xTi_2O_7$ (HYTO) studied by Chang *et al.* [116], with $x = 0.0$, $x = 0.3$ and $x = 1.0$. All three systems produce scattering data very similar to the one shown in figure 5.2a. The similarities with the stoichiometric $x = 0.0$ system are reinforced by the small effect that the Y doping has on the width of the pinch points, as shown in figure 5.2b. Furthermore, the HYTO measurements at 2 K also show a pattern very similar to the one measured by Fennell *et al.* [1] shown in the introductory chapter, showing a crossover from the dipolar spin-ice model (DSM) regime to the nearest neighbour spin ice model (NNSM) regime [68].

The effect of introducing oxygen vacancies and Sc ions on the magnetic properties of the Ho ions was studied in $Ho_2Ti_{2-x}Sc_xO_{7-x/2}$ with $x = 0.0$, $x = 0.1$ and $x = 0.5$. Unlike with $Ho_{2-x}Y_xTi_2O_7$, where the magnetism of particular Ho ions is switched off by replacing them with an Y ion, in this system it is the presence of disorder around the Ho ions which is expected to cause changes to the ground state of Ho. Previous point-charge-model (PCM) calculations performed by Sala *et al.* [223] of the crystal electric field (CEF) energy levels of a Ho in a $Ho_2Ti_2O_7$ next to an O(1) vacancy suggested that these Ho ions become non-magnetic.

This chapter presents neutron scattering data on the disordered spin ice $Ho_2Ti_{2-x}Sc_xO_{7-x/2}$ (HTSO) with $x = 0.0$, $x = 0.1$ and $x = 0.5$. CEF excitation measurements were performed on the three samples in powder form using the MARI spectrometer from ISIS to study the effect of the disorder discussed in the previous chapter on the single-

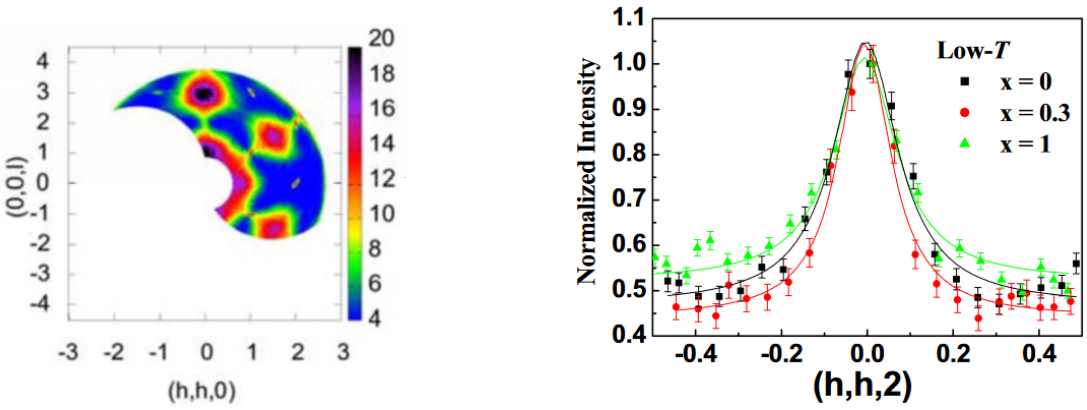

(a) (b)

Figure 5.2: (a) Experimental neutron SF scattering of $Ho_{2-x}Y_xTi_2O_7$ with $x = 0.3$ at 400 mK. (b) Transverse scan of the (0,0,2) pinch point with 3 levels of Y doping extracted from the SF data at low T ($x = 0$ and 1 at $T = 30$ mK and $x = 0.3$ at $T = 400$ mK). Figures acquired from [116].

ion magnetic properties of the system. Knowing the effects, the cooperative magnetism in the $x = 0.1$ and $x = 0.5$ HTSO samples was studied by performing magnetic diffuse scattering measurements on single crystals using the D7 instrument at the ILL.

5.2 CEF excitation measurements

To study the effects of the disorder determined in the previous chapter on the single ion magnetism of the Ho ion in $Ho_2Ti_{2-x}Sc_xO_{7-x/2}$ (HTSO) with $x = 0.0$, $x = 0.1$ and $x = 0.5$, crystal electric field (CEF) measurements were performed using the ToF spectrometer MARI at ISIS. All of the data acquired with MARI shown in this section is on an absolute scale, normalised to a monochromatic vanadium measurement. Powder forms of all samples were studied, with the addition of a powder $Y_2Ti_2O_7$ sample. $Y_2Ti_2O_7$ was used as a phonon blank, this is, a sample that does not have magnetism and is used to correct the phononic contribution in the magnetic sample. When studying any of the three HTSO samples, the resulting data will have both CEF and phononic contribution. However, the phononic contribution can sometimes mask the CEF contribution, which would make modelling the single ion magnetism of this system more challenging. Because of this, $Y_2Ti_2O_7$, which has no magnetic scattering, is used to subtract the phononic contribution from the HTSO data. All samples were grown by Dharmalingam Prabhakaran using the floating zone method at the Clarendon Laboratory, Oxford University.

Table 5.1 shows the temperature and incident energies at which the samples were studied. The $S(\mathbf{Q}, \omega)$ spectra of all 4 samples at 5 K with $E_i = 120$ meV are shown in figure 5.3. As the figure shows, the $x = 0.0$ and $x = 0.1$ HTSO data are very similar, most likely due to the structural similarities found in the previous chapter between both systems. On the other hand, the $x = 0.5$ HTSO sample has a very different spectrum, defined by the lack of low Q excitations below 50 meV and above 70 meV and a very broad feature around 60 meV. Finally, the $Y_2Ti_2O_7$ spectrum has no intensity at low Q, as expected for a system with no magnetism, and all the features increase in intensity with Q, as expected for phononic scattering.

CEF excitations occur at a single site in the crystal and as such are dispersionless and do not have any Q dependence. Furthermore, because the CEF excitations are

Table 5.1: Temperatures and neutron incident energies used to study all four samples.

	5 K	30 K	150 K
HTSO $x = 0.0$	7, 10.5, 25, 40 and 120 meV		7, 10.5, 25, 40 and 120 meV
HTSO $x = 0.1$	7, 10.5, 14, 25, 40 and 120 meV		10.5, 25 and 120 meV
HTSO $x = 0.5$	7, 10.5, 11.7, 25, 29.9, 40, 120 and 180.4 meV	7, 10.5, 25, 40 and 120 meV	7, 10.5, 25, 40 and 120 meV
$Y_2Ti_2O_7$	7, 10.5, 11.7, 25, 29.9, 40, 120 and 180.6 meV		7, 10.5, 25, 40 and 120 meV

magnetic, their intensity falls with Q according to the form factor and will thus only have considerable contribution at very low Q values. Conversely, the phonoic intensity increases with Q^2. From this, it is clear that the low Q features around 20 meV to 30 meV, 60 meV, 75 meV and 80 meV for the $x = 0.0$ and $x = 0.1$ HTSO samples and around

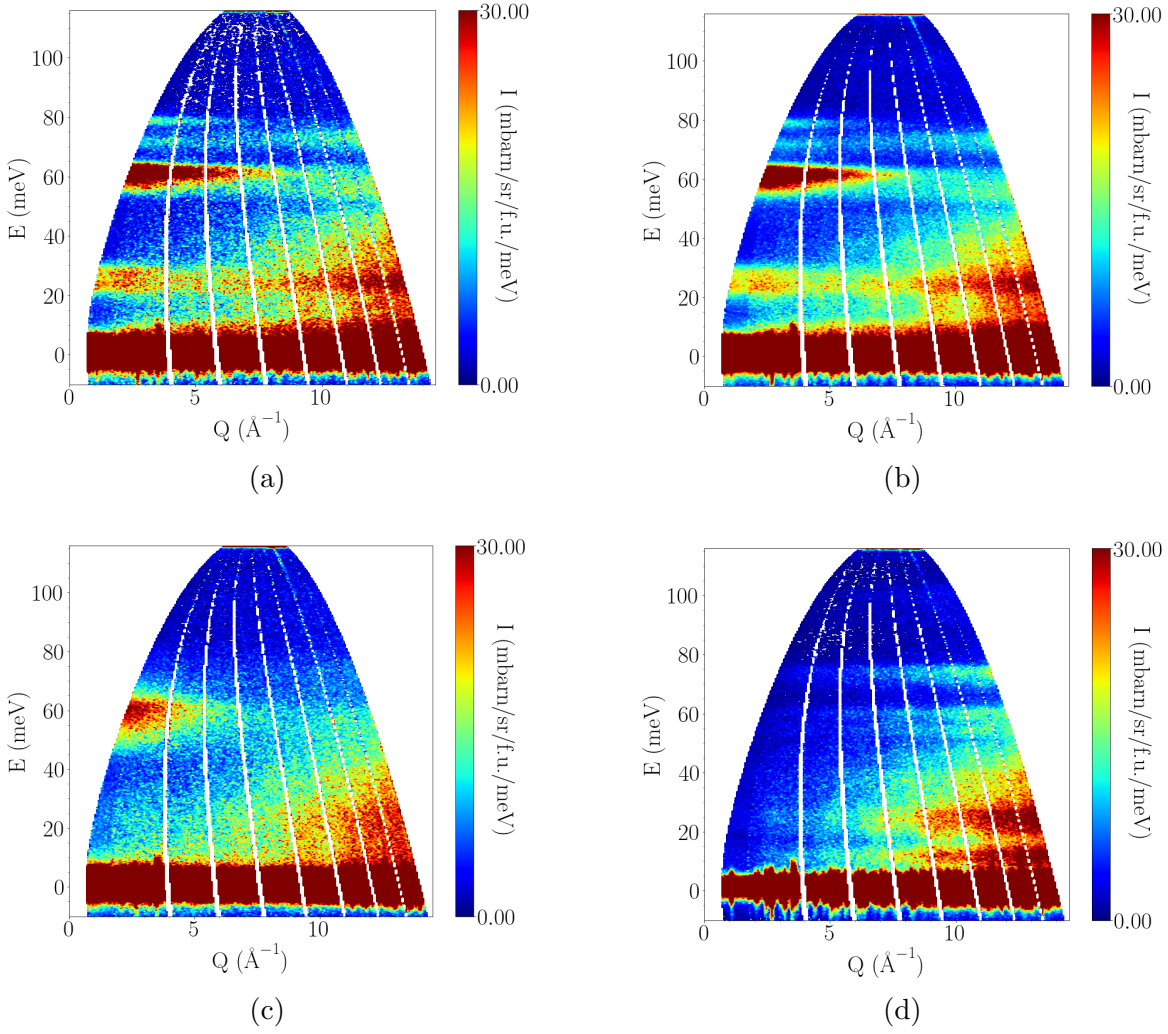

Figure 5.3: Inelastic neutron data of $Ho_2Ti_{2-x}Sc_xO_{7-x/2}$ with (a) $x = 0.0$, (b) $x = 0.1$, (c) $x = 0.5$ and (d) $Y_2Ti_2O_7$ at 5K with an incident neutron energy of 120 meV acquired with MARI.

60 meV for the $x = 0.5$ HTSO samples are CEF excitations. The high Q intensity is all phononic. The $Y_2Ti_2O_7$ sample, however, is purely phononic, which explains the lack of low-Q features. One-dimensional plots of intensity as a function of energy transfer integrated over the full range of Q and by integrating just from 0 $Å^{-1}$ to 2 $Å^{-1}$ are shown in figure 5.4. These figures show better the Q dependence of the magnetic and phononic contributions. The HTSO samples look similar if they are integrated over the reduced low Q or full Q range. However, the Y data is almost flat when it is integrated only over the reduced low Q range but it has more features/peaks when the full Q range is used.

When choosing a phonon blank to correct the CEF data from phonons, it is common to use a non-magnetic ion that is close in the periodic table to the magnetic ion. With Ho this is difficult, since there are not many non-magnetic ions close to Ho that will form a pyrochlore structure with Ti ions. As such, $Y_2Ti_2O_7$ was chosen for convenience. Unfortunately, due to the mass difference between the Y and the Ho, the $Y_2Ti_2O_7$ data cannot be simply subtracted from the HTSO data, since it could over-correct important features. To get the proper multiplication coefficient for the $Y_2Ti_2O_7$, David Voneshen, an instrument scientist from ISIS, extracted the phonon density of states (PDoS) of $Y_2Ti_2O_7$

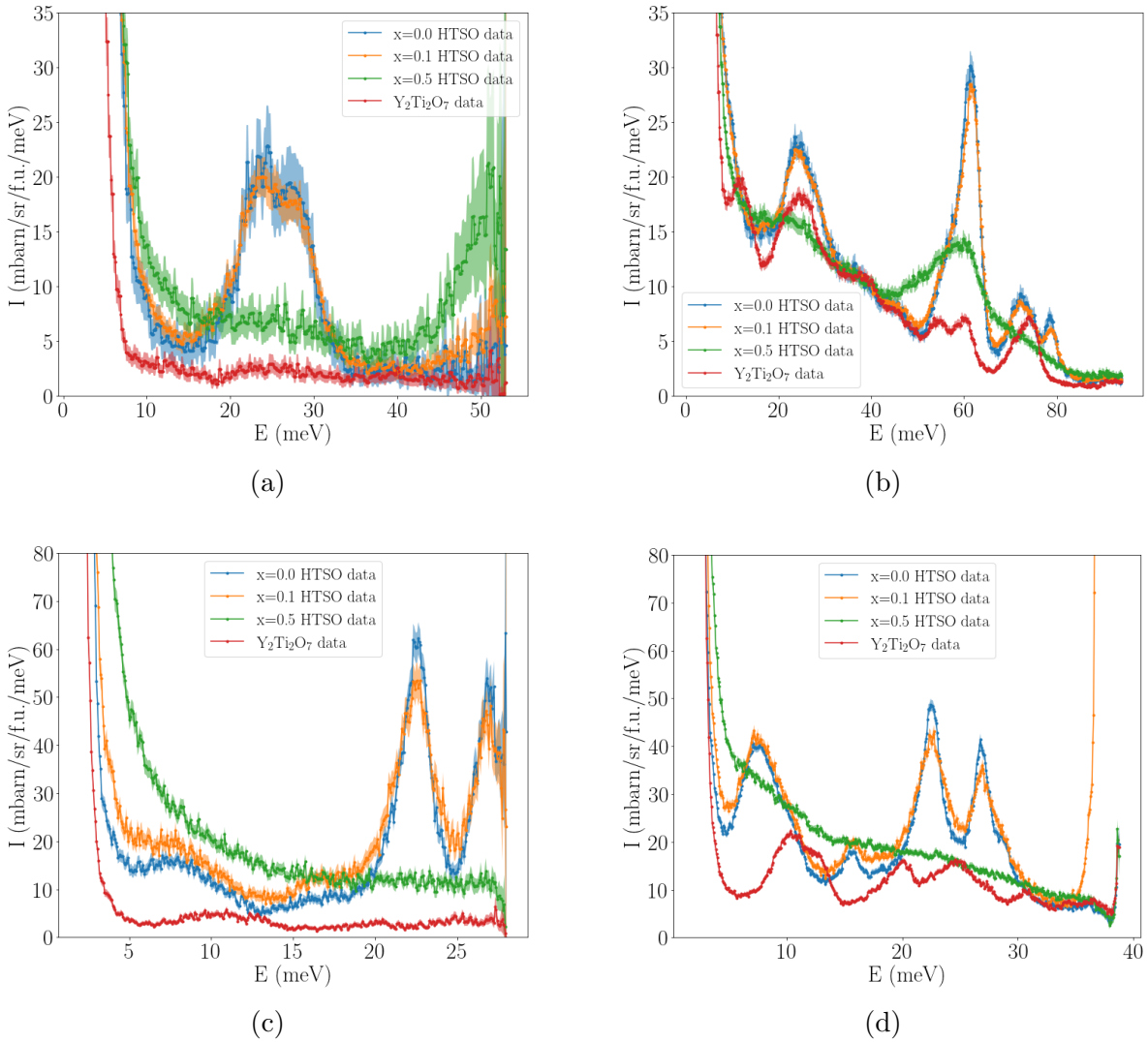

Figure 5.4: 1D cuts of the spectrum data collected with (top) $E_i = 120$ meV and with (bottom) $E_i = 40$ meV acquired with MARI. (a) and (c) integrating only the data from 0 $Å^{-1}$ to 2 $Å^{-1}$ and (b) and (d) integrating over the full Q range.

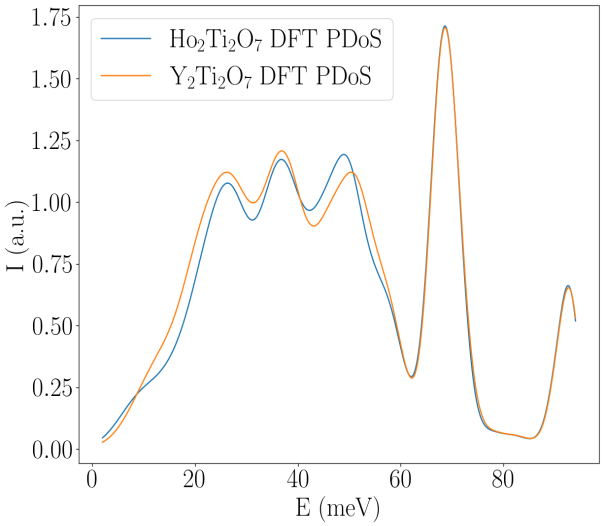

Figure 5.5: Comparison of the two DFT neutron weighted PDoS calculations of $Ho_2Ti_2O_7$ and $Y_2Ti_2O_7$ for an incident energy of 120 meV.

and $Ho_2Ti_2O_7$ with DFT calculations, shown in figure 5.5. With this calculation, the phonon subtraction of the Ho data was performed by first multiplying the $Y_2Ti_2O_7$ data by the ratio of the $Ho_2Ti_2O_7$ DFT PDoS to the $Y_2Ti_2O_7$ DFT PDoS. This would then be subtracted from the HTSO data. However, as it can be seen in figure 5.6 for the $x = 0.0$ HTSO data with $E_i = 120$ meV, due to the large intensity of the $Y_2Ti_2O_7$ experimental data compared with the HTSO data, this subtraction made a large portion of the resulting spectrum negative. Because of this, the $Y_2Ti_2O_7$ data multiplied with the ratio of the PDoS had to be multiplied by an extra constant called the "self-shielding parameter". This parameter depends on aspects such as how much sample was used, the absorption of the material and the shape of the sample holder [227], and thus it was different for each of the three HTSO samples studied.

The phonon correction was performed twice, once with the data integrated over the full Q range and once integrating only from 0 $Å^{-1}$ to 2 $Å^{-1}$. The resulting phonon corrected data is shown in figure 5.7. The reason for looking at two different Q integration ranges

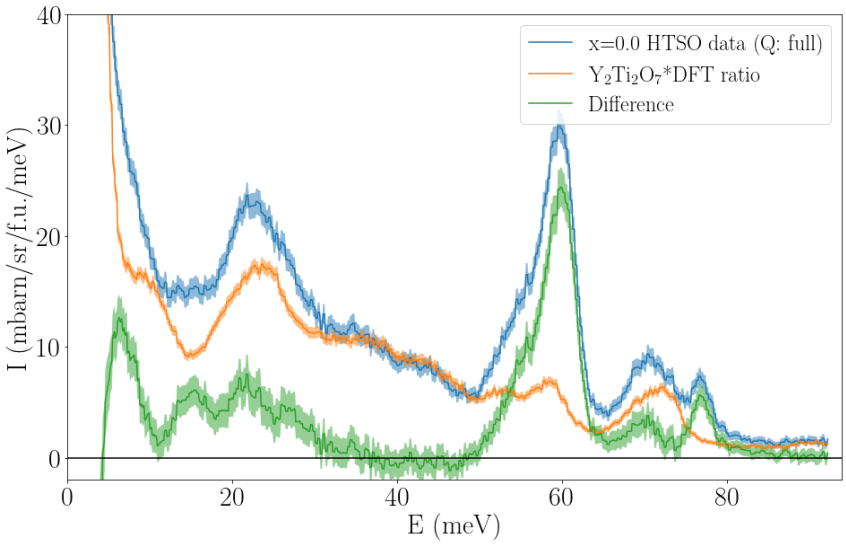

Figure 5.6: Phonon correction of the $x = 0.0$ HTSO sample with no self-shielding parameter.

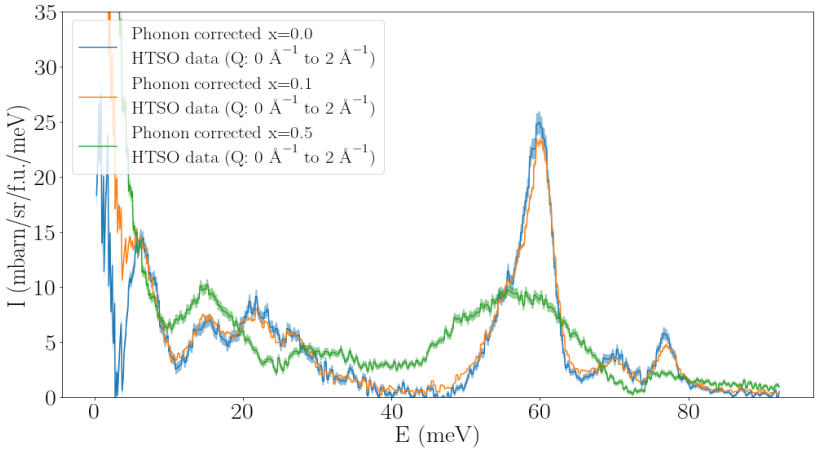

(a)

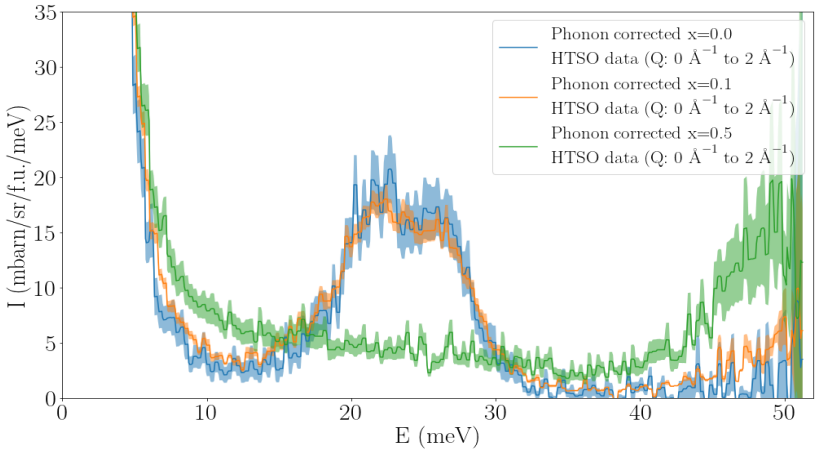

(b)

Figure 5.7: 1D cuts of the phonon corrected inelastic scattering data of all 3 HTSO samples at 5 K with an incident energy of 120 meV acquired with MARI (a) integrating over the full Q range and (b) integrating from 0 Å^{-1} to 2 Å^{-1}.

is to confirm that all the phononic contribution is properly removed. When comparing the data of the $x = 0.0$ HTSO system with previous measurements by Rosenkranz *et al.* [91] of the same system it was found that our corrected data integrated over the full Q range had two extra peaks at around 8 meV and 18 meV. To see if these extra peaks were phonons that the correction method did not take into account, the same procedure of phonon subtraction was followed, but only using the data integrated from 0 Å^{-1} to 2 Å^{-1}. Due to the different Q dependence of the magnetic excitations and the phonons mentioned above, it was expected that at such low Q regions all the phononic contributions should be suppressed, and only magnetic excitations should be present. As figure 5.7b shows, the two peaks at 8 meV and 18 meV present in the data integrated over the full Q range are no longer present in the data integrated over the reduced low Q range, confirming that indeed these two extra peaks arise due to phononic scattering and were not properly corrected with the $Y_2Ti_2O_7$ sample. Figure 5.7 also shows how similar the $x = 0.0$ and $x = 0.1$ HTSO data are, both producing very similar spectra, with the general reduction of the intensity from the $x = 0.1$ HTSO sample being attributed to the presence of Sc doping.

The CEF excitations were analysed using Steven's formalism described in section

3.2.3 by performing individual fits to the data. For this, the Hamiltonian of the Ho ions with and without vacancies are used as a function of the CEF parameters. With the Hamiltonian, the energy levels and CEF spectrum can be calculated and compared with the experimental data.

To model the CEF excitations of a Ho with no nearest neighbour (NN) vacancies ("ideal" Ho site), a D_{3d} symmetry was assumed (see figure 5.8a). This means that only 6 CEF parameters (B_2^0, B_4^0, B_4^3, B_6^0, B_6^3 and B_6^6) are needed to extract the Hamiltonian of a Ho in such a site, and thus only 6 CEF parameters were fitted to the data. Alongside the CEF parameters, a scaling constant and the peak shape were also fitted. For the shape of the peaks, a convolution of a Gaussian with a Lorentzian function was used. The Gaussian function accounted for the experimental resolution, with a known Full Width at Half Maximum (FWHM) given by the instrument. The Lorentzian was purely sample dependant and accounted for aspects such as the lifetime of the excitation and the presence of intrinsic and extrinsic disorder.

For this particular Ho site, the $x = 0.0$ HTSO data was used in the fitting, since it was assumed that most of the CEF contribution would come from a Ho with no vacancies, and the presence of intrinsic disorder or vacancies would be minimal. In addition, the data used in the fitting procedure were not all collected with the same incident energy, but the data at energy transfers between 0 and 35 meV collected with $E_i = 40$ meV were combined with the data at energy transfers from 35 meV onwards collected with $E_i = 120$ meV. This is because, as figure 5.4 shows, at low energies the resolution of the $E_i = 120$ meV data is not as good and the peaks in between 20 and 30 meV are merged together, while with $E_i = 40$ meV the resolution is enough to resolve the data into multiple clear peaks.

The CEF-spectrum fitted to the $x = 0.0$ HTSO system compared with the experimental data is shown in figure 5.9a. The extra intensity below 60 meV is believed to arise from intrinsic disorder such as impurities or extra vacancies. This extra intensity was also found by Rosenkranz *et al.* [91] when studying the same compound. Nevertheless, the calculated spectrum is in very good agreement with the measured data, capturing all the main CEF excitations. Finally, table 5.2 shows a comparison between the fitted CEF parameters with the ones found by Rosenkranz *et al.* [91]. The energy levels resulting from the fitted CEF-Hamiltonian are shown in table 5.4. Since the Ho ions sit in a site with a D_{3d} symmetry, the energy levels are composed of 5 singlets and 6 doublets [160]. The ground state is a well separated doublet composed almost entirely of the $|J, J_z\rangle = |8, \pm 8\rangle$ state, which means that this Ho can be model as having an Ising moment [145]. As mentioned before, Ho^{3+} has an even number of electrons and is thus a non-Kramers ion. Since the ground state is a doublet, as table 5.4 shows, we can conclude that the Ho ions with no NN vacancies are magnetic.

Table 5.2: Fitted B-parameters of the Ho with no NN vacancies in meV.

Index	Fitted	Rosenkranz *et al.* [91]
B_2^0	-0.067(2)	-0.07577
B_4^0	-0.00118(3)	-0.00114
B_4^3	-0.0071(7)	-0.00824
B_6^0	$-7.095(2) \times 10^{-6}$	-7.0183×10^{-6}
B_6^3	$1.063(5) \times 10^{-4}$	1.0356×10^{-4}
B_6^6	$-1.232(3) \times 10^{-4}$	1.2486×10^{-4}

The $x = 0.5$ HTSO data was used to extract the CEF levels of a Ho next to an oxygen vacancy. However, as figure 5.8 shows, any given Ho has 6 NN O(2) ions, and the effect on the CEF levels due to having one vacancy will be different than the effect due to two or more vacancies. As such, Monte-Carlo (MC) calculations were performed to determine the concentration of Ho ions next to one, two or more vacancies and how much they would contribution to the measured CEF spectrum. For this, O(2) ions were removed at random from a $64 \times 64 \times 64$ supercell until the concentration of O(2) vacancies matched the concentration found in the Bragg refinement. This was performed 1000 times, each time calculating the percentage of Ho ions next to zero, one, two or more vacancies. The average percentage from all 1000 calculations was extracted, resulting in 75.61% of the Ho sites with no NN vacancies, 21.64% with one NN vacancy, 2.58% with two NN vacancies and 0.17% with more than two NN vacancies. Since the percentage of Ho ions next to two or more vacancies was so small, it was assumed that the CEF excitations measured in the $x = 0.5$ HTSO data were mainly due to the Ho ions with no vacancies and the Ho ions with one NN vacancy. Similarly, for the $x = 0.1$ HTSO system assuming also O(2) vacancies, the MC calculations predicted 95.16% of the Ho sites with no NN vacancies, 4.74% with one NN vacancy and less than 0.1% with two or more NN vacancies.

To extract the CEF levels of a Ho next to a vacancy, the first step was to determine the number of CEF parameters needed in the fitting procedure. For this, a PCM calculation was performed with the structure shown in figure 5.8b to see how many CEF parameters were non-zero. The calculations predicted that all the CEF parameters with an even n and positive m were non-zero. Thus, B_2^m with m going from 0 to 2 in steps of 1, B_4^m with m going from 0 to 4 in steps of 1, and B_6^m with m going from 0 to 6 in steps of 1 were needed to extract the CEF levels of a Ho next to a vacancy. All 15 possible CEF parameters were required because once an O(2) ion is removed, the symmetry of the system is completely broken and the Ho sits in a site with the lowest possible symmetry.

Knowing which CEF parameters were needed, the CEF levels of a Ho next to a vacancy were extracted by fitting to the $x = 0.5$ HTSO data the sum of the spectrum from a Ho ion

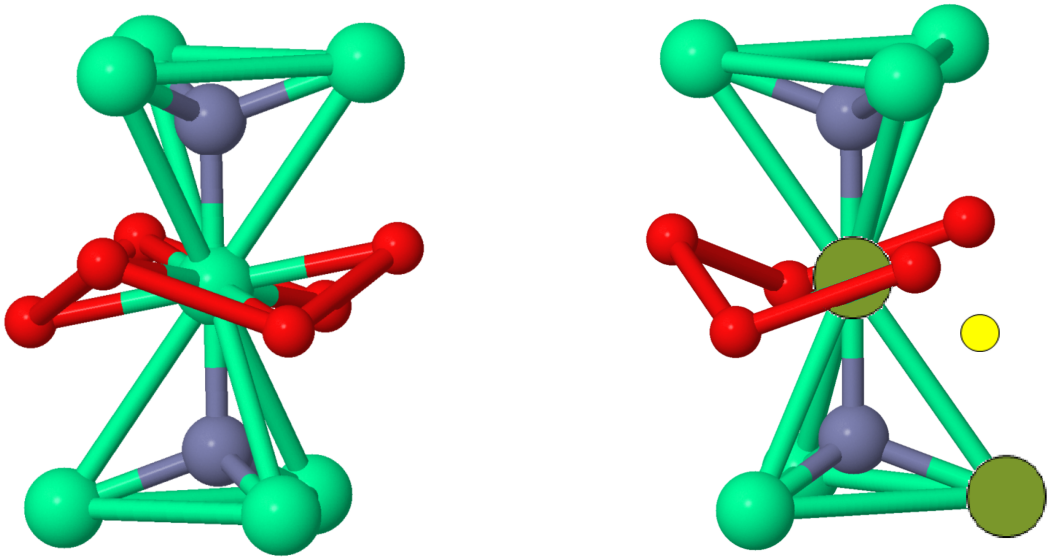

(a) (b)

Figure 5.8: Ho ion in a D_{3d} symmetry site (a) without and (b) with an O(2) vacancy. Red are the O(2) ions, blue the O(1) ions, light green the doublet ground state Ho ions, dark green the singlet ground state Ho ions, and yellow the O(2) vacancy.

with no NN vacancies with the spectrum of a Ho ion with a NN vacancy. Just as with the $x = 0.0$ HTSO data, the Lorentzian widths of the CEF excitations and a scaling constant were also fitted. The resulting fit is shown in figure 5.9c and the fitted CEF parameters are shown in table 5.3. As table 5.3 shows, no error bars were included with the fitted

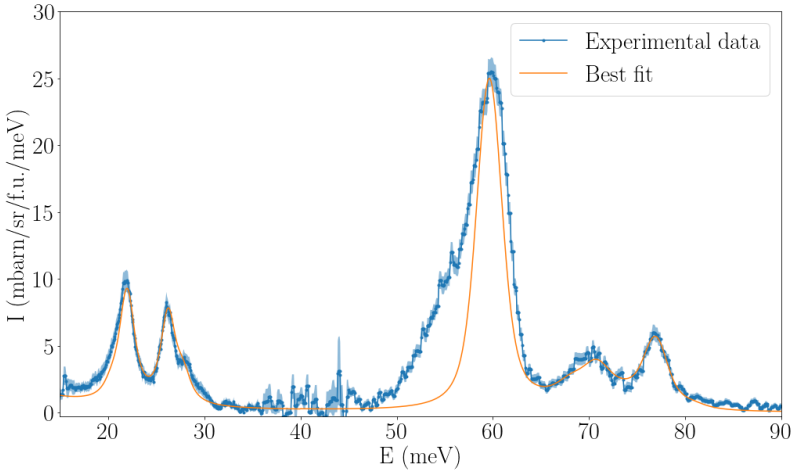

(a)

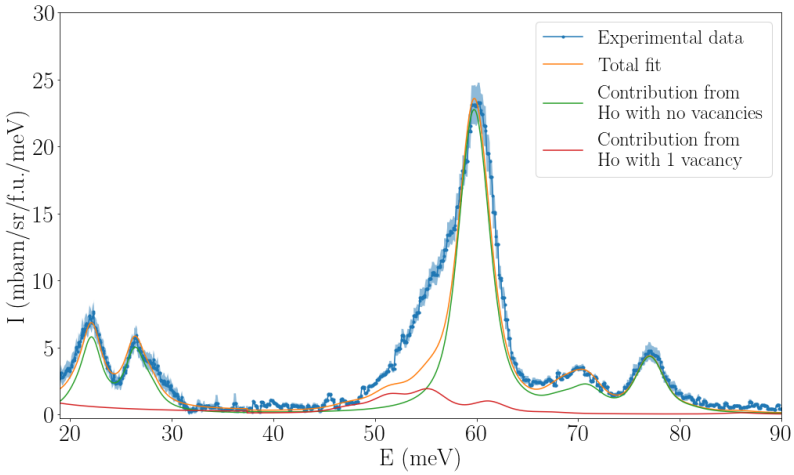

(b)

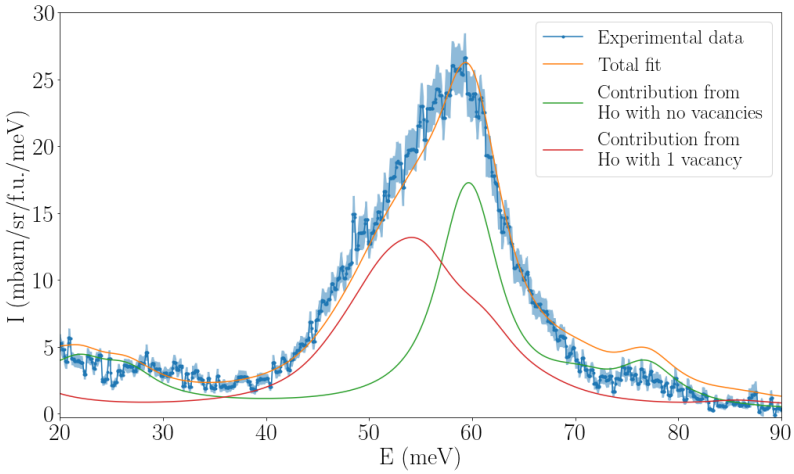

(c)

Figure 5.9: Best fits to the inelastic scattering (a) $x = 0.0$ (b) $x = 0.1$ and (c) $x = 0.5$ HTSO data at 5 K acquired with MARI.

CEF parameters. This was in part due to the instability of the fit. While the fitting procedure was reproducible, the resulting errors not only changed from fit to fit, but also varied widely from CEF parameter to CEF parameter between 0% and 70000%. This was attributed to the large number of fitting parameters needed. Further experimental data, such as magnetization measurements, is needed to constrain the fitting and increase the confidence in the resulting CEF parameters. From the MC calculation, it was assumed that around 75% of the final spectrum would be from the Ho ions with no vacancies and close to 25% from the Ho ions with one vacancy. However, the fitted contribution from each type of Ho ion to the data was 62.17% from the Ho ions with no vacancies and 37.83% from the Ho ions with one vacancy. The energy levels of the Ho ions with a vacancy are shown in table 5.4. As the table shows, all the energy levels of these Ho ions are singlets, including the ground state. This is because the presence of an O(2) vacancy breaks the symmetry of the site, which in turn also breaks the degeneracy of all the Ho ion CEF levels. Thus, following the above description of non-Kramers ions, a Ho next to a vacancy is no longer magnetic. However, it is worth noting that the energy difference between the ground state and first excited state of the Ho ions is small, meaning that the presence of a vacancy simply produces a weak splitting of the ground state doublet. As it will be shown later, this will have an effect on the magnetic correlations of these systems.

Once the CEF parameters of the Ho ions with and without vacancies were known, the $x = 0.1$ HTSO data was fitted by assuming that this system would also have O(2) vacancies. In this case, since the CEF-Hamiltonians were already known, only the peak widths and the relative contribution from the zero and one vacancy spectra were fitted. The resulting fit, shown in figure 5.9b, is in good agreement with the experimental data, showing a clear broadening of the CEF levels with respect to the $x = 0.0$ HTSO data due to the higher degree of disorder in the system. In addition, the contribution of Ho ions with vacancies starts to become more visible, with some extra peaks around 50 meV not present in the $x = 0.0$ HTSO fit. The idea with this fit was that, since this system has 5 times less doping than the $x = 0.5$ HTSO system, the contribution from the Ho ions with one vacancy should be 5 times smaller. However, the final contribution was 79.26% from the Ho ions with no vacancies and 20.74% from the Ho ions with one vacancy. As discussed below, this is likely related to the presence of intrinsic disorder.

One can see that in the fittings performed to both the $x = 0.0$ and $x = 0.1$ HTSO data, there is some extra intensity just below 60 meV that is not accounted for by the fitted spectra. This could be due to intrinsic disorder. In the $x = 0.0$ HTSO data, the intensity

Table 5.3: Fitted B-parameters of the Ho with one NN O(2) vacancies in meV.

B_2^0	B_2^1	B_2^2
-0.31718	0.23593	-0.30721
B_4^0	B_4^1	B_4^2
-1.29213×10^{-3}	-4.76717×10^{-4}	1.90447×10^{-4}
B_4^3	B_4^4	B_6^0
8.73568×10^{-3}	3.58626×10^{-4}	1.52823×10^{-5}
B_6^1	B_6^2	B_6^3
-1.46168×10^{-5}	-6.30729×10^{-5}	-1.98609×10^{-4}
B_6^4	B_6^5	B_6^6
1.02933×10^{-6}	-4.58335×10^{-5}	-3.59492×10^{-5}

Table 5.4: Energy levels of the Ho ion with and without an O(2) vacancy.

Energy levels of Ho with no NN vacancies (meV)	Energy levels of Ho with one NN (meV)
0	0
0	0.124645
20.4141	0.608191
21.9727	0.648415
21.9727	10.9612
26.2378	12.7605
26.2378	47.7667
27.8088	51.7882
59.6323	55.541
59.6323	61.2649
68.1543	67.2132
70.6526	86.4189
71.126	101.612
71.126	107.148
76.9324	111.763
76.9324	115.332
80.8473	120.002

below 60 meV arises most likely due to intrinsic disorder present in the sample such as impurities and the small fraction of O vacancies that was found in the Bragg refinement. In the $x = 0.1$ HTSO data the presence of O(2) vacancies increases and thus we start to see some additional contribution to the intensity below 60 meV, but most of the intensity still arises from intrinsic disorder. As mentioned in the previous chapter, the $x = 0.0$ and $x = 0.1$ HTSO systems have a similar concentration of vacancies, and thus the extra intensity below 60 meV is very similar between both measurements, as can be seen in figure 5.7a. Finally, the $x = 0.5$ HTSO sample contains enough O(2) vacancies that the majority of the intensity below 60 meV arises from these defects, while the intensity from intrinsic defects now is negligible in comparison. This could also explain why the relative contribution of the zero and one vacancy spectrum fitted to the $x = 0.5$ HTSO data does not match the percentages found in the MC calculation, and also why the contribution of the one vacancy spectrum found in the fitting to the $x = 0.1$ HTSO data is not 5 times smaller than the contribution to the $x = 0.5$ HTSO spectrum. Finally, it was found that as the concentration of Sc ions and vacancies increased, the Lorentzian widths of the peaks also increased. This is in agreement with other CEF measurements performed in other disordered pyrochlores, such as Yb stuffed $Yb_2Ti_2O_7$ [217].

Knowing the CEF parameters of the Ho ions with and without vacancies, the magnetisation vector of each Ho ion in a magnetic field was calculated using [214]

$$M_\alpha = g_J \langle J_{M,\alpha} \rangle \tag{5.1}$$

where $\alpha = x, y, z$, $g_J = 1.25$ is the Landé factor for Ho and

$$\langle J_{M,\alpha} \rangle = \sum_i e^{-\beta E_i} \langle \Gamma_i | \widehat{J}_\alpha | \Gamma_i \rangle / Z \tag{5.2}$$

where Z is the partition function, $\beta = 1/k_B T$, and E_i and Γ_i are the eigenvalues and eigenvectors extracted from

$$\mathcal{H}_M = \mathcal{H}_{CEF} + g_J \mu_B \mathbf{B} \cdot \mathbf{J} \tag{5.3}$$

where μ_B is the Bohr magneton in units of meV/T, $\mathbf{B}$ is the applied magnetic field vector and $\mathbf{J} = \left(\widehat{J}_x, \widehat{J}_y, \widehat{J}_z\right)$. The magnetisation calculations were performed at 0.5 K and by applying magnetic fields in random directions with a magnitude of 0.1 T. This helps illustrate the behaviour of the magnetic moment as a function of direction of the field. The calculations for the zero and one vacancy Ho ions are shown in figure 5.10. For the zero vacancy case, the moment points along the z axis in the D_{3d} symmetry, which corresponds to the Ho ion having a strong Ising easy-axis behaviour along the $\langle 111 \rangle$ direction of the tetrahedra in the conventional pyrochlore unit cell. From these calculations it was found that, at 0.5 K and with an applied field of 0.1 T, the Ho magnetic moment is 8.4 μ_B, 16% smaller than the calculated 10 μ_B [95, 96] for $Ho_2Ti_2O_7$.

Furthermore, the Ho ion with one vacancy also produced a magnetisation with a major preference in the z axis (easy axis) but canted in one direction, as figure 5.10b shows. This was a surprise since, as it was described before, the Ho ions next to a vacancy are non-magnetic and thus should not produce a magnetisation. The presence of non-zero magnetisation even with a singlet ground state is due to the small gap between the ground states and the first excited state. When a magnetic field is applied, the wave functions of the ground state and the excited state will mix. These wave functions can mix in such a way that a magnetic moment is developed. Six different point-charge-model (PCM) calculations of this system were performed, each calculation having a different O(2) ion removed from the ring of O(2) ions surrounding the Ho ion. The PCM calculations not only produced a singlet ground state for the Ho ion, but magnetisation calculations at 0.5 K and with an applied field of 0.1 T also produced a similar tilting to the one shown in figure 5.10b. Moreover, it was found that the tilting of the magnetisation was always in the direction of the missing O(2). In the real system this could mean that, since every O(2) vacancy has two NN Ho ions, the moments of each Ho would tilt towards each other, making them more antiparallel, as figure 5.11 shows. Finally, these calculations show that, at 0.5 K and with an applied field of 0.1 T, the Ho ions next to a vacancy have a magnetic moment of 6.2 μ_B in magnitude, close to 40% smaller than the total moment

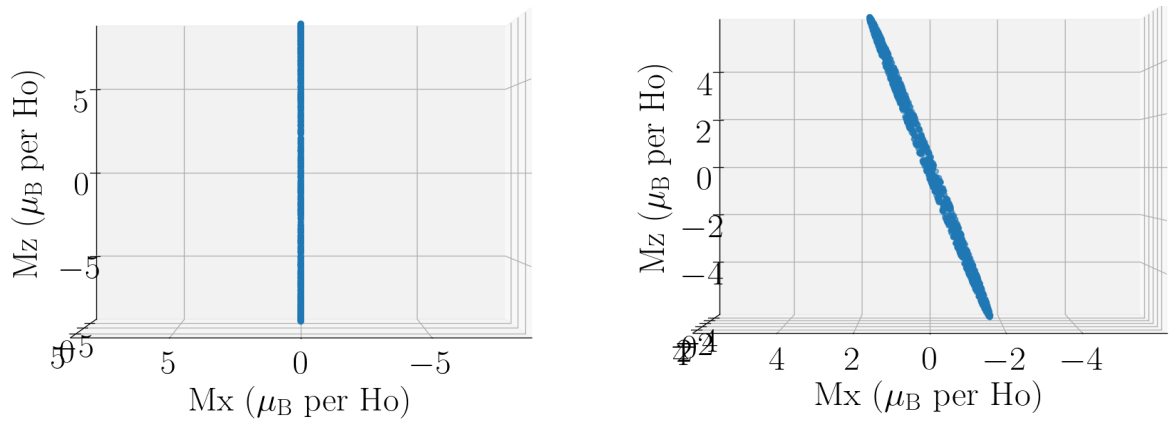

Figure 5.10: Magnetisation of the Ho moment (a) with no vacancies and (b) with one vacancy at 0.5 K and with a field of 0.1 T.

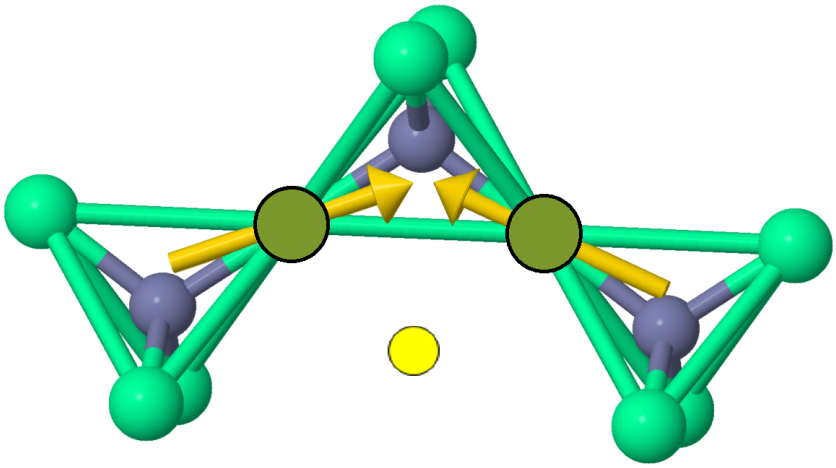

Figure 5.11: Tilting of the spins at Ho sites due to the presence of a NN O(2) vacancy. Blue are the O(1) ions, light green the doublet ground state Ho ions, dark green the singlet ground state Ho ions, yellow the O(2) vacancy and the yellow arrows represent the spins.

but comparable with the calculations of the moment of the Ho ions with no NN vacancies, and with a 15.2° tilt away from the ⟨111⟩ axis.

5.3 Magnetic diffuse scattering

Knowing the effects of the vacancy on the single ion magnetism, the cooperative magnetism of the system was studied. For this, magnetic diffuse scattering measurements were performed on single crystals of the $x = 0.1$ and $x = 0.5$ HTSO samples using the D7 instrument at the ILL. Both single crystals were grown by Prabahkaran at the Clarendon Laboratory, Oxford University, with the $x = 0.5$ HTSO crystal being the same crystal studied in the SXD experiment discussed in the previous chapter.

Because with D7, unlike SXD, only one plane of reciprocal space is accessible, the single crystals had to be aligned so that the reciprocal space plane of interest, in this case the (h,h,l) plane, was the one measured. The Laue diffractometer OrientExpress at the ILL, which uses a beam of neutrons with wavelengths from 0.8 Å to 3.2 Å, was used to rotate the crystals until the z-axis contained the [1-10] direction, the x-axis the [110] and the y-axis the [001]. Figure 5.12 shows both samples already aligned in the copper sample-mount, fixed by nylon screws. The crystals had to be covered with copper foil to improve thermal contact, so that when the temperature is reduced the entire sample reaches a similar temperature and not just the part that is in direct contact with the sample holder.

Just as with SXD, the sample had to be rotated in the sample environment to cover the measured reciprocal plane. Since D7 contains a horizontal line of detectors, and not planes of detectors as with SXD, a single 1D line of the (h,h,l) plane would be measured if the sample is not rotated. Thus, by rotating the sample, different 1D cuts of the (h,h,l) plane can be collected and then recombined to get a full image of the plane. Through the entire experiment, the samples were rotated in steps of 1°, with a neutron incident wavelength of 4.8 Å, which allows for a maximum $|\mathbf{Q}|$ of 2.5 Å^{-1}.

The first system studied was the $x = 0.1$ HTSO sample. This sample was studied using only uniaxial polarisation analysis (PA) so that only spin-flip (SF) and non-spin-flip (NSF) scattering was measured in the Z direction. This analysis was performed with the

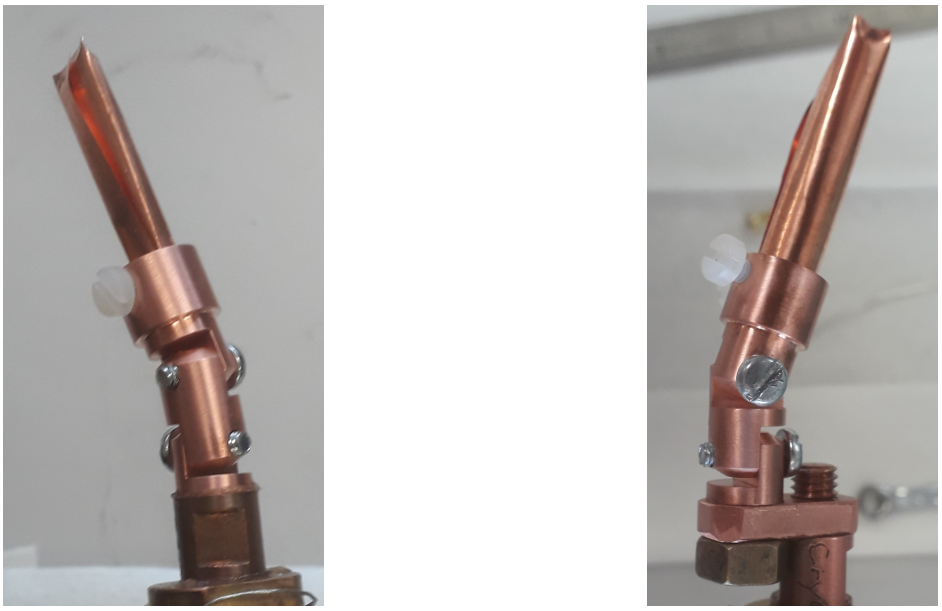

(a) (b)

Figure 5.12: Single-crystal samples of $Ho_2Ti_{2-x}Sc_xO_{7-x/2}$ with (a) $x = 0.1$ and (b) $x = 0.5$.

sample at 50 mK, 650 mK, 5 K, 10 K and 100 K. Since the 50 mK and 650 mK data look identical, figure 5.13 shows only the SF and NSF data at 50 mK. Likewise for the 5 K and 10 K data. The SF data contains the y component of the magnetisation ($M_{\perp y}$) and 2/3 of the spin-incoherent scattering, while the NSF data contains spin-independent nuclear scattering including coherent structural information and isotopic incoherent scattering, the z component of the magnetisation ($M_{\perp z}$) and the rest of the spin-incoherent contribution [46].

As the figure shows, the scattering at 50 mK and 650 mK produce well-defined pinch points despite the Sc doping and the presence of vacancies. At this temperature, the data are qualitatively similar to the measurements of stoichiometric $Ho_2Ti_2O_7$ performed by Chang *et al.* [2] and Fennell *et al.* [1], both producing well-defined pinch points in the SF scattering and a checker-board-like structure in the NSF scattering. As the temperature is increased, the dipolar correlations disappear, producing less pronounced pinch points in the SF cross-section and a less pronounced checker-board-like pattern in the NSF cross-section. At 100 K the sample is well above its Curie-Weiss temperature, and thus it is in a paramagnetic phase. Because of this, we expected the SF and NSF scattering to be flat since at 100 K the electronic and nuclear spin should be incoherent and, from the previous chapter, the diffuse scattering should be negligible. However, as figure 5.14 shows, this is not the case, since there seems to be regions of higher intensity along the [1,1,0] and [-1,-1,1] directions. This extra scattering arises from the spin-incoherent contribution from the nylon screw. This will be made more clear when discussing the $x = 0.5$ HTSO system.

Figure 5.15 shows 1D cuts of all the SF data acquired for the $x = 0.1$ HTSO sample through the (0,0,2) pinch point. At 50 mK and 650 mK the presence of the pinch point produces a very clear saddle point, with a very sharp maximum at (0,0,2) in the transverse scan and minimum close to (0,0,2) in the longitudinal scan. However, as the temperature increases the feature starts to disappear until at 100 K a simple flat background is left. This is due to the redistribution of magnetic intensity from the low-temperature phase, where the spins are frozen due to the system being below or at its freezing temperature,

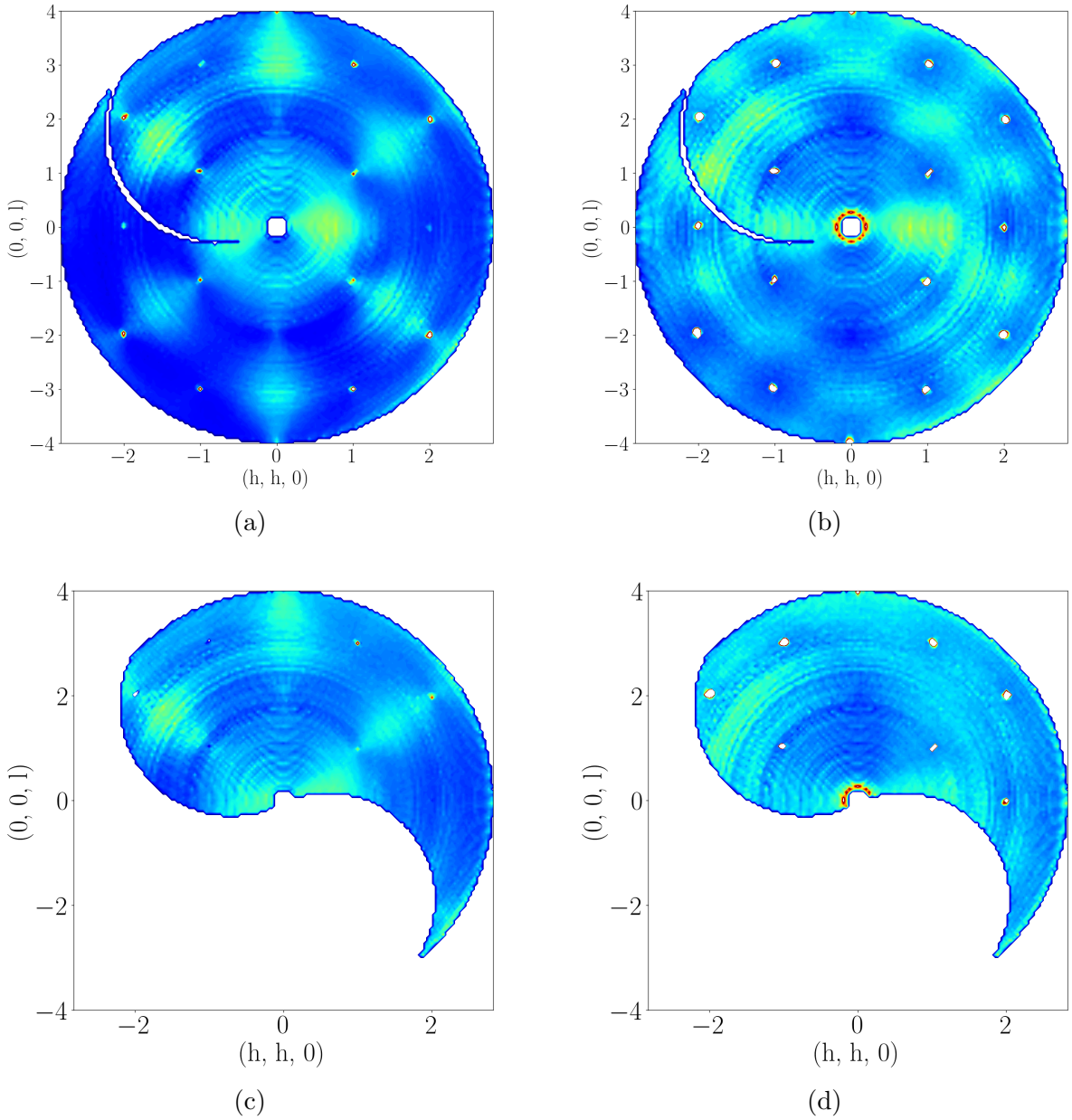

Figure 5.13: Diffuse scattering data in the (h,h,l) plane of the $x = 0.1$ HTSO sample acquired with D7. (a) and (b) show the SF and NSF scattering at 50 mK respectively, and (c) and (d) the SF and NSF data at 5 K.

to a flat scattering from a paramagnet. This transition is visible with the large change between the 650 mK and 5 K data. Due to the low Q-resolution of D7, it is difficult to resolve and extract the temperature evolution of the pinch point width, and thus comparison with the temperature evolution measured by Fennell *et al.* [1] in stoichiometric $Ho_2Ti_2O_7$ is not possible. Furthermore, the extra scattering from the nylon screws makes comparisons with pinch point measurements performed by Fennell *et al.* [1] and Chang *et al.* [116] of stoichiometric and Y diluted $Ho_2Ti_2O_7$ more complicated.

With the $x = 0.5$ HTSO sample, measurements were also performed at 50 mK, 650 mK, 5 K and 10 K using uniaxial PA, but an extra XYZ-PA measurement was performed at 220 K. Unlike with the uniaxial analysis, with the XYZ-PA data full separation of the structural, magnetic and spin-incoherent scattering is possible. The structural diffuse scattering cross-section at 220 K is shown in figure 4.14b, the spin-incoherent scattering

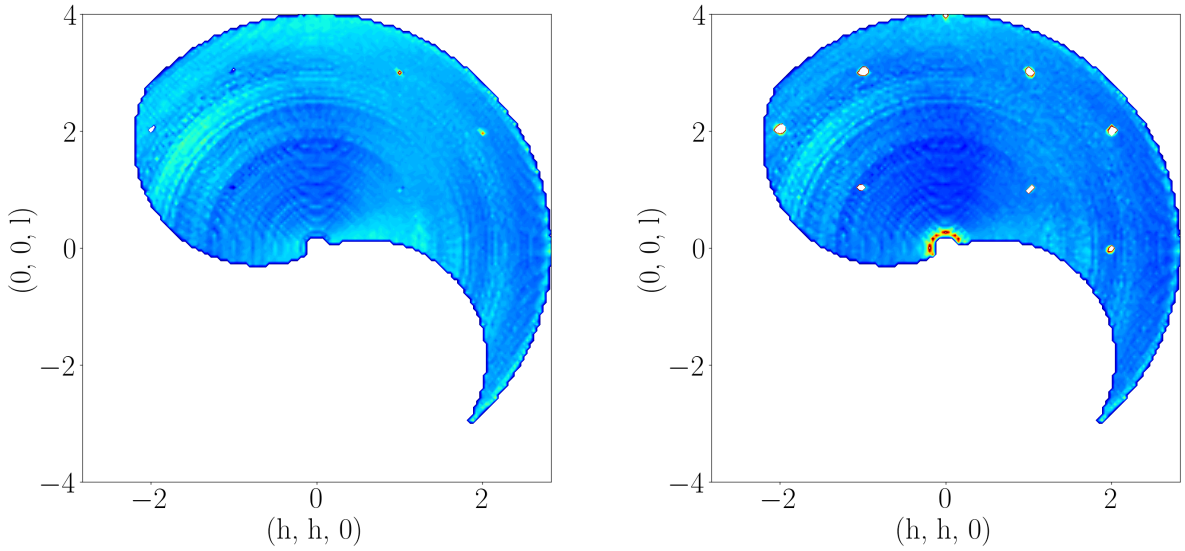

(a) (b)

Figure 5.14: (a) SF and (b) NSF (h,h,l) diffuse scattering data of the $x = 0.1$ HTSO sample acquired with D7 at 100 K.

cross-section in figure 5.16 and the magnetic diffuse scattering cross-section in figure 5.17d. To perform this separation, equations (2.72) for a powder sample were used since these equations can also be used for systems in the paramagnetic phase, which the sample was assumed to be in due to the high temperatures.

The spin of the nuclei only orders at temperatures in the μK or even nK regime, well below the temperature at which the nuclear spin cross-section was measured. As such, these measurements should produce a flat incoherent scattering. However, as figure 5.16 shows, the measured nuclear spin cross-section has some structure. After further investigation, it was found that the shapes seen in the spin-incoherent channel arises from the nylon screws. This is because, as the sample is rotated, the screws will move in and out of the incoming beam. When the beam is rotated in such a way that the beam goes through the nylon screw, the spin-incoherent scattering will be larger in that region of Q space. With this isolated spin-incoherent cross-section at 220 K, the magnetic diffuse scattering

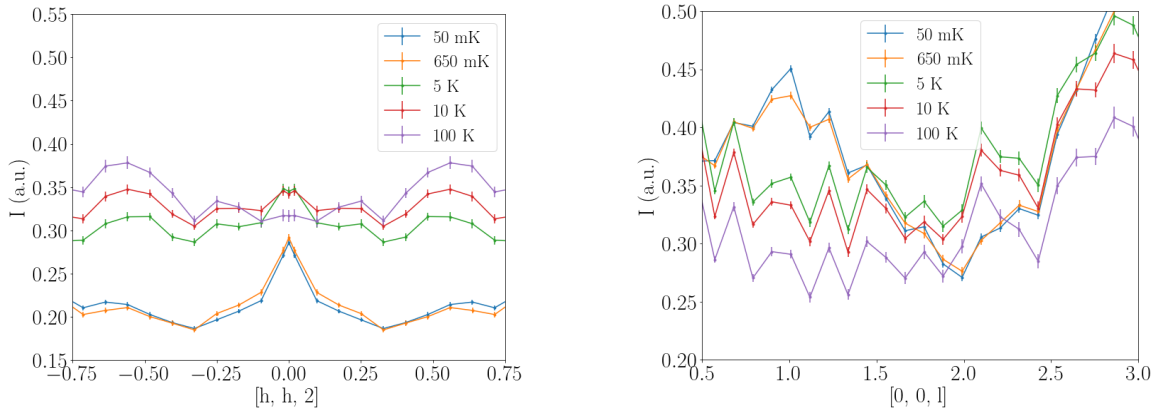

(a) (b)

Figure 5.15: Temperature evolution of the (0,0,2) pinch point from the SF data of the $x = 0.1$ HTSO sample acquired with D7. (a) Transverse [h,h,2] cuts and (b) longitudinal [0,0,l] cuts.

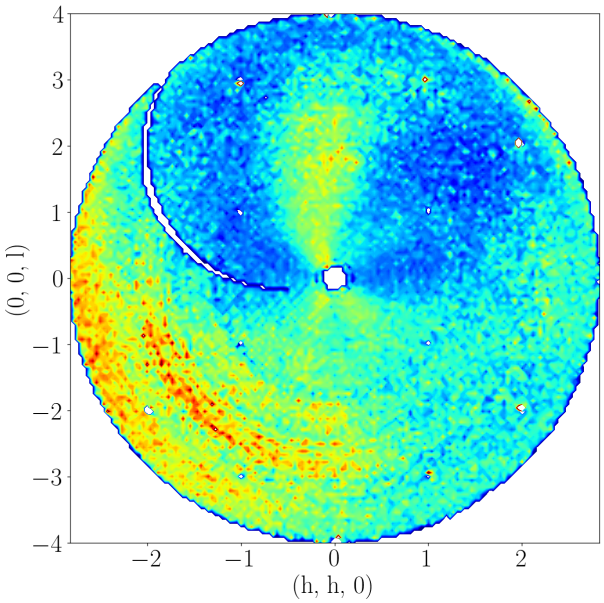

Figure 5.16: Spin-incoherent scattering of the $x = 0.5$ HTSO sample acquired with D7 at 220 K.

at the lower temperatures was extracted from the Z-SF data by using [167]

$$\left(\frac{\mathrm{d}\sigma}{\mathrm{d}\Omega}\right)_{\mathrm{SF}} = \frac{1}{3}\left(\frac{\mathrm{d}\sigma}{\mathrm{d}\Omega}\right)_{\mathrm{Mag}} + \frac{2}{3}\left(\frac{\mathrm{d}\sigma}{\mathrm{d}\Omega}\right)_{\mathrm{SI}} \tag{5.4}$$

where $\left(\frac{\mathrm{d}\sigma}{\mathrm{d}\Omega}\right)_{\mathrm{SF}}$ is the spin flip scattering cross-section, $\left(\frac{\mathrm{d}\sigma}{\mathrm{d}\Omega}\right)_{\mathrm{Mag}}$ is the electronic magnetic scattering cross-section and $\left(\frac{\mathrm{d}\sigma}{\mathrm{d}\Omega}\right)_{\mathrm{SI}}$ the spin-incoherent scattering cross-section. This subtraction was performed for the SF data at all measured temperatures by assuming that the spin-incoherent scattering is temperature independent.

Since, at most temperatures, only half of the (h,h,l) plane was measured, producing data like the one shown for the $x = 0.1$ HTSO sample at 5 K (figure 5.13c) and 100 K (figure 5.14a), the resulting scattering had to be symmetrised. This was achieved by first "folding" the four quadrants of the plane into one quadrant by averaging them, and then "unfolding" to cover the entire plane. This was performed using a function available in the LAMP program. LAMP (Large Array Manipulation Package) is an IDL based data reduction package written at the ILL. It is used to process the measured data and to save it in a more user-friendly way, plot the 2D data and perform 1D cuts, etc. The temperature evolution of the symmetrised magnetic diffuse scattering is shown in figure 5.17. Just as with the $x = 0.1$ HTSO sample, only the 50 mK data is shown because the 50 mK and 650 mK data look identical.

The fully symmetrised data at 50 mK (figure 5.17a) is very similar to the HYTO data from figure 5.2a measured by Chang *et al.* [116]. Both produce a very similar pattern at low Q, with a ring of diffuse scattering close to the origin and higher intensity around the (±1,±1,0) and (0,0,±1) points. This same pattern was also observed in the SF measurements at 30 mK of the stoichiometric system performed by Chang *et al.* [2] and in Bramwell *et al.* [68] dipolar spin ice calculations at 0.6 K. At higher Q, on the other hand, the shape of the scattering around (0,0,3), (3/2,3/2,3/2) and symmetrically equivalent points is different, with the $x = 0.5$ HTSO system having a more diamond-like structure, while the stoichiometric and HYTO systems [2, 116] produced more rounded

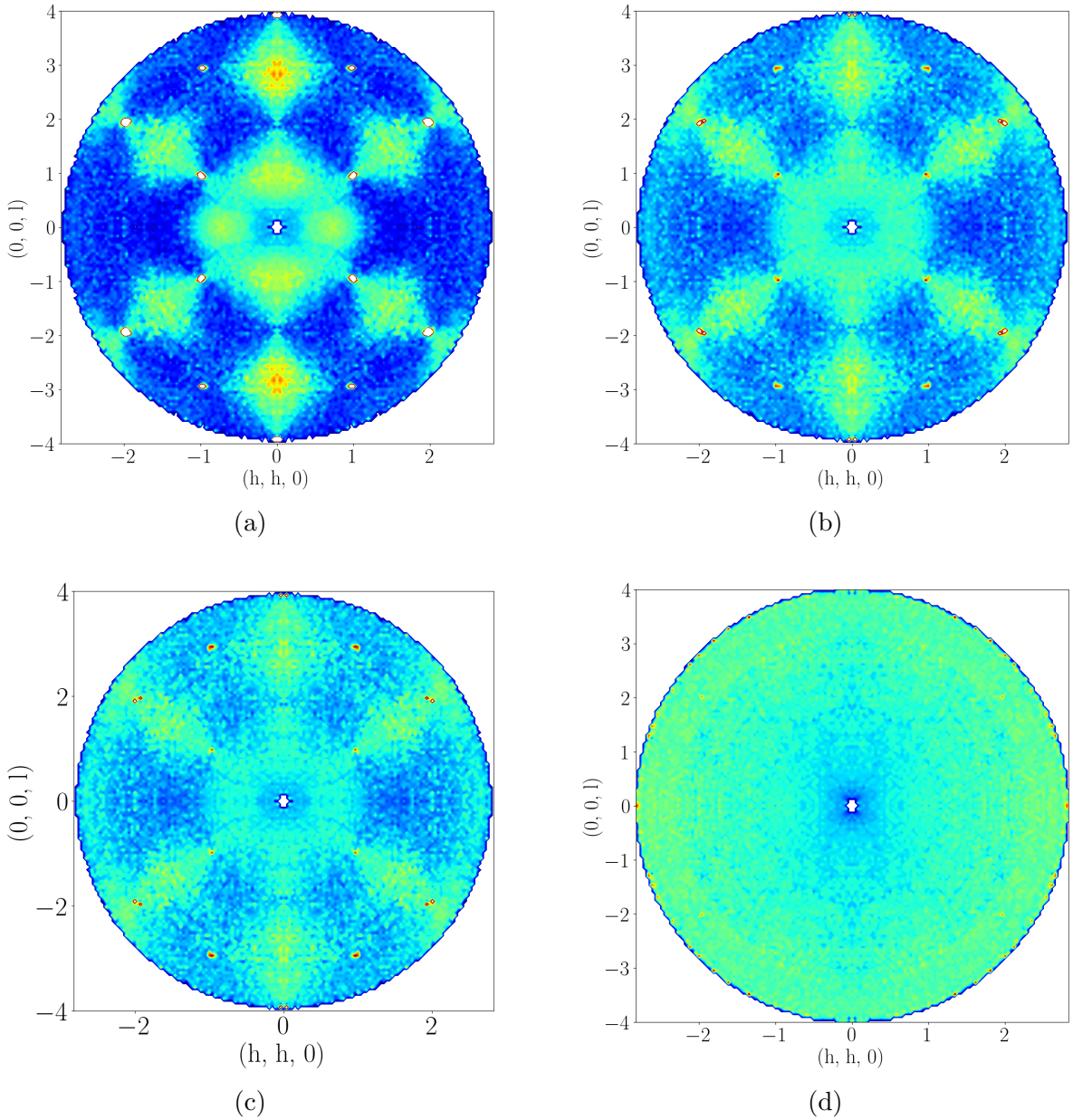

Figure 5.17: Temperature evolution of the spin-flip magnetic data (transverse component) in the (h,h,l) plane of the $x = 0.5$ HTSO sample acquired with D7. Data acquired at (a) 50 mK, (b) 5 K, (c) 10 K and (d) 220 K.

shapes. Similarly, the 5 K data shown in figure 5.17b is very similar to the SF scattering data acquired by Fennell *et al.* [1] at 1.7 K, with the main difference being that Fennell *et al.* have more pronounced pinch points due to the lower temperatures. Furthermore, the calculations in Bramwell *et al.* [68] of the stoichiometric system using the NNSM also produce a very similar structure to the measured 5 K $x = 0.5$ HTSO data. The difference between the 50 mK and 5 K system clearly show the transition from a dipolar spin ice system to a nearest neighbour spin ice system. At 10 K, the nearest neighbour exchange interactions are much weaker than $k_B T$ and the system transitions into its paramagnetic phase. Thus, the characteristic bow-tie-like structure and pinch points are much less pronounced than at lower temperatures. Finally, at 220 K, the system is well into its paramagnetic phase, and only incoherent scattering is measured.

Figure 5.18 shows 1D cuts of all the magnetic diffuse scattering data of the $x = 0.5$

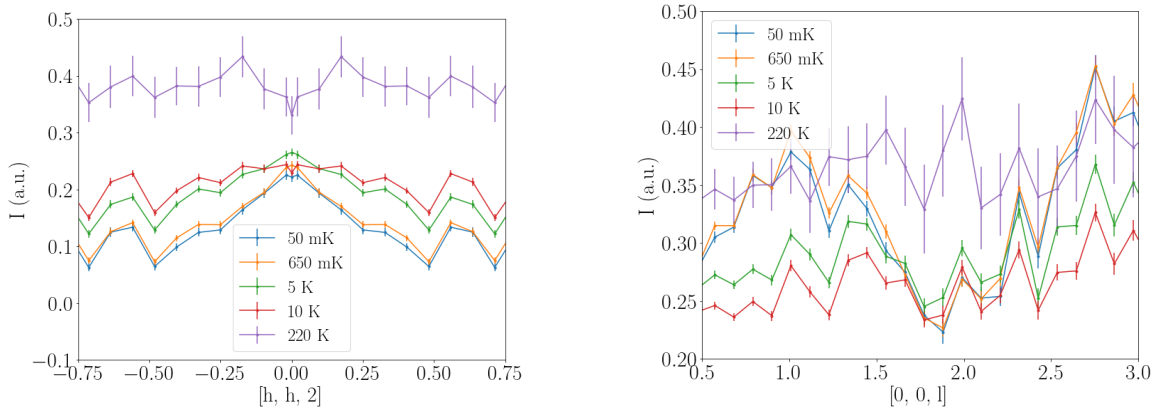

(a) (b)

Figure 5.18: Temperature evolution of the (0,0,2) pinch point from the corrected magnetic diffuse scattering data of the $x = 0.5$ HTSO sample acquired with D7. (a) Transverse [h,h,2] cuts and (b) longitudinal [0,0,l] cuts.

HTSO sample along the (0,0,2) pinch point. Just as with the $x = 0.1$ HTSO sample, at 50 mK and 650 mK the pinch points are clearly visible, with a very sharp maximum at (0,0,2). As the temperature increases, the pinch points mix with the background due to the redistribution of magnetic intensity from the low-temperature phase to a flat scattering from a paramagnet. Finally, at 220 K the system is deep into its paramagnetic phase and a flat scattering is left. Figure 5.19 shows a comparison of the transverse scan of the (0,0,2) pinch point of the $x = 0.1$ and $x = 0.5$ HTSO systems at 50 mK. These data are also compared with the D7 instrumental resolution, showing that at 50 mK the pinch points in these systems are not resolution limited. As the figure shows, there is a clear broadening of the pinch point as the level of Sc doping increases. This is very different to the HYTO system studied by Chang *et al.* [116], where the width of the pinch points show very little change even with 50% of the spins removed ($x = 1.0$ doping), as figure 5.2b shows. A fit to the $x = 0.5$ HTSO pinch point was performed with a Lorentzian function to extract the

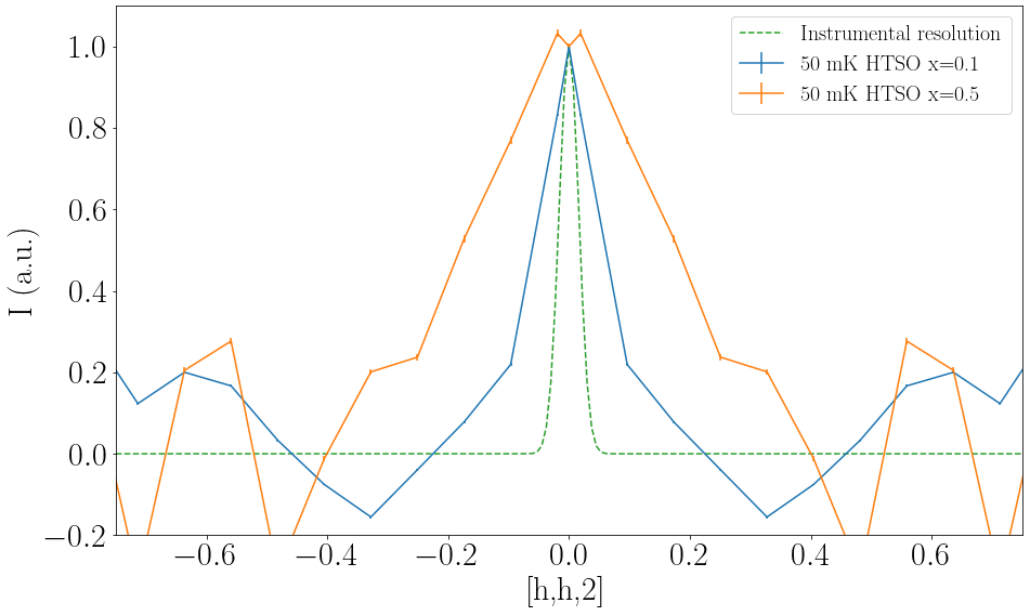

Figure 5.19: Comparison between the transverse scan of the (0,0,2) pinch points of the $x = 0.1$ and $x = 0.5$ HTSO systems at 50 mK and the D7 instrumental resolution.

Full-Width-at-Half-Maximum (FWHM). This resulted in a FWHM of 0.36(4) reciprocal lattice points, almost double the width of the pinch points measured by Chang *et al.* [116] at 30 mK and by Fennell *et al.* [1] at 1.7 K for the stoichiometric system.

Finally, the presence of such sharp pinch points in the magnetic diffuse scattering at 50 mK for the $x = 0.5$ HTSO system, despite the large disorder from the Sc doping, the vacancies, and the presence of non-magnetic Ho ions, is a remarkable result. As mentioned before, from the MC calculations, close to 25% of the Ho ions are next to at least one O(2) vacancy, meaning that around 25% of the Ho ions in this system may have a singlet ground state and are thus non-magnetic. However, as the CEF analysis showed, the presence of vacancies produced a weak splitting of the doublet ground state, resulting in a small energy difference between the ground and first excited state. Due to the Ho ions having such a weak doublet splitting, a magnetic field is able to mix the ground state and first excited state wave functions to generate a magnetic moment.

Since the exchange and dipolar interactions behave similarly to an applied field [228, 229], we concluded that these interactions could also mix these states. As such, at low temperatures we expect that the singlet ground state will mix with the first excited state, and therefore the system will prefer to develop magnetic moments rather than not. This is possible since the splitting is weaker than the nearest neighbour exchange fields of the Ho ions (around 0.15 meV in $Ho_2Ti_2O_7$ [68]). These newly generated moments are very similar to the moments from a doublet-ground state Ho ion, with the moment pointing mainly along the $\langle 111 \rangle$ axis but with a tilt towards the location of the O(2) vacancies. These tilted moments can be decomposed into a longitudinal component along the $\langle 111 \rangle$ direction, which obeys the ice rules at low temperatures, and a transverse component. The key difference between the moments in an ideal spin ice and in the $x = 0.1$ and $x = 0.5$ HTSO is the presence of this extra transverse component at sites next to vacancies. Thus, the broadening of the pinch points with increase in doping could be caused by the presence of the extra transverse moment in conjunction with the disorder caused by the vacancies and Sc doping.

Since the newly generated moments still point mainly along the $\langle 111 \rangle$ direction, at very low temperatures the direction of the moments will be governed by the ice-rules, due to the exchange with dipolar fields trying to satisfy the ice-rules as best as possible. Thus, at low temperature, one would expect dominant spin-ice behaviour. This means that the system will have essentially no monopoles, and we would expect every Ho atom to have a moment close to their full value. Furthermore, it is possible that due to the presence of these defect sites, a new type of excitation exists with respect to spin ice. In an ideal spin ice system, the only possible excitation is flipping a single spin to generate a pair of monopoles (monopole-antimonopole creation). However, in this system, it would require half the energy to reduce the magnetic moment of a Ho ion next to a vacancy to zero. This suggests that it would be interesting to estimate the temperature variation of the average magnetic moment. As the temperature increases, the moments next to vacancies are gradually switched off, until all these moments become zero. This is similar to a system where the density of non-magnetic substitutions on the A sites increases with temperature. Once all the moments next to vacancies are switched off, the orphan spin picture described by Sen *et al.* [226] is recovered.

5.4 Summary

Crystal electric field (CEF) measures of $Ho_2Ti_{2-x}Sc_xO_{7-x/2}$ (HTSO) with $x = 0.0$, $x = 0.1$ and $x = 0.5$ were performed using the MARI instrument at ISIS to determine the effect of O(2) vacancies on the CEF levels of Ho ions. Monte-Carlo (MC) calculations were performed to determine what percentage of Ho ions in the system have at least one nearest neighbour (NN) vacancy. This resulted in around 25% of the Ho ions having at least one NN vacancy in the $x = 0.5$ HTSO sample and close to 5% for the $x = 0.1$ HTSO sample. Through the CEF analysis, it was found that the Ho ions with no NN vacancies had a well separated doublet ground state with an Ising moment, in agreement with previous measurements performed by Rosenkranz *et al.* [91] on $Ho_2Ti_2O_7$. On the other hand, the CEF analysis also showed that the presence of an O(2) vacancy splits the doublet ground state into two singlets, separated by 0.12 meV.

Magnetisation calculations of Ho ions with and without vacancies were performed to study in which direction the magnetic moments point by applying a magnetic field in random directions. It was found that both, the Ho ions with and without a NN vacancy, have a moment. The moment in the Ho ion with a NN vacancy was generated due to the weak splitting of the doublet. Since the energy difference between the ground state and first excited state is low, the magnetic fields can mix the wave functions of both states, generating a magnetic moment. However, while the moments of the Ho ions with no NN vacancies pointed along the line connecting the O(1) ions, as for a Ho with no disorder, the moments of the Ho ions with a NN vacancy also develop a moment mostly along the line connecting the O(1) ions, but with a tilt towards the missing oxygen.

To understand the effect of disorder on the cooperative magnetism, magnetic diffuse scattering measurements were performed on single crystals of the $x = 0.1$ and $x = 0.5$ HTSO systems using the D7 instrument. Qualitatively, both systems produce scattering very similar to that measured by Fennell *et al.* [1] and Chang *et al.* [2, 116] in the stoichiometric and Y doped $Ho_2Ti_2O_7$ systems. However, a transverse scan along the (0,0,2) pinch points shows a broadening of the pinch point as the Sc and vacancy concentration increase, with the FWHM of the $x = 0.5$ HTSO system being almost twice the FWHM of the stoichiometric $Ho_2Ti_2O_7$ pinch point. This is in contrast to the Y doped $Ho_2Ti_2O_7$, which shows very little change in the pinch point width as the doping increases.

Since the exchange and dipolar interaction in this system behave like an applied field, mixing the ground state and first excited state of the Ho ions next to a vacancy due to these interactions is also possible. This would generate a moment at these sites which, as the magnetisation calculations show, point mostly along the line connecting the O(1) ions but with a tilt towards the O(2) vacancy. These tilted moments can be separated into two components, a longitudinal component along the $\langle 111 \rangle$ direction, and a transverse component. It is believed that it is this extra transverse component, in conjunction with the Sc doping and vacancies, which causes a broadening of the pinch points with respect to the stoichiometric $Ho_2Ti_2O_7$ system.

Moreover, it may be possible to distinguish three regions in these systems. At very low temperatures, the system behaves like an ideal spin ice, and thus sharp pinch points are still observed. As the temperature increases, the moments of the singlet ions gradually switch off until all these moments become zero. At this point, the ghost spin picture proposed by Sen *et al.* [226] comes into play.

Chapter 6

Structural disorder in Pr_2ScNbO_7

The structural arrangement of Sc and Nb ions in the highly substituted Pr_2ScNbO_7 system was studied by means of neutron scattering, density functional theory (DFT) analysis and RMC fits. The structural diffuse scattering was measured using SXD and D7 at ISIS and the ILL respectively. DFT calculations were performed with all 97 possible configurations in which the Sc and Nb ions can be arranged on the B sites. It was found that the configuration that produces the lowest total energy contains Sc and Nb ions forming a charge ice structure in the tetrahedra and chains of alternating Sc–Nb. However, this structure is chemically frustrated, and the alternating chains are only observed in particular orientations. Diffuse scattering calculations were performed using a single unit cell of the lowest energy structure, which resulted in a very good agreement with the experimental data. This suggests that Pr_2ScNbO_7 is formed by small domains containing the lowest energy DFT configuration, separated by domain walls with a random arrangement of the Sc and Nb ions. Total scattering measurements were compared with total scattering calculations assuming long range order of the lowest energy DFT structure. These calculations produced extra peaks not present in the experiment, confirming that no long range order of this DFT structure exist in the system.

6.1 Introduction

For a long time, the search for quantum spin liquids in 2D and 3D materials has been focused on defect free systems. This is because disorder induces competing glassy states instead of entangled ones. However, recent theoretical predictions suggest that the presence of structural disorder can be used to stabilise classical and quantum spin liquids, and it can lead to new magnetic degrees of freedom and the formation of entirely novel quantum spin liquids [145, 230]. In the case of spin ice materials with non-Kramers ions, strains can introduce splitting of the ground state doublets akin to the effect of a local disordered transverse field, thus potentially enhancing quantum mechanical effects [145].

One of the most compelling families of materials thought to exhibit a quantum spin ice (QSI) behaviour are praseodymium-based pyrochlores, such as $Pr_2Zr_2O_7$ [3], in which disorder comes into play. Martin *et al.* [231] suggested that a quantum spin liquid state emerges in this system due to the presence of structural disorder in the form of lattice strains. According to Martin *et al.*, the non-spin-flip diffuse scattering in the (h,h,l) plane, shown in figure 6.1, shows anomalies in the (2,2,2), (3,1,1) and (4,0,0) Bragg peaks taking the form of butterfly-like features, indicative of the presence of strains. However, the strength of the disorder is weak and difficult to properly detect with standard diffraction

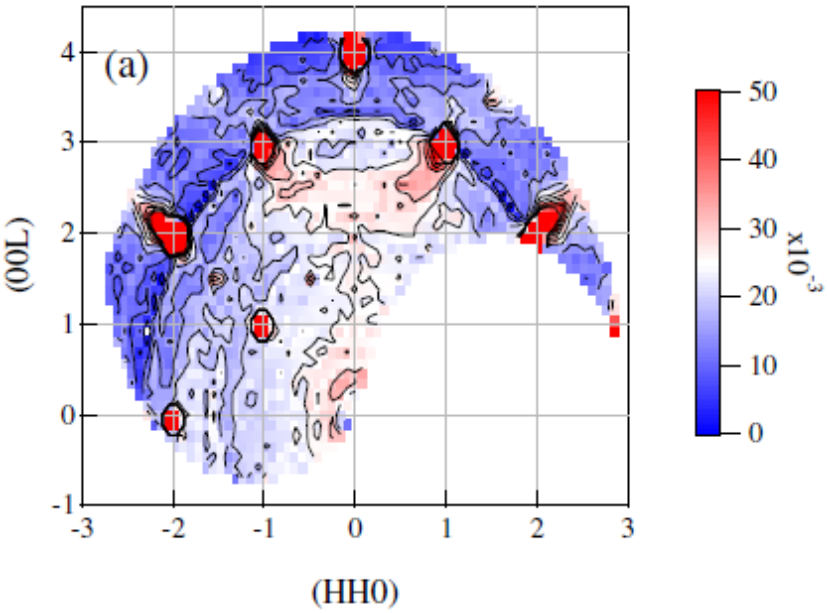

Figure 6.1: Diffuse non-spin-flip scattering map in the (h,h,l) plane at 50 mK of $Pr_2Zr_2O_7$. Intensities are in arbitrary units. Figure acquired from [231].

measurements. The $Pr_2Hf_2O_7$ system measured by Sibille *et al.* [4] and discussed in the introduction chapter is also said to exhibit QSI behaviour. In this system, Sibille *et al.* claimed that the QSI behaviour emerges through anisotropic exchange and not strains, since high sample purity was inferred for this system. To better understand the effects of strains in a praseodymium-based pyrochlore, the highly substituted Pr_2ScNbO_7 system was studied. The combination of trivalent Sc^{3+} and pentavalent Nb^{5+} cations in equal quantities is a way to introduce local strains without the complication of introducing charge-compensating oxygen vacancies.

This chapter presents neutron scattering data on the quantum spin liquid candidate Pr_2ScNbO_7. I will present total scattering data acquired with NOMAD at SNS and structural diffuse scattering data at multiple temperatures acquired with SXD from ISIS and D7 from the ILL. These data were used along with multiple geometrical optimisation density functional theory (DFT) calculations and RMC fits to study the arrangement of the Sc and Nb ions on the B-sites. With the DFT, the configuration of Sc and Nb ions that produced the lowest energy was found, with which diffuse scattering calculations were performed and compared with the experimental data. Finally, RMC fits were performed to the diffuse scattering and pair distribution function (PDF) data, assuming a random arrangement of Sc and Nb ions and long range order of the lowest energy DFT structure.

6.2 Structural diffuse scattering measurements

Structural diffuse scattering measurements were performed on a single-crystal sample of Pr_2ScNbO_7 grown by Dharmalingam Prabhakaran using the floating zone method at the Clarendon Laboratory, Oxford University. This crystal was studied at 3 different temperatures using the Single-Crystal Diffractometer SXD at ISIS: at room temperature with the crystal in 13 different orientations, at 30 K with the crystal in 7 different orientations, and at 4 K with the crystal in 4 different orientations. The sample was measured initially at room temperature, and this told us how many orientations were needed at the other two temperatures with the remaining time. The (h,k,4.5), (h,k,5.5) and (h,k,7) planes

at 30 K and room temperature are shown in figure 6.2. The data was treated using the SXD2001 software where all the measured orientations were combined, and the volume was symmetrised using the $Fd\bar{3}m$ symmetry, the appropriate crystal symmetry for this system [6]. It is worth noting that one needs to take care when symmetrizing diffuse scattering data. In general, defect clusters have lower symmetry than the host lattice. It is, therefore, necessary to average over all of the possible orientations of the cluster relative to the lattice. If all possible orientations occur with equal probability, the diffuse scattering data can be symmetrized using symmetry operations of the underlying lattice. This assumption can be tested by inspection of unsymmetrized data. We find that fits of the diffuse scattering and PDF data are not significantly affected by symmetrization, but for the improvement in counting statistics and revealing the form of the diffuse scattering, it is helpful to present the symmetrized results. In addition, the (h,h,l) plane, shown in figure 6.3, was also studied at 50 mK using the D7 instrument at the ILL. More details of the D7 experiment and the data processing will be given when discussing the magnetic diffuse scattering in the following chapter. The diffuse scattering in the (h,h,l) plane is significantly different from the $Pr_2Zr_2O_7$ diffuse scattering in figure 6.1. The differences between the data sets suggest that the intrinsic defects in $Pr_2Zr_2O_7$ are different to the strain fields in Pr_2ScNbO_7.

As figure 6.2 shows, the (h,k,7) plane has very strong features at odd integer values of h and k. These are the tail ends of the Bragg peaks expected for an integer l plane. On the other hand, if the crystal is much larger than the unit cell of the system, which is the case for this sample, the Bragg scatting in the (h,k,4.5) and (h,k,5.5) planes should be insignificant, since these are half-integer l planes and Bragg scattering is only found at all integer values of h, k and l. However, these planes still contain very pronounced sharp features at integer values of h and k, such as the (0,4,4.5), (4,8,4.5) and symmetrically equivalent points. Upon further investigation, it was found that these sharp features are truncation rods from the Bragg peaks due to the finite size of the system. This can be seen in the (h,k,7) plane, how the width of some of the Bragg peaks span a range of ± 0.5 from an integer h or k value. The contamination of the data due to phonons was also studied by comparing the 30 K and room temperature data. The change in shape of the scattering around the (0,4,4.5), (4,8,4.5) and symmetrically equivalent points is indicative of contamination by acoustic phonons. Similarly, the temperature dependence of the broad features near the (± 10,± 10,4.5) Bragg points also suggest a phononic contribution. All of this (phononic contribution and Bragg peak leakage) was taken into account when comparing with the modelling of the structural diffuse scattering, which aims to understand the temperature-independent features in between Bragg peaks.

One key difference between the diffuse scattering from this system and the previous Sc doped $Ho_2Ti_2O_7$ (HTSO) system studied, apart from the shape, is the strength. In HTSO, the diffuse scattering was strong enough that it was clearly visible in integer l planes, where the Bragg intensity is at its largest. However, in this Pr_2ScNbO_7 system, the diffuse scattering is much weaker and the maximum contour intensity needs to be reduced significantly. As such, when calculations or fittings to the diffuse scattering were performed, the focus was mainly on planes of the form (h,k,l) with l a half-integer, since it is in these planes where the Bragg intensity and acoustic phonons are at its lowest. This is due to the type of disorder, since in the HTSO systems disorder arose not only from the Sc doping, but also from the presence of vacancies. The presences of vacancies in the sample causes additional constructively interfering diffuse scattering. On the other hand, in the Pr_2ScNbO_7 system the combination of Sc and Nb ions in equal quantities means that

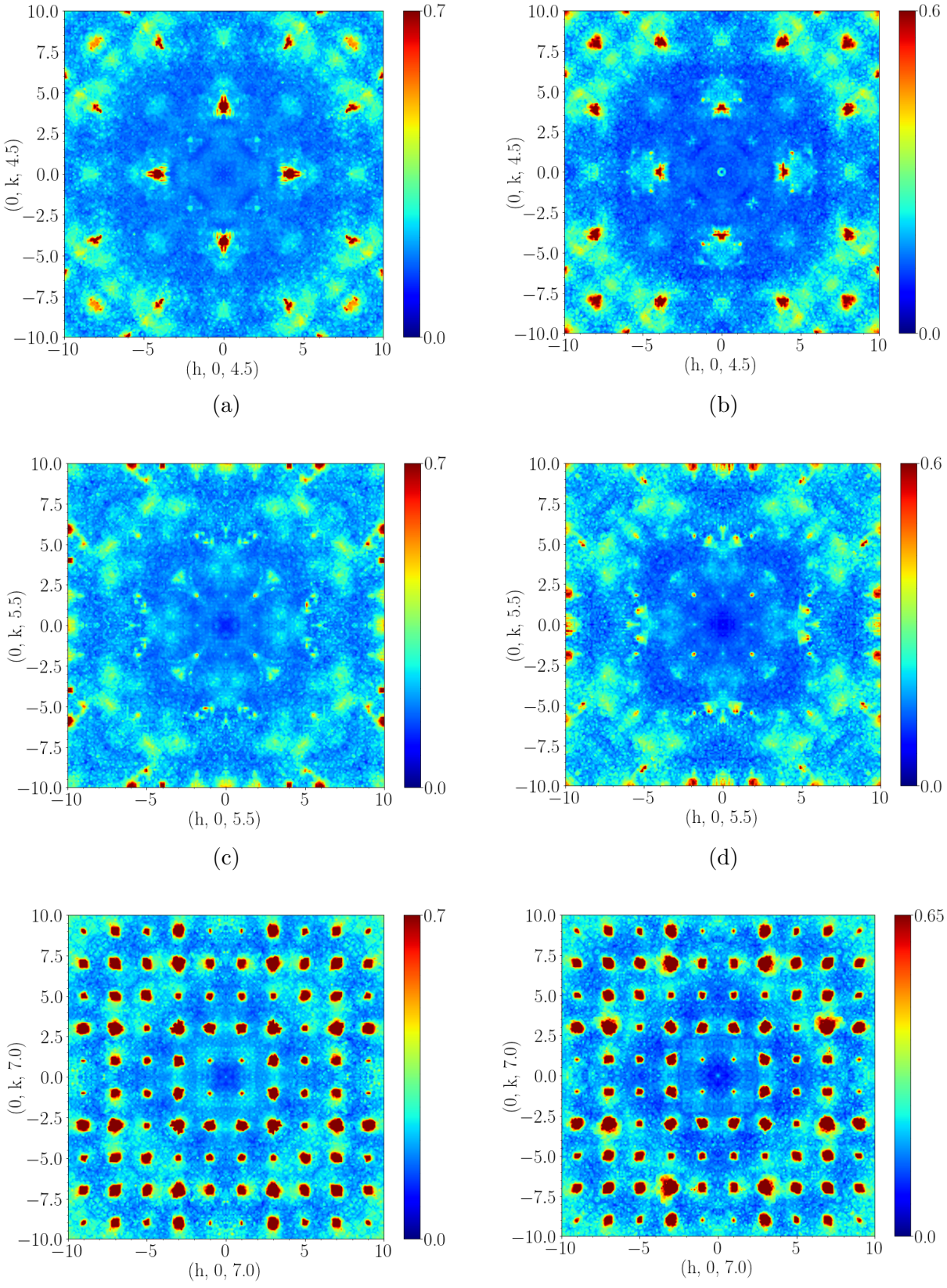

Figure 6.2: Structural diffuse scattering of Pr_2ScNbO_7 in the (top) (h,k,4.5), (middle) (h,k,5.5) and (bottom) (h,k,7) planes at (left) 30 K and (right) room temperature measured on SXD at ISIS.

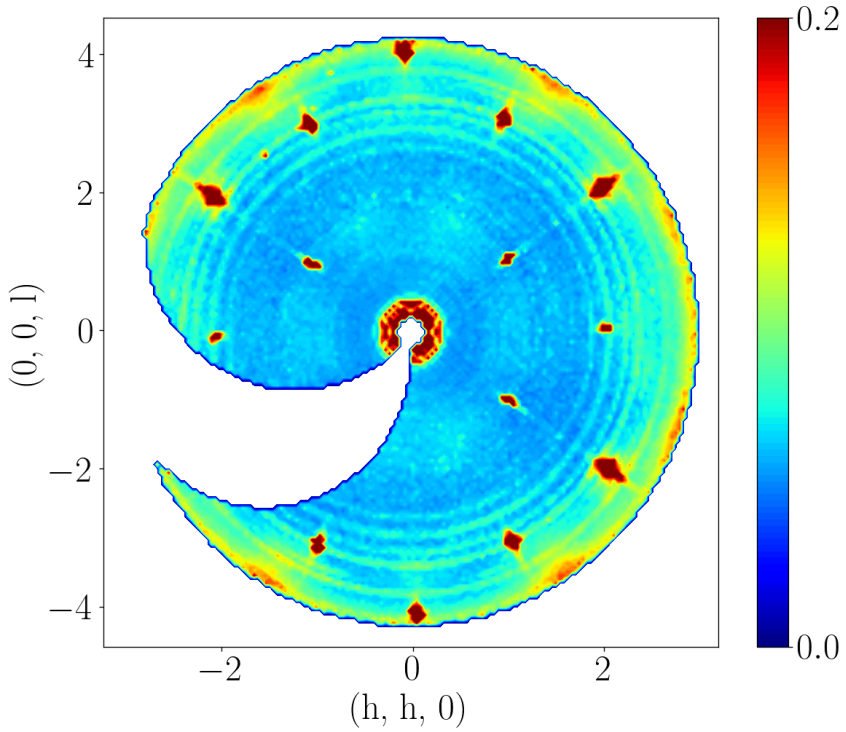

Figure 6.3: Structural diffuse scattering in the (h,h,l) plane of Pr_2ScNbO_7 measured at 50 mK with D7 at the ILL.

there is no need to introduce vacancies and the disorder arises only from strain effects due to the arrangement of the Sc/Nb ions on the B-sites. These strain effects cause a much smaller displacement of the ions from their ideal sites when compared to displacements due to vacancies. This results in a weaker disorder and a much weaker diffuse scattering intensity. Furthermore, as figures 6.2 and 6.3 show, the diffuse scattering from the SXD data is more pronounced than the diffuse scattering from the D7 experiment. This is because the distortions produced by the B-sites disorder are similar in nature to the displacements of atoms caused by phonons. Just as for phonons, the intensity of the diffuse scattering from such a distortion field tends to increase as $|\mathbf{Q}|^2$.

In addition to the structural diffuse scattering, total scattering measurements were also

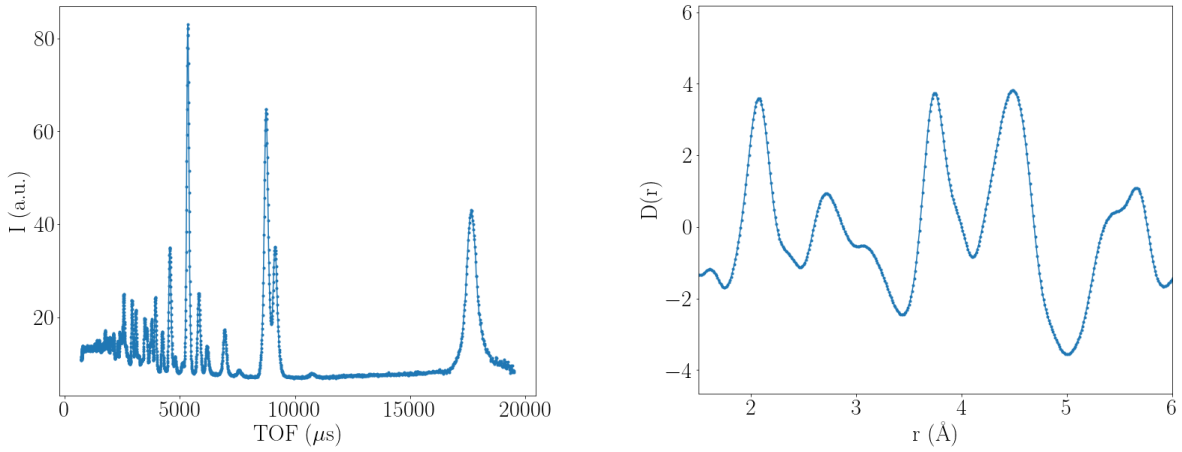

(a) (b)

Figure 6.4: (a) Total scattering data of Pr_2ScNbO_7 in bank 1 of the NOMAD instrument and (b) the reduced PDF of the same sample.

Table 6.1: Refined parameters of the Pr_2ScNbO_7 sample.

Lattice parameter (Å)	x coordinate	Sc/Nb concentration (%)	R_{Bragg} bank 1
10.70(3)	0.329(2)	50/50 (fixed)	6.27 %

performed by Cole Mauws using the NOMAD instrument from SNS. The measurements were performed at room temperature with a Pr_2ScNbO_7 powder. The Bragg refinement was performed assuming a perfect 50/50 concentration of the Sc and Nb ions on the B-sites for charge neutrality. The data from detector bank 1 from the NOMAD instrument and the reduced PDF (D(r)) are shown in figure 6.4. The resulting refined parameters are shown in table 6.1.

6.3 DFT and RMC analysis

Since, in this system, the diffuse scattering is present due to the Sc/Nb arrangement on the B-sites, the effects of ordering the Sc and Nb ions in different ways was studied. In a conventional unit cell, 97 symmetrically inequivalent arrangements of Sc and Nb exist. Thus, DFT calculations of all the 97 possible structures were performed to determine which structure produced the lowest energy, as well as the final displacements of the Sc, Nb, O, and Pr ions from the ideal sites. These calculations were performed by Thomas Hicken from Royal Holloway University of London.

Two parameters were used to characterise the distribution of energies in all the structures: the number of Sc ions on the B-site tetrahedra and on the B-site chains. Each B ion is shared between three chains, and all the chains in each plane are separated by a chain of Pr ions. Since, on average, the number of Sc ions in each tetrahedron and chain would be the same as the number of Nb ions due to the 50/50 distribution, the energy distribution was studied as a function of the variance of the number of Sc ions in each tetrahedron (σ_T^2) and as a function of the variance of the number of Sc ions in each chain (σ_C^2). For example, consider a system of 4 tetrahedra with the following distribution of Sc ions in each tetrahedron: 1, 2, 3, 2. This will result in an average of 2 Sc ions per tetrahedron and a $\sigma_T^2 = 0.5$ calculated using

$$\sigma_T^2 = \frac{1}{N_T} \sum_{i=1}^{N_T} (x_i - \bar{x})^2 \tag{6.1}$$

where N_T is the number of tetrahedra, x_i the number of Sc ions in each tetrahedron and $\bar{x}$ the average number of Sc ions per tetrahedron. The same analysis would follow for σ_C^2. The resulting energy distribution as a function of σ_T^2 and σ_C^2 is shown in figure 6.5. The structures labelled with the square, triangle, rhombus and star are the 4 configurations with a charge ice structure in the B sites, that is, all the tetrahedra have 2 Sc and 2 Nb, where the highest energy structure of the four (star) is one where B-site chains in particular directions are formed by all-Sc or all-Nb ions.

As the calculations show, there is an overall 25 meV gap between the lowest energy structure and the second lowest. The lowest energy configuration has σ_T^2 and σ_C^2 equal to zero. This is charge ice ordering with alternating Sc–Nb on chains in particular directions, as it will be discussed below. The DFT calculations are for a conventional unit cell and they assume periodic boundary conditions. If the structure really did have such long-range order, it would produce Bragg peaks with no diffuse scattering between them. The

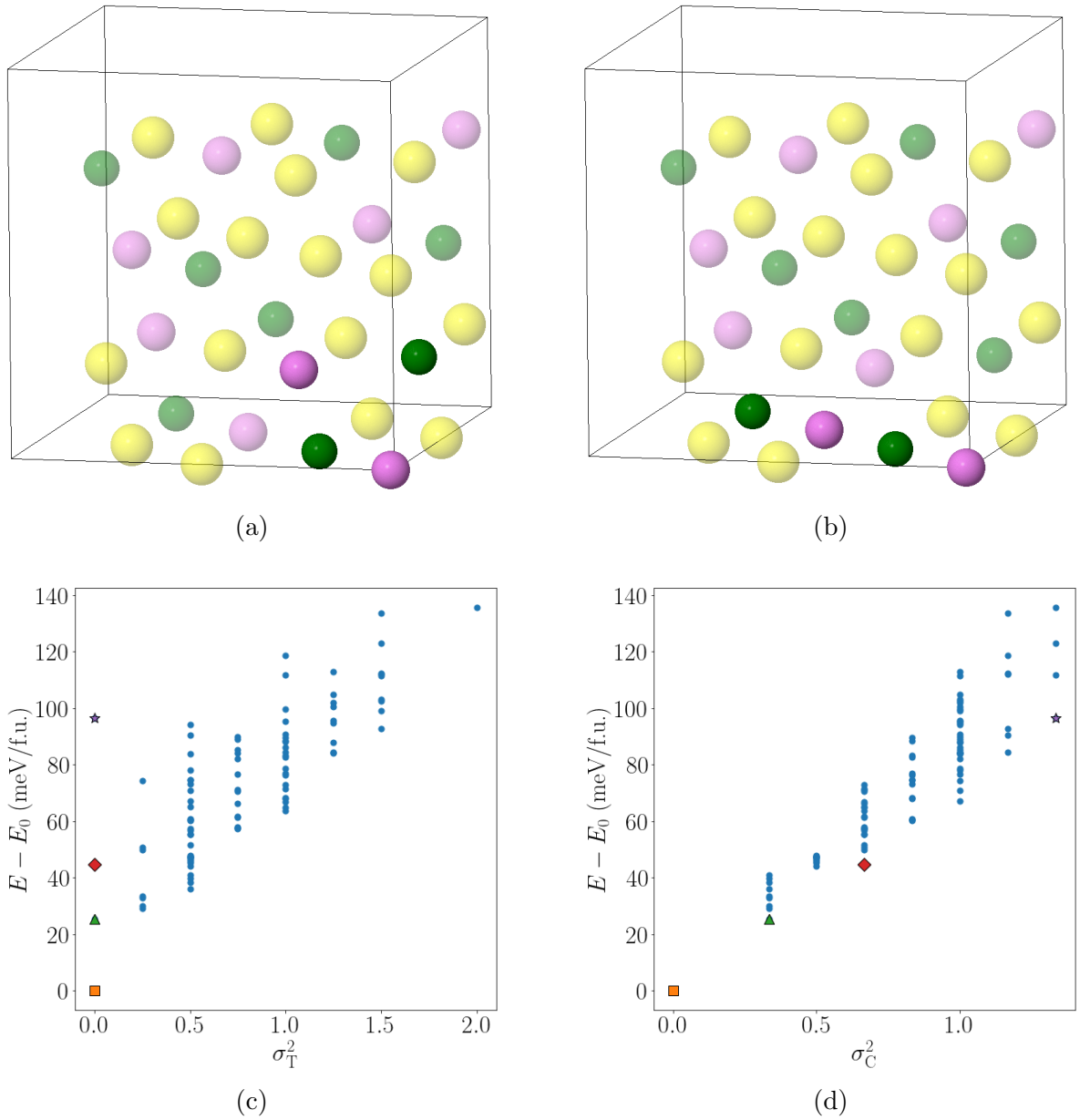

Figure 6.5: Conventional unit cell of Pr_2ScNbO_7 for the lowest energy DFT configuration highlighting (a) a single tetrahedron and (b) a chain of B ions. The yellow spheres are the Pr ions, violet the Sc and green the Nb. The oxygen ions were removed for visual purposes. Difference in energy per formula unit (f.u.) with respect to the lowest energy structure (E_0) as a function of the variance of the number of Sc ions in each (c) tetrahedron (σ_{T}^2) and in each (d) chain (σ_{C}^2) for each configuration. The structures marked with the square, triangle, rhombus and star indicate structures with charge ice ordering.

fact that the experimental diffuse scattering does not show sharp features representing long range order, only broad features, implies that the Sc–Nb ordering found in the lowest energy DFT structure is only over a short range.

The lowest energy configuration in an (a,b,c) orientation is shown in figure 6.6a, where the (1,1,0) and (1,-1,0) chains have alternating Sc–Nb. However, this structure breaks rotational symmetry, since the system no longer has alternating Sc–Nb in the corresponding directions when the structure is rotated into a (b,c,a) orientation, as figure 6.6b shows.

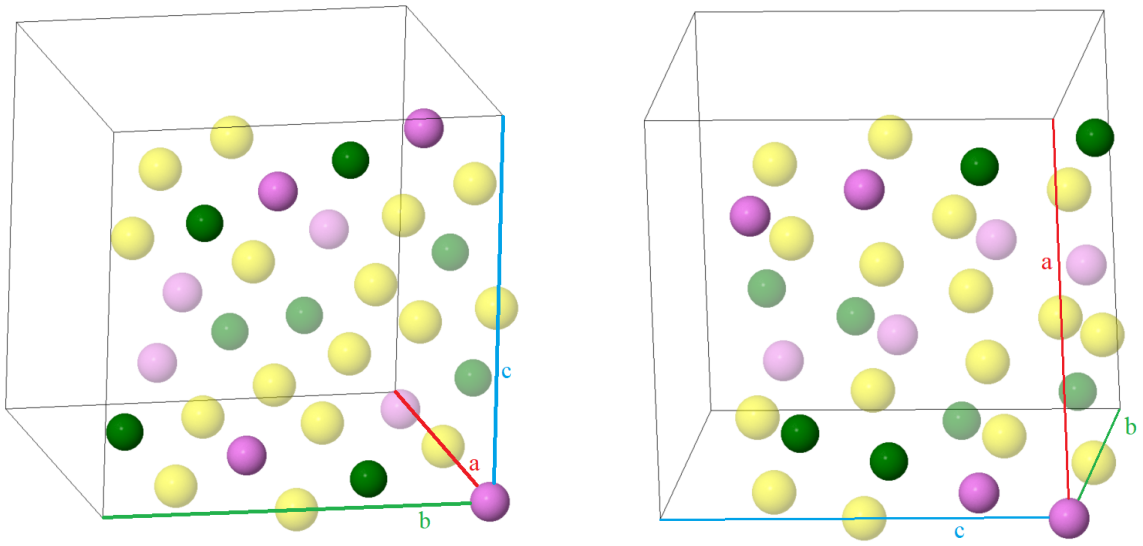

(a) (b)

Figure 6.6: Lowest energy structure predicted by the DFT calculations from two different orientations. The yellow spheres are the Pr ions, violet the Sc and green the Nb. The oxygen ions have been removed for visual purposes.

Thus, once a configuration like this is formed, the system "selects" a local z-axis, resulting in locally having a special axis, and at different locations in the system, the lowest energy structure would have the special axis pointing in another direction. This is a form of chemical frustration, which would result in this system having domains of the lowest energy DFT structure, each domain having its own special axis, and the transition from one domain to another (domain wall) having a random arrangement of Sc/Nb on each site.

With this lowest energy structure, the structural diffuse scattering was computed by using the difference method described in section 2.4.1. In this case, the structure that was being subtracted was one with a perfect 50/50 distribution of Sc and Nb on the B-sites. This is equivalent to having a system with a pure random alloy on the B-sites, with the scattering length given by an average of the Sc and Nb scattering length, but in one single location of this random alloy a unit cell that matches this lowest energy structure is inserted. Thus, the size of the coherent defective region is assumed to be that of the conventional unit cell. The justification for choosing just a single conventional unit cell is that the width of the diffuse peaks in Q is comparable to the experimental widths. However, the real system is most likely formed by many domains of the lowest energy structure, each one with its own special axis pointing in different directions. As such, the calculations were performed with the unit cell of the lowest energy structure in multiple orientations, with all the calculated patterns added incoherently. As figure 6.7 shows, the agreement with the (h,k,4.5) SXD data is good, specially at the higher Q values. The agreement with the (h,k,5.5) is also good, but the calculation produces some features that are not in the experimental data, such as the intensity around (±8,±8,5.5), and it misses other features, for example around (±3,±3,5.5). Nevertheless, all the general shapes of the diffuse scattering are properly reproduced. This is confirmation that the crystal most likely is composed of small domains, in the order of one conventional unit cell, containing the lowest energy DFT structure.

In addition to comparing the diffuse scattering calculation with experimental data,

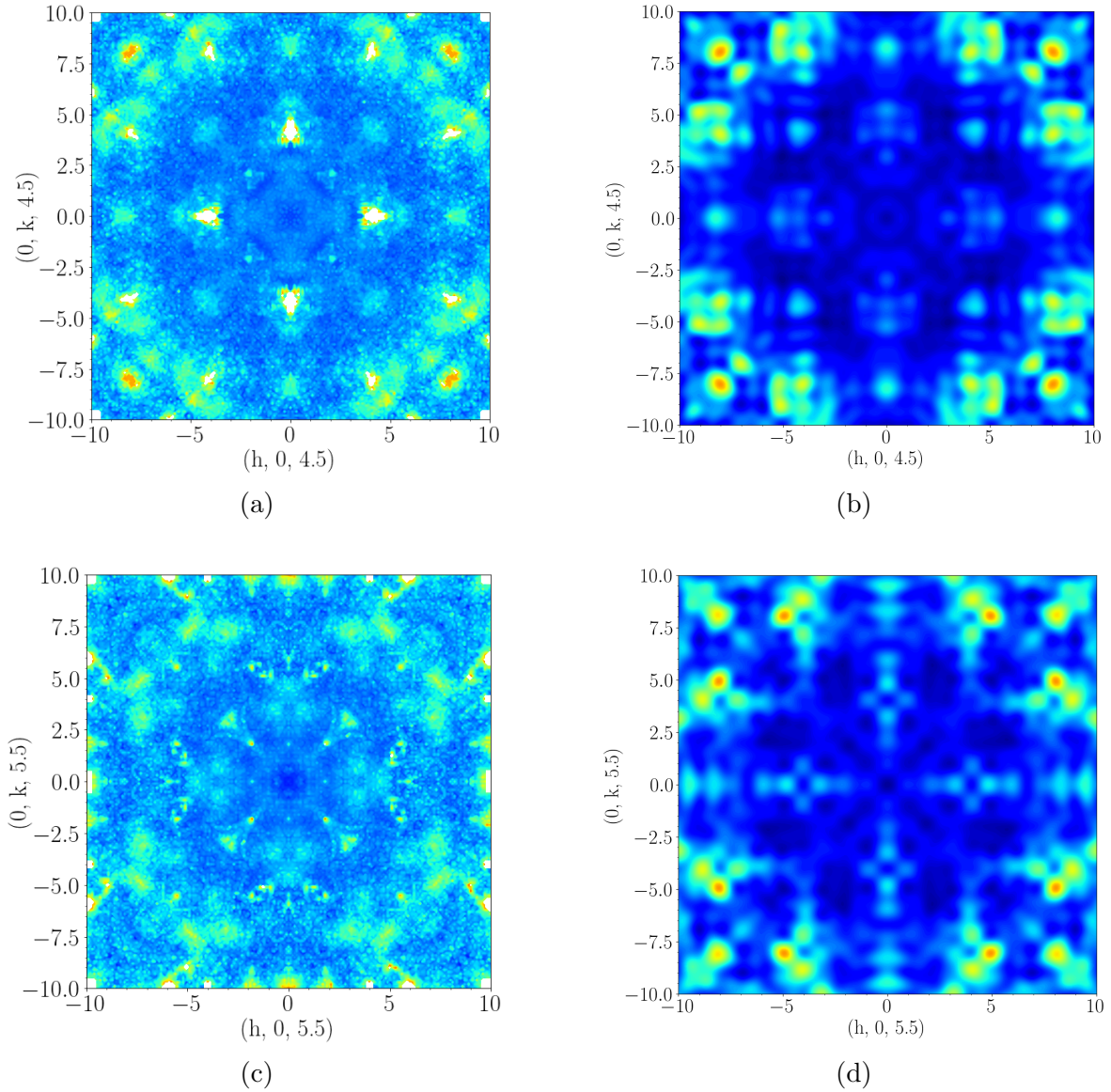

Figure 6.7: Comparison between (left) the SXD experimental data at 30 K and (right) the structural diffuse scattering calculated with the lowest energy DFT structure in the (top) (h,k,4.5) and (bottom) (h,k,5.5) planes. The features from the experimental data that were identified as truncation rods from the Bragg peaks and the phononic features have been removed.

the total scattering data acquired with NOMAD was compared with the total scattering calculations produced by a system with a random arrangement of Sc/Nb ions (perfect alloy) and by a system with the lowest energy DFT structure in one particular orientation, as figure 6.8 shows. The latter was calculated assuming that the lowest energy DFT structure was repeated along the entire sample. In both cases, a P1 symmetry group was used with the pyrochlore conventional unit cell (88 atoms) and the parameters found in the refinements shown in table 6.1. Since this was just to compare the effect of having long range order of the lowest energy DFT structure with a pure random alloy, no further refinements were performed. The presence of extra peaks produced by the lowest energy DFT structure shows that clearly the real system does not have any kind of long range ordering of the lowest energy DFT structure in one particular orientation. It is thus more likely to have domains of this structure separated by randomly arranged Sc/Nb ions. This

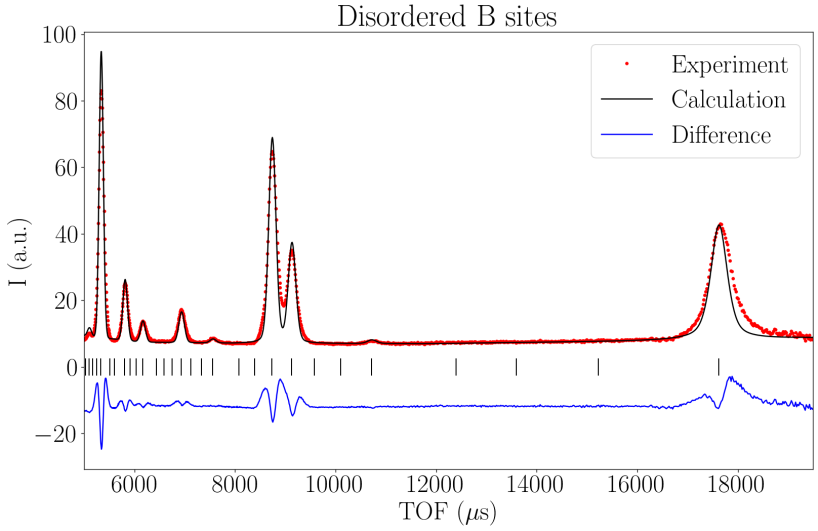

(a)

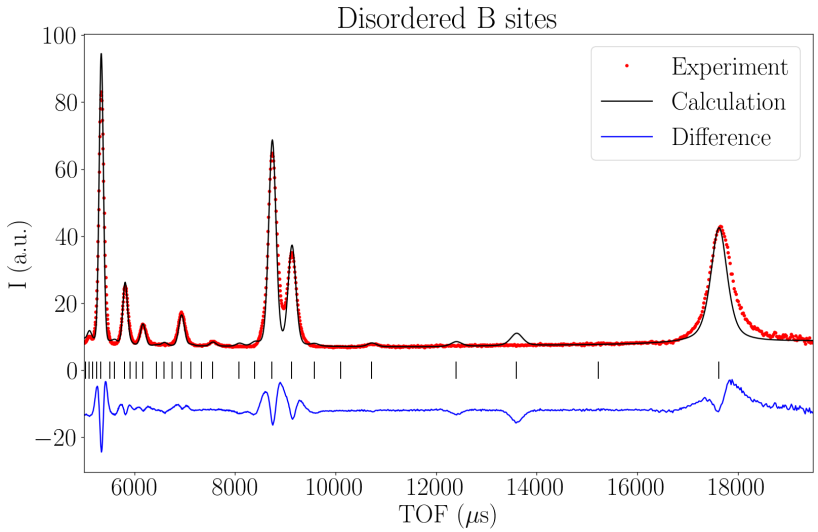

(b)

Figure 6.8: Comparison of the experimental total scattering data measured with NOMAD with the spectrum calculated using (a) a structure with a random arrangement of Sc and Nb ions in the B sites, and (b) with long range order of the lowest energy DFT structure. The black vertical markers are the Bragg positions.

is in agreement with the DFT calculations, where single unit cells of the lowest energy structure were used.

Finally, two sets of RMC fits were performed: with the entire supercell formed exclusively by the lowest energy DFT structure and with a supercell with a disorder distribution of the Sc/Nb ions on the B-sites. These RMC fits were performed only to the NOMAD reduced PDF data and the SXD (h,k,4.5) and (h,k,5.5) planes, where the intensity of the diffuse scattering is strong. However, as figure 6.9 shows, the resulting fits to the diffuse scattering are very similar, independent of the starting condition. One explanation for this is that the change in diffuse scattering between having the lowest energy DFT structure and a disordered system is small, and the RMC calculations are not sensitive enough to differentiate between both scattering patterns.

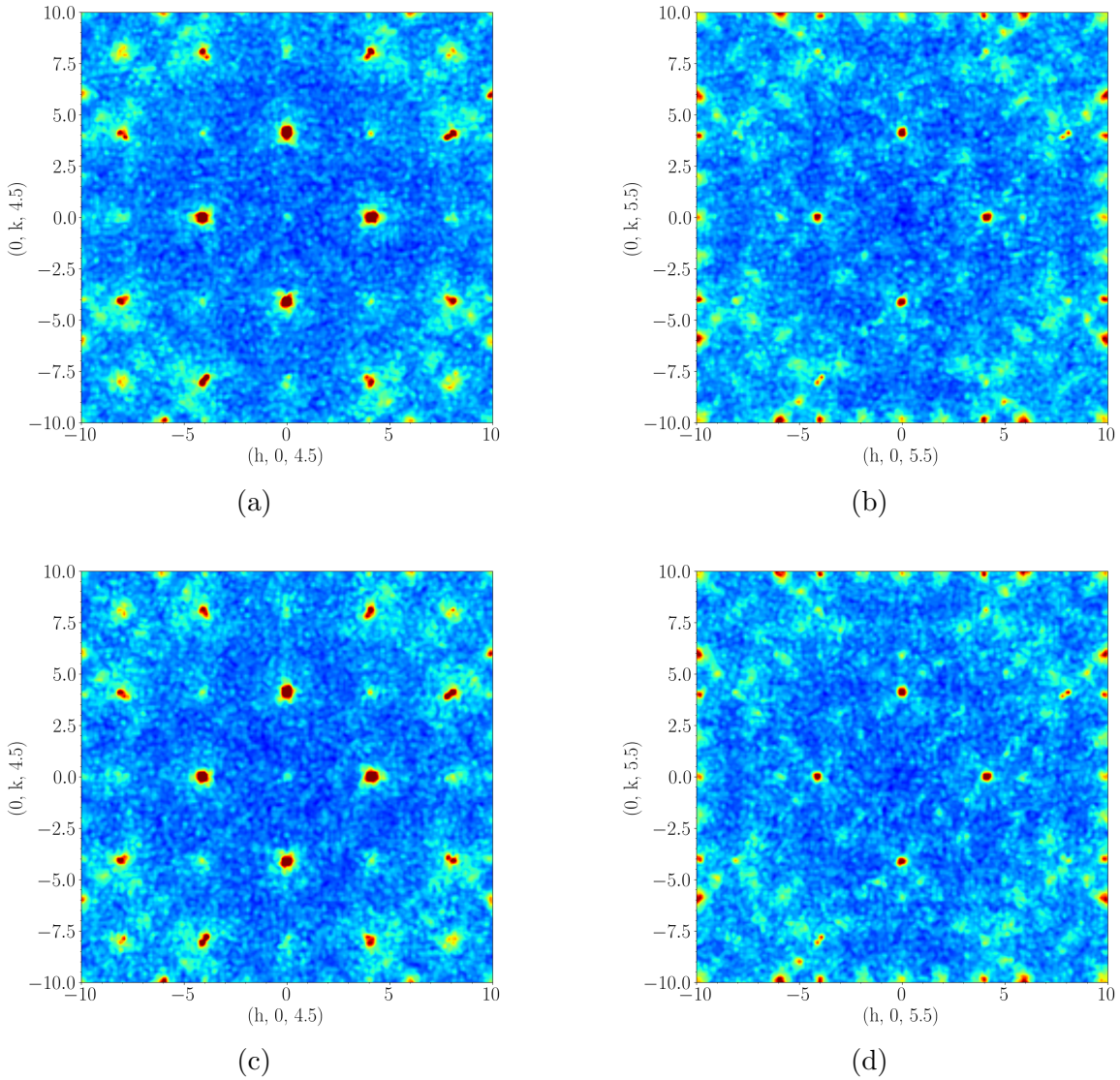

Figure 6.9: RMC fits to (left) the SXD (h,k,4.5) and (right) (h,k,5.5) scattering planes using a supercell formed (top) by a random arrangement of Sc/Nb ions on the B sites and (bottom) using a supercell formed exclusively by the lowest energy DFT structure.

6.4 Summary

Structural diffuse scattering measurements of Pr_2ScNbO_7 were performed at 4 K, 30 K and room temperature using SXD at ISIS and at 50 mK using D7 at the ILL. It was found that, due to the type of disorder, the resulting experimental data produced weak diffuse scattering masked by the presence of large Bragg peaks. As such, the analysis of the diffuse scattering was focused on the (h,k,4.5) and (h,k,5.5) planes, where the diffuse scattering is strongest and Bragg peaks weakest.

Since, in a conventional unit cell, the Sc and Nb ions can be arranged in 97 symmetrically inequivalent ways, density functional theory (DFT) calculations of all configurations were performed to study which arrangement produced the lowest energy. It was found that the configuration of Sc/Nb ions that produced the lowest energy has charge ice ordering on the tetrahedra and alternating Sc–Nb on the B-site chains. However, this structure is chemically frustrated, since the alternating chains are only observed when the lowest energy DFT structure is in particular orientations.

The diffuse scattering produced by the lowest energy DFT structure was compared with the (h,k,4.5) and (h,k,5.5) planes from the SXD experiment, producing good agreement with the experimental diffuse scattering. These calculations were performed by assuming a crystal with a perfect random distribution of Sc and Nb ions on the B-sites, but changing a unit cell of this structure by a unit cell of the lowest energy structure. The calculations were repeated multiple times, with all possible orientations of the lowest energy structure, and adding all the calculated patterns incoherently. From this, we concluded that this system must be formed by small domains, of the order of one unit cell, with the lowest energy DFT configuration, each domain being in a different orientation and with the domain walls having a random distribution of Sc and Nb ions.

Finally, total scattering measurements were performed on powder Pr_2ScNbO_7 to extract the pair distribution function (PDF) of the system. The data was compared with scattering calculated assuming a perfect random arrangement of Sc/Nb ions and assuming long range order of the lowest energy DFT structure. The latter produced extra peaks not present in the experimental data, while the former produced a much better agreement. This is further confirmation that the lowest energy DFT structure cannot form any kind of long range order. RMC fits were then performed to the reduced PDF data and the (h,k,4.5) and (h,k,5.5) planes from the NOMAD and SXD experiments respectively. Two calculations were performed: using a supercell cell with a random arrangement of Sc/Nb ions and a supercell with long range order of the lowest energy DFT structure. Both RMC calculations produced very similar results, indicative of these calculations not being sensitive enough for this kind of disorder.

Chapter 7

Magnetic defects and correlations in Pr_2ScNbO_7

The effect of disorder on the magnetic properties of Pr_2ScNbO_7 were studied by means of neutron scattering, point-charge-model (PCM) calculations and crystal electric field (CEF) fitting. The single ion magnetic properties of this system were studied using the SEQUOIA instrument from SNS. A set of CEF parameters were fitted to the data, assuming a D_{3d} symmetry, resulting in a doublet ground state with the first excited state at 2.7 meV. In addition, PCM CEF calculations were performed using the DFT structure with the arrangement of Sc and Nb ions which minimised the total energy, which contains two inequivalent Pr sites, each of them forming one-dimensional chains. The PCM calculations predicted both Pr sites to be singlets. It was proposed that, if these calculations are correct, the transverse field generated from the Sc/Nb disorder could mix the ground and first excited states of the Pr ions, generating a moment. Finally, magnetic diffuse scattering measurements were performed using the D7 instrument, producing uncorrelated scattering. These measurements were used to extract a Pr effective magnetic moment of 2.10(8) μ_B. The measured uncorrelated scattering could be due to quantum fluctuations from the one-dimensional chains, or due to the system being in a paramagnetic phase as a consequence of the large degree of disorder from the Sc/Nb ions. To differentiate between these two possibilities, low energy transfer measurements were performed with the LET spectrometer from ISIS. These measurements revealed the presence of a low energy transfer peak, believed to be a signature of quantum fluctuations in other Pr based pyrochlores [3, 4].

7.1 Introduction

One of the most compelling pieces of evidence to date of quantum spin-ice correlations has been provided by studies of $Pr_2Zr_2O_7$, where the presence of structural disorder comes into play [3, 231, 233], and $Pr_2Hf_2O_7$, where high sample purity is inferred, and it is claimed that anisotropic exchange is responsible for the quantum fluctuations [4]. Both systems have very similar crystal electric field levels, as figure 7.1 shows, both having a well separated ground state doublet with the first excited state at 9.5 meV and 9.1 meV for the $Pr_2Zr_2O_7$ and $Pr_2Hf_2O_7$ system respectively. However, in the $Pr_2Zr_2O_7$ system, Martin *et al.* [231] suggest that the presence of strains caused by magneto-elastic coupling [234] causes the ground state doublet to split into singlets in a random fashion. The wave function of both singlet states recombined in tunnel-like states by creating superpositions

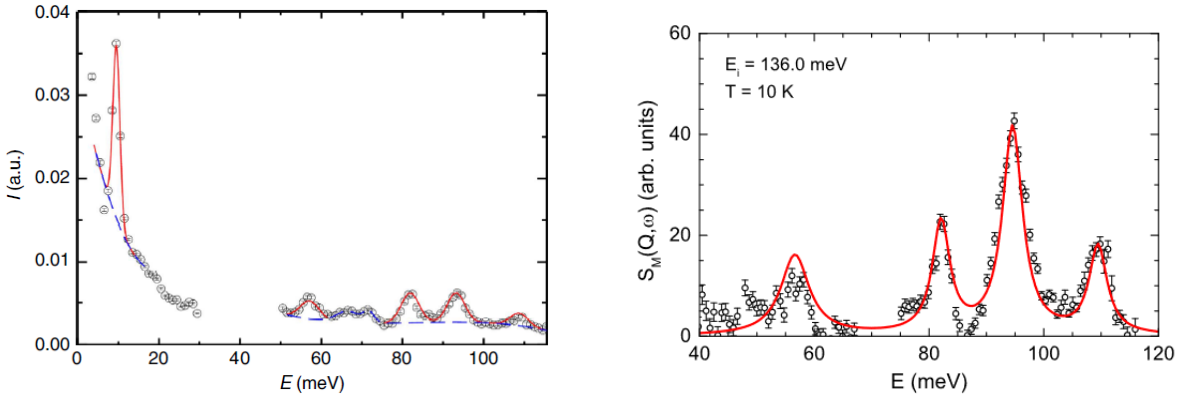

(a) (b)

Figure 7.1: (a) Inelastic neutron scattering spectrum of $Pr_2Zr_2O_7$ obtained by combining T=7.8 K data for two incident beam energies: $E_i = 40$ meV and $E_i = 120$ meV. The blue dashed line denotes fitted polynomial backgrounds. The red solid line is the calculated best fit. (b) Inelastic neutron scattering spectrum of $Pr_2Hf_2O_7$ obtained at 10 K with $E_i = 136$ meV. The red solid line is the calculated best fit. Figures acquired from [3] and [232] respectively.

within states, i.e. the new wave functions are form by superpositions of the old wave functions. Furthermore, the very low energy transfer data of the $Pr_2Zr_2O_7$ and $Pr_2Hf_2O_7$

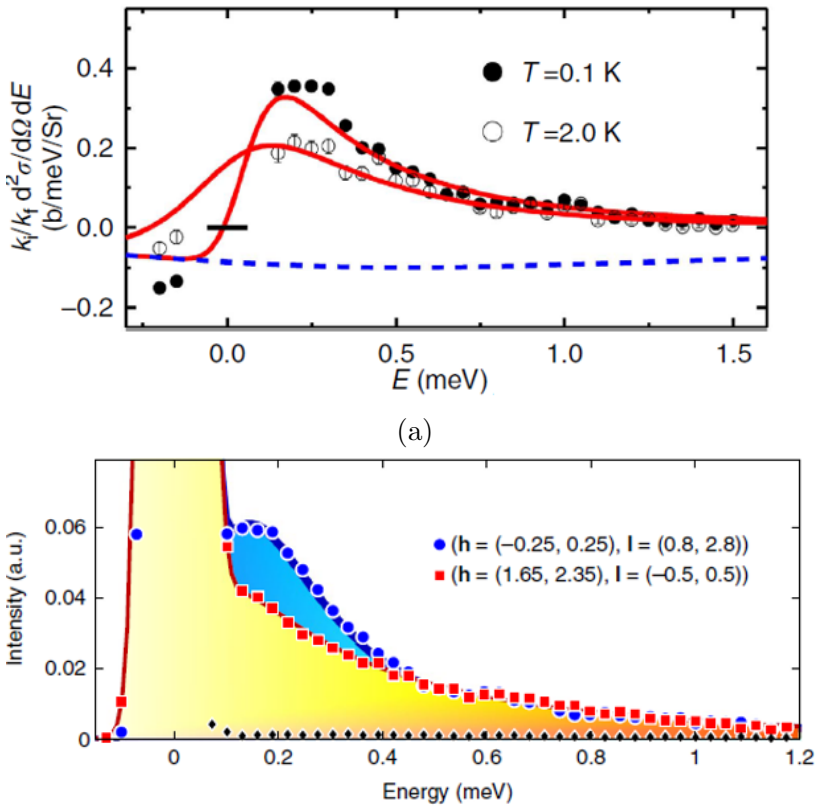

(a)

(b)

Figure 7.2: (a) Inelastic neutron scattering spectra of $Pr_2Zr_2O_7$ at Q=(0,0,3) and at T=0.1 K (solid circle) and 2.0 K (open circle) after subtraction of the 15 K data at the same Q. (b) Inelastic neutron scattering spectra of $Pr_2Hf_2O_7$ at T=0.05 K. Figures acquired from [3] and [4] respectively.

samples, shown in figure 7.2, highlight the existence of an extra feature at around 0.2 meV, which was interpreted for both systems as a signature of cooperative quantum fluctuations [235].

Finally, Wen *et al.* [233] and Sibille *et al.* [4] performed studies of the magnetic diffuse scattering in the (h,h,l) plane on the $Pr_2Zr_2O_7$ and $Pr_2Hf_2O_7$ systems with different neutron energy transfers, as figure 7.3 shows. At zero energy transfer (elastic channel) pinch points are still visible (see figure 1.26a for $Pr_2Hf_2O_7$), but as the energy transfer is increased, the pinch points broaden until the starfish like structure shown for an energy transfer of 0.2 meV appears. At much higher energy transfers, the scattering becomes featureless, as it is shown for an energy transfer of 0.5 meV. Wen *et al.* [233] claimed that this is due to the continuum of fractional excitations which, just as with the excitation found at 0.2 meV in both systems, is associated with quantum fluctuations.

To separate the contribution from structural disorder and anisotropic exchange, the highly substituted Pr_2ScNbO_7 system was studied. The strain from the difference in

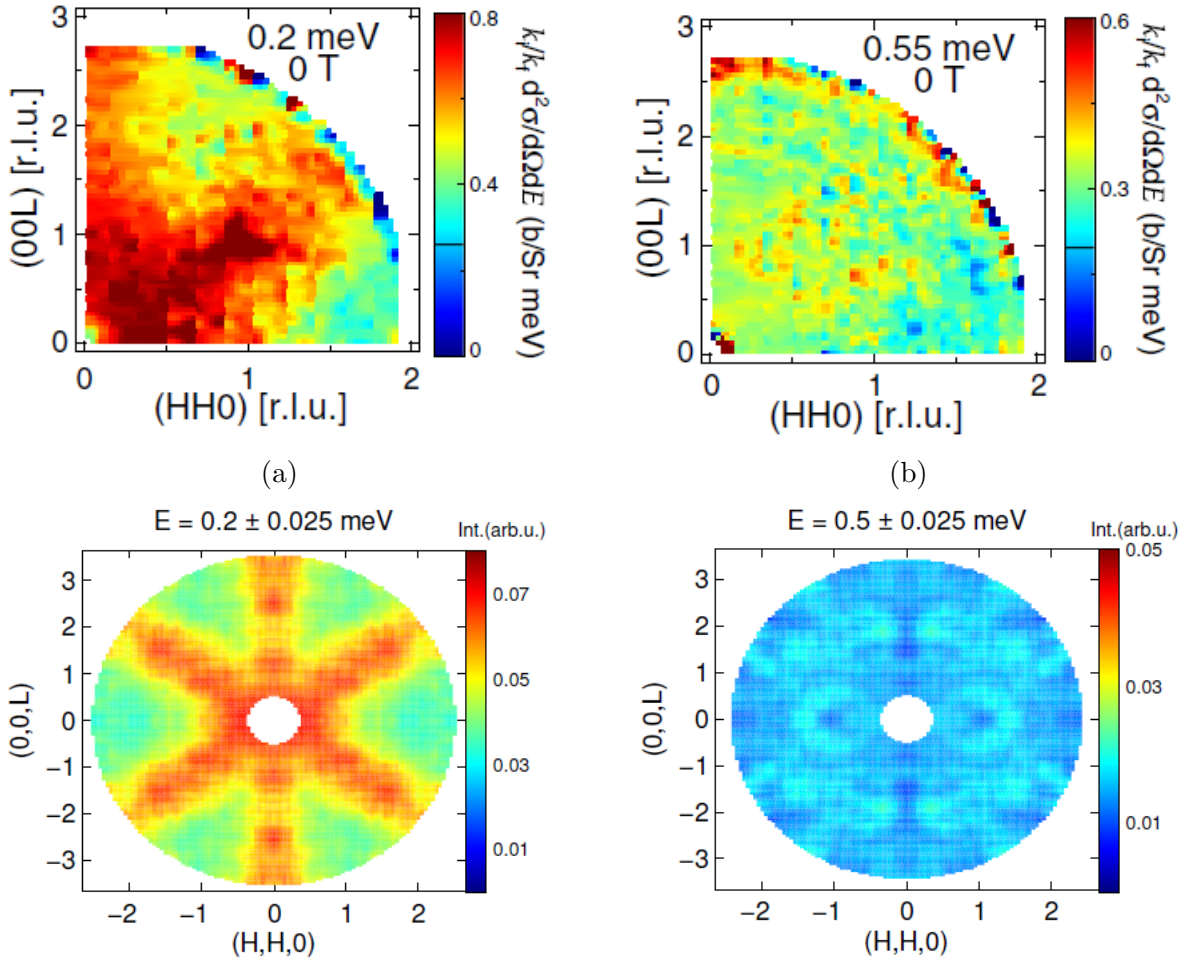

Figure 7.3: Scattering data of $Pr_2Zr_2O_7$ in the (h,h,l) plane at the fixed energy transfers of (a) 0.2 meV and (b) 0.55 meV. Scattering data of $Pr_2Hf_2O_7$ in the (h,h,l) plane at fixed energy transfers of (c) 0.2 meV and (d) 0.5 meV. For both systems the data were collected on single-crystal samples using time-of-flight inelastic neutron scattering at 50 mK with unpolarised neutrons. Figures (a) and (b) acquired from [233] and figures (c) and (d) acquired from [4].

the ionic radii and the modulation in charge from the Sc^{3+} and Nb^{5+} ions will tune the exchange and the CEF with the prospect of inducing novel quantum spin liquid behaviour.

This chapter presents magnetic neutron scattering data on the quantum spin liquid candidate Pr_2ScNbO_7. I will present magnetic excitation measurements performed using the SEQUOIA instrument from SNS to study the single-ion magnetic properties of the system. The CEF excitations were analysed by performing individual fits to the data and point charge calculations using the lowest energy DFT structures from the previous chapter. To study the magnetic correlations in this system, diffuse scattering measurements were performed on a single crystal using the D7 instrument at the ILL. From the analysis of these data, further study of the low energy excitations were performed using the LET spectrometer at ISIS.

7.2 CEF excitation measurements

To study the effect of the strains due to the B-site disorder on the single-ion magnetism of Pr ions, CEF measurements were performed on a Pr_2ScNbO_7 powder sample using the SEQUOIA instrument at SNS in the USA. All of the data acquired with SEQUOIA shown in this section is on an absolute scale, normalised to a monochromatic vanadium measurement. A non-magnetic La_2ScNbO_7 powder sample was also measured to subtract the phonon contribution from the magnetic Pr_2ScNbO_7 sample. A benefit of the proximity of Pr to La in the periodic table is that it is not necessary to correct for mass difference by performing DFT calculations of the phonon density of states. As such, the La_2ScNbO_7 data, multiplied by a self-shielding factor if needed, can be directly subtracted from the Pr_2ScNbO_7 sample to remove the phononic contribution. All the samples were grown by Dharmalingam Prabhakaran using the floating zone method at the Clarendon Laboratory, Oxford University.

Both powder samples were measured at 5 K with incident energies of 11.5 meV, 25 meV, 60 meV, 120 meV, 350 meV and 500 meV, and at 30 K with incident energies of 25 meV, 60 meV and 120 meV. The $S(\mathbf{Q},\omega)$ spectra for Pr_2ScNbO_7 are compared with those of La_2ScNbO_7 with $E_i = 25$ meV and 120 meV at a temperature of 5 K in figure 7.4. The phonon corrected data was obtained by subtracting the La_2ScNbO_7 data directly from the Pr_2ScNbO_7 data, and the resulting plots of $S(\mathbf{Q},\omega)$ are shown for $E_i = 25$ meV and 120 meV at 5 K in figure 7.5. One-dimensional plots of intensity as a function of energy transfer integrated over the full range of Q are also shown.

CEF fits were performed to the phonon corrected data to extract the CEF levels of the Pr ions. Despite the presence of the disorder, and for simplicity, it was assumed that the Pr environment still maintained a D_{3d} symmetry. Thus, only 6 CEF parameters were needed to fit a Pr CEF-Hamiltonian to the data. Since Pr^{3+} has $J = 4$ and it is a non-Kramers ion, only 6 levels are allowed (ground state and 5 excited states), 3 doublets and 3 singlets [160]. From figure 7.5a, it is clear that the features around 2.5 meV, 6.5 meV and 13.5 meV are magnetic, since the decrease in intensity with Q is the same as the Pr^{3+} magnetic form factor squared, as figure 7.6 shows. Figure 7.5b contains multiple extra features that could possibly be magnetic. The features near 57.5 meV and 90 meV are also magnetic, since the intensity decay with Q is the same as the Pr^{3+} form factor squared, as figure 7.6 shows. The one-dimensional cuts shown in figure 7.6 were extracted by integrating in energy the intensity as a function of Q around the energy where the features are found. It was found that the best comparison resulted when the upper and lower limits of the energy integration were 1–2 meV away from the location of the feature.

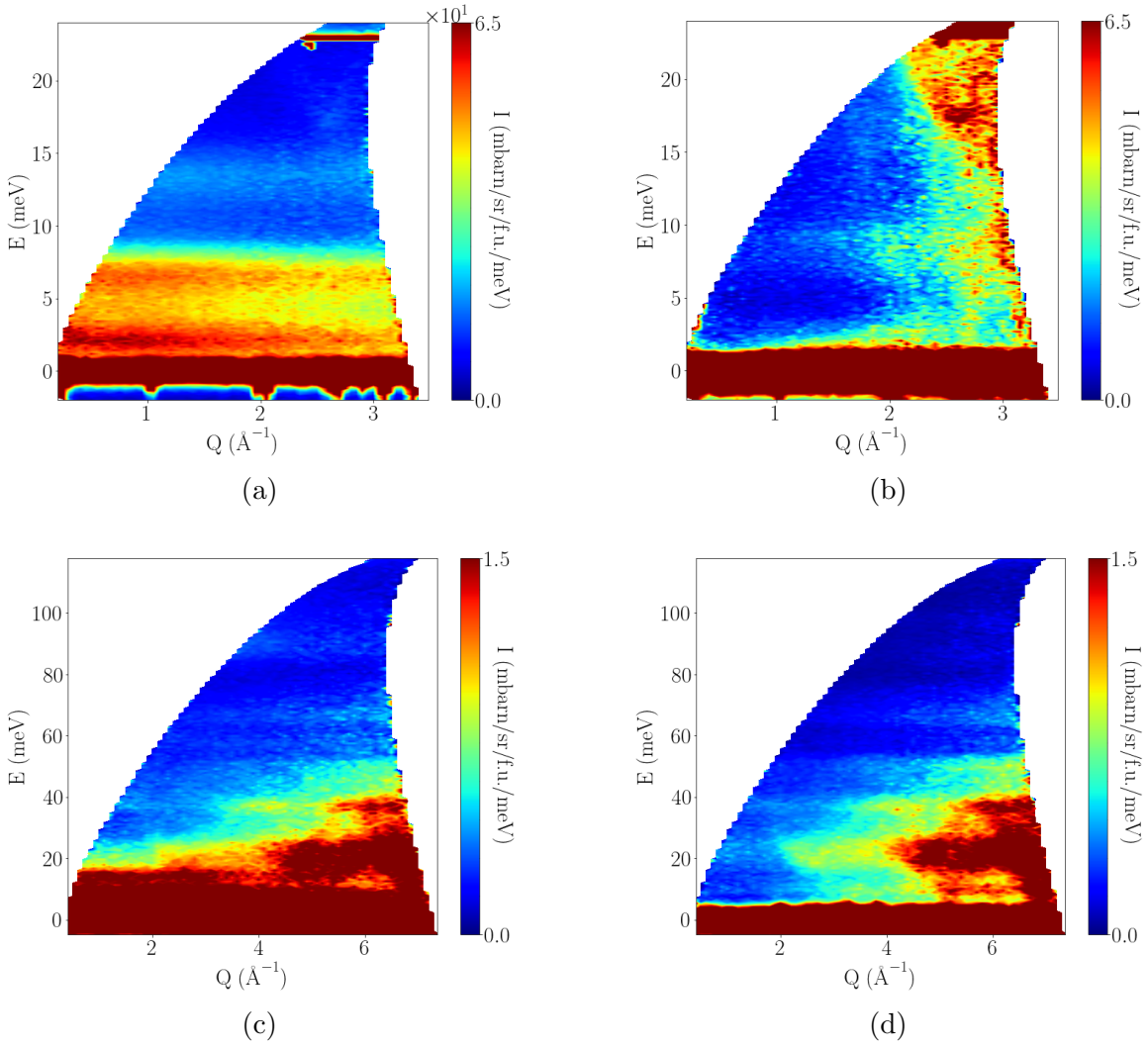

Figure 7.4: Inelastic scattering data of (left) Pr_2ScNbO_7 and (right) La_2ScNbO_7 at 5 K with an incident energy of (top) 25 meV and (bottom) 120 meV acquired with SEQUOIA.

The three additional features at 45 meV, 75 meV, 105 meV were excluded from the fit. The faint features at 75 meV and 105 meV were difficult to differentiate from the strong 57.5 meV and 90 meV peaks or to compare with the Pr^{3+} magnetic form factor. Similarly, the data around 45 meV was very noisy, and thus it was difficult to compare with the Pr^{3+} magnetic form factor. Figure 7.7 shows the phonon corrected Pr_2ScNbO_7 data with incident energies of 120 meV at a temperature of 30 K. The fact that the intensity of the 45 meV feature increases with temperature is inconsistent with a purely magnetic excitation from the ground state.

Hence, in the initial modelling and for simplicity, it was assumed that only the 2.5 meV, 6.5 meV, 13.5 meV, 57.5 meV and 90 meV excitations are real magnetic features and the rest can be treated as a background. A convolution of a Gaussian and Lorentzian was assumed for the shape of the peaks, with the Gaussian width given by the instrument resolution and the Lorentzian width being a fitting parameter. Since the resolution of the $E_i = 120$ meV data at low energy transfers is not as good as the resolution of the $E_i = 25$ meV data at the same energy transfers, the data used in the fitting was formed by combining the $E_i = 25$ meV data (0 meV to 23 meV energy transfer) with

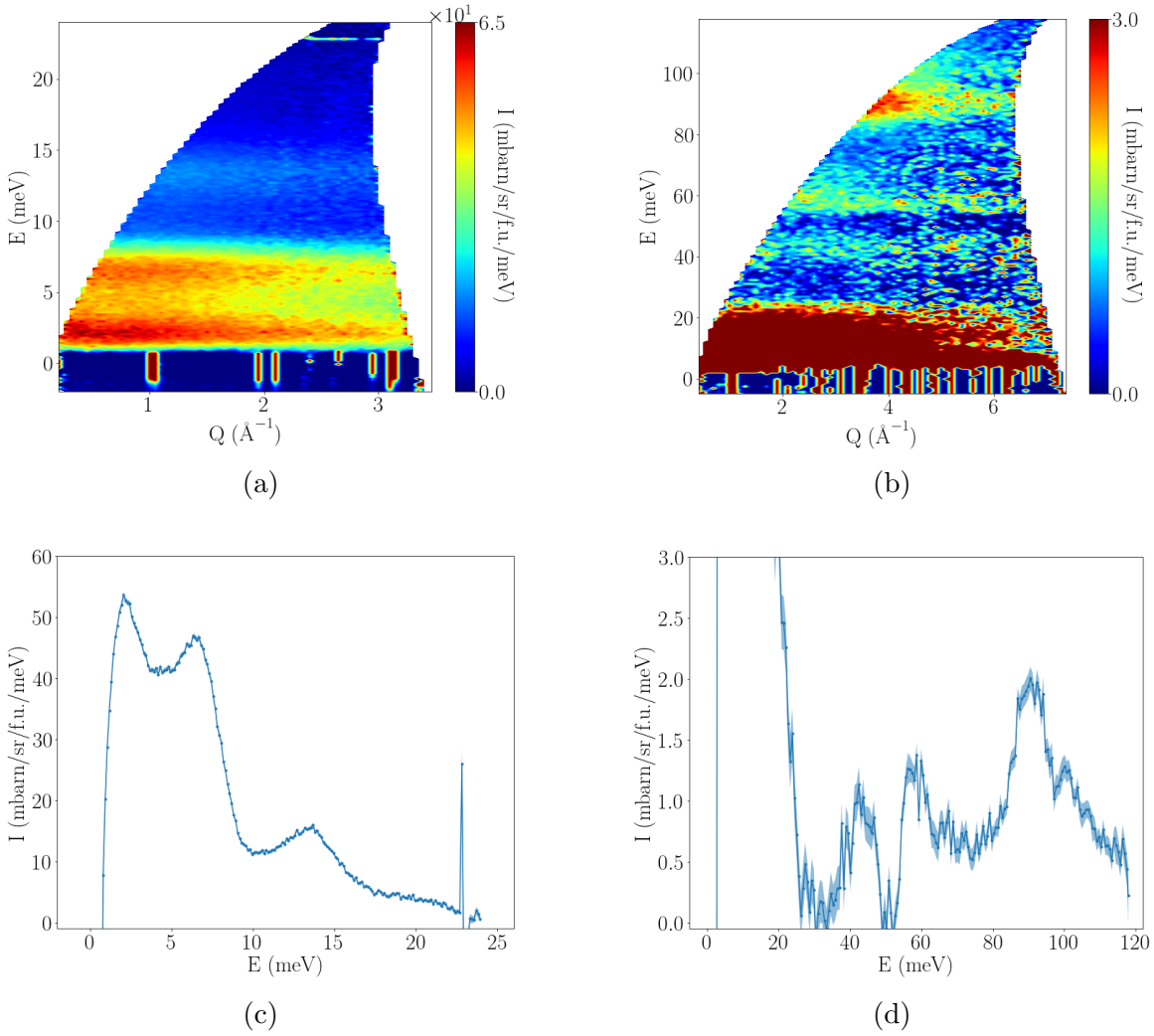

Figure 7.5: Phonon corrected Pr_2ScNbO_7 data at 5 K acquired with SEQUOIA with incident energies of (a) 25 meV and (b) 120 meV. Intensity as a function of energy spectrum integrated over the full Q range measured at 5 K with incident energies of (c) 25 meV and (d) 120 meV.

the $E_i = 120$ meV data (23 meV to 116 meV energy transfer). The resulting fit is shown in figure 7.8, the fitted B-parameters in table 7.1 and the calculated energy levels in table 7.2. This analysis suggests that not only the ground state is a magnetic doublet, but also it is composed almost entirely of the $|J, J_z\rangle = |4, \pm 4\rangle$ state, just like the Pr^{3+} in $Pr_2Zr_2O_7$. This means that, under the assumption that the D_{3d} symmetry is preserved, the magnetic moments of this system have a strong $\langle 111 \rangle$ Ising anisotropy, as in a classical spin ice systems.

Finally, as it can be seen in figure 7.8, a complex background had to be chosen to get a good fit to the data. It is possible that, due to the disorder, the Pr ions sit in multiple environments, each with a different distortion of the surrounding O ions due to the Sc/Nb arrangement, and thus each producing a different CEF spectrum. This would mean that the energy levels in table 7.2 correspond to the levels of Pr in the most common environment, with sharper features, while the background is formed by the CEF contribution from other less common environments, with broader features. This would explain the presence of the peak like feature around 6 meV in figure 7.8 needed for the background. A similar argument was also used by Mauws *et al.* [236] when studying

Nd_2ScNbO_7, where a set of CEF excitations sat on top of a much broader excitation. This is consistent with the findings in the previous chapter of having small domains of the lowest energy DFT structure with a random arrangement of the Sc/Nb ions in the domain walls.

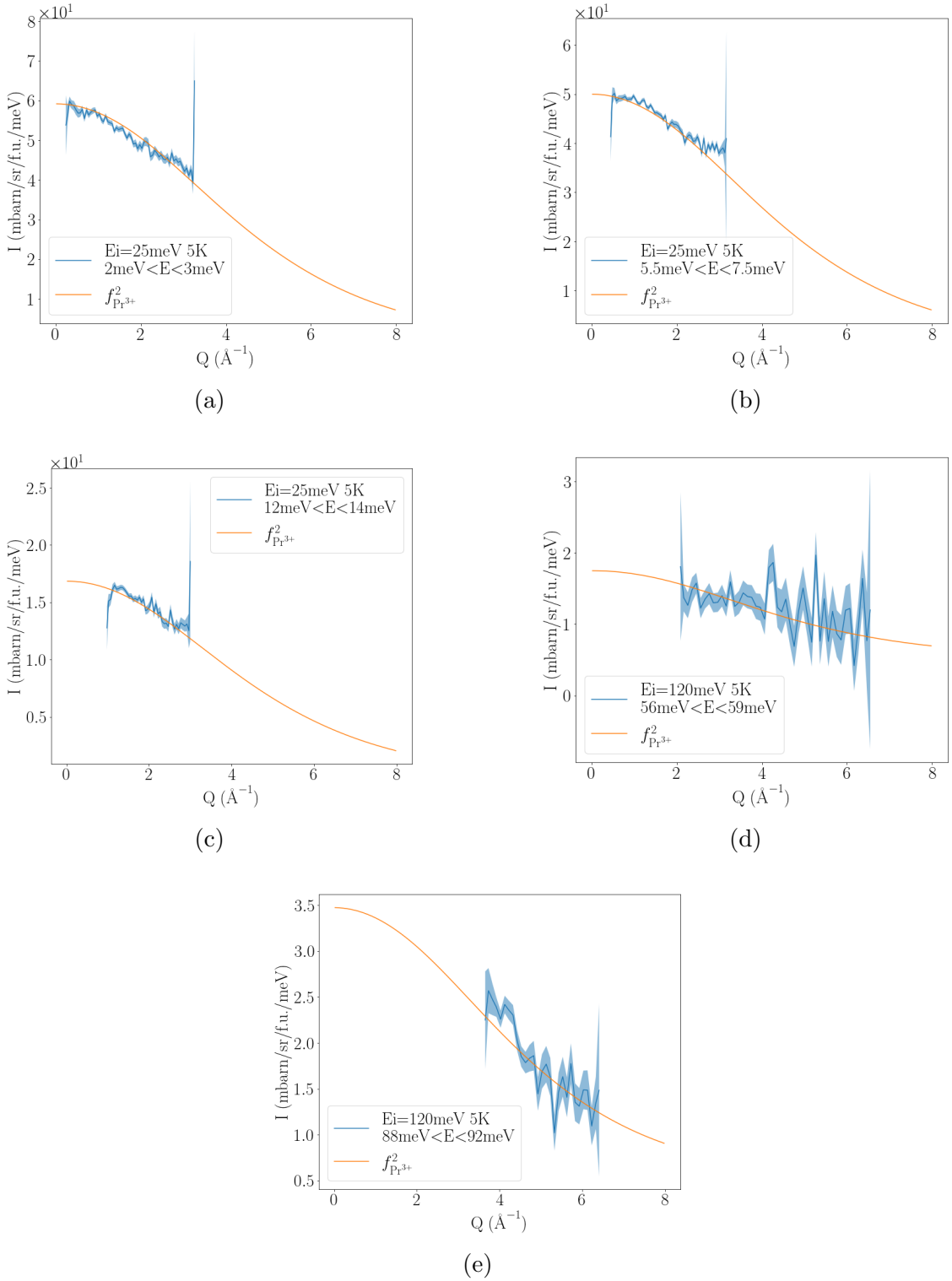

Figure 7.6: Comparison between the form factor of Pr^{3+} and one-dimensional plots of intensity as a function of Q integrated over a small energy range around the (a) 2.5 meV, (b) 6.5 meV, (c) 13.5 meV, (d) 57.5 meV, (e) 90 meV features of the data in figure 7.5.

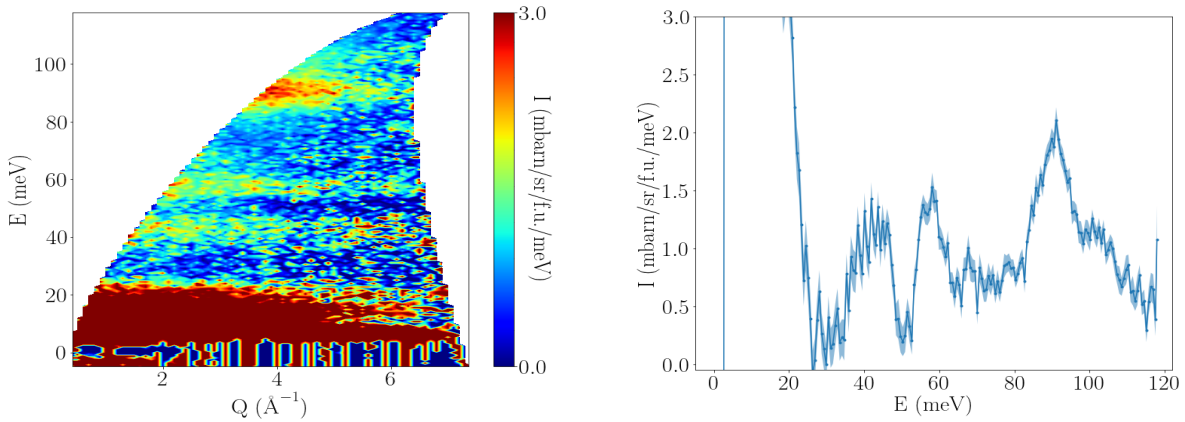

(a) (b)

Figure 7.7: (a) Phonon corrected Pr_2ScNbO_7 data at 30 K acquired with SEQUOIA with incident energies of 120 meV. (b) Intensity as a function of energy spectrum extracted by integrating through the full Q range.

In addition to this fit, point-charge-model (PCM) calculations were also performed using the lowest energy DFT structure discussed in the previous chapter. According to the DFT, two inequivalent Pr sites exist, each one having the nearest neighbour O(1) and O(2) ions at different distances, as it can be seen in figure 7.9. Furthermore, both Pr sites had a disordered arrangement of O ions, and thus none of them preserved the D_{3d} symmetry. This not only meant that in the PCM calculations all the available CEF parameters could be used, but also that all the energy levels become singlets. In the real system, the presence of distortions intrinsic in the lattice could make the Pr ions non-magnetic. A similar effect was observed by Foronda *et al.* [237] in $Pr_2Zr_2O_7$, where the distortions due to muons also invoke singlet ground states. Since Pr^{3+} is a non-Kramers ion, both of the Pr ions in the lowest energy DFT structure are non-magnetic. This is consistent with the $Pr_2Zr_2O_7$ system where, by virtue of the magneto-elastic coupling, the strains split the non-Kramers doublet of the rare-earth ions in a random fashion [231]. The energy levels for both Pr sites are shown in table 7.3.

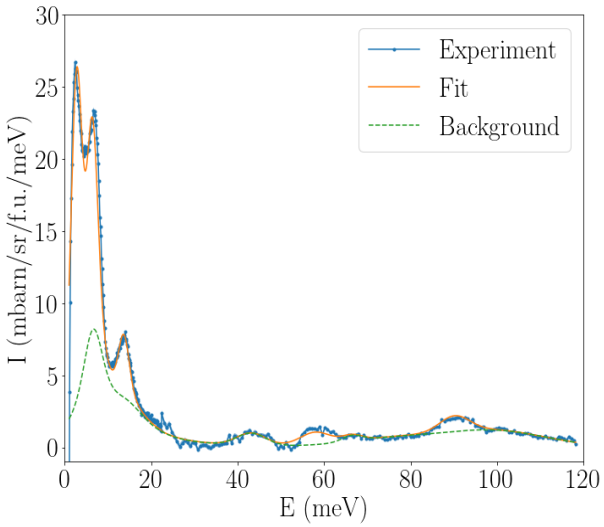

Figure 7.8: Fit to the phonon corrected Pr_2ScNbO_7 data at 5 K acquired with SEQUOIA showing the used background. Spectrum obtained by combining the $E_i = 25$ meV data with the $E_i = 120$ meV data.

Table 7.1: Fitted B-parameters of Pr in meV.

B_2^0	B_4^0	B_4^3	B_6^0	B_6^3	B_6^6
-0.81(1)	-0.0095(6)	-0.21(2)	0.0015(3)	-0.008(2)	-0.0012(5)

Table 7.2: Energy levels of the Pr ions in meV from the fitted B-parameters assuming a D_{3d} symmetry. The first column contains the energy levels of the doubly degenerate states, while the second column contains the levels of the singly degenerate states.

Doublet	Singlet
0.0	2.73106
57.9158	6.3775
90.1777	13.6608

The excitation spectrum produce by the lowest energy DFT structure was calculated and compared with the experimental data. This calculation was also performed for an average of all possible Sc/Nb configurations, where the spectra produced by the Pr ions in each of the 97 DFT structures was computed. With this, the average of all spectra, weighted by the number of realisations for each Sc/Nb arrangement, was calculated. This average structure spectrum was assumed to be equivalent to the spectrum produced by a system with a perfectly disordered arrangement of Sc and Nb ions on the B-sites. As figure 7.10 shows, the low energy DFT structure produces an excitation spectrum with features that, while not at the correct locations and not with the correct intensities, are qualitatively similar to the ones from the experimental data. The similarities between the PCM calculation and the experiment are especially pronounced at low energy transfers. Furthermore, the average structure spectrum is similar to the background chosen to fit the data from figure 7.8. A possible explanation for this is that this system has some short range order that gives us the main peaks, but it is sitting on top of something relatively random. This is consistent with the idea proposed of having domains containing the lowest energy DFT structure, and the domain walls having a random arrangement of Sc/Nb ions on the B-sites. It is worth noting that one feature that the low energy DFT structure spectrum and the average structure spectrum have in common is the lack of a

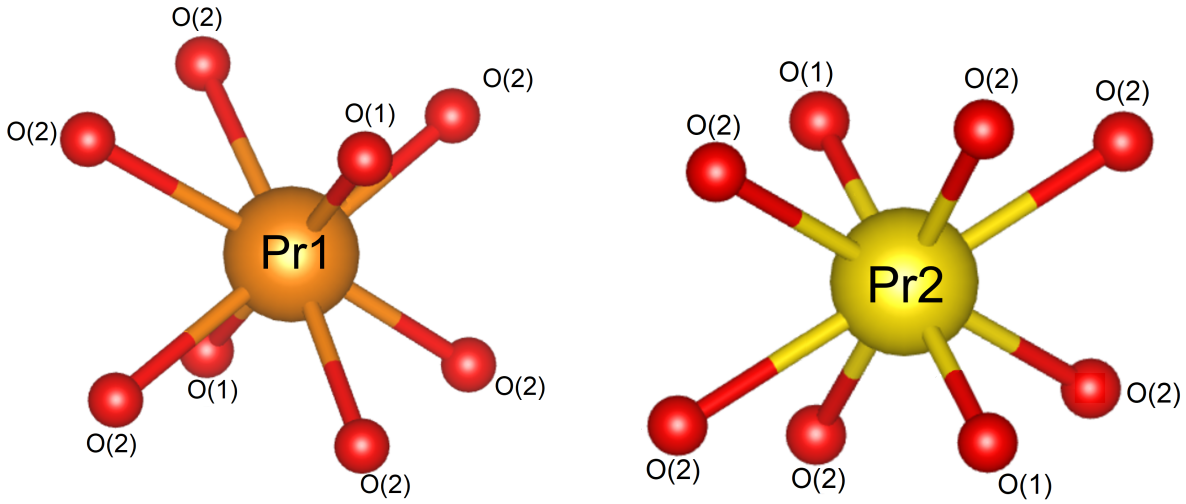

(a) (b)

Figure 7.9: The two Pr environments found by CASTEP in the lowest energy DFT structure.

Table 7.3: Energy levels of the two inequivalent Pr sites in the lowest energy DFT structure.

Pr1 (meV)	Pr2 (meV)
0	0
1.203	4.567
24.232	12.874
62.830	60.636
71.669	70.896
100.476	92.817
115.471	97.635
117.235	112.523
122.851	116.987

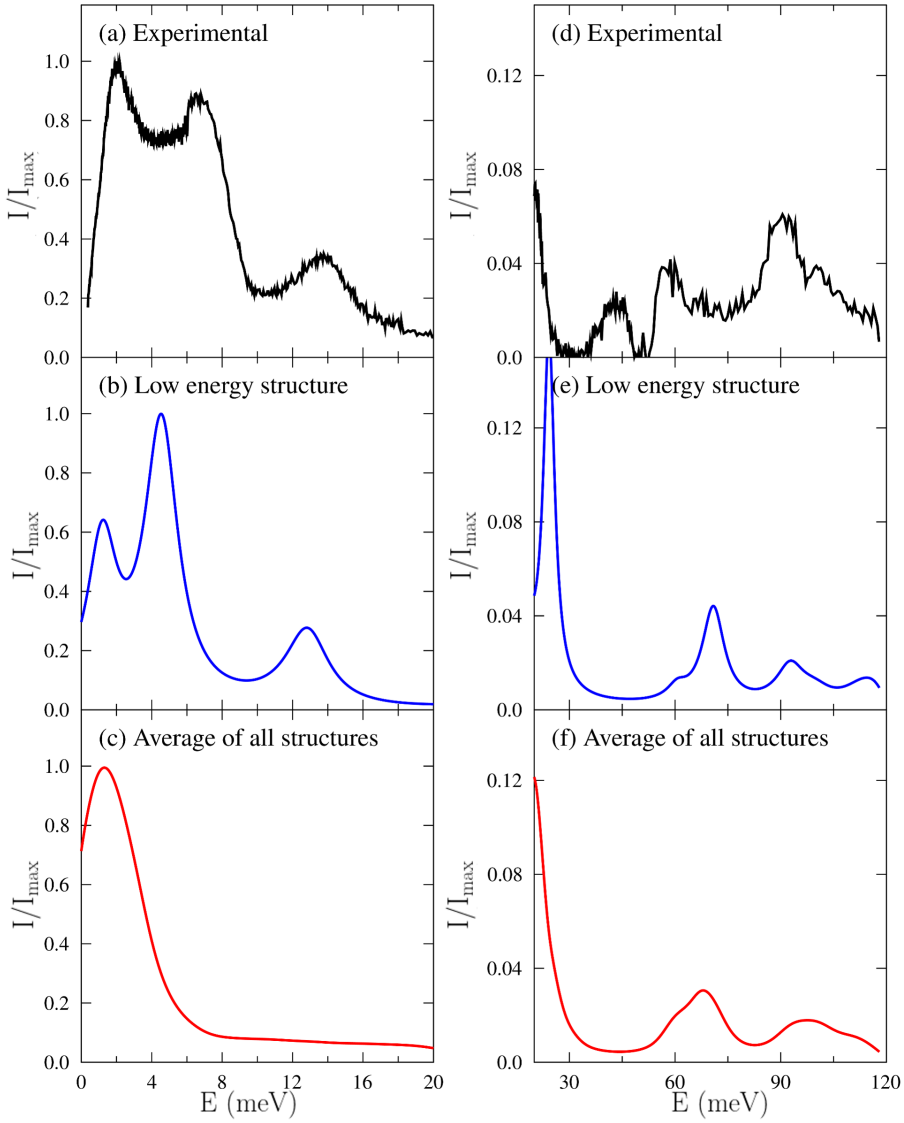

Figure 7.10: Comparison of the normalized experimental inelastic data of Pr_2ScNbO_7 acquired with SEQUOIA with the PCM calculation using the lowest energy DFT structure and an average of all 97 structures. (a) to (c) for the $E_i = 25$ meV data and (d) to (f) for the $E_i = 120$ meV data.

peak around 45 meV. This could be indicative that, as previously discussed, this feature is not of pure magnetic origin.

From these PCM calculations, it could be that the first excited state from the CEF fitting corresponds to the Pr1 first excited state, the second excited state from the fitting corresponds to the Pr2 first excited state and the third excited state from the fitting corresponds to the Pr2 second excited state. One issue with these PCM calculations is that both of the Pr ions have a singlet ground state, and therefore should be non-magnetic. However, the D7 experiment discussed below clearly shows a magnetic signal in the magnetic cross-section. One possible explanation for this is that the system is mixing the ground state and first excited state, which could generate a magnetic moment. This is very similar to the Ho ions next to a vacancy in HTSO and will be explained in more detail later on in this chapter.

7.3 Magnetic diffuse scattering

Knowing the effects of the disorder on the single ion magnetism of this system, a 7.05 g single crystal of Pr_2ScNbO_7 was studied with the D7 diffractometer at the ILL to determine the effects of the disorder on the cooperative magnetism of the system. The crystal was grown by Dharmalingam Prabhakaran using the floating zone method at the Clarendon Laboratory, Oxford University. Since the plane of interest was the (h,h,l) plane, the Laue diffractometer OrientExpress was used to properly align the sample. Figure 7.11 shows the aligned sample on the sample mount, where the crystal is covered in copper foil to improve thermal contact and a brass screw is used to hold the sample in the correct orientation. The reason the mount is holding the crystal from the middle and not from one end is due to the large tilt and the size of the sample environment. The dilution fridge insert used in this experiment has a diameter of around 36 mm. If this crystal was attached to the sample mount by one end, the circle formed by the other end of the crystal as it is rotated would have a diameter larger than the dilution insert. Thus, the sample mount shown in the figure was constructed to shift the centre of rotation. An issue with this sample mount is that the sample now has an irregular shape and, at certain

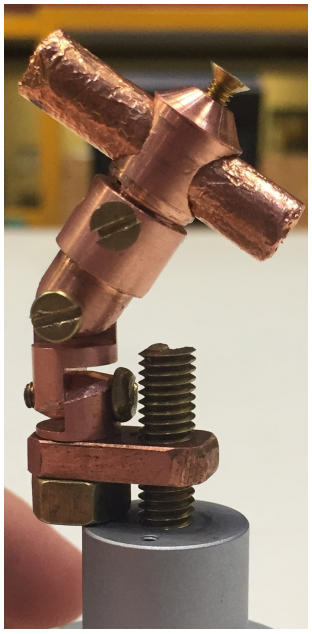

Figure 7.11: Single crystal Pr_2ScNbO_7 on its mount.

orientations, the beam of neutrons will need to traverse the screw and part of the sample mount before reaching the crystal. As it will be shown, this will have an effect on the final scattering.

Measurements were performed with a neutron incident wavelength of 4.8 Å and rotating the sample in steps of 1°. According to susceptibility measurements performed by Kimura *et al.* [3] on $Pr_2Zr_2O_7$, Pr^{3+} has a magnetic moment of 2.5 μ_B, 4 times smaller than the magnetic moment of the Ho ion or, due to the μ_B^2 dependence of the magnetic intensity [46], a magnetic intensity 16 times weaker. As such, the Pr_2ScNbO_7 single crystal was measured only at 50 mK for an entire week using XYZ polarisation analysis (XYZ-PA) to get good data and statistics. The resulting measured magnetic, structural and nuclear spin-incoherent scattering cross-sections are shown in figure 7.12, extracted using equations (2.74) for a single crystal.

In this system, the spin-incoherent scattering can arise from the Pr, O, Nb and Sc

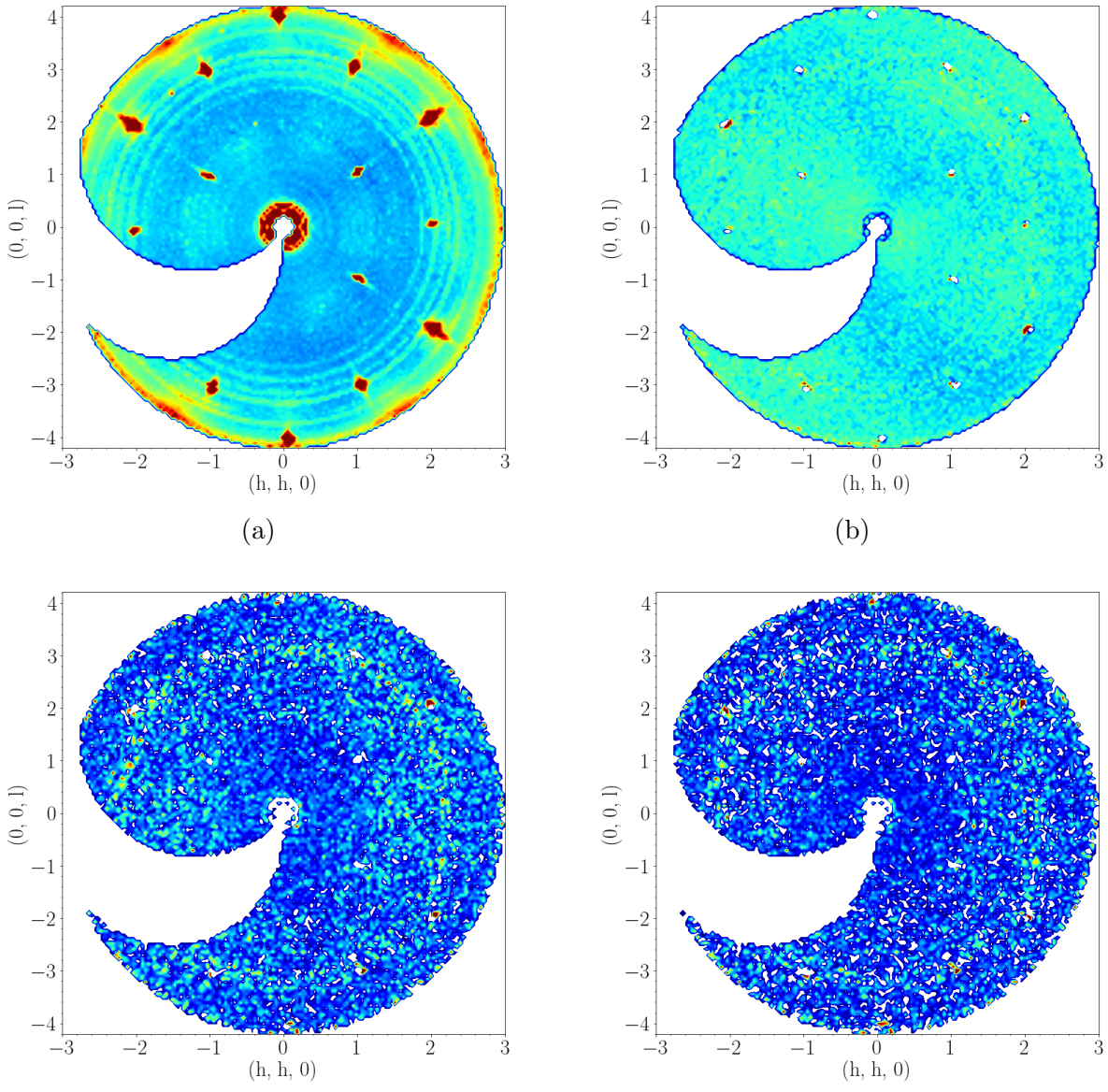

Figure 7.12: (a) Structural, (b) spin-incoherent, (c) $M_{\perp y}$ and (d) $M_{\perp z}$ scattering of Pr_2ScNbO_7 at 50 mK acquired with D7 at the ILL.

in the sample, from the Cu in the sample mount and from the Zn in the brass screws holding the sample. Of all these, the ion with the largest spin-incoherent cross-section is Sc, with Cu an order of magnitude lower and the rest being negligible. The absence of correlations means that the intensity of spin-incoherent scattering is expected to be flat. However, as figure 7.12b shows, the spin-incoherent data is not flat, but it has regions with higher and lower intensity which approximately match the high and low intensity regions of the magnetic and structural scattering. Upon further investigation, it was found that this change in intensity is due to absorption. Because the spin-incoherent scattering is dominated by scattering from the sample, the spin-incoherent scattering was used to correct for absorption by dividing the different scattering cross-sections by it. This can be understood as follows. The measured spin-incoherent is given by the real spin-incoherent, which is flat, with absorption. The measured magnetism is also given by the real magnetism and that same absorption. By dividing the measured magnetism over the measured spin-incoherent scattering, the absorption is cancelled out, and since the spin-incoherent is flat, dividing the real magnetism by the real spin-incoherent simply gives the real magnetism. The same procedure follows for the structural scattering. However, the spin-incoherent data shown in figure 7.12b were not used to correct the data, since these data are very noisy. Instead, a phenomenological function was fitted to the spin-incoherent data to smooth the features, and the resulting fit was used to correct the magnetic and structural data.

The resulting corrected structural and magnetic diffuse scattering cross-sections are shown in figures 6.3 and 7.13 respectively. As the figure shows, apart from some additional scattering that can be attributed to noise and bad correction from the background subtraction and the mount, the magnetic diffuse scattering seems to be featureless, with all the features observed previously for $Pr_2Zr_2O_7$ and $Pr_2Hf_2O_7$ [3, 4, 233], such as the pinch points in the elastic scattering channel and the starfish-like pattern in the inelastic line shown in figure 7.3, absent.

Furthermore, the powder average of the magnetic data, shown in figure 7.13c, also does not have any strong variations in the intensity with Q. These data were extracted by first combining the magnetism in two directions using $\sqrt{M_{\perp y}^2 + M_{\perp z}^2}$, and averaging all the intensities at the same Q value. The powder average data was compared with the Pr^{3+} magnetic form factor squared, as figure 7.13c shows. If the spins were uncorrelated, such as for a paramagnet or uncorrelated quantum fluctuations, the Q dependence would follow the magnetic form factor from a single ion [46]. While this seems to be the case for this system, since the comparison in the figure shows a good agreement between the experimental data and the magnetic form factor, the data is very noisy to exclude the possibility of the data not following the magnetic form factor indicating other forms of cooperative magnetism. Assuming good agreement between the powder averaged data and the magnetic form factor, the effective Pr magnetic moment μ_{eff} was extracted using [46]

$$\frac{\mathrm{d}\sigma}{\mathrm{d}\Omega}(|\mathbf{Q}| = 0) = \frac{2}{3}\left(\frac{\gamma r_0}{2}\right)^2 \mu_{\text{eff}}^2 \tag{7.1}$$

where, from figure 7.13c, $\frac{\mathrm{d}\sigma}{\mathrm{d}\Omega}(|\mathbf{Q}| = 0) \approx 0.42(5)$ barn/sr/f.u., $r_0 = 2.818$ fm and $\gamma = 1.913$. This gives, for the 7.05 g crystal used in this experiment, a Pr effective magnetic moment of $\mu_{\text{eff}} = 2.10(8)\ \mu_{\text{B}}$, close to the 2.5 μ_{B} measured by Kimura *et al.* [3] from the susceptibility measurements of $Pr_2Zr_2O_7$.

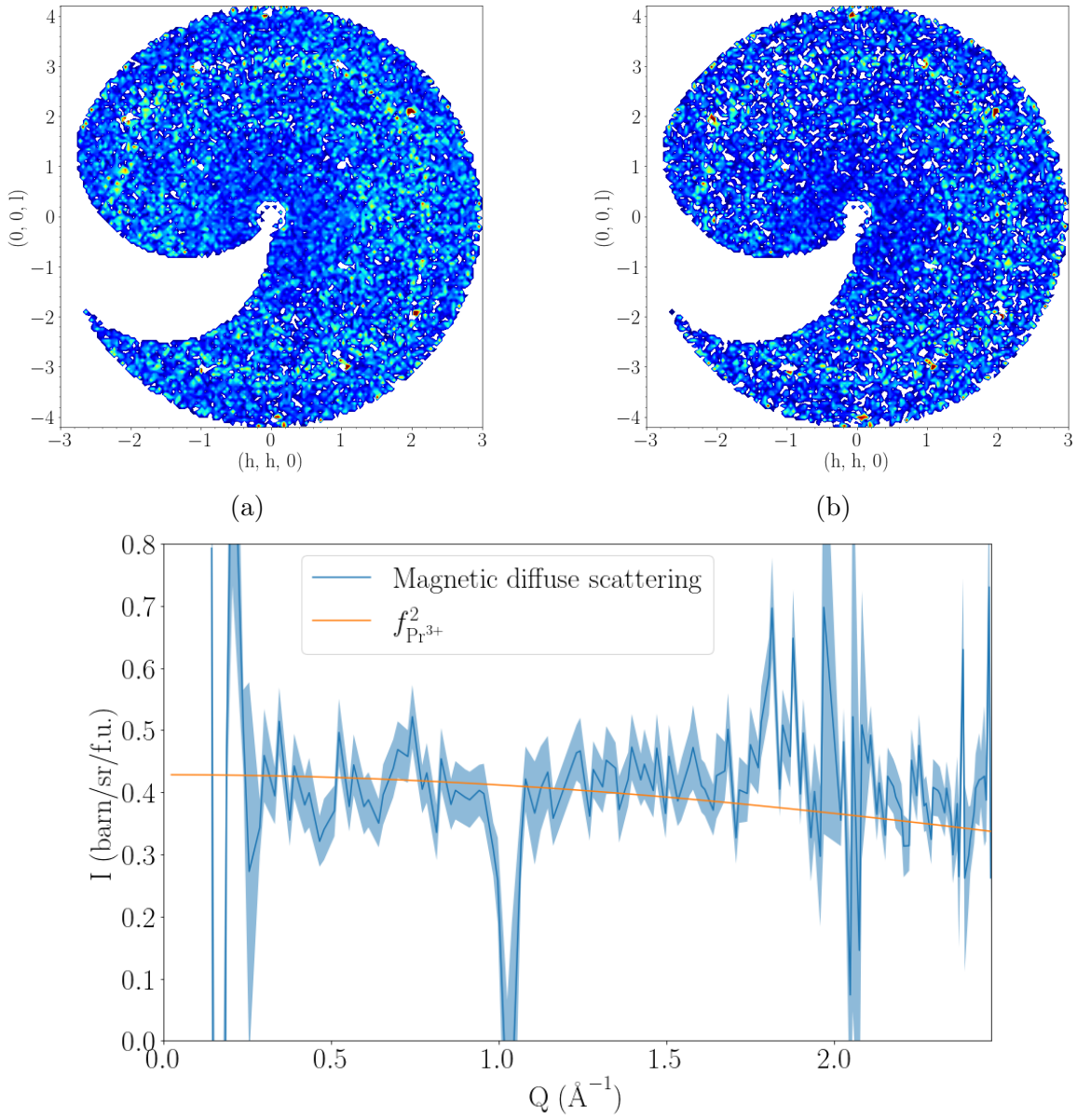

Figure 7.13: Corrected (a) $M_{\perp y}$ and (b) $M_{\perp z}$ scattering acquired with D7. (c) Comparison of the powder average corrected magnetic diffuse scattering data of Pr_2ScNbO_7 with the form factor of Pr^{3+}. The data shown in (c) is in absolute units.

As it was shown in the introduction of this chapter, three distinct regimes exist in the magnetic diffuse scattering of $Pr_2Zr_2O_7$ and $Pr_2Hf_2O_7$: the elastic line where pinch points are visible [3, 4], with an energy transfer of 0.2 meV where a starfish-like pattern emerges [4, 233], and with an energy transfer of 0.5 meV where the scattering is featureless which is attributed to uncorrelated quantum fluctuations [4, 233]. In the D7 experiment, on the other hand, the energy analysis option was not used. Since the neutrons used in the experiment had an incident wavelength of around 4.8 Å, the intensity shown in figures 7.13 is actually the intensity integrated from -10 meV to around 3.55 meV energy transfer. As such, the results could be consistent with either enhanced quantum fluctuations by the strains, since it looks very similar to the 0.55 meV data measured by Wen *et al.* [233], or the system being in a paramagnetic phase due to the large strains (too much disorder) [145]. However, the CEF data clearly shows a CEF excitation around 2.5 meV,

below the integration limit of the D7 experiment. As such, the data shown in figure 7.13 also contains CEF excitation information. Thus, if the magnetic scattering below the excitation has a weak Q dependence, it might be hidden by the presence of the much larger CEF excitation. Furthermore, including this excitation in the data would add a form factor decay to the magnetism below it. This means that it is possible for the effective Pr magnetic moment to be smaller than what was extracted from the powder average data.

7.4 Low energy excitations

To distinguish if the uncorrelated magnetic scattering measured with D7 is due to the system being in a paramagnetic phase or is a quantum spin liquid, low energy transfer measurements were performed with the LET spectrometer from ISIS. With LET, a powder sample of Pr_2ScNbO_7 was studied at multiple temperatures between 50 mK and 200 K, with multiple incident energies, as figure 7.14 shows. All of the data acquired with LET shown in this section is on an absolute scale, normalised to a monochromatic vanadium measurement. A powder sample of La_2ScNbO_7 used for phonon subtraction was also analysed at the same incident energies and at temperatures between 1.7 K and 200 K. Both samples were grown by Cole Mauws using the floating zone method at the Clarendon Laboratory, Oxford University.

The resulting one-dimensional energy cuts extracted by integrating over the full measured Q range is shown in figure 7.14. As the figures show, all the data at 30 K and below converge to zero intensity at zero energy transfers, but the 100 K and 200 K data converge to a non-zero value. This is easily seen in the 1.45 meV, 2.2 meV and 3.7 meV incident energy data. The same effect was observed by Sibille *et al.* [4, 235] when studying the low energy excitations of $Pr_2Hf_2O_7$ and by Mook *et al.* [238] in EuO when studying spin waves above and below its critical temperature. Collins *et al.* [239] theoretical studies suggest that, in the paramagnetic regime, quasi-elastic scattering is developed with a shape that is approximately Gaussian centred at zero. Thus, the non-zero intensity convergence at low energy transfers for the 100 K and 200 K measurements, in the paramagnetic phase of this system, can be attributed to the development of quasi-elastic scattering.

In addition, differences were found between the SEQUOIA data acquired at 5 K and $E_i = 25$ meV and the LET measurements at 5 K and $E_i = 22.78$ meV. Both produce peaks at similar locations, but the intensity is not the same. In the SEQUOIA data there is a clear difference between the intensities of the 2.5 meV and 6.5 meV peaks, while in the LET data both peaks are of similar intensity. In addition, the LET peak at 13.5 meV is sharper and more intense, while the same peak measured with SEQUOIA is broader and less intense. The possibility of this being an artefact of both instruments having different instrumental resolution was discarded since, not only both instruments have very similar resolution, but also these features are not resolution limited. This was confirmed by doing measurements in high flux/lower resolution mode and in intermediate flux/higher resolution mode and seeing no significant change between both measurements. The differences are most likely due to differences between the two samples. In particular, there is a relatively high magnetic background due to structural disorder at low energy transfers according to the PCM calculations, and this could be the origin of the difference. It is possible that the sample measured with SEQUIA has fewer domains with the lowest energy DFT structure and a more random distribution of the Sc and Nb ions. Thus, the peak at low energies predicted by DFT for the random distribution is stronger in this

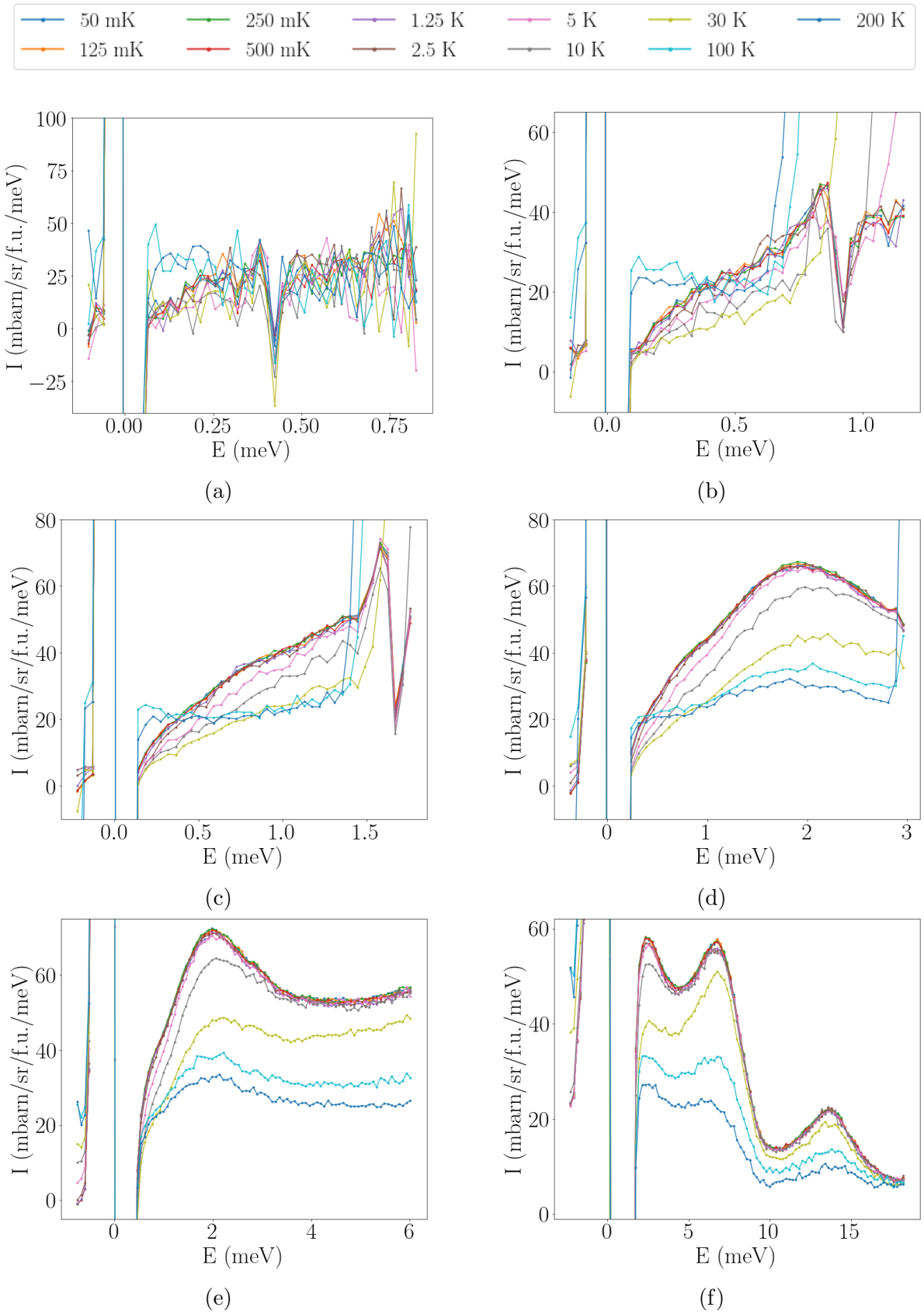

Figure 7.14: Temperature evolution of the phonon corrected LET data of Pr_2ScNbO_7 at incident energies of (a) 1.03 meV, (b) 1.45 meV, (c) 2.2 meV, (d) 3.7 meV, (e) 7.52 meV and (f) 22.78 meV. For visual purposes, the error bars have been excluded.

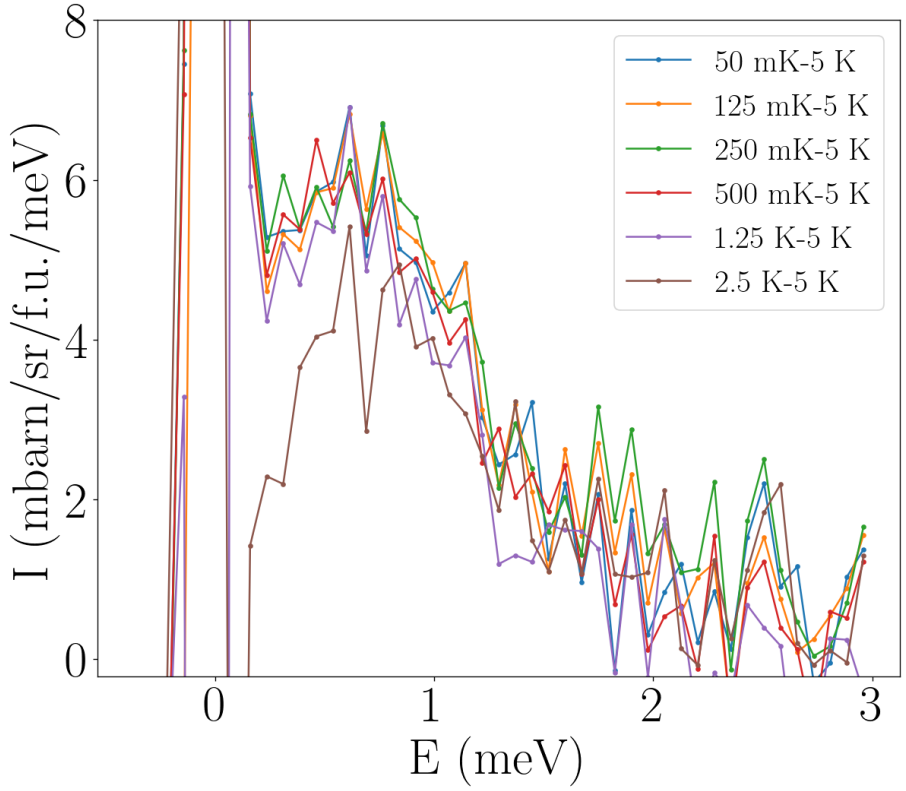

Figure 7.15: Temperature evolution of the phonon corrected LET Pr_2ScNbO_7 data with $E_i = 3.7$ meV after subtracting the 5 K data. For visual purposes, the error bars have been excluded.

sample, making the 2.5 meV peak stronger.

Just as Kimura *et al.* [3] did with $Pr_2Zr_2O_7$, the 5 K phonon corrected data was subtracted from the lower temperature phonon corrected data. The subtraction of the 5 K data was performed because, according to Kimura *et al.* [3], this leaves behind the low energy quantum fluctuations. As figure 7.15 shows for the $E_i = 3.7$ meV data, there is a clear feature around 0.7 meV after the 5 K data is subtracted. This feature is very similar to the one found by Kimura *et al.* [3] for $Pr_2Zr_2O_7$ and Sibille *et al.* [4] for $Pr_2Hf_2O_7$ in figures 7.2a and 7.2b respectively. Both Kimura and Sibille interpret this extra peak at 0.2 meV as a signature of cooperative quantum fluctuations. It is reasonable to conclude that Pr_2ScNbO_7 behaves similarly to $Pr_2Zr_2O_7$.

To understand a possible origin of the uncorrelated quantum magnetism, it is instructive to examine the lowest energy structure identified by the DFT calculations discussed in the previous chapter. Figure 7.16a shows the tetrahedra form by the two Pr ions and their bond lengths, and figure 7.16b shows the lowest energy DFT structure with the arrangement of the two Pr ions in the unit cell. The chain of constant 3.73 Å bond lengths is formed by alternating Pr sites, and it is parallel to the chain of alternating Sc–Nb ions in figure 6.6a. The shortest bond lengths, 3.69 Å and 3.71 Å, shown in dark and light blue in figure 7.16b connect Pr1 and Pr2 ions and form chains in a direction roughly perpendicular to the alternating Sc–Nb ions. Since the exchange interaction falls off exponentially with distance [1], the chains with the shortest bond lengths may well dominate.

If the "PCM CEF calculations" picture is to be believed, the Pr ions would need to develop a magnetic moment, since with the diffuse scattering measurements, a magnetic

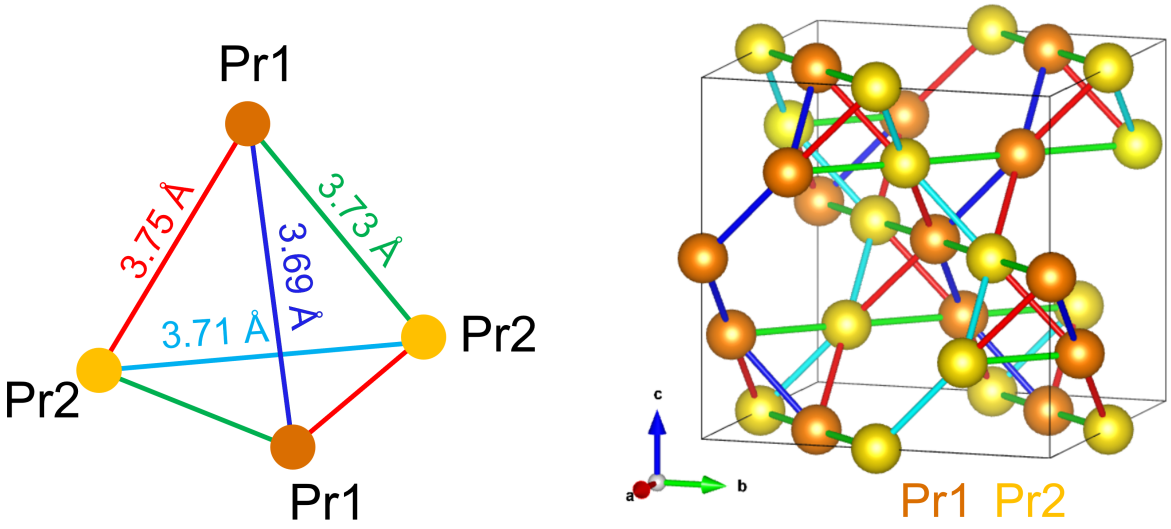

(a) (b)

Figure 7.16: (a) Bond lengths between the two Pr environments found in the lowest energy DFT structure. (b) Arrangement of the Pr tetrahedra in a unit cell.

signal is detected. For this to be possible, the ground state and first excited state would have to mix and generate a moment. It was first considered the possibility of the exchange interaction between the Pr ions to be strong enough to mix the wave functions of the ground state and first excited state, generating a moment. However, for this to be possible and generate moments at least along the chain of Pr1 ions, the exchange constant of the Pr ions needs to be on the order of the energy gap between the ground state and first excited state. This is not the case for Pr^{3+} since, according to thermal conductivity measurements on $Pr_2Zr_2O_7$ performed by Tokiwa *et al.* [240], the Pr exchange constant is on the order of 0.1 meV, smaller than the energy gap of the Pr1 sites. Thus, the exchange fields by themselves are not strong enough to mix the ground state and first excited state and generate a moment.

Another method in which these two states could mix is through the disorder transverse field proposed by Savary *et al.* [145]. The disorder of the Sc and Nb ions around the Pr sites will act as a transverse field which could mix both states in "tunnel-like" states, just as Martin *et al.* [231] found with $Pr_2Zr_2O_7$. Nevertheless, the effect would be similar to the one described with the HTSO system, mixing the ground and first excited state wave functions and generating moments at the Pr sites. On the other hand, if the "CEF fitting" picture is trusted, then no extra transverse fields would be needed since the Pr ions are already predicted to be magnetic. Regardless of the picture, it may be possible for the Pr ions in this system to form one-dimensional magnetic chains that do not order and instead exhibit quantum fluctuations. Hence, it is conceivable that one-dimensional magnetism is responsible for the observed quantum fluctuations in this system.

7.5 Summary

CEF excitation measurements on Pr_2ScNbO_7 were performed using the SEQUOIA spectrometer from SNS. The data was first analysed by assuming a D_{3d} symmetry and fitting 6 B-parameters. Due to this symmetry constraint, the fitting predicted a doublet ground state with the first excited state at 2.7 meV. However, to do this, a complex background had to be chosen to get a good fit. In addition to this fitting, point-charge-model (PCM) calculations were performed with the Pr ions from the lowest energy DFT

structure described in the previous chapter. According to the DFT calculations, the lowest energy structure contained two inequivalent Pr sites, both of them with a D_{3d} broken symmetry. As such, the PCM calculations of both Pr ions produced non-magnetic singlet ground states, with the first excited state at 1.2 meV and 4.6 meV above the ground state.

The excitation spectrum produced by the lowest energy DFT structure was computed, producing a very similar pattern to the experimental data, but with the wrong intensity. In addition, the excitation spectrum given by the average of the 97 different DFT calculations performed for all the possible Sc/Nb arrangements was also computed, with the assumption that this would be the spectrum produced by a perfectly disordered Sc/Nb system. The resulting spectrum resembled the background that had to be used in the initial fitting. This is in agreement with the idea of the system having domains of the lowest energy DFT structure, with a random arrangement of Sc and Nb ions on the B sites in between the domains.

The magnetic correlations of this system were studied using D7. The measured magnetic cross-section resulted in flat, uncorrelated scattering. This featureless scattering could represent either quantum fluctuations or a paramagnetic phase, since the disorder of the B-sites is so high that all the fluctuations could have been washed out. To distinguish between these two possibilities, low energy inelastic measurements were performed at multiple temperatures using the LET spectrometer from ISIS. The subtraction of the 5 K data from the low temperature data resulted in a hidden feature around 0.7 meV. Kimura *et al.* [3] and Sibille *et al.* [4] also found a similar feature when studying $Pr_2Zr_2O_7$ and $Pr_2Hf_2O_7$ respectively, and suggested that these features could be due to quantum fluctuations. Finally, the magnetic diffuse scattering data was used to extract a Pr effective magnetic moment of 2.10(8) μ_B.

In the lowest energy DFT structure, the two distinct Pr sites form one-dimensional chains. If one of the Pr sites was magnetic, this system would be formed by one-dimensional magnetic chains which never order and would be responsible for the observed quantum fluctuations in this system. However, according to the PCM calculations, none of the Pr ions are magnetic. Only through the mixing of the ground state and first excited state, these ions could generate a moment. One mechanism in which this can be achieved is through the transverse field in the system generated by the Sc/Nb disorder. This field could mix both states in "tunnel-like" states, just as Martin *et al.* [231] found with $Pr_2Zr_2O_7$.

Chapter 8

Conclusion and future work

8.1 $Ho_2Ti_{2-x}Sc_xO_{7-x/2}$

8.1.1 Conclusion

The effect on the magnetism due to substitution and vacancies in $Ho_2Ti_{2-x}Sc_xO_{7-x/2}$ (HTSO) with $x = 0.0$, $x = 0.1$ and $x = 0.5$ was studied, where Ti^{4+} ions were replaced by Sc^{3+} ions in the stoichiometric system. Due to the charge difference between the Sc and Ti ions, this doping resulted in the need of charge compensating oxygen vacancies to maintain sample charge neutrality. Total scattering measurements and Bragg refinements were used to determine the location of the vacancies. For the $x = 0.5$ HTSO system not only was it found that the charge compensating oxygen vacancies are located at the O(2) sites, with a concentration of 3.9%, close to the nominal 4.17% that was initially expected, but, in addition, an extra 0.65% of different O(2) ions were displaced towards the centre of the tetrahedra formed by the B-sites, known as 8a sites. On the other hand, Bragg refinements performed on the $x = 0.1$ and $x = 0.0$ HTSO systems showed that both have similar levels of O(2) vacancies, explaining the similarities in the measured spectrum. Furthermore, no A-B intersite mixing was found in any sample. In addition, DFT calculations predict that to minimise the energy, an O(2) vacancy and an O(2) ion displaced towards an 8a site are needed, in perfect agreement with the Bragg refinement. The resulting structural diffuse scattering calculations using the DFT structure are in excellent agreement with the measured data. Finally, the DFT calculations and RMC fits to the structure diffuse scattering and PDF predict no correlations between the Sc ions.

Knowing the location of the oxygen vacancies, their effects on the single-ion magnetism was studied. It was found that, while the Ho ions with no nearest neighbour vacancies have a doublet ground state with a strong $\langle 111 \rangle$ Ising anisotropy, in excellent agreement with previous measurements performed by Rosenkranz *et al.* [91] on the same system, the ground state of the Ho ions next to a single vacancy is split into two singlets separated by 0.12 meV. Due to such a weak splitting, magnetisation calculations at 0.5 K and with a 0.1 T applied field resulted in the Ho ions with a vacancy developing a 6.2 μ_B moment mainly pointing along the $\langle 111 \rangle$ direction, but with a 15.2° tilt towards the location of the vacancy. The contribution to the CEF spectrum from Ho ions next to 2 or more vacancies was ignored, since their contribution to the experimental data is minimal.

Despite this, magnetic diffuse scattering measurements on the $x = 0.1$ and $x = 0.5$ HTSO systems still produce scattering qualitatively very similar to the ones measured by Fennell *et al.* [1] and Chang *et al.* [2, 116] in the stoichiometric and Y diluted $Ho_2Ti_2O_7$.

However, unlike the Y diluted $Ho_2Ti_2O_7$ systems, where the pinch point width does not change with increasing levels of doping, the pinch point width of the HTSO system increased as the number of vacancies increased. It is possible that the exchange and dipolar fields of the Ho ions are sufficiently strong to mix the wave functions of the ground and first excited states, generating the tilted magnetic moment found in the magnetisation calculations. As such, it was proposed that the tilted moments at the defect Ho sites could be responsible for the broadening of the pinch points. It was also predicted that three regions could exist in these systems: a low temperature regime, where the system behaves like an ideal spin ice, an intermediate temperature regime, where the moments at the defect sites are gradually switched off until all these moments become zero, and a high temperature regime, where the ghost spin picture proposed by Sen et al. [226] comes into play.

8.1.2 Future work

Since the DFT calculations were performed using $Y_2Ti_2O_7$, these need to be repeated, but with the correct chemical composition. DFT calculations with magnetic rare-earth ions are complex to perform due to the size and spin state of the ions. Furthermore, the DFT calculations will allow to fully determine the presence of any kind of Sc ordering.

To fully characterise the effect of O(2) vacancies and tilted moments on these systems, further measurements are still needed. Magnetisation measurements of these systems would also be of great use, since it would allow to further constrain the CEF modelling, resulting in a more precise determination of the CEF levels and magnetic moments. Due to the presence of two types of moments, tilted and non-tilted, it might be possible to observe two plateaus in the magnetisation, one for each type of moment. To study the dynamics of these systems, μSR and ac-susceptibility measurements would be of great use, since they would provide valuable information on the propagation of monopoles in the presence of this type of disorder.

Finally, heat capacity measurements in conjunction with the ac-suspectivility findings would allow the characterisation of the temperature dependence of the spin dynamics in these systems. In particular, it might be possible to distinguish the three different temperature regions described above. From a computational modelling point of view, MC calculations of the magnetic diffuse scattering may be useful to determine if it is the presence of the tilted moments that causes the broadening of the pinch points. For this, calculations of the stoichiometric $Ho_2Ti_2O_7$, of HTSO with no spins at the Ho sites next to a vacancy (ghost spin picture) and of HTSO with tilted moments at the Ho sites next to a vacancy would be ideal to compare the widths of all pinch points.

8.2 Pr_2ScNbO_7

8.2.1 Conclusion

Structural and magnetic studies were performed on the highly substituted Pr_2ScNbO_7 system, where the combination of trivalent Sc^{3+} and pentavalent Nb^{5+} cations in equal quantities is a way to introduce local strains without the complication of introducing charge-compensating oxygen vacancies. Through DFT calculations, it was found that the lowest energy configuration has charge ice ordering, with alternating Sc-Nb ions on the chains. However, this structure is chemically frustrated, since the alternating chains cannot be accommodated in all directions. Furthermore, this ordering is only over a short range, since the diffuse scattering is broad. If it was obeyed over long distances, the

scattering would produce sharp superstructure peaks with very little diffuse scattering between them. The resulting structural diffuse scattering calculations using a single unit cell of the lowest energy structure are in excellent agreement with the measured data. From this, it was concluded that this system is formed by small domains of the lowest energy DFT structure, each domain with the structure in different orientations, and with the domain walls having a random arrangement of the Sc and Nb ions. Finally, total scattering measurements of this system were compared with calculations assuming long range order of the lowest energy DFT structure. These calculations produce extra peaks not present in the experimental data, confirming that long range order of this structure does not exist.

To study the effect of the disorder on the single-ion magnetic properties of Pr_2ScNbO_7, CEF measurements were performed to determine the CEF excitations of the Pr ions. To do this, two different approaches were followed. First, a set of CEF parameters were fitted to the data assuming a D_{3d} symmetry. This produced a magnetic doublet ground state with a strong $\langle 111 \rangle$ Ising anisotropy. In addition, point-charge-model (PCM) CEF calculations were performed using the lowest energy DFT structure which contained two inequivalent Pr sites, each forming one-dimensional chains. These calculations predicted singlet ground states for both Pr sites, with the first excited state at 1.2 meV and 4.6 meV. However, magnetic diffuse scattering measurements produce a measurable signal, indicating that the Pr ions have a moment.

Finally, the magnetic diffuse scattering measurements produced a flat scattering. While this could be a signature of quantum fluctuations, it is also possible that, due to the significant disorder from the Sc/Nb distribution, the system is in a paramagnetic phase. Regardless of the origin of the signal, the data was used to extract an effective Pr^{3+} magnetic moment of 2.10(8) μ_B. To differentiate between paramagnetic and quantum fluctuations, low energy transfer measurements were performed. Similar to what Kimura *et al.* [3] did when studying the $Pr_2Zr_2O_7$ system, the 5 K data was subtracted from the low temperature data. This highlighted the existence of a peak around 0.7 meV. A similar peak was found by Kimura *et al.* [3] and Sibille *et al.* [4] when studying $Pr_2Zr_2O_7$ and $Pr_2Hf_2O_7$, respectively, both suggesting that this is a signature of cooperative quantum fluctuations.

If the PCM calculations are to be believed, the Pr ions would need to develop a magnetic moment to explain the measured magnetic signature. Previous studies on $Pr_2Zr_2O_7$ result in a Pr exchange constant in the order of 0.1 meV, much smaller than the excitation gap, and thus the exchange interactions alone cannot generate a moment. It is thus possible that the disorder transverse fields, generated due to the disordered arrangement of the Sc and Nb ions, could be strong enough to mix the states and generate a magnetic moment. If this is the case, the Pr ions could form one-dimensional magnetic chains that do not order and instead exhibit quantum fluctuations. If the CEF fits are to be believed, no transverse fields would be needed. Regardless of the origin, it is conceivable that one-dimensional magnetism is responsible for the observed uncorrelated scattering.

8.2.2 Future work

To fully characterise the effect of the Sc/Nb disorder in this system, further measurements are still needed. Low energy inelastic neutron scattering measurements of a single crystal would be of great use to study the (h,h,l) plane at multiple neutron energy transfers. Since with the D7 experiment the scattering measured is integrated up to 3.55 meV, the magnetic diffuse scattering includes the first CEF level. As such, these measurements

will allow the study of the magnetism below the first CEF excitation, resulting in a better understanding of the Q dependence found in the D7 experiment and a correct extraction of the Pr effective magnetic moment. Furthermore, the scattering along the $\langle 111 \rangle$, $\langle 001 \rangle$, $\langle 110 \rangle$ directions at different energies could be compared with theoretical calculations of one-dimensional chains.

Theoretical calculations of this system are complicated due to the nature of the disorder. Since this system is formed by multiple domains with the lowest energy structure in different orientations, the chain of Pr ions would not form long straight chains. In reality, it most likely would form winding chains in 3D with 90° turns, which could complicate the physics of the interactions.

Magnetisation measurements of this system would also be of great use, since it would allow to further constrain the CEF modelling, resulting in a more precise determination of the CEF levels. However, previous magnetisation measurements on $Pr_2Zr_2O_7$ show no saturation even at 10 T, and it is thus possible that large magnetic fields would be needed. Finally, ac-susceptibility and heat capacity measurements would allow to fully characterise the temperature dependence of the spin dynamics in this system. Unfortunately, μSR measurements are difficult because, as it was found by Foronda *et al.* [237], it is complicated to extract the intrinsic properties in Pr systems, since they are dominated by the intrinsic distortions related to the muon.

Bibliography

[1] T. Fennell, P. P. Deen, *et al.*, "Magnetic Coulomb Phase in the Spin Ice $Ho_2Ti_2O_7$". *Science*, vol. 326, no. 5951, pp. 415–417, 2009.

[2] L. J. Chang, Y. Su, *et al.*, "Magnetic correlations in pyrochlore spin ice as probed by polarized neutron scattering". *J. Phys. Conf. Ser.*, vol. 211, 2010.

[3] K. Kimura, S. Nakatsuji, *et al.*, "Quantum fluctuations in spin-ice-like $Pr_2Zr_2O_7$". *Nat. Commun.*, vol. 4, no. 1, 2013.

[4] R. Sibille, N. Gauthier, *et al.*, "Experimental signatures of emergent quantum electrodynamics in $Pr_2Hf_2O_7$". *Nat. Phys.*, vol. 14, no. 7, pp. 711–715, 2018.

[5] F. Jona, G. Shirane, and R. Pepinsky, "Dielectric, X-Ray, and Optical Study of Ferroelectric $Cd_2Nb_2O_7$ and Related Compounds". *Phys. Rev.*, vol. 98, pp. 903–909, 1955.

[6] M. A. Subramanian, G. Aravamudan, and G. V. Subba Rao, "Oxide pyrochlores – A review". *Prog. Solid. State Ch.*, vol. 15, no. 2, pp. 55–143, 1983.

[7] J. S. Gardner, M. J. P. Gingras, and J. E. Greedan, "Magnetic pyrochlore oxides". *Rev. Mod. Phys.*, vol. 82, pp. 53–107, 2010.

[8] C. P. Brock, T. Hahn, *et al.*, *International tables for crystallography volume A: Space-group symmetry*. Dordrecht, The Netherlands: Wiley Online Library, 2016.

[9] M. Hanawa, Y. Muraoka, *et al.*, "Superconductivity at 1 K in $Cd_2Re_2O_7$". *Phys. Rev. Lett.*, vol. 87, 2001.

[10] H. Sakai, K. Yoshimura, *et al.*, "Superconductivity in a pyrochlore oxide, $Cd_2Re_2O_7$". *J. Phys. Condens. Matter*, vol. 13, no. 33, pp. L785–L790, 2001.

[11] L. Schwertmann, A. Grünert, *et al.*, "Understanding the Influence of Lattice Composition on the Photocatalytic Activity of Defect-Pyrochlore-Structured Semiconductor Mixed Oxides". *Adv. Funct. Mater.*, vol. 25, no. 6, pp. 905–912, 2015.

[12] M. Deepa, P. Prabhakar Rao, *et al.*, "Pyrochlore type semiconducting ceramic oxides in Ca-Ce-Ti-M-O system (M=Nb or Ta)—Structure, microstructure and electrical properties". *Mater. Res. Bull.*, vol. 44, no. 7, pp. 1481–1488, 2009.

[13] M. A. Subramanian, C.C. Torardi, *et al.*, "Ferromagnetic $R_2Mn_2O_7$ pyrochlores (R = Dy-Lu, Y)". *J. Solid State Chem.*, vol. 72, no. 1, pp. 24–30, 1988.

[14] J. S. Gardner, B. D. Gaulin, *et al.*, "Glassy Statics and Dynamics in the Chemically Ordered Pyrochlore Antiferromagnet $Y_2Mo_2O_7$". *Phys. Rev. Lett.*, vol. 83, pp. 211–214, 1999.

[15] J. S. Gardner, G. Ehlers, *et al.*, "Spin dynamics in geometrically frustrated antiferromagnetic pyrochlores". *J. Phys. Condens. Matter*, vol. 16, S643–S651, 2004.

[16] R. R. Jitta, R. Gundeboina, *et al.*, "Defect pyrochlore oxides: as photocatalyst materials for environmental and energy applications - a review". *J. Chem. Technol. Biotechnol.*, vol. 90, no. 11, pp. 1937–1948, 2015.

[17] T. Takeda, R. Kanno, *et al.*, "New Cathode Materials for Solid Oxide Fuel Cells Ruthenium Pyrochlores and Perovskites". *J. Electrochem. Soc.*, vol. 147, no. 5, 2000.

[18] R. C. Ewing, W. J. Weber, and J. Lian, "Nuclear waste disposal—pyrochlore ($A_2B_2O_7$): Nuclear waste form for the immobilization of plutonium and "minor" actinides". *J. Appl. Phys.*, vol. 95, no. 11, pp. 5949–5971, 2004.

[19] E. R. Aluri and A. P. Grosvenor, "A Review of X-Ray Absorption Near-Edge Spectroscopic Studies of Pyrochlore-Type Oxides Proposed for Nuclear Materials Applications". *Reference Module in Chemistry, Molecular Sciences and Chemical Engineering*. Elsevier, 2016.

[20] H. S. Horowitz, J. M. Longo, and H. H. Horowitz, "Oxygen Electrocatalysis on Some Oxide Pyrochlores". *J. Electrochem. Soc.*, vol. 130, no. 9, pp. 1851–1859, 1983.

[21] J. Park and J. Cho, "Advances in Understanding Mechanisms of Perovskites and Pyrochlores as Electrocatalysts using In-Situ X-ray Absorption Spectroscopy". *Angew. Chem., Int. Ed. Engl.*, vol. 59, no. 36, pp. 15314–15324, 2020.

[22] F. Li, L. Zhou, *et al.*, "High-entropy pyrochlores with low thermal conductivity for thermal barrier coating materials". *J. Adv. Ceram.*, vol. 8, no. 4, pp. 576–582, 2019.

[23] J. W. Fergus, "Zirconia and Pyrochlore Oxides for Thermal Barrier Coatings in Gas Turbine Engines". *Metall. Mater. Trans. E*, vol. 1, no. 2, pp. 118–131, 2014.

[24] A. V. Shlyakhtina, D. A. Belov, *et al.*, "δ-Phase to defect fluorite (order–disorder) transition in the R_2O_3–MO_2 (R=Sc, Tm, Lu; M=Zr, Hf) systems". *Mater. Res. Bull.*, vol. 46, no. 4, pp. 512–517, 2011.

[25] A. R. Cleave, "Atomic Scale Simulations for Waste Form Applications". PhD thesis. Imperial College of Science, Technology and Medicine, London, United Kingdom, 2006.

[26] D. L. Drey, Eric C. O'Quinn, *et al.*, "Disorder in $Ho_2Ti_{2-x}Zr_xO_7$: pyrochlore to defect fluorite solid solution series". *RSC Adv.*, vol. 10, pp. 34632–34650, 2020.

[27] G. C. Lau, R. S. Freitas, *et al.*, "Structural disorder and properties of the stuffed pyrochlore Ho_2TiO_5". *Phys. Rev. B*, vol. 76, 2007.

[28] D. M. Anderson, S. M. Gruner, and S. Leibler, "Geometrical aspects of the frustration in the cubic phases of lyotropic liquid crystals". *Proc. Natl. Acad. Sci*, vol. 85, no. 15, pp. 5364–5368, 1988.

[29] Y. Shokef, Y. Han, *et al.*, "Buckled colloidal monolayers connect geometric frustration in soft and hard matter". *Soft Matter*, vol. 9, pp. 6565–6570, 2013.

[30] H. Pais and J. R. Stone, "Exploring the Nuclear Pasta Phase in Core-Collapse Supernova Matter". *Phys. Rev. Lett.*, vol. 109, 2012.

[31] L. Pauling, "The Structure and Entropy of Ice and of Other Crystals with Some Randomness of Atomic Arrangement". *J. Am. Chem. Soc.*, vol. 57, no. 12, pp. 2680–2684, 1935.

[32] G. H. Wannier, "Antiferromagnetism. The Triangular Ising Net". *Phys. Rev.*, vol. 79, pp. 357–364, 1950.

[33] R. M. F. Houtappel, "Order-disorder in hexagonal lattices". *Physica*, vol. 16, no. 5, pp. 425–455, 1950.

[34] M. Semjan and M. Žukovič, "Magnetocaloric Properties of an Ising Antiferromagnet on a Kagome Lattice". *Acta Phys. Pol. A*, vol. 137, no. 5, pp. 622–624, 2020.

[35] S. Deng, Y. Sun, *et al.*, "Frustrated Triangular Magnetic Structures of Mn_3ZnN: Applications in Thermal Expansion". *J. Phys. Chem. C*, vol. 119, no. 44, pp. 24983–24990, 2015.

[36] V. Fritsch, J. D. Thompson, *et al.*, "Correlation between magnetic frustration and electrical conductivity in $RInCu_4$ compounds (R = Gd−Tm)". *Phys. Rev. B*, vol. 73, 2006.

[37] L. T. Nguyen, T. Halloran, *et al.*, "Geometrically frustrated trimer-based Mott insulator". *Phys. Rev. Mater.*, vol. 2, 2018.

[38] Y. Tokiwa, S. Bachus, *et al.*, "Frustrated magnet for adiabatic demagnetization cooling to milli-Kelvin temperatures". *Commun. Mater*, vol. 2, no. 1, 2021.

[39] K. Stenning, A. Vanstone, *et al.*, "Ice Sculpting: Neuromorphic Training of Geometrically-Frustrated Magnetic Metamaterials". *APS March Meeting Abstracts*. Vol. 2019. APS Meeting Abstracts, 2019.

[40] A. P. Ramirez, "Chapter 4 Geometrical frustration". Vol. 13. Handbook of Magnetic Materials. Elsevier, 2001.

[41] A. A. Zvyagin, "New physics in frustrated magnets: Spin ices, monopoles, etc. (Review Article)". *Low Temp. Phys.*, vol. 39, no. 11, pp. 901–922, 2013.

[42] M. Steiner and K. Siemensmeyer, "Chapter 7 - Nuclear Magnetism and Neutrons". *Neutron Scattering - Magnetic and Quantum Phenomena*. Ed. by F. Fernandez-Alonso and D. L. Price. Vol. 48. Experimental Methods in the Physical Sciences. Academic Press, 2015.

[43] R. P. Boardman, "Computer simulation studies of magnetic nanostructures". PhD thesis. University of Southampton, Southampton, United Kingdom, 2016.

[44] J. Wen, S.-L. Yu, *et al.*, "Experimental identification of quantum spin liquids". *npj Quantum Mater.*, vol. 4, no. 1, 2019.

[45] C. P. Poole, H. A. Farach, *et al.*, "1 - Properties of the Normal State". *Superconductivity (Second Edition)*. Ed. by C. P. Poole, H. A. Farach, *et al.* Second Edition. Amsterdam: Academic Press, 2007.

[46] A. T. Boothroyd, *Principles of Neutron Scattering from Condensed Matter*. Oxford, England: Oxford University Press, 2020.

[47] L. Balents, "Spin liquids in frustrated magnets". *Nature*, vol. 464, no. 7286, pp. 199–208, 2010.

[48] L. D. C. Jaubert, "Topological Constraints and Defects in Spin Ice". PhD thesis. Ecole normale supérieure de Lyon, Lyon, France, 2009.

[49] A. P. Ramirez, "Strongly Geometrically Frustrated Magnets". *Annu. Rev. Mater. Sci.*, vol. 24, no. 1, pp. 453–480, 1994.

[50] J. E. Greedan, "Geometrically frustrated magnetic materials". *J. Mater. Chem.*, vol. 11, pp. 37–53, 2001.

[51] M. F. Collins and O. A. Petrenko, "Triangular antiferromagnets". *Can. J. Phys*, vol. 75, 1997.

[52] L. Baraban, "Capped colloids as model systems for condensed matter". PhD thesis. Universität Konstanz Fachbereich Physik, Konstanz, Germany, 2008.

[53] M. E. Zhitomirsky, "Octupolar ordering of classical kagome antiferromagnets in two and three dimensions". *Phys. Rev. B*, vol. 78, 2008.

[54] S. K. Pati and C. N. R. Rao, "Kagome network compounds and their novel magnetic properties". *Chem. Commun.*, pp. 4683–4693, 2008.

[55] O. Götze, D. J. J. Farnell, *et al.*, "Heisenberg antiferromagnet on the kagome lattice with arbitrary spin: A higher-order coupled cluster treatment". *Phys. Rev. B*, vol. 84, 2011.

[56] G. Paul, A. Choudhury, and C. N. R. Rao, "An organically templated iron sulfate with a distorted Kagome lattice exhibiting unusual magnetic properties". *Chem. Commun.*, pp. 1904–1905, 2002.

[57] H. D. Zhou, B. W. Vogt, *et al.*, "Partial field-induced magnetic order in the spin-liquid kagome $Nd_3Ga_5SiO_{14}$". *Phys. Rev. Lett.*, vol. 99, no. 23, 2007.

[58] D. I. Gorbunov, M. S. Henriques, *et al.*, "Electronic properties of a distorted kagome lattice antiferromagnet $Dy_3Ru_4Al_{12}$". *Phys. Rev. B*, vol. 90, 2014.

[59] E. D. T. de Lacheisserie and D. Gignoux, *Magnetism 1- Fundamentals*. Ed. by M. Schlenker. Vol. 1. New York, USA: Springer Science & Business Media, 2005.

[60] M. J. Harris, S.T. Bramwell, *et al.*, "Magnetic structures of highly frustrated pyrochlores". *J. Magn. Magn. Mater.*, vol. 177-181, pp. 757–762, 1998.

[61] L. Savary and L. Balents, "Quantum spin liquids: a review". *Rep. Prog. Phys.*, vol. 80, no. 1, 2016.

[62] Z. Hiroi, M. Hanawa, *et al.*, "Spin-1/2 Kagome-Like Lattice in Volborthite $Cu_3V_2O_7(OH)_2{\cdot}2H_2O$". *J. Phys. Soc. Jpn*, vol. 70, no. 11, pp. 3377–3384, 2001.

[63] D. Boldrin, B. Fåk, *et al.*, "Haydeeite: A spin-$\frac{1}{2}$ kagome ferromagnet". *Phys. Rev. B*, vol. 91, 2015.

[64] R. Sibille, E. Lhotel, *et al.*, "Candidate Quantum Spin Liquid in the Ce^{3+} Pyrochlore Stannate $Ce_2Sn_2O_7$". *Phys. Rev. Lett.*, vol. 115, 2015.

[65] M. Yamashita, N. Nakata, *et al.*, "Highly Mobile Gapless Excitations in a Two-Dimensional Candidate Quantum Spin Liquid". *Science*, vol. 328, no. 5983, pp. 1246–1248, 2010.

[66] E. Kermarrec, R. Kumar, *et al.*, "Classical Spin Liquid State in the $S = \frac{5}{2}$ Heisenberg Kagome Antiferromagnet $Li_9Fe_3(P_2O_7)_3(PO_4)_2$". *Phys. Rev. Lett.*, vol. 127, 2021.

[67] J. Snyder, B. G. Ueland, *et al.*, "Low-temperature spin freezing in the $Dy_2Ti_2O_7$ spin ice". *Phys. Rev. B*, vol. 69, 2004.

[68] S. T. Bramwell, M. J. Harris, *et al.*, "Spin Correlations in $Ho_2Ti_2O_7$: A Dipolar Spin Ice System". *Phys. Rev. Lett.*, vol. 87, 2001.

[69] J. Villain, "Insulating spin glasses". *Z Physik B*, vol. 33, no. 1, pp. 31–42, 1979.

[70] S.-H. Lee, C. Broholm, *et al.*, "Local Spin Resonance and Spin-Peierls-like Phase Transition in a Geometrically Frustrated Antiferromagnet". *Phys. Rev. Lett.*, vol. 84, pp. 3718–3721, 2000.

[71] S. Klotz, K. Komatsu, *et al.*, "Ice VII from aqueous salt solutions: From a glass to a crystal with broken H-bonds". *Sci. Rep.*, vol. 6, no. 1, 2016.

[72] V. F. Petrenko and R. W. Whitworth, *Physics of ice*. Oxford: Oxford University Press, 1999.

[73] O. Benton, O. Sikora, and N. Shannon, "Classical and quantum theories of proton disorder in hexagonal water ice". *Phys. Rev. B*, vol. 93, 2016.

[74] *Hydrogen-Bonding and Water*. `https://chem.libretexts.org/Bookshelves/General_Chemistry/Book%3A_Chem1_(Lower)/07%3A_Solids_and_Liquids/7.03%3A_Hydrogen-Bonding_and_Water`. Accessed: 2021-10-31.

[75] J. D. Bernal and R. H. Fowler, "A Theory of Water and Ionic Solution, with Particular Reference to Hydrogen and Hydroxyl Ions". *J. Chem. Phys.*, vol. 1, no. 8, pp. 515–548, 1933.

[76] W. F. Giauque and J. W. Stout, "The Entropy of Water and the Third Law of Thermodynamics. The Heat Capacity of Ice from 15 to 273° K." *J. Am. Chem. Soc.*, vol. 58, no. 7, pp. 1144–1150, 1936.

[77] E. O. Wollan, W. L. Davidson, and C. G. Shull, "Neutron Diffraction Study of the Structure of Ice". *Phys. Rev.*, vol. 75, pp. 1348–1352, 1949.

[78] J. C. Li, V. M. Nield, *et al.*, "Diffuse neutron-scattering study of deuterated ice I_h". *Philos. Mag. B*, vol. 69, no. 6, pp. 1173–1181, 1994.

[79] W. F. Kuhs and M. S. Lehmann, "The structure of the ice I_h by neutron diffraction". *J. Phys. Chem.*, vol. 87, no. 21, pp. 4312–4313, 1983.

[80] C. Janiak, T. G. Scharmann, and S. A. Mason, "Two-Dimensional Water and Ice Layers: Neutron Diffraction Studies at 278, 263, and 20 K". *J. Am. Chem. Soc.*, vol. 124, no. 47, pp. 14010–14011, 2002.

[81] M. J. P. Gingras, "Spin Ice". *Introduction to Frustrated Magnetism: Materials, Experiments, Theory*. Ed. by C. Lacroix, P. Mendels, and F. Mila. Berlin, Heidelberg: Springer Berlin Heidelberg, 2011.

[82] P. W. Anderson, "Ordering and Antiferromagnetism in Ferrites". *Phys. Rev.*, vol. 102, pp. 1008–1013, 1956.

[83] M. J. Harris, S. T. Bramwell, *et al.*, "Geometrical Frustration in the Ferromagnetic Pyrochlore $Ho_2Ti_2O_7$". *Phys. Rev. Lett.*, vol. 79, pp. 2554–2557, 1997.

[84] K. Matsuhira, Z. Hiroi, *et al.*, "A new macroscopically degenerate ground state in the spin ice compound $Dy_2Ti_2O_7$ under a magnetic field". *J. Phys. Condens. Matter*, vol. 14, no. 29, pp. L559–L565, 2002.

[85] R. G. Melko and M. J. P. Gingras, "Monte Carlo studies of the dipolar spin ice model". *J. Phys. Condens. Matter*, vol. 16, no. 43, 2004.

[86] M. Léger, E. Lhotel, *et al.*, "Spin Dynamics and Unconventional Coulomb Phase in $Nd_2Zr_2O_7$". *Phys. Rev. Lett.*, vol. 126, 2021.

[87] J. Snyder, J. S. Slusky, *et al.*, "How 'spin ice' freezes". *Nature*, vol. 413, no. 6851, pp. 48–51, 2001.

[88] J. T. Chalker, "Spin liquids and frustrated magnetism". *Topological Aspects of Condensed Matter Physics: Lecture Notes of the Les Houches Summer School*. Ed. by C. Chamon, M. O. Goerbig, *et al.* Vol. 3. Oxford: Oxford University Press, 2017.

[89] A. P. Ramirez, A. Hayashi, *et al.*, "Zero-point entropy in 'spin ice'". *Nature*, vol. 399, no. 6734, pp. 333–335, 1999.

[90] M. Ruminy, E. Pomjakushina, *et al.*, "Crystal-field parameters of the rare-earth pyrochlores $R_2Ti_2O_7$ (R = Tb, Dy, and Ho)". *Phys. Rev. B*, vol. 94, 2016.

[91] S. Rosenkranz, A. P. Ramirez, *et al.*, "Crystal-field interaction in the pyrochlore magnet $Ho_2Ti_2O_7$". *J. Appl. Phys.*, vol. 87, no. 9, pp. 5914–5916, 2000.

[92] J. G. Rau and M. J. P. Gingras, "Magnitude of quantum effects in classical spin ices". *Phys. Rev. B*, vol. 92, 2015.

[93] B. C. den Hertog and M. J. P. Gingras, "Dipolar Interactions and Origin of Spin Ice in Ising Pyrochlore Magnets". *Phys. Rev. Lett.*, vol. 84, pp. 3430–3433, 2000.

[94] K. Vlášková, M. Diviš, and M. Klicpera, "The magnetic behaviour of $Dy_2Ir_2O_7$ – Beyond the mean field approximation". *J. Magn. Magn. Mater.*, vol. 538, 2021.

[95] S. T. Bramwell, M. N. Field, *et al.*, "Bulk magnetization of the heavy rare earth titanate pyrochlores - a series of model frustrated magnets". *J. Phys.: Condens. Matter*, vol. 12, no. 4, 2000.

[96] H. Cao, A. Gukasov, *et al.*, "Ising versus XY Anisotropy in Frustrated $R_2Ti_2\mathbf{O}_7$ Compounds as "Seen" by Polarized Neutrons". *Phys. Rev. Lett.*, vol. 103, 2009.

[97] T. Fennell, O. A. Petrenko, *et al.*, "Neutron scattering investigation of the spin ice state in $Dy_2Ti_2O_7$". *Phys. Rev. B*, vol. 70, 2004.

[98] T. Yavors'kii, T. Fennell, *et al.*, "$Dy_2Ti_2O_7$ Spin Ice: A Test Case for Emergent Clusters in a Frustrated Magnet". *Phys. Rev. Lett.*, vol. 101, 2008.

[99] S. T. Bramwell and M. J. Harris, "The history of spin ice". *J. Phys. Condens. Matter*, vol. 32, no. 37, 2020.

[100] C. L. Henley, "The "Coulomb Phase" in Frustrated Systems". *Annu. Rev. Condens. Matter Phys.*, vol. 1, no. 1, pp. 179–210, 2010.

[101] R. Youngblood, J. D. Axe, and B. M. McCoy, "Correlations in ice-rule ferroelectrics". *Phys. Rev. B*, vol. 21, pp. 5212–5220, 1980.

[102] S. V. Isakov, K. Gregor, *et al.*, "Dipolar Spin Correlations in Classical Pyrochlore Magnets". *Phys. Rev. Lett.*, vol. 93, 2004.

[103] C. L. Henley, "Power-law spin correlations in pyrochlore antiferromagnets". *Phys. Rev. B*, vol. 71, 2005.

[104] O. Benton, O. Sikora, and N. Shannon, "Seeing the light: Experimental signatures of emergent electromagnetism in a quantum spin ice". *Phys. Rev. B*, vol. 86, 2012.

[105] C. Castelnovo, R. Moessner, and S. L. Sondhi, "Magnetic monopoles in spin ice". *Nature*, vol. 451, no. 7174, pp. 42–45, 2008.

[106] D. J. P. Morris, D. A. Tennant, *et al.*, "Dirac Strings and Magnetic Monopoles in the Spin Ice $Dy_2Ti_2O_7$". *Science*, vol. 326, no. 5951, pp. 411–414, 2009.

[107] P. A. M. Dirac, "Quantised singularities in the electromagnetic field," *Proceedings of the Royal Society of London. Series A, Containing Papers of a Mathematical and Physical Character*, vol. 133, no. 821, pp. 60–72, 1931.

[108] J. D. Jackson, *Classical electrodynamics*. New York, USA: American Association of Physics Teachers, 1999.

[109] J. A. Quilliam, L. R. Yaraskavitch, *et al.*, "Dynamics of the magnetic susceptibility deep in the Coulomb phase of the dipolar spin ice material $Ho_2Ti_2O_7$". *Phys. Rev. B*, vol. 83, 2011.

[110] L. R. Yaraskavitch, H. M. Revell, *et al.*, "Spin dynamics in the frozen state of the dipolar spin ice material $Dy_2Ti_2O_7$". *Phys. Rev. B*, vol. 85, 2012.

[111] A. Farhan, M. Saccone, *et al.*, "Emergent magnetic monopole dynamics in macroscopically degenerate artificial spin ice". *Sci. Adv.*, vol. 5, no. 2, 2019.

[112] G. Sala, "Spin ice: a Wonderful World". PhD thesis. Royal Holloway University of London, London, United Kingdom, 2014.

[113] H. Kadowaki, Naohiro Doi, *et al.*, "Observation of Magnetic Monopoles in Spin Ice". *J. Phys. Soc. Jpn*, vol. 78, no. 10, 2009.

[114] S. T. Bramwell, S. R. Giblin, *et al.*, "Measurement of the charge and current of magnetic monopoles in spin ice". *Nature*, vol. 461, no. 7266, pp. 956–959, 2009.

[115] S. R. Dunsiger, A. A. Aczel, *et al.*, "Spin Ice: Magnetic Excitations without Monopole Signatures Using Muon Spin Rotation". *Phys. Rev. Lett.*, vol. 107, 2011.

[116] L. J. Chang, Y. Su, *et al.*, "Magnetic correlations in the spin ice $Ho_{2-x}Y_xTi_2O_7$ as revealed by neutron polarization analysis". *Phys. Rev. B*, vol. 82, 2010.

[117] P. W. Anderson, "Resonating valence bonds: A new kind of insulator?" *Mater. Res. Bull.*, vol. 8, no. 2, pp. 153–160, 1973.

[118] M. Serbyn, "Spin liquids: mean field and beyond". PhD thesis. Massachusetts Institute of Technology, Massachusetts, 2014.

[119] L. Balents, *Lecture notes in Quantum Spin Liquids: answers to questions*. 2011.

[120] W. Rantner and X.-G. Wen, "Electron Spectral Function and Algebraic Spin Liquid for the Normal State of Underdoped High T_c Superconductors". *Phys. Rev. Lett.*, vol. 86, pp. 3871–3874, 2001.

[121] T. Imai and Y. S. Lee, "Do quantum spin liquids exist?" *Phys. Today*, vol. 69, no. 8, pp. 30–36, 2016.

[122] K. Matsuhira, Y. Hinatsu, and T. Sakakibara, "Novel dynamical magnetic properties in the spin ice compound $Dy_2Ti_2O_7$". *J. Phys. Condens. Matter*, vol. 13, no. 31, 2001.

[123] Wang Y., T. Reeder, *et al.*, "Monopolar and dipolar relaxation in spin ice $Ho_2Ti_2O_7$". *Sci. Adv.*, vol. 7, no. 25, 2021.

[124] P. J. Mosley, *Lecture notes in Quantum and Atomic Physics*. 2016.

[125] N. D. H. Dass, *The principles of thermodynamics*. 6000 Broken Sound Parkway NW: CRC Press, 2013.

[126] C. Balz, B. Lake, *et al.*, "Physical realization of a quantum spin liquid based on a complex frustration mechanism". *Nat. Phys.*, vol. 12, no. 10, pp. 942–949, 2016.

[127] M. Klanjšek, A. Zorko, *et al.*, "A high-temperature quantum spin liquid with polaron spins". *Nat. Phys.*, vol. 13, no. 11, pp. 1130–1134, 2017.

[128] K. Y. Zeng, L. Ma, *et al.*, "NMR study of the spin excitations in the frustrated antiferromagnet $Yb(BaBO_3)_3$ with a triangular lattice". *Phys. Rev. B*, vol. 102, 2020.

[129] A. Ribak, I. Silber, *et al.*, "Gapless excitations in the ground state of $1T-TaS_2$". *Phys. Rev. B*, vol. 96, 2017.

[130] S.-S. Lee, P. A. Lee, and T. Senthil, "Amperean Pairing Instability in the U(1) Spin Liquid State with Fermi Surface and Application to $\kappa-(BEDT-TTF)_2Cu_2(CN)_3$". *Phys. Rev. Lett.*, vol. 98, 2007.

[131] Y. J. Yu, Y. Xu, *et al.*, "Heat transport study of the spin liquid candidate $1T-TaS_2$". *Phys. Rev. B*, vol. 96, 2017.

[132] M. Kratochvilova, A. D. Hillier, *et al.*, "The low-temperature highly correlated quantum phase in the charge-density-wave $1T-TaS_2$ compound". *npj Quantum Mater.*, vol. 2, no. 1, 2017.

[133] T.-H. Han, J. S. Helton, *et al.*, "Fractionalized excitations in the spin-liquid state of a kagome-lattice antiferromagnet". *Nature*, vol. 492, no. 7429, pp. 406–410, 2012.

[134] S. Chillal, Y. Iqbal, *et al.*, "Evidence for a three-dimensional quantum spin liquid in $PbCuTe_2O_6$". *Nat. Commun.*, vol. 11, no. 1, 2020.

[135] B. Koteswararao, R. Kumar, *et al.*, "Magnetic properties and heat capacity of the three-dimensional frustrated $S = \frac{1}{2}$ antiferromagnet $PbCuTe_2O_6$". *Phys. Rev. B*, vol. 90, 2014.

[136] Z. Ma, J. Wang, *et al.*, "Spin-Glass Ground State in a Triangular-Lattice Compound $YbZnGaO_4$". *Phys. Rev. Lett.*, vol. 120, 2018.

[137] G. Semeghini, H. Levine, *et al.*, "Probing topological spin liquids on a programmable quantum simulator". *Science*, vol. 374, no. 6572, pp. 1242–1247, 2021.

[138] P. W. Anderson, "The Resonating Valence Bond State in La_2CuO_4 and Superconductivity". *Science*, vol. 235, no. 4793, pp. 1196–1198, 1987.

[139] Y.-T. Jia, C.-S. Gong, *et al.*, "Mott Transition and Superconductivity in Quantum Spin Liquid Candidate $NaYbSe_2$". *Chin. Phys. Lett.*, vol. 37, no. 9, 2020.

[140] K. M. Ranjith, S. Luther, *et al.*, "Anisotropic field-induced ordering in the triangular-lattice quantum spin liquid $NaYbSe_2$". *Phys. Rev. B*, vol. 100, 2019.

[141] M. J. P. Gingras and P. A. McClarty, "Quantum spin ice: a search for gapless quantum spin liquids in pyrochlore magnets". *Rep. Prog. Phys.*, vol. 77, no. 5, 2014.

[142] N. Shannon, O. Sikora, *et al.*, "Quantum Ice: A Quantum Monte Carlo Study". *Phys. Rev. Lett.*, vol. 108, 2012.

[143] L. Brewer, "Systematics of the Properties of the Lanthanides". *Systematics and the Properties of the Lanthanides*. Ed. by Shyama P. S. Dordrecht, Hollan: D. Reidel Publishing Company, 1983.

[144] S. Onoda and Y. Tanaka, "Quantum Melting of Spin Ice: Emergent Cooperative Quadrupole and Chirality". *Phys. Rev. Lett.*, vol. 105, 2010.

[145] L. Savary and L. Balents, "Disorder-Induced Quantum Spin Liquid in Spin Ice Pyrochlores". *Phys. Rev. Lett.*, vol. 118, 2017.

[146] S. Crampin, *Lecture notes in Condensed Matter Physics 1*. 2017.

[147] J. R. Hook and H. E. Hall, *Solid States Physics*. University of Manchester: Manchester Physics Series, 2013.

[148] S. W. Lovesey, *Theory of Neutron Scattering from Condensed Matter*. Oxford, England: Clarendon Press, 1984.

[149] G. L. Squires, *Introduction to the Theory of Thermal Neutron Scattering*. Cambridge, England: Cambridge University Press, 2012.

[150] D. S. Sivia, *Elementary Scattering Theory: For X-ray and Neutron Users*. Oxford, England: Oxford University Press, 2011.

[151] R. Serimaa, *Lecture notes in X-ray methods for nanoscience*. 2015.

[152] V. F. Sears, "Neutron scattering lengths and cross sections". *Neutron News*, vol. 3, no. 3, pp. 26–37, 1992.

[153] G. Shirane, S. M. Shapiro, and J. M. Tranquada, *Neutron Scattering with a Triple-Axis Spectrometer*. Cambridge, England: Cambridge University Press, 2002.

[154] M. Enderle, "Neutrons and magnetism". *JDN*, vol. 13, 2014.

[155] P. M. Gehring, *Lecture notes in Basic Elements of Neutron Inelastic Scattering*. 2012.

[156] A. J. Jacobson, B. C. Tofield, and B. E. F. Fender, "The magnetic form factor of Mn^{2+}in MnO by powder neutron diffraction". *J. Phys. C: Solid State Phys.*, vol. 6, no. 9, pp. 1615–1622, 1973.

[157] R. Pynn, "Neutron Scattering—A Non-destructive Microscope for Seeing Inside Matter". *Neutron Applications in Earth, Energy and Environmental Sciences*. Ed. by L. Liang, R. Rinaldi, and H. Schober. Boston, MA: Springer US, 2009.

[158] R. Scherm and B. Fåk, "Inelastic Neutron Scattering: Introduction". *Neutron and X-ray Spectroscopy*. Ed. by Françoise Hippert, Erik Geissler, *et al.* Dordrecht, The Netherlands: Springer Netherlands, 2006.

[159] Q. Berrod, K. Lagrené, *et al.*, "Inelastic and quasi-elastic neutron scattering. Application to soft-matter". *EPJ Web of Conferences*, vol. 188, 2018.

[160] U. Walter, "Treating crystal field parameters in lower than cubic symmetries". *J. Phys. Chem. Solids.*, vol. 45, no. 4, pp. 401–408, 1984.

[161] A. T. Boothroyd, C. H. Gardiner, *et al.*, "Localized $4f$ States and Dynamic Jahn-Teller Effect in PrO_2". *Phys. Rev. Lett.*, vol. 86, pp. 2082–2085, 2001.

[162] B. Lake, *Lecture notes in Measuring Spin-Waves*. 2021.

[163] B. J. Campbell, R. Osborn, *et al.*, "Structure of nanoscale polaron correlations in $La_{1.2}Sr_{1.8}Mn_2O_7$". *Phys. Rev. B*, vol. 65, 2001.

[164] R. A. Cowley, S. N. Gvasaliya, *et al.*, "Relaxing with relaxors: a review of relaxor ferroelectrics". *Adv. Phys.*, vol. 60, no. 2, pp. 229–327, 2011.

[165] M. T. Hutchings, K. Clausen, *et al.*, "Investigation of thermally induced anion disorder in fluorites using neutron scattering techniques". *J. Phys. C: Solid State Phys.*, vol. 17, no. 22, pp. 3903–3940, 1984.

[166] S.-H. Lee, C. Broholm, *et al.*, "Emergent excitations in a geometrically frustrated magnet". *Nature*, vol. 418, no. 6900, pp. 856–858, 2002.

[167] J. R. Stewart, P. P. Deen, *et al.*, "Disordered materials studied using neutron polarization analysis on the multi-detector spectrometer, D7". *J. Appl. Crystallogr.*, vol. 42, no. 1, pp. 69–84, 2009.

[168] I. Mirebeau, "Diffuse scattering". *EPJ Web Conf.*, vol. 155, 2017.

[169] J. R. Stewart, "Disordered materials studied using neutron polarization analysis". *Collection de la Société Française de la Neutronique*, vol. 7, pp. 173–197, 2007.

[170] D. Hohlwein, J.-U. Hoffmann, and R. Schneider, "Magnetic interaction parameters from paramagnetic diffuse neutron scattering in MnO". *Phys. Rev. B*, vol. 68, 2003.

[171] D. A. Keen and A. L. Goodwin, "The crystallography of correlated disorder". *Nature*, vol. 521, no. 7552, pp. 303–309, 2015.

[172] J. P. Goff, W. Hayes, *et al.*, "Defect structure of yttria-stabilized zirconia and its influence on the ionic conductivity at elevated temperatures". *Phys. Rev. B*, vol. 59, pp. 14202–14219, 1999.

[173] D. A. Keen, "A comparison of various commonly used correlation functions for describing total scattering". *J. Appl. Crystallogr.*, vol. 34, no. 2, pp. 172–177, 2001.

[174] H. E. Fischer, A. C. Barnes, and P. S. Salmon, "Neutron and x-ray diffraction studies of liquids and glasses". *Rep. Prog. Phys.*, vol. 69, no. 1, pp. 233–299, 2005.

[175] G. M. King, *Lecture notes in Introduction to Pair Distribution Function Analysis*. 2015.

[176] X. Wang, S. Tan, *et al.*, "Pair distribution function analysis: Fundamentals and application to battery materials". *Chin. Phys. B*, vol. 29, no. 2, 2020.

[177] J. Schweizer, "CHAPTER 4 - Polarized Neutrons and Polarization Analysis". *Neutron Scattering from Magnetic Materials*. Ed. by T. Chatterji. Amsterdam: Elsevier Science, 2006.

[178] S. Langridge, *Lecture notes in Polarised Neutrons: Theoretical and Experimental Techniques for the Study of Atomic, Molecular and Nanoscale Systems*. 2021.

[179] S. M. Blinder, "Chapter 18 - Nuclear magnetic resonance". *Introduction to Quantum Mechanics (Second Edition)*. Ed. by S. M. Blinder. Second Edition. San Diego: Academic Press, 2021.

[180] R. M. Moon, T. Riste, and W. C. Koehler, "Polarization Analysis of Thermal-Neutron Scattering". *Phys. Rev.*, vol. 181, pp. 920–931, 1969.

[181] W. Schweika, "XYZ-polarisation analysis of diffuse magnetic neutron scattering from single crystals". *J. Phys. Conf. Ser.*, vol. 211, 2010.

[182] O. Schärpf and H. Capellmann, "The XYZ-difference method with polarized neutrons and the separation of coherent, spin incoherent, and magnetic scattering cross sections in a multidetector". *Phys. Status Solidi A, Applied Research*, vol. 135, no. 2, pp. 359–379, 1993.

[183] *Description of the ILL high-flux reactor*. https://www.ill.eu/reactor-and-safety/high-flux-reactor/technical-characteristics. Accessed: 2022/02/20.

[184] *Characteristics of a pulsed source*. https://www.isis.stfc.ac.uk/Pages/Characteristics-of-a-pulsed-source.aspx. Accessed: 2022/02/20.

[185] *How SNS Works*. https://neutrons.ornl.gov/content/how-sns-works. Accessed: 2022/02/20.

[186] D. A. Keen, M. J. Gutmann, and C. C. Wilson, "SXD – the single-crystal diffractometer at the ISIS spallation neutron source". *J. Appl. Crystallogr.*, vol. 39, no. 5, pp. 714–722, 2006.

[187] *SXD*. https://www.isis.stfc.ac.uk/Pages/sxd.aspx. Accessed: 2022/02/27.

[188] F. Mezei, "Neutron spin echo: A new concept in polarized thermal neutron techniques". *Zeitschrift für Physik A Hadrons and nuclei*, vol. 255, no. 2, pp. 146–160, 1972.

[189] *D7 Diffuse Scattering Spectrometer*. https://www.ill.eu/users/instruments/instruments-list/d7/characteristics. Accessed: 2022/02/27.

[190] T. Fennell, L. Mangin-Thro, *et al.*, "Wavevector and energy resolution of the polarized diffuse scattering spectrometer D7". *Nucl. Instrum. Methods. Phys. Res. A*, vol. 857, pp. 24–30, 2017.

[191] L. Mangin-Thro, "Ordre magnétique à q=0 dans les cuprates supraconducteurs à haute température critique". PhD thesis. Université Paris-Saclay, Paris, France, 2016.

[192] R. I. Smith, S. Hull, *et al.*, "The upgraded Polaris powder diffractometer at the ISIS neutron source". *Rev. Sci. Instrum.*, vol. 90, no. 11, 2019.

[193] J. Neuefeind, M. Feygenson, *et al.*, "The Nanoscale Ordered MAterials Diffractometer NOMAD at the Spallation Neutron Source SNS". *Nucl. Instrum. Methods. Phys. Res. B*, vol. 287, pp. 68–75, 2012.

[194] *Polaris Technical Information*. https://www.isis.stfc.ac.uk/Pages/Polaris-technical-information.aspx. Accessed: 2022/02/27.

[195] *Nanoscale-Ordered Materials Diffractometer NOMAD — BL-1B — SNS*. https://neutrons.ornl.gov/nomad. Accessed: 2022/02/24.

[196] *MARI*. https://www.isis.stfc.ac.uk/Pages/mari.aspx. Accessed: 2022/02/26.

[197] G. E. Granroth, A I Kolesnikov, *et al.*, "SEQUOIA: A Newly Operating Chopper Spectrometer at the SNS". *J. Phys. Conf. Ser.*, vol. 251, 2010.

[198] *Science on MARI*. https://www.isis.stfc.ac.uk/Pages/Science-on-MARI.aspx. Accessed: 2022/02/26.

[199] *MARI technical specification*. https://www.isis.stfc.ac.uk/Pages/MARI-technical-specification.aspx. Accessed: 2022/02/26.

[200] *Fine-Resolution Fermi Chopper Spectrometer SEQUOIA — BL-17 — SNS*. https://neutrons.ornl.gov/sequoia. Accessed: 2022/02/24.

[201] *LET*. https://www.isis.stfc.ac.uk/Pages/let.aspx. Accessed: 2022/02/26.

[202] R.I. Bewley, J.W. Taylor, and S.M. Bennington., "LET, a cold neutron multi-disk chopper spectrometer at ISIS". *Nucl. Instrum. Methods. Phys. Res. A*, vol. 637, no. 1, pp. 128–134, 2011.

[203] *LET Science*. `https://www.isis.stfc.ac.uk/Pages/Let-science.aspx`. Accessed: 2022/02/26.

[204] N. Metropolis and S. Ulam, "The Monte Carlo Method". *J. Am. Stat. Assoc.*, vol. 44, no. 247, pp. 335–341, 1949.

[205] R. L. McGreevy and L. Pusztai, "Reverse Monte Carlo Simulation: A New Technique for the Determination of Disordered Structures". *Mol. Simul.*, vol. 1, no. 6, pp. 359–367, 1988.

[206] D. F. Bowman, "The defect structure and magnetic ground state of ytterbium titanate". PhD thesis. Royal Holloway University of London, London, United Kingdom, 2018.

[207] *RMCProfile*. `https://rmcprofile.pages.ornl.gov/`. Accessed: 2022/03/12.

[208] M. D. Segall, Philip J D Lindan, *et al.*, "First-principles simulation: ideas, illustrations and the CASTEP code". *J. Phys. Condens. Matter*, vol. 14, no. 11, pp. 2717–2744, 2002.

[209] T. J. Hicken, "Muon-spin spectroscopy studies of materials hosting topological magnetic states". PhD thesis. Durham University, Durham, United Kingdom, 2021.

[210] N. Argaman and G. Makov, "Density functional theory: An introduction". *Am. J. Phys.*, vol. 68, no. 1, pp. 69–79, 2000.

[211] P. Hohenberg and W. Kohn, "Inhomogeneous Electron Gas". *Phys. Rev.*, vol. 136, B864–B871, 1964.

[212] W. Kohn and L. J. Sham, "Self-Consistent Equations Including Exchange and Correlation Effects". *Phys. Rev.*, vol. 140, A1133–A1138, 1965.

[213] S. J. Clark, Matthew D. Segall, *et al.*, "First principles methods using CASTEP". *Zeitschrift für Kristallographie - Crystalline Materials*, vol. 220, no. 5-6, pp. 567–570, 2005.

[214] A. Scheie, "*PyCrystalField*: software for calculation, analysis and fitting of crystal electric field Hamiltonians". *J. Appl. Crystallogr.*, vol. 54, no. 1, pp. 356–362, 2021.

[215] M. T. Hutchings, "Point-Charge Calculations of Energy Levels of Magnetic Ions in Crystalline Electric Fields". *Solid State Phys.*, vol. 16, pp. 227–273, 1964.

[216] K. W. H. Stevens, "Matrix Elements and Operator Equivalents Connected with the Magnetic Properties of Rare Earth Ions". *Proc. Phys. Soc. A*, vol. 65, no. 3, pp. 209–215, 1952.

[217] G. Sala, D. D. Maharaj, *et al.*, "Crystal field excitations from Yb^{3+} ions at defective sites in highly stuffed $Yb_2Ti_2O_7$". *Phys. Rev. B*, vol. 97, 2018.

[218] O. Moze, "Chapter 4 Crystal field effects in intermetallic compounds studied by inelastic neutron scattering". Vol. 11. Handbook of Magnetic Materials. Elsevier, pp. 493–624, 1998.

[219] H. M. Rietveld, "Line profiles of neutron powder-diffraction peaks for structure refinement". *Acta Crystallogr.*, vol. 22, no. 1, pp. 151–152, 1967.

[220] H. M. Rietveld, "A profile refinement method for nuclear and magnetic structures". *J. Appl. Crystallogr.*, vol. 2, no. 2, pp. 65–71, 1969.

[221] B. H. Toby, "R factors in Rietveld analysis: How good is good enough?" *Powder Diffraction*, vol. 21, no. 1, pp. 67–70, 2006.

[222] *What is FullProf?* `https://www.ill.eu/sites/fullprof/php/programs8809.html?pagina=FullProf`. Accessed: 2022/03/06.

[223] G. Sala, M. J. Gutmann, *et al.*, "Vacancy defects and monopole dynamics in oxygen-deficient pyrochlores". *Nat. Mater*, vol. 13, no. 5, 2014.

[224] D. F. Bowman, E. Cemal, *et al.*, "Role of defects in determining the magnetic ground state of ytterbium titanate". *Nat. Commun.*, vol. 10, no. 1, 2019.

[225] R. D. Shannon, "Revised effective ionic radii and systematic studies of interatomic distances in halides and chalcogenides". *Acta Crystallogr. A*, vol. 32, no. 5, pp. 751–767, 1976.

[226] A. Sen and R. Moessner, "Topological Spin Glass in Diluted Spin Ice". *Phys. Rev. Lett.*, vol. 114, 2015.

[227] M. Janoschek, P. Das, *et al.*, "The valence-fluctuating ground state of plutonium". *Sci. Adv.*, vol. 1, no. 6, 2015.

[228] B. Tomasello, C. Castelnovo, *et al.*, "Single-ion anisotropy and magnetic field response in the spin-ice materials $Ho_2Ti_2O_7$ and $Dy_2Ti_2O_7$". *Phys. Rev. B*, vol. 92, 2015.

[229] G. Sala, C. Castelnovo, *et al.*, "Magnetic Coulomb Fields of Monopoles in Spin Ice and Their Signatures in the Internal Field Distribution". *Phys. Rev. Lett.*, vol. 108, 2012.

[230] O. Benton, "Instabilities of a U(1) Quantum Spin Liquid in Disordered Non-Kramers Pyrochlores". *Phys. Rev. Lett.*, vol. 121, 2018.

[231] N. Martin, P. Bonville, *et al.*, "Disorder and Quantum Spin Ice". *Phys. Rev. X*, vol. 7, 2017.

[232] V. K. Anand, L. Opherden, *et al.*, "Physical properties of the candidate quantum spin-ice system $Pr_2Hf_2O_7$". *Phys. Rev. B*, vol. 94, 2016.

[233] J.-J. Wen, S. M. Koohpayeh, *et al.*, "Disordered Route to the Coulomb Quantum Spin Liquid: Random Transverse Fields on Spin Ice in $Pr_2Zr_2O_7$". *Phys. Rev. Lett.*, vol. 118, 2017.

[234] X. Z. Lu, X. Wu, and H. J. Xiang, "General microscopic model of magnetoelastic coupling from first principles". *Phys. Rev. B*, vol. 91, 2015.

[235] R. Sibille, E. Lhotel, *et al.*, "Candidate quantum spin ice in the pyrochlore $Pr_2Hf_2O_7$". *Phys. Rev. B*, vol. 94, 2016.

[236] C. Mauws, N Hiebert, *et al.*, "Magnetic ordering in the Ising antiferromagnetic pyrochlore Nd_2ScNbO_7". *J. Phys. Condens. Matter*, vol. 33, no. 24, 2021.

[237] F. R. Foronda, F. Lang, *et al.*, "Anisotropic Local Modification of Crystal Field Levels in Pr-Based Pyrochlores: A Muon-Induced Effect Modeled Using Density Functional Theory". *Phys. Rev. Lett.*, vol. 114, 2015.

[238] H. A. Mook, "Temperature Dependence of the Spin Dynamics of EuO". *Phys. Rev. Lett.*, vol. 46, pp. 508–511, 1981.

[239] M. F. Collins and C. G. Windsor, "The paramagnetic scattering of neutrons from an Ising system". *Proc. Phys. Soc.*, vol. 90, no. 4, pp. 1015–1018, 1967.

[240] Y. Tokiwa, T. Yamashita, *et al.*, "Discovery of Emergent Photon and Monopoles in a Quantum Spin Liquid". *J. Phys. Soc. Jpn*, vol. 87, no. 6, 2018.